

Micromechanical modelling of strain path dependency in FCC metals

Citation for published version (APA):

Viatkina, E. M. (2005). *Micromechanical modelling of strain path dependency in FCC metals*. [Phd Thesis 1 (Research TU/e / Graduation TU/e), Mechanical Engineering]. Technische Universiteit Eindhoven. <https://doi.org/10.6100/IR613593>

DOI:

[10.6100/IR613593](https://doi.org/10.6100/IR613593)

Document status and date:

Published: 01/01/2005

Document Version:

Publisher's PDF, also known as Version of Record (includes final page, issue and volume numbers)

Please check the document version of this publication:

- A submitted manuscript is the version of the article upon submission and before peer-review. There can be important differences between the submitted version and the official published version of record. People interested in the research are advised to contact the author for the final version of the publication, or visit the DOI to the publisher's website.
- The final author version and the galley proof are versions of the publication after peer review.
- The final published version features the final layout of the paper including the volume, issue and page numbers.

[Link to publication](#)

General rights

Copyright and moral rights for the publications made accessible in the public portal are retained by the authors and/or other copyright owners and it is a condition of accessing publications that users recognise and abide by the legal requirements associated with these rights.

- Users may download and print one copy of any publication from the public portal for the purpose of private study or research.
- You may not further distribute the material or use it for any profit-making activity or commercial gain
- You may freely distribute the URL identifying the publication in the public portal.

If the publication is distributed under the terms of Article 25fa of the Dutch Copyright Act, indicated by the "Taverne" license above, please follow below link for the End User Agreement:

www.tue.nl/taverne

Take down policy

If you believe that this document breaches copyright please contact us at:

openaccess@tue.nl

providing details and we will investigate your claim.

Micromechanical modelling of strain path dependency in FCC metals

Ekaterina Viatkina



Netherlands Institute
for Metals Research

This research was carried out under project number MC2.00079 in the framework of the Strategic Research Programme of the Netherlands Institute for Metals Research (NIMR).

CIP-DATA LIBRARY TECHNISCHE UNIVERSITEIT EINDHOVEN

Viatkina, Ekaterina

Micromechanical modelling of strain path dependency in FCC metals
by Ekaterina Viatkina. – Eindhoven : Technische Universiteit Eindhoven, 2005.

Proefschrift. – ISBN-10: 90-77172-19-x

– ISBN-13: 978-90-77172-19-3

This thesis has been prepared with \LaTeX 2 ϵ .

Reproduction: Universiteitsdrukkerij TU Eindhoven, Eindhoven, The Netherlands.

Micromechanical modelling of strain path dependency in FCC metals

PROEFSCHRIFT

ter verkrijging van de graad van doctor
aan de Technische Universiteit Eindhoven,
op gezag van de Rector Magnificus, prof.dr.ir. C.J. van Duijn,
voor een commissie aangewezen door het College voor Promoties
in het openbaar te verdedigen op
woensdag 21 december 2005 om 16.00 uur

door

Ekaterina Viatkina

geboren te Perm, Rusland

Dit proefschrift is goedgekeurd door de promotor:

prof.dr.ir. M.G.D. Geers

Copromotor:

dr.ir. W.A.M. Brekelmans

Contents

Summary	vii
Samenvatting	ix
1 Introduction	1
1.1 Forming limits	1
1.2 Strain path dependency in FCC metals	2
1.3 Objective and outline	4
2 A crystal plasticity based estimate for forming limit diagrams from textural inhomogeneities	7
2.1 Introduction	8
2.2 Crystal plasticity model	10
2.3 Finite element approximation	12
2.4 Localisation criteria	13
2.5 Forming limit analysis	14
2.6 Conclusions	18
3 Phenomenological modelling of strain path change effects based on cell structure evolution	19
3.1 Introduction	20
3.1.1 Experimental observations of the dislocation cell structure	21
3.1.2 Objectives	23
3.2 Composite model	24
3.3 Evolution of the internal variables	25
3.3.1 Monotonic deformation	26
3.3.2 Cell dissolution	27
3.3.3 Cell disruption	29
3.4 Results	29
3.5 Discussion	35
3.6 Conclusions	37
4 Modelling of the internal stresses in dislocation cell structures	39
4.1 Introduction	40
4.1.1 Experimental observations of the dislocation cell structure	42
4.2 Composite cell structure model	44
4.3 Constitutive equations	47
4.4 Statistically stored dislocations	50
4.5 Internal stress	50
4.5.1 Geometrically necessary dislocations	50

4.5.2	Approximation of the internal stress field	57
4.6	Computation of the internal stress	61
4.6.1	Continuum case	61
4.6.2	Discrete approximation	64
4.7	Numerical analysis	66
4.7.1	Parameter identification	66
4.7.2	Model verification	69
4.8	Discussion	73
4.8.1	Monotonic deformation	73
4.8.2	Strain path change: Reloading yield stress	75
4.8.3	Strain path change: Transient hardening	80
4.8.4	Reversed loading	81
4.8.5	Composite model	83
4.8.6	Internally stored energy as a function of cell geometry	83
4.9	Conclusions	85
5	Modelling the dislocation structure evolution upon stress reversal	89
5.1	Introduction	90
5.1.1	Experimental observations of the dislocation structure	91
5.2	Cell structure model	93
5.3	Dislocation density evolution	94
5.3.1	Dislocation density fundamentals	94
5.3.2	Dislocation evolution in the cell structure	96
5.3.3	Annihilation and statistical remobilisation	98
5.3.4	Dislocation flux $\rho^{c \rightarrow w}$	99
5.3.5	Dislocation structure evolution after a strain path change	100
5.4	Numerical analysis	107
5.4.1	Parameter identification	107
5.4.2	Model verification	109
5.5	Discussion	111
5.5.1	Stress reversal: effect of the internal stress	111
5.5.2	Stress reversal: Effect of the dislocation evolution	113
5.5.3	Stress reversal: transient hardening	115
5.5.4	Strain path change effect	117
5.6	Conclusions	118
6	The role of plastic slip anisotropy in the modelling of strain path change effects	121
6.1	Introduction	121
6.2	Cell structure model	123
6.2.1	Crystal plasticity	124
6.2.2	Statistically stored dislocations	125
6.2.3	Polycrystal model	127
6.3	Results	127
6.3.1	Polycrystal with random grain orientation	129
6.3.2	Polycrystal with cube texture	130
6.4	Conclusions	131
7	Conclusions	133
	Bibliography	137
	Acknowledgements	145
	Curriculum Vitae	147

Summary

Most industrial metal forming processes are characterised by a complex strain path history, which results from the sequential processing steps following each other. A change in strain path may have a significant effect on the mechanical response of metals. Macroscopically, the effect of a certain prestrain becomes manifest through an altered reloading yield stress, transient hardening and strain at rupture, compared to a monotonic deformation path of the same base material. Due to the complexity and significance of these effects numerical simulations are an efficient tool for optimisation of forming operations. This thesis focuses on the micromechanical modelling of strain path change effects with the aim to supply essential fundamental knowledge leading to an adequate model for numerical simulations.

The physical origins of the strain path dependency reside in the textural anisotropy of the material, anisotropy of the dislocation structure and the slip anisotropy. Each of these factors is addressed in this thesis. In the first part, a crystal plasticity based procedure to determine forming limit diagrams from textural inhomogeneities is proposed. The following three parts concentrate on continuum modelling of dislocation structures and their effects on the macroscopical behaviour. In the last part, the proposed model is extended to incorporate crystal plasticity aspects and the associated slip anisotropy effects.

After an introduction to the subject in the first chapter, the effect of deformation texture on the formability is dealt with in chapter two of the thesis. The initial crystallographic orientation inhomogeneity is considered as a natural microstructure imperfection, potentially triggering deformation instabilities. The structural instability criterion is used as an approximate localisation indicator. A viscous crystal plasticity approach is employed for the microscopic material behaviour which is implemented in a finite element framework. Proportional loading of a metal sheet with an initially random distribution of the crystal lattice orientations has been analysed using different uniform strain paths. The results demonstrate the ability of the method to describe the development of strain localisation bands, from which the formability can be assessed.

Next, the attention is concentrated on dislocation cell structures in chapter three. Their presence and evolution in a material is commonly associated with an altered reloading yield stress and transient hardening after a strain path change. The present research deals with the explicit description of the dislocation cell structure. First, a phenomenological model is proposed to capture the main influence of a cell structure on the overall mechanical response. The structure is modelled as a composite consisting of a periodic array of two phases: hard cell walls and soft cell interiors. For the scalar internal variables figuring in the model –cell size, wall thickness, and dislocation density inside the walls– evolution equations are proposed to

describe the cell development, dissolution and disruption. The simulations show a dependency of the reloading yield stress on the amount of prestrain and the amplitude of the strain path change. The predictions are in a good agreement with experimental data, including the cross and Bauschinger effects.

In the fourth chapter the cell structure model is enhanced to gain more physical insight. Investigation of the dislocation interactions in the cell structure material necessitates the introduction of geometrically necessary dislocations (GNDs) at the interfaces between the walls and the cell interiors. GNDs naturally induce a long range internal stress field in the material. For the cell structure material, the internal stress is found as a function of the plastic deformation incompatibility and the cell geometry, and is incorporated in the model via kinematic hardening. The predicted macroscopic effects of moderate strain path changes are consistent with experimental data. A numerical analysis showed that the reloading yield stress after moderate strain path changes is determined by the influence of the geometrical anisotropy due to the cell structure morphology and by the internal stresses developed during prestraining. The transient hardening behaviour after a strain path change is related to the adjustment of the internal stresses to the new loading.

The fifth chapter deals with the evolution of statistically stored dislocations (SSDs). Evolution equations for SSD densities inside the cells and walls are defined. They describe the formation of the cell structure during monotonic deformation as well as the dissolution of the cells after a strain path change. Including these equations in the cell structure model results in improved predictions for large strain path changes. The simulation results show a good agreement with experimental data, including the well-known Bauschinger effect.

Finally, the cell structure model is modified to include crystal plasticity in chapter six. This allows slip anisotropy and texture to be accounted for, but requires a proper adjustment of the model to deal with polycrystal material. The proposed model is used to analyse the combined effect of the dislocation structure, the slip anisotropy and the texture on the macroscopic behaviour after a strain path change.

Summarising, a micromechanical approach to the modelling of the macroscopic material behaviour of metals containing a dislocation cell structure is proposed. While the attention is mainly focused on the cell structure, the effects of the slip and texture anisotropy are also addressed. The developed approach is capable of describing material behaviour for deformation processes with strain path changes. The implementation of the model is well established, resulting in a computationally efficient method enabling its use in macroscopic engineering computations.

Samenvatting

De meeste industriële metaal omvormprocessen worden gekarakteriseerd door een complexe rekgeschiedenis. Deze is het gevolg van opeenvolgende bewerkingsstappen. Een verandering van rekweg kan een significante invloed hebben op de mechanische responsie van metalen. Vergeleken met monotone vervorming van een bepaald materiaal, manifesteert een bepaalde voordeformatie zich op macroscopisch niveau door een veranderde vloeispanning na herbelasting, tijdelijke versteviging, en een veranderde breukrek. Vanwege de complexiteit en het belang van deze effecten, zijn numerieke simulaties een efficiënt middel voor de optimalisatie van vormgevingsprocessen. Dit proefschrift richt zich op de micromechanische modellering van rekwegveranderingseffecten met het doel essentiële fundamentele kennis te vergaren, leidend tot een geschikt model voor numerieke simulaties.

De fysische achtergrond van de rekweg afhankelijkheid moet gezocht worden in de anisotropie van de textuur van het materiaal, de anisotropie van de dislocatie structuur en de anisotropie van de plastische slip. Elk van deze factoren wordt afzonderlijk behandeld in dit proefschrift. In het eerste gedeelte wordt een procedure gebaseerd op de theorie der kristalplasticiteit voorgesteld om vervormingslimietdiagrammen te bepalen uitgaande van de inhomogeniteit van de textuur. De volgende drie delen richten zich op de continuüm modellering van de dislocatie structuren en hun effecten op het macroscopisch gedrag van het materiaal. In het laatste gedeelte wordt het voorgestelde model uitgebreid met aspecten van de kristal plasticiteit theorie om slip anisotropie effecten in rekening te brengen.

Na een introductie van het onderwerp in het eerste hoofdstuk, wordt in het tweede hoofdstuk van dit proefschrift de invloed van deformatie textuur op de vervormbaarheid behandeld. De inhomogene initiële oriëntatie van de kristallen wordt beschouwd als een natuurlijke microstructurele imperfectie, die potentieel kan leiden tot deformatie instabiliteit. Een structureel instabiliteitscriterium wordt gebruikt om lokalisatie te detecteren. Viskeuze kristalplasticiteitstheorie is toegepast voor de beschrijving van het microscopische materiaalgedrag. Ter bepaling van de macroscopische responsie is de theorie geïmplementeerd in een eindige elementen methode programma. De proportionele belasting van een metalen plaat met een initieel willekeurige verdeling van de kristal rooster oriëntaties is geanalyseerd uitgaande van verschillende uniforme rekwegen. De resultaten tonen het vermogen van de methode om de ontwikkeling van reklokalisatiebanden te beschrijven, aan de hand waarvan de vervormbaarheid beoordeeld kan worden.

Vervolgens wordt in hoofdstuk drie de aandacht gevestigd op celstructuren gevormd door ongelijkmatig verdeelde dislocatiedichtheden. Met hun aanwezigheid en evolutie in een materiaal wordt normaal gesproken met een veranderde vloeispanning en tijdelijke

versteving na herbelasting in een andere richting geassocieerd. Het huidige onderzoek behandelt de expliciete beschrijving van de dislocatiecelstructuur. Allereerst wordt een fenomenologisch model gepresenteerd met de belangrijkste invloeden van de celstructuur op de totale mechanische responsie. De dislocatiecelstructuur is gemodelleerd als een composiet, bestaande uit twee periodiek geordende fasen: harde celwanden, met een relatief hoge dislocatiedichtheid, en een zachte celkern, met een relatief lage dislocatiedichtheid. Voor de interne variabelen die een rol spelen in het model –de afmetingen van de cellen, de dikte van de celwanden, en de dislocatiedichtheden van deze componenten– worden evolutie vergelijkingen geponeerd die de celontwikkeling, celdissolutie en celverstoring beschrijven. De simulaties behorende bij een plotselinge rekwegverandering tonen een afhankelijkheid van de vloeispanning op de hoeveelheid vooraf ondergane rek en de grootte van de verandering. De voorspellingen laten een goede overeenkomst zien met experimentele gegevens, onder andere voor de ‘cross test’ en voor volledige omkering van de belasting (met het Bauschinger effect).

In het vierde hoofdstuk wordt het celstructuurmodel uitgebreid om een beter fysisch inzicht te verkrijgen in het materiaalgedrag. Onderzoek van de interacties tussen dislocaties in het celstructuurmateriaal maakt het nodig om geometrisch noodzakelijke dislocaties (GNDs) te introduceren op de grenzen tussen de celwanden en de celkernen. GNDs veroorzaken door hun ordening een ‘long-range’ spanningsveld in het celstructuurmateriaal waarbij de interne spanningen kunnen worden bepaald als een functie van de plastische deformatie incompatibiliteit en de celgeometrie. De interne spanningen komen in het model tot uitdrukking in de vorm van kinematische versteving. De voorspelde macroscopische effecten veroorzaakt door beperkte veranderingen van de rekweg zijn consistent met experimentele waarnemingen. De numerieke analyse wees uit dat de vloeispanning na herbelasting bepaald wordt door de geometrische anisotropie veroorzaakt door de celstructuurmorfologie en door de interne spanningen opgebouwd tijdens de initiële deformatie. Het tijdelijke verstevinggedrag na een verandering van de rekweg is gerelateerd aan het aanpassen van de interne spanningen aan de nieuwe belasting.

Het vijfde hoofdstuk behandelt de evolutie van de statistisch opgeslagen dislocaties (SSDs). Vergelijkingen voor de ontwikkeling van de SSD dichtheden in de celkernen en de celwanden worden opgesteld. De ontwikkeling van de celstructuur gedurende monotone deformatie wordt beschreven, zowel als de afbraak van de cellen na een rekwegverandering. De resultaten van de simulaties laten een goede overeenkomst zien met experimentele gegevens, inclusief het bekende Bauschinger effect.

Tenslotte wordt in hoofdstuk zes het modelverfijnd door het gedrag van de componenten te beschrijven met de theorie der kristalplasticiteit. Op deze manier kunnen slip anisotropie en textuur mee in beschouwing genomen worden, na een herformulering van het model ten behoeve voor toepassing op een polykristallijn. Het aangepaste model is gebruikt om een analyse uit voeren van het gecombineerde effect van de dislocatiestructuur, de anisotropie van de kristalformatie en de textuur, op het macroscopische materiaalgedrag na een rekwegverandering.

Samengevat, een micromechanisch model is behandeld om het macroscopisch gedrag van een metaal met een celstructuur, ontstaan door een ongelijkmatige verdeling van dislocaties, te beschrijven. De aandacht is vooral gevestigd op de celstructuur, maar de invloed van de anisotropie van de plastische slip en de textuur worden ook besproken. Met het model kan het materiaalgedrag tijdens complexe deformatieprocessen, inclusief veranderingen in de rekweg, beschreven worden. De implementatie van het model leidt tot een efficiënt

berekeningsalgoritme, dat gebruikt kan worden voor simulaties van het macroscopisch gedrag van configuraties uit de ingenieurspraktijk.

Chapter 1

Introduction

The analysis of the formability of metals is a traditional topic in mechanical engineering, which is still characterised by many open issues. In spite of many decades of research, this field continues to trigger new challenges, especially promoted by industrial progress. The growing need for more precision in forming processes and the exploitation of more complex manufacturing processes, necessitates a better understanding of the relevant micromechanical processes and the development of more sophisticated engineering tools.

The physical origins of the complex deformation behaviour observed for metals, reside, among others, in the textural anisotropy of the material and the anisotropy of the dislocation structures accompanying the plastic deformation. The microscopic deformation mechanisms, associated with the presence and development of these microstructural entities, affect the macroscopical behaviour of a metal, altering its formability.

This thesis addresses two major aspects of the formability analysis of metals, both based on the underlying evolving microstructure: (1) the prediction of forming limits and (2) the prediction of strain path change effects. The following sections shortly highlight the challenges in these fields, from which the research scope of the thesis has been derived.

1.1 Forming limits

In industrial sheet metal forming, localised necking is known to be an important limitation of the formability. For a wide range of metals and loading modes, experimental data on forming limits are collected in handbooks in the form of commonly used forming limit diagrams (FLDs). A forming limit diagram for a given sheet material is a curve in the major strain ε_1 - minor strain ε_2 plane, connecting the loci of failure instabilities for a range of different, usually uniform, strain paths. Fig. 1.1 shows an example of an FLD obtained for uniform and complex strain paths. The experimental determination of FLDs is, however, time consuming and tedious even in the case of pure proportional stretching. Furthermore, the formability in the context of subsequent forming steps depends strongly on the deformation history of the material and therefore demands the investigation of each individual case. The intrinsic strain path dependency that characterises these more complex forming operations, needs to be addressed in detail before trying to predict forming limits in their presence. This is outlined in

section 1.2.

Theoretical formability analyses often deal with the occurrence of a strain instability in a uniform deformation process due to imperfections initially present in the material. This is a realistic approach, since inhomogeneities of either geometrical or material origin are unavoidable in practise. The most popular method widely used in engineering tools is based on the Marciniak-Kuczynski (MK) approach [Marciniak and Kuczynski, 1967], where localised necking is assumed to be initiated through a pre-existing groove-like thickness imperfection. The results obtained with this MK method, however, are very sensitive to the geometry of the initial imperfection prescribed. Since the geometrical input in the model is mostly an assumption, the classical MK approach remains a diagnostic tool rather than a predictive one.

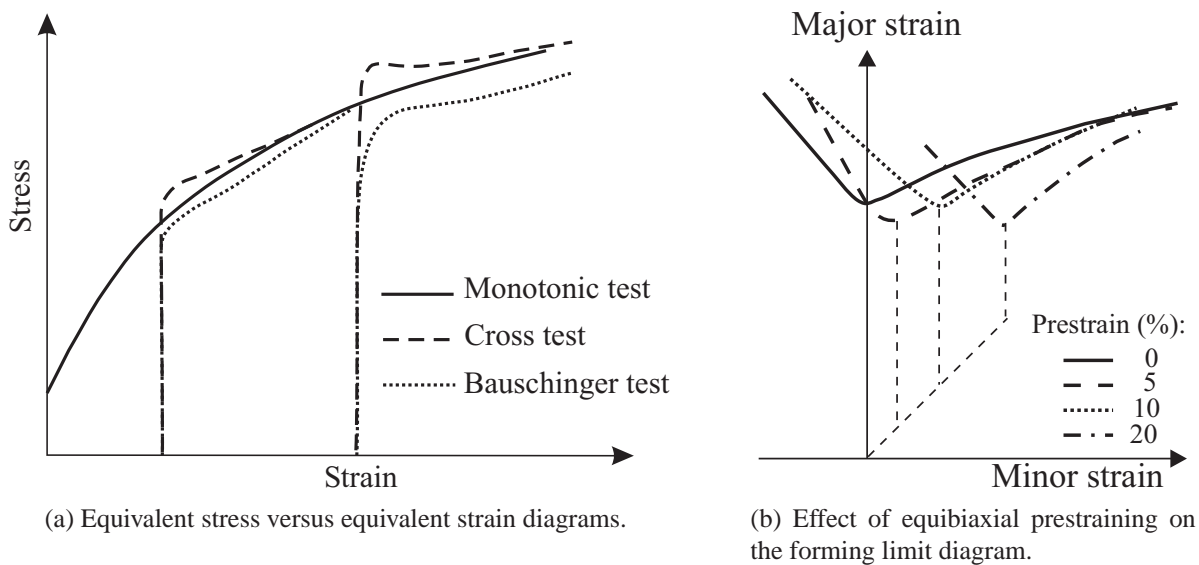


Figure 1.1 — Schematic representation of strain path change effects.

In this thesis, an effort is done to develop a formability tool independent of any geometrical imperfections, allowing the prediction of deformation localisation. The initial texture inhomogeneity is considered as a natural microstructure imperfection, which is present in any real metal, potentially triggering deformation instabilities.

1.2 Strain path dependency in FCC metals

Most of the industrial metal forming processes are characterised by a non-monotonic strain history, in which different processing steps rapidly succeed each other. The induced changes in strain path have a significant influence on the mechanical response of the metal involved, thereby affecting the performance of the final product. Due to the complexity of the strain path change effects, optimisation of forming operations by experimental means is time consuming and expensive. This is the area where numerical simulations can provide a valuable contribution to the designing process. This thesis focuses on the micromechanical modelling of strain path change effects with the aim to supply essential fundamental knowledge leading to an adequate basis for numerical simulations.

Strain path change effects are typically studied with the use of two-step tests. In the first step,

also called the prestrain step, the loading is applied to produce a certain amount of initial deformation in a given direction. Next, the specimen is unloaded and immediately reloaded with a deformation mode different from the initial one. The magnitude of a strain path change is commonly characterised by the measure ϑ :

$$\vartheta = \frac{\dot{\boldsymbol{\epsilon}}_1^p : \dot{\boldsymbol{\epsilon}}_2^p}{\|\dot{\boldsymbol{\epsilon}}_1^p\| \|\dot{\boldsymbol{\epsilon}}_2^p\|} \quad (1.1)$$

where $\dot{\boldsymbol{\epsilon}}_1^p$ and $\dot{\boldsymbol{\epsilon}}_2^p$ are the plastic strain rate tensors prior to and after the strain path change. The Bauschinger and the cross tests are typical examples of loading sequences including a strain path change. The Bauschinger test is defined by $\vartheta = -1$ and the cross test by $\vartheta = 0$.

Macroscopically, the effect of a certain prestrain becomes manifest through an altered reloading yield stress, transient hardening, hardening recovery and failure shift compared to the response during a monotonic deformation of the virgin material. In a quantitative sense, the effect is influenced by the amount of prestrain. Furthermore, the effect is strongly anisotropic and depends on the orientational difference between the successive deformation modes. Typical engineering characteristics of the effect for FCC metals with a high stacking fault energy are schematised in Fig. 1.1. The stress-strain curves in the left figure represent the responses of a previously deformed material, whereby both the amount and orientation of the prestrain have been varied. The amount of prestrain experienced by the material corresponds to the horizontal shift along the global strain axis. Obviously, the response clearly depends on the prestrain mode as well as on the amount of the prestrain applied. The right figure depicts forming limit diagrams for a virgin metal specimen and for specimens prestrained by equibiaxial stretching. Depending on the amount and orientation, prestrain can cause a significant reduction or increase of the formability.

Hardening behaviour of metals physically originates from a complex microstructure evolution. The macroscopic strain path change effect at intermediate strains is commonly associated with the development of dislocation structures under deformation. This work concentrates on the proper understanding and modelling of the contribution of the dislocation cell structure to the strain path change effect.

In undeformed material, the dislocation distribution is close to statistically homogeneous. However, at the beginning of a deformation process, interacting dislocations tend to cluster and form tangles, thereby creating regions with relatively increased dislocation densities. As the strain increases, more dislocations participate in the evolution of the structure and the tangles link up to form dislocation walls which envelop regions relatively free of dislocations. This dislocation network, consisting of areas with low and high dislocation densities, is known as a cell structure, Fig. 1.2.

The dislocation cell structure is formed under deformation and accommodates the current deformation history at the microscopical level. The morphology of the dislocation structure reflects characteristics of the deformation process that created it. After a strain path change, the previously formed dislocation structure becomes 'unstable' under a new loading since its morphology is not 'favourable' anymore. and, moreover, it degenerates by micromechanical mechanisms promoting the new deformation. The resistance and adaptation of the dislocation structure to a new loading is typically associated with the observed macroscopic strain path change effects.

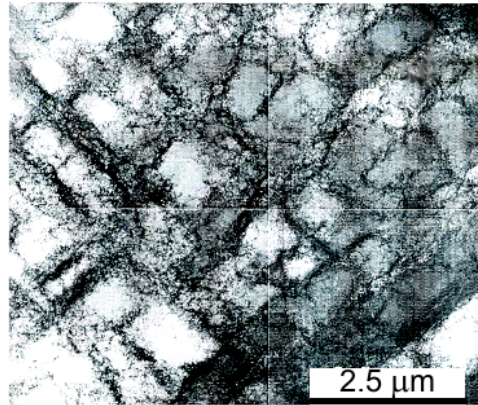


Figure 1.2 — Dislocation cell structure in copper [McCabe et al., 2004].

1.3 Objective and outline

This research concentrates on the micromechanical modelling of the mentioned aspects of the deformation behaviour of FCC metals, from which macroscopic effects should result. The objective of the study is to develop an adequate approach to the modelling of complex deformation processes that incorporates the essential deformation mechanisms in a physically-based manner. From an engineering perspective, the modelling should result in a computationally efficient method which is well applicable in macroscopic engineering computations.

First, the formability effects are addressed in Chapter 2. A computational tool is developed here to predict the formability of metals on the basis of the underlying microstructure, i.e. the texture. The initial crystallographic orientation inhomogeneity is considered as a natural microstructural imperfection, potentially triggering deformation instabilities.

Next, the attention is concentrated on the modelling of the deformation behaviour of metals with a dislocation cell structure, from which the proper prediction of the macroscopic effects of strain path changes should result. The proposed model fits in a ‘material point’ implementation and lends itself for use in macroscopic engineering computations, such as the formability assessment tool introduced in Chapter 2.

The approach introduced in Chapters 3–6 is based on the assumption that the strain path change effects originate from the deformation response of a material with inhomogeneities, which is here provided by a dislocation cell structure. The research addresses the mechanical effect of the presence of a dislocation structure in a material on the macroscopic response. Mesoscopic mechanisms promoting the deformation in an inhomogeneous metal with a cell structure are studied, as well as mechanisms assisting the evolution of the dislocation structure and, consequently, the evolution of the material inhomogeneity. The mechanisms identified as relevant and significant are incorporated in the resulting continuum model.

The analysis done is restricted to moderate deformations of FCC metals with a high stacking fault energy at room temperature. The study concentrates on the dislocation cell structure only. Other types of dislocation structures are left out of consideration.

Chapter 3 proposes a phenomenological relation between the evolution of the cell structure and the strain path change effect. This preliminary study aims to address two questions:

(1) Is the presence and evolution of the cell structure responsible for the strain path change hardening effects? (2) If so, which features of the cell structure and its evolution contribute to the macroscopical effect? The result of this study indicates directions for a detailed modelling of the dislocation structure and the strain path change effects.

The objective of Chapter 4 is to develop a continuum model of the cell structure that incorporates internal stresses in a physically-based manner. The internal stresses are derived here as a natural result of plastic deformation incompatibility. The approach also incorporates the morphology and orientation anisotropy of the cell structure in an idealised manner. The model offers a tool to predict strain path change effects and enables a theoretical study of the internal stress and its influence on the macroscopic behaviour.

In chapter 5 the evolution of the dislocation structure is studied in more detail. The dislocation redistribution in the cell structure upon load reversals is considered with the aim to describe the macroscopical effects after large strain path changes, e.g. the Bauschinger effect. The corresponding dislocation processes are incorporated in the continuum cell structure model via evolution equations for the dislocation densities.

Chapter 6 concentrates on the contribution of plastic slip anisotropy to the strain path change effects. The cell structure model is extended by employing a classical crystal plasticity model for the local material behaviour. The simulation results are compared to the previously obtained predictions to reveal the effect of slip anisotropy on the strain path change effect.

Chapter 2

A crystal plasticity based estimate for forming limit diagrams from textural inhomogeneities

Reproduced from: Viatkina, E.M., Brekelmans, W.A.M., and Geers, M.G.D., (2005). *A crystal plasticity based estimate for forming limit diagrams from textural inhomogeneities*. *Journal of Materials Processing Technology*, 168: pp. 211–218.

2.1 Introduction

In industrial sheet metal forming, localised necking is known to be an important limitation on the formability. For a wide range of metals and loading modes experimental data on forming limits are collected in handbooks in the form of commonly used forming limit diagrams (FLDs). A forming limit diagram for a given sheet material is a curve in the major strain ε_1 - minor strain ε_2 plane, connecting the loci with principal strains at failure instabilities for a range of different, usually uniform, strain paths. Fig. 2.1 shows an example of an FLD obtained for uniform strain paths. FLDs offer a convenient and useful tool for the formability prediction in the analysis of sheet products manufacturing processes. The experimental determination of FLDs is, however, time consuming and tedious even in the case of pure proportional stretching. Furthermore, the formability in the context of subsequent forming steps depends strongly on the deformation history of the material and therefore demands the investigation of each individual case. This actuates the development of an efficient theoretical method for formability prediction.

A variety of theoretical approaches have been developed to predict the forming limits. The first analytical method was proposed by Hill [1952] considering strain instability as a bifurcated state from an initially homogeneous sheet. The original bifurcation analysis was developed to predict the loss of uniformity in the deep-drawing range ($\varepsilon_2 < 0$). Later the analysis was extended by Stören [1975] to permit the bifurcation prediction in the whole relevant range of strain ratios. The perturbation technique of Molinari, e.g. [Fressengeas and Molinari, 1987; Boudeau and Gelin, 2000], also makes use of a stability analysis.

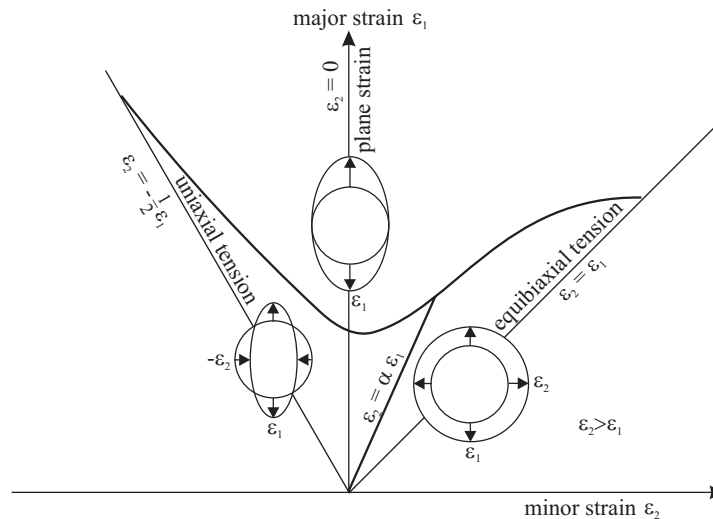


Figure 2.1 — Forming limit diagram.

An alternative approach to formability prediction deals with the occurrence of a strain instability in a uniform deformation process due to imperfections initially present in the material. This is realistic, since inhomogeneities of either geometrical or material origin are unavoidable in practise. Most of the theoretical predictions in this field are based on the Marciniak-Kuczynski (MK) approach [Marciniak and Kuczynski, 1967], where localised necking is assumed to be initiated through a pre-existing groove-like thickness imperfection. As a result, the plastic strain accumulates in the groove; thinning occurs there at a higher rate than outside the region and eventually leads to strain localisation. In order to use this method to

evaluate the forming limit for a single strain path, it is necessary to perform calculations using a considerable number of different initial groove angles in order to assess the formability based on the minimum limit strain.

The MK analysis was successfully used to predict the formability under monotonic deformation [Marciniak and Kuczynski, 1967; Hutchinson and Neale, 1978] and deformation with strain path changes [Mesrar et al., 1998; Wu et al., 1998; Kuroda and Tvergaard, 2000a]. Within the MK framework, the influence of various constitutive features on FLDs has been explored using phenomenological plasticity models [Kuroda and Tvergaard, 2000b; Friedman and Pan, 2000]. It is well known now that the FLD result is sensitive to the shape of the yield surface and the material parameters [Zhao et al., 1996; Xu and Weinmann, 2000] used for the material modelling. Supplementary crystal plasticity models were applied in combination with the MK analysis for a more careful description of the microstructure and texture evolution during deformation [Zhou and Neale, 1995; Wu et al., 1998].

Though in the last three decades the MK analysis proved to be a popular and effective tool for the formability prediction, it was experienced that the results are very sensitive to the choice of the shape and the size of the initial imperfection prescribed [Zhou and Neale, 1995]. Wu et al. [1997] offers an extensive analysis of the influence of the initial imperfection, as well as other model parameters, on the predicted FLD. Nevertheless, the indeterminacy of the initial imperfection size and shape remains a limitation to the MK approach. Thus, the classical MK approach remains a diagnostic tool rather than a predictive one. The mentioned paper also suggests a methodology to account for these effects and, in this way, improves predictions. Another imperfection based method overcomes this drawback by pursuing a limit analysis based on local fluctuations in the microstructure such as voids or particles of a second phase material [Gänsler et al., 2000]. In this case the deformation instability will be obtained as a natural result of the strain field fluctuations caused by the microstructural inhomogeneities initially prescribed. Data about microstructural inhomogeneities can often be collected experimentally or predicted using a microstructure evolution model. By employing realistic initial imperfections and by applying the appropriate material model, the actual development of the localisation can be obtained. The purpose of the present contribution is to develop a numerical method for predicting the formability of pure metal sheet under uniform and nonuniform deformations. Essentially, the method based on microstructure imperfections is applied, adapted here for pure polycrystalline materials by introducing the initially present textural inhomogeneities to trigger the localisation process. Similar ideas were used by Inal et al. [2002a,b] to analyse instability phenomena and localised deformation in polycrystalline sheet under uniaxial tension.

To describe the material behaviour of FCC sheet metal a viscous crystal plasticity theory is elaborated in this paper. The choice of the model is based on the investigation of Barlat [1987] where, in the context of the MK approach, it has been shown that the application of crystal plasticity to FLD prediction results in a better agreement with experimental observations than the predictions from classical continuum plasticity. Besides, a crystal plasticity description is able to deal successfully with texture and microstructure evolutions that have a significant influence on the formability.

To pursue the evolution of strain inhomogeneity the rate-dependent crystal plasticity theory is incorporated here within the framework of the finite element method. Plane stress conditions are applied. To accommodate the polycrystalline nature of the material, each individual integration point of the finite element mesh is supposed to be composed of a discrete number of

single crystals which are coupled according to a Taylor interaction approach. The initial lattice orientations of the single crystals are sampled from a given nonuniform distribution providing inhomogeneity of the texture field of the continuum. This initial texture inhomogeneity is considered as a natural microstructure imperfection which is physically present in any real metal, and which is sufficient to trigger a deformation instability. It should be emphasised that the occurrence of nonuniform deformations in the actual study is the result of the textural inhomogeneity only; no other imperfections are required to generate instabilities.

To assess the predictive capability, the method was applied for proportional stretching of an aluminium sheet with an initially random texture. In the following sections the details of the applied crystal plasticity framework and its finite element implementation are outlined, and the results and potentials of the approach are discussed.

2.2 Crystal plasticity model

Crystal plasticity theories originate from the early work of Taylor and Elam [1923] who presented a quantitative description of plastic deformation in single crystals based on crystallographic slip. Plastic deformation is assumed to be the result of distinct shear contributions on well-defined slip systems given by the crystallographic planes and the directions of the highest atomic density. The theory was further developed in the works of Lee [1969]; Rice [1971]; Hill and Rice [1972]; Asaro and Rice [1977]. The formulation of the rate-dependent crystal plasticity theory used in the present work is briefly summarised below.

The kinematics commonly used in crystal plasticity includes the multiplicative decomposition of the deformation gradient tensor \mathbf{F} into an elastic and a plastic part

$$\mathbf{F} = \mathbf{F}_e \cdot \mathbf{F}_p \quad (2.1)$$

where the elastic deformation is represented by \mathbf{F}_e , which also accounts for superimposed rigid body rotations, and where \mathbf{F}_p is the plastic contribution arising solely from crystallographic slip in the undeformed configuration. The slip systems α , defined by the normal to the slip planes \vec{n}^α and the slip directions \vec{m}^α in the initial configuration, contribute to the plastic deformation gradient tensor \mathbf{L}_p with slip rates through the following superposition:

$$\mathbf{L}_p = \sum_{\alpha} \dot{\gamma}^{\alpha} \vec{m}^{\alpha} \vec{n}^{\alpha} \quad (2.2)$$

where \mathbf{L}_p determines the evolution of the plastic deformation gradient tensor \mathbf{F}_p according to:

$$\dot{\mathbf{F}}_p = \mathbf{L}_p \cdot \mathbf{F}_p \quad (2.3)$$

For the elastic behaviour, the fictitious stress-free intermediate configuration defined by the plastic deformation gradient tensor \mathbf{F}_p is considered as the reference state, implicitly assuming that the elastic behaviour is not affected by the plastic slip. In this contribution the elasticity tensor \mathbb{C} relates the stress tensor $\boldsymbol{\tau}$ to the elastic Green-Lagrange strain tensor \mathbf{E}_e in a conventional manner

$$\boldsymbol{\tau} = \mathbb{C} : \mathbf{E}_e, \quad \mathbf{E}_e \equiv \frac{1}{2}(\mathbf{F}_e^T \cdot \mathbf{F}_e - \mathbf{I}) \quad (2.4)$$

The stress measure $\boldsymbol{\tau}$ used here is the second Piola-Kirchhoff stress related to the stress-free intermediate configuration and connected to the Cauchy stress tensor $\boldsymbol{\sigma}$ by:

$$\boldsymbol{\tau} \equiv \mathbf{F}_e^{-1} \cdot [\det(\mathbf{F}_e)\boldsymbol{\sigma}] \cdot \mathbf{F}_e^{-T} \quad (2.5)$$

Further, in the present rate-dependent formulation each slip rate $\dot{\gamma}^\alpha$ is assumed to depend on the actual resolved shear stress τ^α and slip resistance s^α on that slip system according to the slip law:

$$\dot{\gamma}^\alpha = \dot{\gamma}_0 \left\{ \frac{|\tau^\alpha|}{s^\alpha} \right\}^{1/m} \text{sign}(\tau^\alpha), \quad \tau^\alpha \equiv \boldsymbol{\tau} : \vec{m}^\alpha \vec{n}^\alpha \quad (2.6)$$

where $\dot{\gamma}_0$ denotes a reference value of the slip rate, s^α is the slip resistance and m is the strain rate sensitivity parameter. It is worth noting that the introduction of the stress measure $\boldsymbol{\tau}$ in the intermediate stress-free configuration allows to obtain the resolved shear stress through the slip system vectors \vec{n}^α and \vec{m}^α related to the initial configuration.

The description of hardening used in this paper is adopted from Asaro and Needleman [1985]. The slip resistance s^α is determined by the current strain hardening state of the crystal and its evolution, for which the following equation is used:

$$\dot{s}^\alpha = \sum_{\alpha} h^{\alpha\beta} |\dot{\gamma}^\alpha| \quad (2.7)$$

The hardening moduli $h^{\alpha\beta}$ are assumed to have the form:

$$h^{\alpha\beta} = h^\beta q^{\alpha\beta} \quad (2.8)$$

where h^β is a single slip hardening rate, and $q^{\alpha\beta}$ represents a matrix describing the latent hardening behaviour of the crystallite. The matrix components are taken to be equal to 1 on coplanar slip systems and to 1.4 on non-coplanar slip systems. This choice has been motivated by experimental observations performed by Kocks [1970]. The single slip hardening law employed in this paper has the form of a power function in terms of the accumulated slip [Asaro and Needleman, 1985]:

$$h^\beta = h_0 \left(\frac{h_0 \Gamma}{\tau_0 n} + 1 \right)^{n-1} \quad (2.9)$$

where h_0 and τ_0 are the slip system initial hardening rate and initial hardness respectively, n is the hardening exponent and

$$\Gamma = \int_0^t \sum_{\alpha} |\dot{\gamma}^\alpha| dt \quad (2.10)$$

is the accumulated slip. The slip system parameters h_0 , τ_0 and n are taken identical for all slip systems. Together, the Eqs. (2.1)–(2.10) describe the rate-dependent constitutive behaviour of a single crystal. The response of a polycrystal comprised of a number of single crystal contributions is obtained here by invoking the Taylor assumption. Consequently, the deformation in each separate grain of the polycrystal is taken equal to the macroscopic deformation of the polycrystal; the macroscopic values of quantities like stress are obtained by averaging their respective values over the total number of grains.

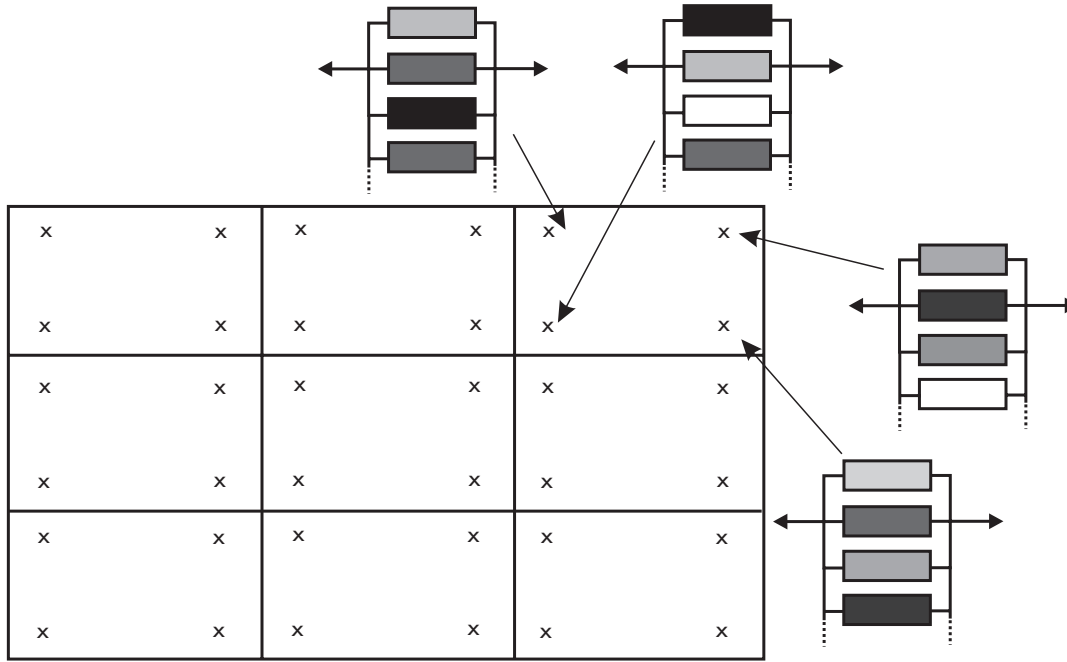


Figure 2.2 — Finite element representation of a polycrystalline specimen. Each integration point represent a polycrystalline aggregate, combined according to the Taylor interaction approach.

2.3 Finite element approximation

A finite element implementation is next considered to model the deformation of a representative volume element (RVE) of a metal sheet. To analyse localisation triggered by texture inhomogeneities, the representative volume element should contain a sufficient number of grains to provide an adequate description of the texture. However, the finite element analysis of an assembly of a large number of single crystals would be computationally rather expensive. To reduce the number of calculations required, single crystals are first combined into polycrystalline aggregates with N single crystals each, according to the Taylor interaction approach as indicated above. The finite element method was then applied to assemble polycrystalline aggregates and to determine the response of the corresponding material points, Fig. (2.2). In this approach, the number of grains per integration point N becomes a parameter of the model. It determines the local anisotropy of the material behaviour. For large values of N , the fluctuations of the texture distribution from point to point will be negligible and the material will deform homogeneously. To capture local fluctuations of the texture, the number of grains N in a point should be selected in correspondence with the scale of the fluctuations. Therefore, in this model the value of N defines the length scale of the fluctuations triggering the localisation. A method of establishing a proper value of N is not addresses in this paper.

The finite element discretisation of the RVE was realised with two-dimensional isoparametric elements with four nodes and four integration points. Each individual integration point of the finite element mesh is characterised by a 3D polycrystalline aggregate. Yet, since the attention is focused on the forming of thin sheet with an in-plane external loading, the stress state of the polycrystal in every integration point is restricted to be plane:

$$\vec{e}_3 \cdot \boldsymbol{\sigma} = \vec{0} \quad (2.11)$$

$$\vec{e}_3 \cdot \mathbf{F} \cdot \vec{e}_1 = 0, \quad \vec{e}_3 \cdot \mathbf{F} \cdot \vec{e}_2 = 0 \quad (2.12)$$

and plane stress elements were used for the approximation of the in-plane equilibrium conditions of the deformed metal sheet. In Eq. (2.11) \vec{e}_3 denotes the normal vector on the sheet plane, \vec{e}_1 and \vec{e}_2 are the in-plane base vectors. Condition (2.12) could be treated as a restriction on the deformation whereby material line elements in the plane of the sheet are required to remain in that plane.

Proportional stretching of a uniformly loaded sheet is simulated by applying periodic boundary conditions to an RVE and prescribing the displacements of the corner nodes. The prescribed displacements are imposed such as to provide deformation at a constant rate with a given ratio α between the macroscopic principal strains ε_i :

$$\varepsilon_2 = \alpha \varepsilon_1, \quad \varepsilon_i = \ln\left(\frac{l_i}{l_i^0}\right) \quad (2.13)$$

where l_i and l_i^0 are, respectively, the current and initial length of a material line segment in the direction of the principal strain ε_i .

2.4 Localisation criteria

The formability of the material is limited by failure, and as a natural consequence, the experimental FLDs display principal strains at failure of the material. Simulations of deformation processes with continuum methods do, in the classical context, not allow accounting for failure discontinuity. Instead, localisation criteria are commonly used to determine forming limits in engineering practise.

Localisation of deformation refers to the occurrence of narrow regions in a structure where all further deformation tends to concentrate, in spite of the fact that the external actions continue to follow a monotonic loading prescribed. The remaining parts of the structure usually unload. The phenomenon of localisation has a detrimental effect on the integrity of the structure and often acts as a direct precursor to structural failure. Therefore, being only an omen of failure, localisation criteria usually underestimate the formability.

For loading paths with $-1/2 < \alpha < 1$, necking is the most likely mode of deformation localisation. The onset of necking is often defined by the appearance of a much higher strain rate inside a shear band than outside. That definition is successfully exploited within the framework of the MK approach [Marciniak and Kuczynski, 1967; Hutchinson and Neale, 1978; Mesrar et al., 1998; Kuroda and Tvergaard, 2000a; Friedman and Pan, 2000] where the location of a shear band is known. In the case of a material imperfection based method the morphology of the localisation zone is unknown and therefore this straightforward approach cannot be pursued. Quantitative criteria for the initiation of necking in this case remain a matter of discussion [Inal et al., 2002b].

In this paper it is assumed that localisation occurs when the macroscopically uniform solution of the equilibrium problem becomes unstable. Consequently the criterion of structural instability is applied here to indicate strain localisation. It should be noted however, that the loss of stability is the necessary but not sufficient condition for the occurrence of localisation.

Therefore the results obtained with the use of the actual instability criterion should be considered as a lower formability bound.

The maximum of the external equivalent load Q is taken here as the criterion of structural instability. The external equivalent load Q is defined through the external power instantaneously applied to the RVE. To determine Q the external power increment δW applied to the RVE at a time increment δt is firstly calculated from

$$\delta W = \frac{1}{V_0} \int_{V_0} \mathbf{P} : \delta \mathbf{F}^T dV_0 \quad (2.14)$$

where $\delta \mathbf{F} = \mathbf{F}_n \cdot \mathbf{F}_{n-1}^{-1}$ is the incremental deformation gradient tensor determined by the deformation gradient tensors at the current \mathbf{F}_n and previous \mathbf{F}_{n-1} increment. In Eq. (2.14), \mathbf{P} is the first Piola-Kirchhoff stress tensor which is related to the Cauchy stress tensor by:

$$\mathbf{P} = J \boldsymbol{\sigma} \cdot \mathbf{F}^{-T}, \quad J = \det(\mathbf{F}) \quad (2.15)$$

Then, the equivalent incremental deformation δF is evaluated by an invariant of the incremental deformation gradient tensor $\delta \mathbf{F}$ averaged over the RVE:

$$\delta F = \sqrt{\delta \hat{\mathbf{F}} : \delta \hat{\mathbf{F}}^T}, \quad \delta \hat{\mathbf{F}} = \frac{1}{V} \int_V \delta \mathbf{F} dV \quad (2.16)$$

Finally, the external equivalent load applied to the RVE is obtained as the external power increment δW divided by the equivalent deformation increment δF :

$$Q = \frac{\delta W}{\delta F} \quad (2.17)$$

The macroscopic principal strains corresponding to the maximum of the external equivalent load Q are suggested to represent the formability limit for the given loading and these values are used to compose the forming limit diagram. The criterion $\max(Q)$ is a generalisation of the Hill's definition [Hill, 1958] of a structural instability criterion for large deformations. A similar principle was used by Gänser et al. [2000] to determine localisation in a two-phase material.

2.5 Forming limit analysis

In this contribution proportional straining of an aluminium sheet with an initially random texture is considered to assess the validity of the model proposed. The RVE consists of an array of 8×8 two-dimensional bilinear elements with four integration points and each integration point represents 10 single crystals, accordingly the RVE covers 2560 single crystals. Fig. 2.3 shows the $\{001\}$ stereographic pole figure of the initial texture distribution provided by all grains in the RVE. The material parameters used for the calculations are given in Table 2.1. The components C_{1111} , C_{1122} , C_{1212} fully determine the elasticity tensor \mathbb{C} for FCC materials. The hardening parameters for the constitutive model are taken from the paper of Wu et al. [1998] for aluminium alloy sheet AA6111-T4-C. The parameters identified in that contribution are valid for crystal plasticity simulations employing the same hardening law as in this paper. Fig. 2.4 demonstrates that applying the parameters from Wu et al. [1998] to the model proposed gives a good fit of the numerical simulations to the experimental data [Wu et al., 1998].

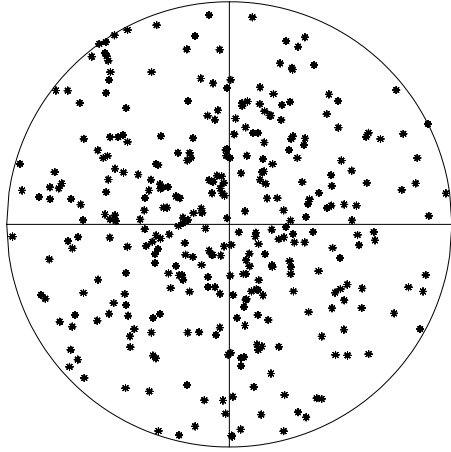


Figure 2.3 — Initial texture distribution represented by the {001} stereographic pole figure.

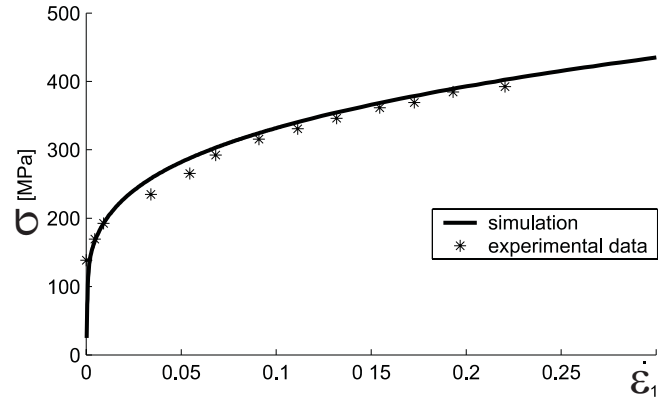


Figure 2.4 — Tensile stress-strain response in uniaxial tensions.

The random character of the grain orientations provides fluctuations of the texture distribution in the RVE and, therefore, a slight inhomogeneity of the mechanical properties of the continuum under deformation. The texture inhomogeneity does not disturb the uniform elastic deformation but shows local effects in the plastic regime. According to the slip law in Eq. (2.6), the slip intensity and the slip distribution in a single crystal will depend on the single crystal orientation. Consequently, along with the onset of the plastic deformation, strain fluctuations occur due to differences in grain orientations. Fig. 2.5 shows the distribution of the second invariant ¹ of the strain tensor $\mathbf{E} \equiv \frac{1}{2}(\mathbf{F}^T \cdot \mathbf{F} - \mathbf{I})$ at the moment that the plastic deformation reached 0.2% in the calculations for $\alpha = 0$. A small random fluctuation in the strain can be observed and it is this slight initial fluctuation - in the order of 0.02% - that triggers further local deformation instabilities.

To analyse the development of deformation localisation during proportional straining, the calculations have been performed with strain ratio $\alpha \in [-0.5; 1]$. The values $\alpha = -0.5, 0, 1$ represent uniaxial tension, in-plane plane strain stretching and equi-biaxial stretching, respectively. Fig. 2.6 shows the distributions of the second invariant of the strain tensor after 30% of deformation for different values of α . All simulations were performed with

Table 2.1 — Parameters for aluminium.

Variable	Symbol	Unit	Value
Elastic coefficient	C_{1111}	[GPa]	206
Elastic coefficient	C_{1122}	[GPa]	118
Elastic coefficient	C_{1212}	[GPa]	54
Strain rate sensitivity	m	[-]	0.002
Reference slip rate value	$\dot{\gamma}_0$	[1/s]	0.001
Hardening parameter	τ_0	[MPa]	47
Hardening parameter	h_0	[MPa]	1410
Hardening parameter	n	[-]	0.23

¹ $I_2(\mathbf{A}) = \sqrt{\mathbf{A} : \mathbf{A}}$

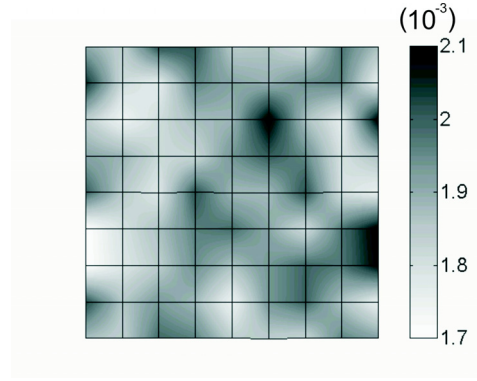


Figure 2.5 — Distribution of $I_2(E)$ following the onset of the plastic deformation for $\alpha = 0$.

the same initial random texture distribution; nevertheless, initially random fluctuations of the strain evolve to localised strain patterns that vary with the type of loading. In plane stretching calculations, a well-defined band develops perpendicular to the direction of the major strain ϵ_1 . For a negative strain ratio, the slope of the localisation band with respect to the minor strain axis ϵ_2 increases up to 30° . The same dependency of the localisation pattern on the loading mode has been found by Gänser et al. [2000] using a micromechanical approach, where some inclusions of a second material played the role of initial imperfection. The analysis of the formability using the Marciniak-Kuczynski approach [Wu et al., 1998; Laukonis and Ghosh, 1978] also provides data on critical directions of the localisation groove that are in agreement with the directions of the localisation bands indicated here. However, when the strain ratio α is increased to 1, the localisation mode obtained becomes more diffuse and does not show a band anymore.

The forming limit in the calculations was established as the deformation state where the criterion of structural instability, defined by Eqs. (2.14)–(2.17), was reached. The forming limit diagram for aluminium was obtained by plotting the principal strains corresponding to the loss of the structural stability in the calculations for different values of α , see Fig. 2.7. The result demonstrates a good agreement with experimental data [Wu et al., 1998] for small values of $|\alpha|$. However the formability prediction at proportional stretching with a higher strain

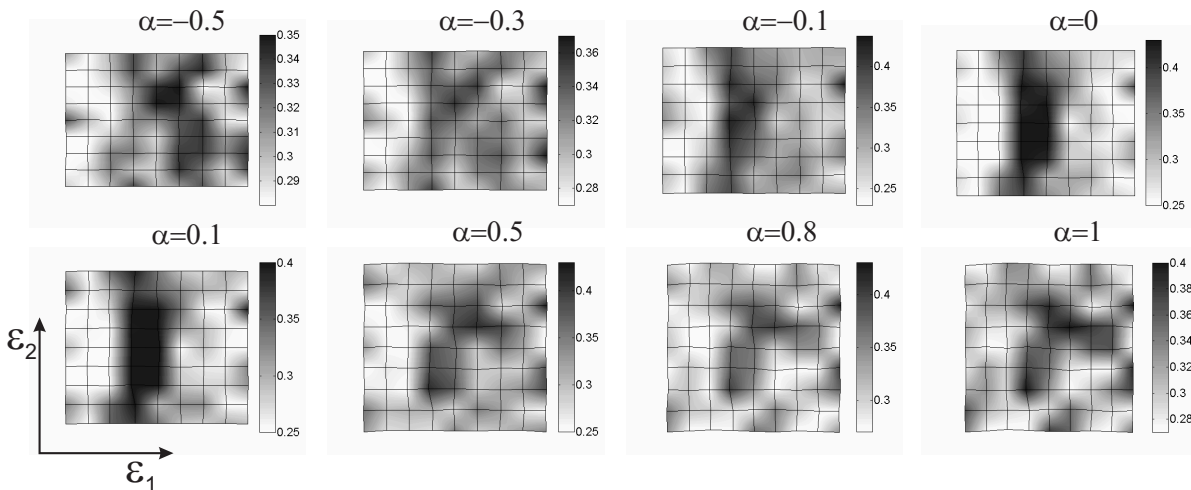


Figure 2.6 — Distributions of $I_2(E)$ for different proportional stretching at $I_2(\epsilon) = 0.3$.

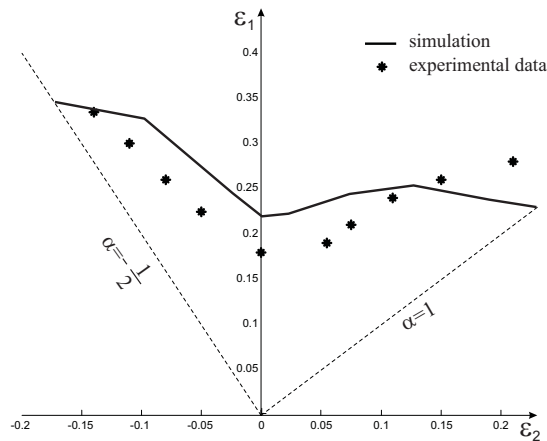


Figure 2.7 — Forming limit diagram calculated for aluminium.

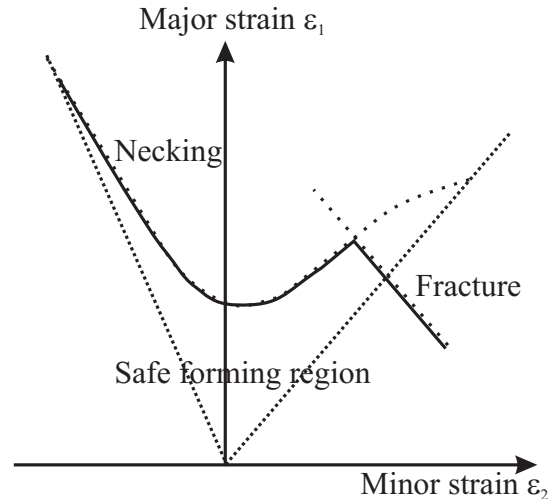


Figure 2.8 — The various limits to a sheet forming process (after Marciniak et al. [1992]).

ratio clearly constitutes a lower bound of the experimental results. In equi-biaxial tension, for instance, the formability calculated is about 75% of the experimental one. In these calculations with high values of α the deformation initially develops in a diffuse mode (Fig. 2.6) and a pronounced localisation band appears much later. Since the instability criterion adopted here accounts for diffuse localisation as well as for necking, this criterion indicates failure at the early diffuse localisation phase, before the band appears. However, experimental FLDs are commonly based on the physical appearance of a localisation band. Therefore the result of the model should rather be compared to experimental data registering also other types of failure.

Indeed, there are other limitations of the formability [Marciniak et al., 1992] such as wrinkling and fracture. Wrinkling is usually associated with compressive instabilities and occurs in deformations not considered here ($\alpha < -1$). But fracture can affect the stretch deformations commonly associated with necking. Fracture is typically the result of localisation of strain in a volume even smaller than the volume associated with a local neck or groove. Experimental observations [Marciniak et al., 1992] report that, for deformation modes close to equi-biaxial tension or uniaxial tension, the fracture limit can be lower than the forming limit given by necking strains. Therefore the border of the safe formability region (Fig. 2.8) can be lower on the right and left sides when compared to the forming limit diagram. This is also the tendency observed in the data calculated here.

Summarising, for small values of $|\alpha|$ the instabilities obtained in the calculations clearly indicate localisation in a band and therefore the predicted formability is in good agreement with the experimental forming limits. In biaxial tension with a high strain ratio, the model indicates failure by diffused localisation and the corresponding formability limits are related to fracture limits. In any case the approach proposed here is capable to predict the lower bound of the safe forming region, restricted not only by necking but also by fracture.

2.6 Conclusions

An alternative method to predict forming limits for sheet metal forming has been presented. Deformation instabilities occurred here as a natural result of strain field fluctuations caused by textural inhomogeneities. The method is based on an underlying rate-dependent crystal plasticity theory, elaborated in the context of the finite element method. Structural instability is determining the localisation criterion.

Proportional loadings with a strain ratio $\alpha \in [-0.5; 1]$ have been analysed for aluminium with a random texture. The results demonstrate the ability of the method to describe the development of strain localisation. The approach proposed is capable to predict the lower bound of the safe forming region. For smaller values of $|\alpha|$ the computational results are in good agreement with the experimental forming limit diagram. For the larger values of $|\alpha|$ the calculations are restricted by the strain localisation developing in the diffuse mode which can be a precursor of damage. Thus the selection of the instability criterion may have to be reconsidered in order to be consistent with criteria used in experimental FLDs.

Chapter 3

Phenomenological modelling of strain path change effects based on cell structure evolution

Reproduced from: Viatkina, E.M., Brekelmans, W.A.M., and Geers, M.G.D.,(2003). Strain path dependency in metal plasticity. Journal de Physique IV, 105: pp. 355-362.

3.1 Introduction

Most of the industrial metal forming processes are characterised by a non-monotonic strain history, in which different processing steps rapidly succeed each other. The induced changes in the strain path have a significant effect on the mechanical response of the metal involved and therefore influence the material behaviour of a blank during subsequent forming, thereby affecting the performance of the final product. The complexity and significance of strain path change effects require a careful investigation of the associated physical origins to enable an adequate modelling of the resulting deformation behaviour.

Macroscopically, the effect of a certain prestrain becomes manifest by an altered reloading yield stress, transient hardening, hardening recovery and failure shift compared to a monotonic deformation of the virgin material. In a quantitative sense the effect is influenced by the amount of prestrain. Besides, the effect is strongly anisotropic and depends on the “magnitude” of the change in the strain path. Typical features of the effect for FCC metals with a high stacking fault energy are schematised in Fig. 3.1. The stress-strain curves represent the responses of a material previously subjected to deformations, different from the current one, and to different amounts of prestrain. The amount of prestrain undergone by the material corresponds to the shift along the global strain axis. It can be seen that, depending on the prestrain, the material exhibits a softer or a harder response compared to non-prestrained material. After the initial yield stress is reached, the response shows some drop of the hardening with subsequent recovery. As the deformation proceeds in the new direction, the material clears the strain path change and its stress-strain diagram approaches the one for monotonic deformation. Besides, the change in the deformation history also affects failure.

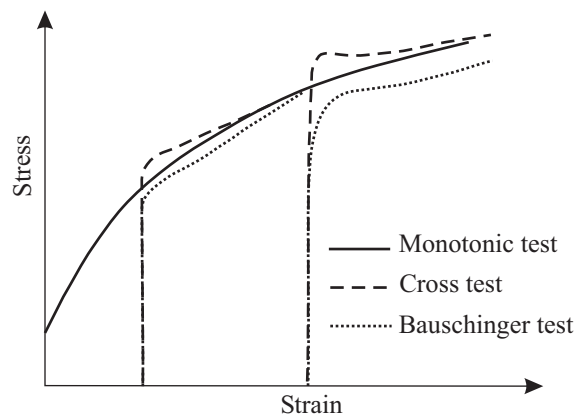


Figure 3.1 — Stress-strain diagrams demonstrating strain path change effects.

The hardening behaviour of metals physically originates from a complex microstructure evolution. Both, the texture and the dislocation structure influence the macroscopic behaviour of polycrystals. It has been proven by many experimental observations [Barlat et al., 2003] that the macroscopic strain path change effect at intermediate strains is related to the dislocation structure evolution rather than textural effects. The dislocation structure formed in FCC metals with a medium to high stacking fault energy can be subdivided into two components: a cell structure and a cell-block structure. Both cell and cell-block structures affect the macroscopic deformation behaviour, the cell-blocks, however, appear at larger strains. The effect of the cell structure, therefore, can be studied solely at strains up to an intermediate level, when the cell-block structure is not yet formed and therefore does not interfere. This paper concentrates

on the contribution of the cell structure in this limited strain range.

3.1.1 Experimental observations of the dislocation cell structure

Experimental investigations of dislocation structures developing in metals under deformation have been carried out for half a century. Extensive information on the morphology of the structures, their formation and evolution under various loading conditions can be found in the literature, e.g. Young et al. [1986]; Mughrabi et al. [1986]; Barker et al. [1989]; Bay et al. [1992]; Hansen et al. [2001]; Huang and Hansen [1997]; Hansen and Huang [1997]; Winther et al. [2000]; Liu et al. [1998]; Zimmer et al. [1983]; Ungar et al. [1984]; Park and Parker [1989]; Liu and Hansen [1995]; Hughes et al. [1997]. The essential features are shortly summarised below.

Dislocation cell structures are the first evolving structures recognised as such in deforming metals. In undeformed material, the dislocation distribution is close to statistically homogeneous. However, at the beginning of the deformation process, dislocations interact and cluster to form tangles, which can be seen as regions with relatively increased dislocation densities. As the strain increases, more dislocations participate in the evolution of the structure and the tangles link up to form dislocation boundaries which envelop regions with a low dislocation density. The structure created in this way can be observed as a network of volume elements within which the dislocation density is well below average, mutually connected through boundaries in which dislocations are concentrated. This structure is known as a cell structure (Fig. 3.2) and the dislocation boundaries constituting this structure are the so-called cell walls.

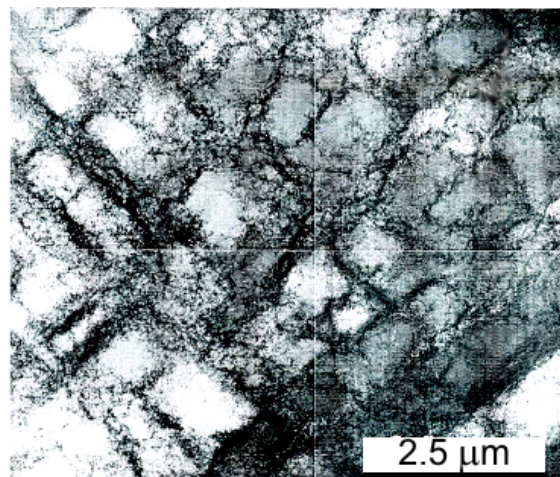


Figure 3.2 — Dislocation cell structure in copper [McCabe et al., 2004].

Upon visualisation through TEM, the cells appear in equi-axed or elongated two-dimensional shapes with a size in the order of a few microns. The dislocation walls, or boundaries, are distinguishable as areas with a high concentration of dislocations occupying about 10% – 20% of the total volume. The dislocations inside the walls are irregularly jogged and tangled and therefore do not produce high lattice curvatures (in aluminium about $1.5^\circ - 2^\circ$). The cell structure differs from other dislocation structures, such as cell-blocks and shear bands, by the low misorientation of the dislocation boundaries, i.e. there is a negligible variation in the slip activity across the cell walls.

During monotonic deformation the cell structure appears in some grains after only 5% of strain and becomes fully developed throughout the specimen at about 10% of strain. As the strain increases, the cells retain the same morphology; the mean size of the cells, however, decreases rapidly up to strain levels of about 25% and then continues to decrease at a much slower rate. The dislocation density inside the cell walls also increases as the deformation proceeds which can be observed as sharpening of the walls. In parallel to this, a lattice curvature appears across the cell walls, and this increases at a negligible rate up to a strain of about 25%. At a higher strain the lattice misorientation across the cell walls rises rapidly indicating the development of the structure into another type.

At intermediate strains, a new dislocation structure appears at a larger length scale. This structure consists of dislocation boundaries with a high lattice misorientation that envelop a number of cells to form cell-blocks. A cell-block structure is recognisable by a high lattice misorientation across its boundaries and, therefore, nonuniform plastic slip over these boundaries. The cell-blocks develop in the material together with the cells and also influence the macroscopic response. However, the considerations in this paper are restricted to the more uniform case and, thus, cell-block structures are left out of consideration.

The morphology and the orientation of the cell structure is related to the deformation mode applied. The orientation of the cell walls is commonly associated with the loading axis or the slip systems activated by the applied loading. The shapes of the cells also results from the loading. For instance, in aluminium, as reported by Barlat et al. [2003], uniaxial tension forms equi-axed cells while shear triggers more elongated rectangular cells. Since the dislocation structure and applied deformation mode are closely related, a change in the strain path affects the microstructure. Published data in the literature on the structure evolution under complex deformations is scarce and incomplete. Below, an attempt is made to summarise and systematise the information available in the literature on this experimental subject.

It is well established that a rapid change in a strain path causes a nearly immediate change in the dislocation structure. The changes observed in FCC metals are rather gradual and diffuse as opposed to microbanding of the type found in steels after a deformation change.¹ The structure observed shortly after the beginning of plastic deformation in a new direction is often characterised as distorted, dissolved or disrupted [Fernandes et al., 1993; Bate, 1993]. However, as the deformation proceeds in a new direction, the structure recovers and evolves in a structure typical for the corresponding monotonic deformation.

The type and magnitude of the structure changes after a strain path change depend on the differences between the successive deformation modes. Generally, during the first loading, the dislocation structure evolves in correspondence to the first deformation mode applied. After a change the structure adjusts to the new loading and the features of the evolution under the first loading disappear as the deformation proceeds in the new direction. However, there is no clear understanding of what is happening with the structure during the adaptation nor is there a unique terminology to describe this evolution. Here we will distinguish between two different scenarios - dissolution of cells in the cross test and disruption under reversed loading. There appears to be no consistency in the literature in the use of these terms, moreover, any cell evolution in FCC metals after a strain path change is often described as “a

¹Microbands have been observed in FCC metals only in orthogonal tensile-shear tests [Lewandowska, 2003; Fernandes et al., 1993], which seems to be particular rather than general. Besides, Barlat et al. [2003] did not find any microbands in the same test in aluminium. No microbands appear to have been found in other realisations than the orthogonal test.

dissolution process”. Indeed, both dissolved and disrupted structures appear as disorganised structures with a higher degree of homogeneity compared to the state before the strain path change. Nevertheless, it is believed that there is a morphological difference between these two scenarios in correspondence with the difference between the driving forces and their physical origins.

A cross test, e.g. a shear-shear test with 45° angle between the shearing directions, is accompanied by a cell evolution process called dissolution [Schmitt et al., 1991; Fernandes et al., 1993; Bate, 1993]. After the strain path change, the cell walls appear to become considerably thicker and less dense. In this way, the dislocation distribution is more uniform and the structure is less organised. The dissolution proceeds in the next few percent of deformation and can cause partial or complete dissolution of the cell walls. Simultaneously, while the deformation proceeds in the new direction, a new cell structure develops addressing the current loading - with a morphology related to the new loading direction and a cell size corresponding to the level of the total deformation. As the new structure develops and the old structure dissolves, after about 10% of strain the new structure replaces the old one completely and the structure development proceeds in a manner that is not distinguishable from the development of the cell structure in the as-received material under the same loading.

The evolution of the cell structure after a stress reversal received more attention due to its relation to the well-known Bauschinger effect [Christodoulou et al., 1986; Hasegawa et al., 1975]. The evolution of the structure associated with a Bauschinger test is due to the disruption of the cell walls. The thickness of the walls does not reduce significantly but the walls are “breaking apart” under the reverse loading. Experimental observations mention also a strong flux of dislocations from the walls to the cell interiors, decreasing the wall density and increasing the density in the cell interiors. In this way the homogenisation of the dislocation distribution is attributed to an increase of cell size and a dislocation redistribution. As deformation proceeds, the cell walls reappear and the cell structure is rebuilt.

Evolutions of the cell structure under more complex deformation paths deal with features of dissolution and disruption, depending of the strain path change. In the case of small changes, the cell structure formed during the preceding deformation is almost the same as the one accommodating the new loading and only small adjustments are required. Therefore, only a slight dissolution of the cell structure is observed. More pronounced changes in the strain path need more adaptation and therefore cause more dissolution. When the strain path change is large enough to include partially reversed loading, the cell disruption mechanism appears. For intermediate strain path changes, the two scenarios of cell evolution are expected to coexist.

3.1.2 Objectives

The goal of this paper is to propose a phenomenological relation between the cell structure evolution and the strain path change effect. The evolution, dissolution and reappearance, of cells after a strain path change accompanies the macroscopic effects of transient hardening and hardening recovery. However, there is no clear understanding of the intrinsic relation between all features of the structure evolution and the resulting macroscopic effect. Therefore, this study aims to address two questions: (1) Is the presence and evolution of the cell structure responsible for the strain path change hardening effects? (2) If so, which features of the cell structure and its evolution contribute to the macroscopical effect? The result of this

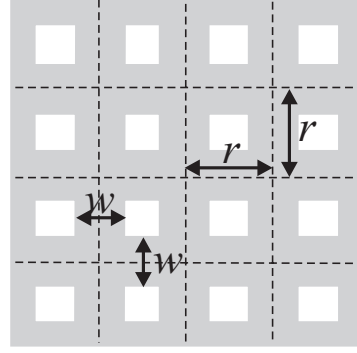


Figure 3.3 — Composite representation of the cell structure.

study is meant to indicate directions for a detailed modelling of the dislocation structure and the strain path change effects. Furthermore, the modelling approach pursued, serves as a phenomenological engineering tool to incorporate these effects in predictive analyses.

A composite elastoplastic approach is employed to model the mechanical behaviour of FCC metals with a dislocation cell structure. Phenomenological laws are proposed for the evolution of the dislocation density, cell size and thickness of cell walls. The cell development, dissolution and disruption are considered and modelled through the corresponding evolution of the incorporated variables.

3.2 Composite model

As have been proposed by Mughrabi [1987], a dislocation cell structure is idealised here as a two phase composite consisting of cell walls and cell interiors. The dislocation density is considered to be the only parameter discriminating one component from the other. The two-dimensional morphology of the composite is shown in Fig. 3.3 and represents the cell structure built by two sets of cell walls which are regularly spaced and oriented in the directions of the principal strains. The cell structure is characterised by the wall thickness w , the cell size r , the dislocation densities in the cell walls ρ_w and in the cell interiors ρ_c . Here and further on the subscripts w and c are used for the variables characterising the wall and the cell interior components, respectively.

The deformation behaviour of each composite constituent is modelled by employing the standard theory of small strain Von Mises elastoplasticity with isotropic hardening. The typical equations of the strain rate decomposition, elastic deformation and plastic yield are as follows (with $i = w, c$ denoting the components):

$$\dot{\boldsymbol{\epsilon}}_i = \dot{\boldsymbol{\epsilon}}_i^e + \dot{\boldsymbol{\epsilon}}_i^p \quad (3.1)$$

$$\dot{\boldsymbol{\sigma}}_i = \mathbb{C} : \dot{\boldsymbol{\epsilon}}_i^e \quad (3.2)$$

$$\dot{\boldsymbol{\epsilon}}_i^p = \mathbf{0} \quad \begin{cases} \text{if } \bar{\sigma}_i < \sigma_i^y(\bar{\boldsymbol{\epsilon}}_i^p) & \text{or} \\ \text{if } \bar{\sigma}_i = \sigma_i^y(\bar{\boldsymbol{\epsilon}}_i^p) & \text{and } \boldsymbol{\sigma}_i^d : \dot{\boldsymbol{\epsilon}}_i \leq 0 \end{cases} \quad (3.3)$$

$$\dot{\boldsymbol{\epsilon}}_i^p = \frac{3}{2} \frac{\boldsymbol{\sigma}_i^d \boldsymbol{\sigma}_i^d}{\left(1 + \frac{H_i}{3G}\right) \bar{\sigma}_i^2} : \dot{\boldsymbol{\epsilon}}_i \quad \text{if} \quad \bar{\sigma}_i = \sigma_i^y(\bar{\epsilon}_i^p) \quad \text{and} \quad \boldsymbol{\sigma}_i^d : \dot{\boldsymbol{\epsilon}}_i > 0 \quad (3.4)$$

where $\bar{\sigma}_i$ is the equivalent Von Mises stress, $\sigma_i^y(\bar{\epsilon}_i^p)$ is the actual yield stress (dependent on the effective plastic strain $\bar{\epsilon}_i^p$, which is defined through its rate $\dot{\bar{\epsilon}}_i^p = \sqrt{\frac{2}{3} \dot{\boldsymbol{\epsilon}}_i^p : \dot{\boldsymbol{\epsilon}}_i^p}$), H_i is the hardening modulus defined by $H_i = d\sigma_i^y/d\bar{\epsilon}_i^p$, $\dot{\boldsymbol{\epsilon}}_i$, $\dot{\boldsymbol{\epsilon}}_i^e$ and $\dot{\boldsymbol{\epsilon}}_i^p$ are the total, elastic and plastic strain rates, respectively, $\boldsymbol{\sigma}_i$, $\boldsymbol{\sigma}_i^d$, $\dot{\boldsymbol{\sigma}}_i$ are the stress tensor, the deviatoric part of the stress and the stress rate tensor, whereas \mathbb{C} is the elastic Hookean material tensor which is defined by two constants, the bulk modulus K and the shear modulus G , for an isotropic material.

The composite model represents a medium with a piecewise homogeneous distribution of dislocations. The yield stress, which is locally related to the dislocation density, is therefore also piecewise homogeneous, and inside each component the following relation between the local dislocation density ρ_i and the corresponding local flow stress can be adopted:

$$\sigma_i^y = \alpha G b \sqrt{\rho_i} \quad (3.5)$$

with b the magnitude of the Burgers vector. The material constant α accounts for the microscopic details of the elementary glide processes involved, which, for simplicity, are assumed to be similar for both components. As the cell walls are defined as volume fractions with a higher dislocation density, relation (3.5) identifies the walls as the hard component in contrast to the soft cell interior component.

To calculate the mechanical response of the entire composite, the Taylor averaging assumption is applied, such that the local stresses in both composite components lead to the externally applied stress according to the rule of mixtures:

$$\boldsymbol{\sigma} = f \boldsymbol{\sigma}_w + (1 - f) \boldsymbol{\sigma}_c \quad (3.6)$$

where f is the volume fraction of the cell walls. The volume fraction of the walls can be expressed in the relevant dimensions w and r according to:

$$f = \frac{V_w}{V} = 2 \frac{w}{r} - \left(\frac{w}{r}\right)^2 \quad (3.7)$$

where V and V_w are the volumes of the entire composite and the wall component, respectively.

In the model determined by the Eqs. (3.1)–(3.7) the wall thickness w , the cell size r and the dislocation densities ρ_w and ρ_c are still to be quantified. Experimental observations suggest that these parameters of the cell structure evolve with the strain applied and as such are dependent on the deformation history; therefore in this contribution w , r , ρ_w and ρ_c are considered as internal state variables. The corresponding evolution equations should describe the cell structure evolution and complete the system of Eqs. (3.1)–(3.7) for the cell structure model.

3.3 Evolution of the internal variables

The evolution of the two-phase cell structure can be summarised in terms of the following major features, see Fig. 3.4. Under monotonic deformation a cell structure appears which

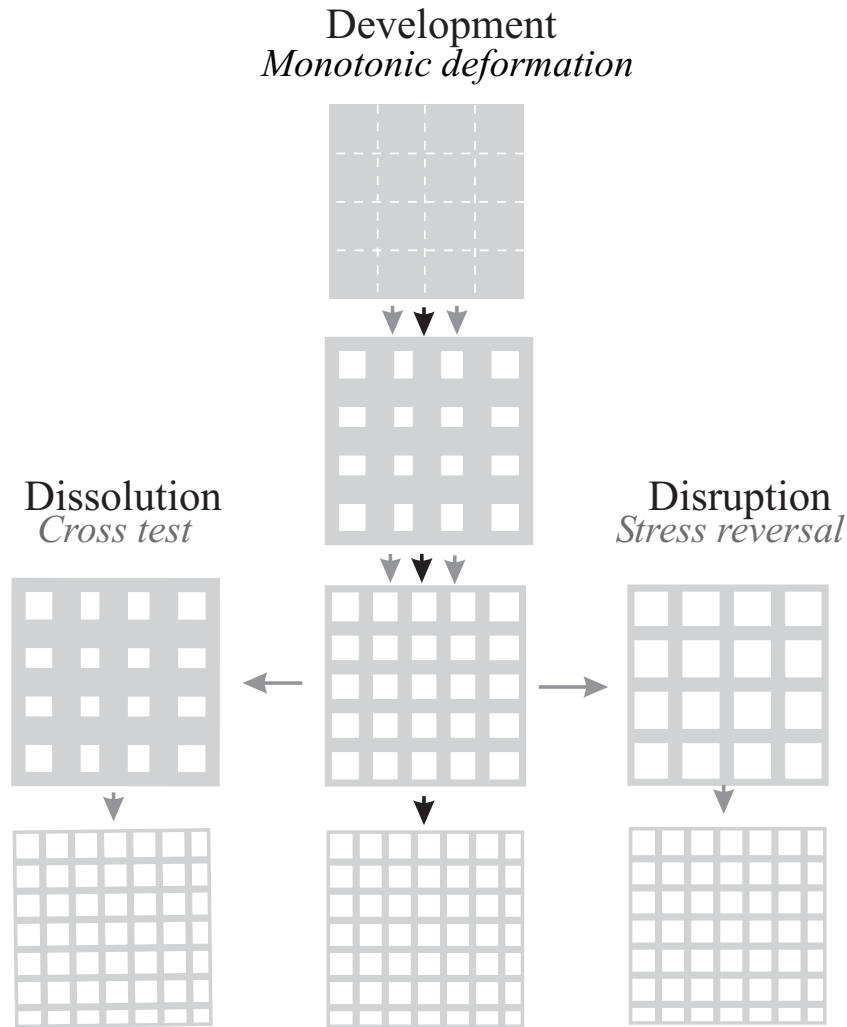


Figure 3.4 — Scheme of the cell structure evolution under monotonic loading (middle branch), cross test (left branch) and stress reversal (right branch).

evolves by a decreasing cell size r and wall thickness w and an increasing dislocation density ρ_w in the dislocation walls. After a strain path change, depending on the relation between the successive deformation modes, the cell structure dissolves or becomes disrupted. In the case of dissolution, the wall thickness increases and the dislocation density in walls decreases. The intensity of the dissolution depends on the "magnitude" of the strain path change; the cell size is not directly affected by the strain path change but depends on the total strain level. In the case of disruption, the cell size increases rapidly but the wall thickness remains unchanged. After the transient stage, the cell structure evolution continues to develop in the same manner as under monotonic deformation but with an orientation related to the new deformation mode.

3.3.1 Monotonic deformation

Dislocation density

Experimental observations [Mughrabi et al., 1986] suggest that the dislocation density inside the cell interiors does not change significantly during deformation. On this basis, a constant dislocation density ρ_c in the cell interior component is assumed here. The evolution of the

dislocation density ρ_w in the walls is based on the commonly used difference between the multiplication of mobile dislocations and the annihilation events:

$$\dot{\rho}_w = \frac{1}{b}(I\sqrt{\rho_w} - R\rho_w)\dot{\epsilon}_w^p + \frac{\rho_c - \rho_w}{f}\dot{f} \quad (3.8)$$

where I and R are a material parameter and the recovery length, respectively. The second term in the right hand side of this evolution equation accounts for the change in volume occupied by the wall material.

Cell size

For the case of monotonic deformation, the following empirical relation between the mean cell size and the flow stress is adopted:

$$\sigma^y = \frac{CGb}{r^m} \quad (3.9)$$

which is consistent with experimental observations [Barker et al., 1989] and commonly used in theoretical investigations [Mughrabi, 1987]. Here C is a material constant and the exponent m is usually close to unity for cell structures. Accordingly, the evolving cell size will be approximated by:

$$r = \frac{CGb}{f\sigma_w^y + (1-f)\sigma_c^y} \quad (3.10)$$

Wall thickness

The evolution of the wall thickness w is assumed to be governed by the average effective plastic strain rate $\dot{\epsilon}^p = f\dot{\epsilon}_w^p + (1-f)\dot{\epsilon}_c^p$ according to

$$\dot{w} = k_m(w_{inf} - w)\dot{\epsilon}^p \quad (3.11)$$

This evolution law reflects a decrease of the wall thickness with a saturation rate k_m (positive) until the saturation value w_{inf} is reached.

In this paper, the initially uniform distribution of dislocations prior to the cell structure development is modelled by an internal state of the composite where all material volume is occupied by the wall component. This point of departure suggests the initial value w_0 to be equal to the initial cell size r_0 and the initial dislocation density in walls to be equal to the dislocation density ρ_0 of the initially uniform distribution.

3.3.2 Cell dissolution

The cell dissolution is modelled here through an increase of the wall thickness. Following this assumption, the walls thickness increases during dissolution, so that in the limit the wall occupy whole material, i.e. $w = r$. The limiting case of complete dissolution is however rarely observed. Typically, partial dissolution is followed by the formation of new cells corresponding to the new loading. Next, the cell size and dislocation density are assumed to evolve in the same way as under monotonic deformation. I.e. the dislocation density in the walls keeps increasing with deformation and remains constant in the cell interiors. The latter is assumed for reasons of convenience and does not necessarily reflect reality. The

actual dislocation density might decrease during dissolution, however conclusive experimental evidence on this subject is lacking.

Wall thickness

In terms of the wall thickness, the dissolution can be identified as an increase of w :

$$\dot{w} = k_d(r - w)\dot{\bar{\epsilon}}^p \quad (3.12)$$

where k_d (positive) denotes the dissolution rate. In here the saturation value of the wall thickness is equal to the cell size r corresponding to the complete dissolution of the cells, modelled again by walls occupying the entire volume. Complete dissolution, however, actually occurs almost never. Continuing on the transient stage, commonly associated with the dissolution, the cell structure develops again driven by an increase of the strain in the new loading direction. At moderate strains after the strain path change, the cell evolution is therefore comparable to the evolution that would occur under monotonic deformation and the evolution law (3.11) is applicable again.

To take into account both the dissolution and the redevelopment of the cell structure, Eqs. (3.11) and (3.12) are combined as follows:

$$\dot{w} = (1 - p)k_m(w_{inf} - w)\dot{\bar{\epsilon}}^p + pk_d(r - w)\dot{\bar{\epsilon}}^p \quad (3.13)$$

where the first part accounts for the development and the second part accounts for the dissolution. The weight parameter p determines the relative contribution of the dissolution process in the evolution of w . As a first estimate, p is specified by assuming that the dissolution process depends only on the relation between the successive deformation paths and that its effect disappears as the deformation proceeds in the new direction. In the context of this idealisation, the following evolution of the internal variable p is suggested:

$$p = (1 - |\vartheta|) \exp[-B(\bar{\epsilon}^p - \bar{\epsilon}_{pre}^p)] \quad (3.14)$$

where ϑ is a scalar measure that identifies the magnitude of the strain path change and $\bar{\epsilon}_{pre}^p$ indicates the plastic deformation accumulated during prestraining (i.e. prior to the strain path change). To characterise the magnitude of a strain path change a commonly used definition of ϑ is adopted here:

$$\vartheta = \frac{\dot{\bar{\epsilon}}_1^p : \dot{\bar{\epsilon}}_2^p}{\|\dot{\bar{\epsilon}}_1^p\| \|\dot{\bar{\epsilon}}_2^p\|} \quad (3.15)$$

where $\dot{\bar{\epsilon}}_1^p$ and $\dot{\bar{\epsilon}}_2^p$ are the plastic strain rate tensors prior to and after the strain path change. Thus, $\vartheta = 1$ defines monotonic deformation, $\vartheta = 0$ a cross test, and $\vartheta = -1$ reverse deformation.

As a result, Eqs. (3.13) and (3.14) describe the evolution of the wall thickness during the whole deformation process. During monotonic deformation $\vartheta = 1$ and Eq. (3.13) consequently reduces to Eq. (3.11) describing cell wall thinning. After a strain path change, the dissolution is initiated with an intensity proportional to $(1 - |\vartheta|)$ and the walls start widening governed by a competition between the new structure development (3.11) and old structure dissolution (3.12). As the deformation proceeds in the new direction, the dissolution process vanishes ($p \rightarrow 0$) due to (3.14) and the wall thickness tends to decrease again according to (3.11). Note, that the cross test with $\vartheta = 0$ provides the highest value of p , thus, the strongest dissolution. On the other hand, considering the wall thickness w only, the Bauschinger test with $\vartheta = -1$ and thus $|\vartheta| = 1$ is so far equivalent to the monotonic deformation case and will not exhibit cell dissolution.

3.3.3 Cell disruption

The evolution of the cell structure after stress reversal, i.e. cell disruption, is modelled by a temporary increase of the cell size. The wall thickness and dislocation density are assumed to evolve in the same way as under monotonic deformation.

Cell size

The disruption of cells under stress reversal is considered as a rapid process compared to the subsequent reconstruction process. In other words, the size of the cells increases rapidly after a stress reversal and then slowly decreases. As deformation proceeds in the new direction the cell size recovers to the level corresponding to the total deformation (3.10). To model this temporary increase of the cell size, an additional contribution is incorporated in the equation for the cell size evolution (3.10):

$$r = \frac{CGb}{f\sigma_w^y + (1-f)\sigma_c^y} + A \exp[-k_c(\bar{\epsilon}^p - \bar{\epsilon}_{pre}^p)] \quad (3.16)$$

Here A defines the degree of disruption and k_c represents the strain drive recovery. According to (3.16), the cell size increases immediately after a stress reversal, then decreases with progressing strain (with a rate depending on k_c) to a level corresponding to the current yield stress and then follows the evolution as set in the monotonic deformation case. To reflect the fact that the cell disruption is triggered by a stress reversal, the coefficient A depends on the strain path change measure:

$$A = \begin{cases} a|\vartheta| & \text{if } \vartheta < 0 \\ 0 & \text{if } \vartheta > 0 \end{cases} \quad (3.17)$$

where a is a fitting parameter. Consequently, the Bauschinger test triggers the highest disruption. For more complex strain path changes with negative values of ϑ both Eqs. (3.13) and (3.16) have nonzero strain path change contributions ($p > 0$ and $A > 0$), that describes a process with coexisting dissolution and disruption of cells.

3.4 Results

The cell structure model is described by the system of equations (3.1)–(3.7) and the evolution equations (3.8), (3.13), and (3.16), where K , G , α , b , I , R , C are material parameters and ρ_0 , ρ_c , r_0 , w_{inf} , k_m , k_d , B , k_c , and a are parameters associated with the cell structure evolution to be determined from experimental cell observations and/or strain path change tests. It seems reasonable to assume $\rho_0 = \rho_c$. The initial cell size r_0 can be derived from (3.10) and (3.5) for the initial state where $\rho_w = \rho_0$ and $f = 1$. The parameters k_m and w_{inf} can be identified from observations during monotonic deformation. The saturation rate of the wall thickness development k_m can be estimated by a single measurement of the wall thickness w_{obs} and the corresponding ϵ_{obs}^p using relation (3.11):

$$k_m = \frac{1}{\epsilon_{obs}^p} \ln \left(\frac{r_0 - w_{inf}}{w_{obs} - w_{inf}} \right) \quad (3.18)$$

Finally, k_d and B are parameters to be quantified by fitting predicted stress-strain results to experimental data for deformations with a strain path change. Likewise the parameters a and k_c should be identified by considering the Bauschinger effect in a stress reversal experiment.

Table 3.1 — Material parameters for copper.

Paramter	Symbol	Unit	Value
Shear modulus	G	[GPa]	41.7
Bulk modulus	K	[GPa]	88.0
Length of the Burgers vector	b	[nm]	0.257
Material constant	α	[-]	1
Material constant	C	[-]	20
Dislocation creation rate parameter	I	[-]	0.228
Dislocation annihilation rate parameter	R	[nm]	5.1

Table 3.2 — Fitting parameters for copper.

Parameter	Symbol	Unit	Value
Initial dislocation density	ρ^0	[m ⁻²]	10 ¹⁴
Wall thickness saturation value	w_{inf}	[μ m]	0.18
Observed wall thickness	w_{obs}	[μ m]	0.27
Strain corresponding to w_{obs}	ε_{obs}^p	[-]	0.01

Monotonic deformation

To validate the cell structure model derived, it was applied to describe the deformation behaviour of copper. The material parameters used for the calculations are given in Table 3.1 and Table 3.2. Partly, the parameters in the Table 3.2 were determined by fitting the calculation results to the experimental data for uniaxial tension of pure copper [Mughrabi et al., 1986]. The evolution of the wall dislocation density was used to determine the parameters I , R , ρ_0 (Fig. 3.5a). The parameters of the cell structure ε_{obs}^p , w_{obs} , w_{inf} are taken from cell observations presented in Mughrabi et al. [1986].

Figs. 3.5b and 3.5c display the evolutions of the wall thickness, the cell size and the volume fraction of the walls. Here and further on, $\varepsilon = \sqrt{\boldsymbol{\varepsilon}:\boldsymbol{\varepsilon}}$ is the measure of the macroscopic deformation. The graphs demonstrate a realistic level of the values of the variables and tendencies as qualitatively described in many experimental observations, e.g. Mughrabi et al. [1986]. Yet, the cell size calculated with the model still appears to be twice as low as the mean size reported by Mughrabi et al. [1986]. The model assumptions adopted do not allow the elimination of the initial drop in the curve for the cell size evolution. The reason for these discrepancies might be found in the assumed constant dislocation density inside cells, which is likely too stringent. The experimental data (Fig. 3.5a) also suggest a slow evolution which, when taken into account, may correct the predicted cell size evolution.

Cell dissolution

The performance of the model in the context of a complex deformation path is here evaluated by analysing the response of copper subjected to a sequence of two uniaxial tension tests in different directions. The model results are compared with experimental observations of Schmitt et al. [1991], who examined various tension sequences, with angles ξ between the succeeding tensile directions equal to 15°, 45° and 90° and with different amounts of prestrain $\varepsilon_{pre} = 0.06, 0.12$ and 0.18 . Their paper contains data on the stress and hardening evolution under complex deformation together with a qualitative description of the structure development accompanying the strain path change. The cell structure dissolution was the

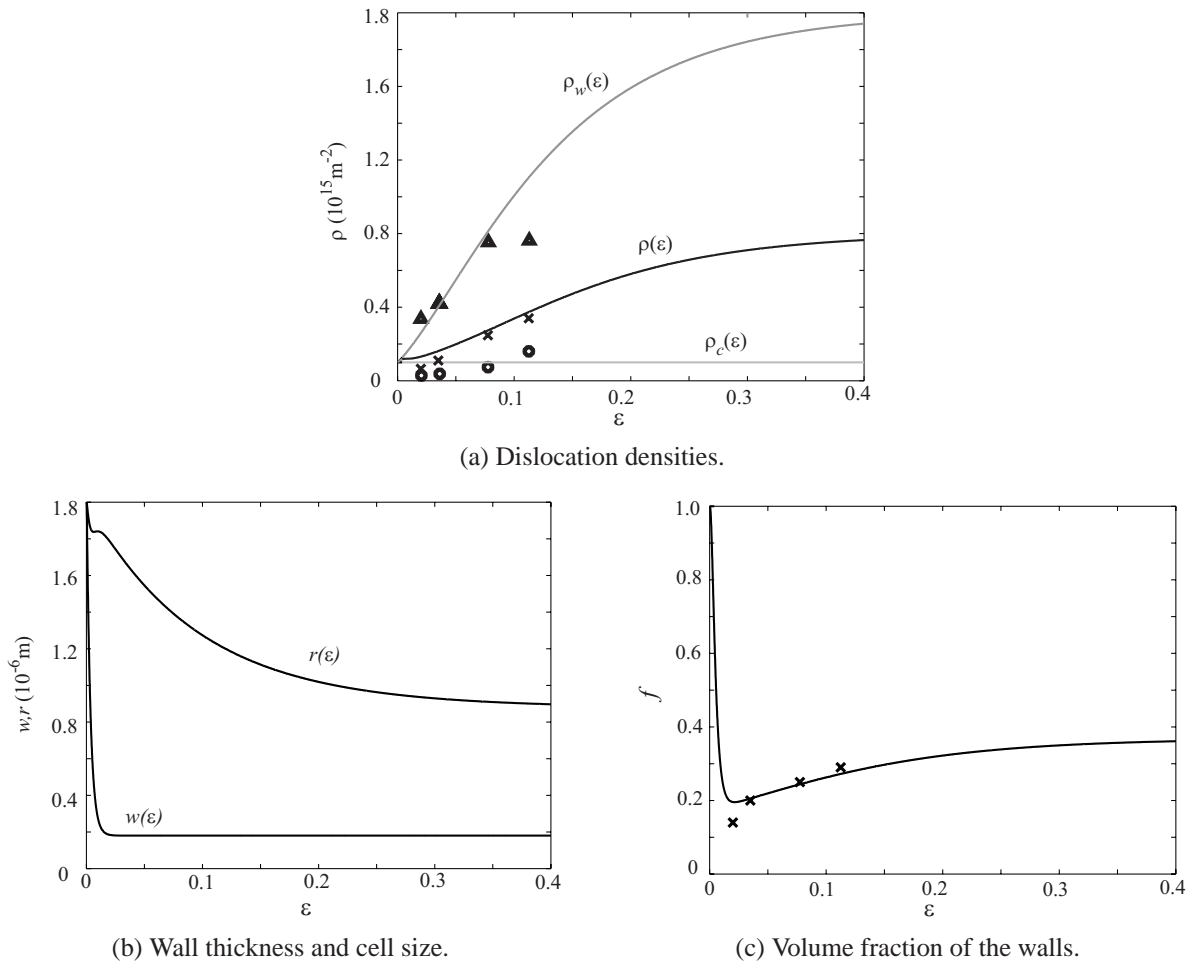


Figure 3.5 — Evolutions of the internal variables during monotonic tension of copper. Experimental data (marks) according to Mughrabi et al. [1986] and model predictions (lines).

only phenomenon reported by Schmitt et al. [1991], and no evidence of the development of cell-blocks was found during the applied deformation. This supports the case examined here, where the cell structure development is the only mechanism associated to the strain path change effect.

First, the parameters $B = 21.3$ and $k_d = 5.7$ were identified by fitting the theoretical and experimental stress-strain curves for the tests with $\xi = 45^\circ$ and $\varepsilon_{pre} = 0.12$. The sequence of two uniaxial tests with 45° between the tensile axes is characterised by $\vartheta = 0.25$. Compared to other experiments, with $\xi = 15^\circ$ ($\vartheta \sim 0.9$) and 90° ($\vartheta = -0.5$), this test is the closest to a cross test and expected to exhibit the highest cell dissolution and no cell disruption. The resulting response is depicted in Fig. 3.6a. The evolution of the model variables corresponding to the macroscopic response are shown in Figs. 3.6b and 3.6c. The graphs demonstrate a rapid increase in the wall thickness and a decrease in the cell size after the strain path change, causing a sudden rise in the wall volume fraction. After a strain of about 10% in the new direction, all variables tend to evolve in a manner similar to their characteristic evolution during monotonic deformation at the same total strain. This behaviour agrees well with the concept of the temporary dissolution of cells, as typically observed in experiments after a strain path change. It is reported by Schmitt et al. [1991] that, after the strain path change, “the dislocation wall thickness increases and the dislocation density seems to decrease in the walls”, “at low

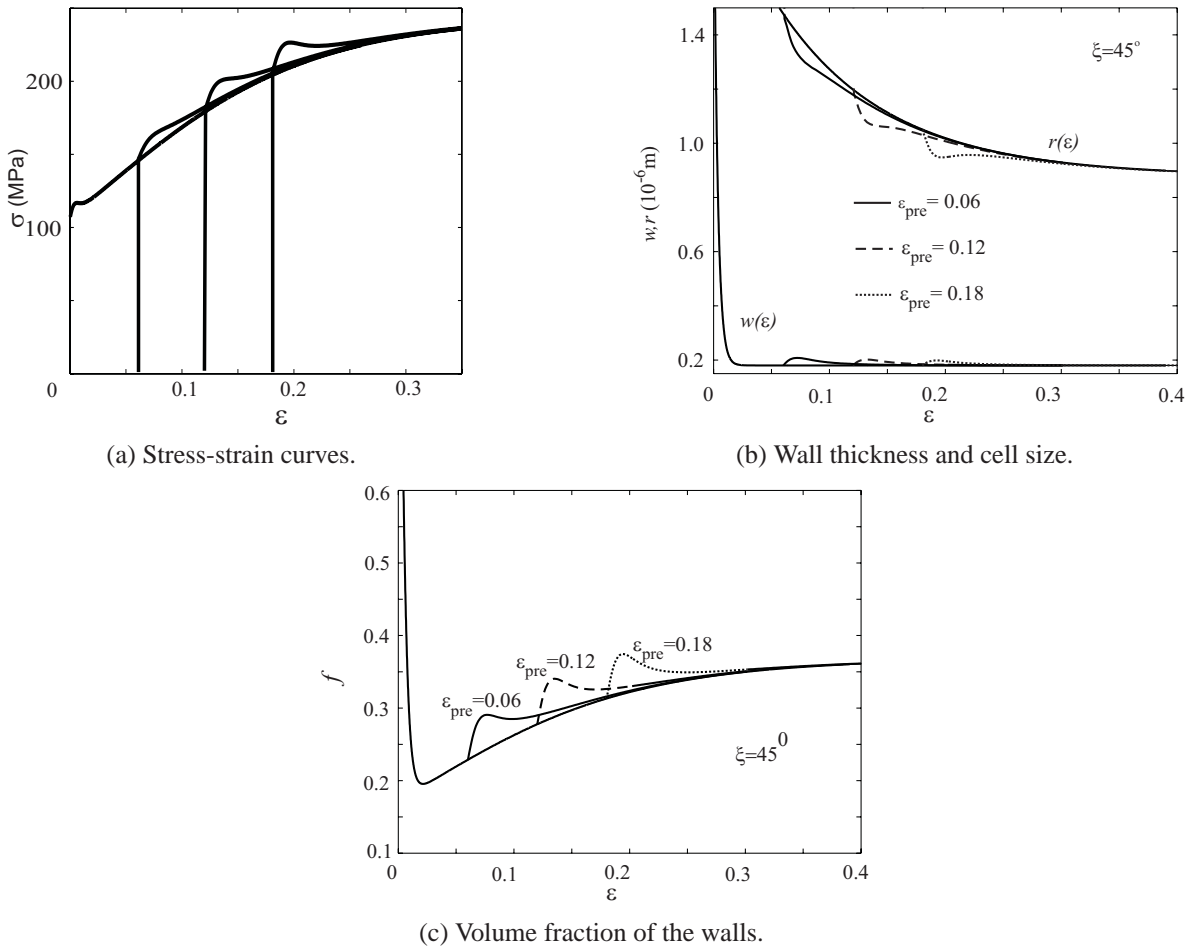


Figure 3.6 — Deformation behaviour predicted for monotonic tension and tension with a strain path change ($\xi = 45^\circ$, $\varepsilon_{pre} = 0.06, 0.12, 0.18$, copper).

strains, after reloading (about 0.025 of strain), the dislocation structure is unrecognised”, then “new dislocation walls appear progressively as the strain increases”, and finally, after a strain value of about 0.10 along the second strain path, “the dislocation cell structure tends to be similar to the structure which developed during a monotonic tension”.

The simulations, however, do not predict a dissolution as strong as observed in the experiments. In the calculations, the maximum thickness of $0.22 \mu\text{m}$ reached after the strain path change provides a wall volume fraction equal to 0.34. Such a low volume fraction of the walls and a high dislocation density inside the walls (12 times higher than in the cell interior) cannot be qualified as an unrecognisable structure. This discrepancy probably originates from the simplified dislocation density evolution used here. After a strain path change the dislocation density is assumed to evolve in the same way as during monotonic deformation. The decrease of the dislocation density in the walls that accompanies the cell dissolution is neglected. A decrease of ρ_w would allow a stronger increase of f at the same level of macroscopic deformation.

In Fig. 3.6, the dependency of the deformation behaviour on the amount of prestrain is shown for the strain path change defined by $\xi = 45^\circ$ ($\varepsilon_{pre} = 0.06, 0.12, 0.18$). As the amount of prestrain increases, an increase in the deviation from the monotonic behaviour can be noticed in the stress-strain curves and the cell size evolution; the maximum of the wall thickness

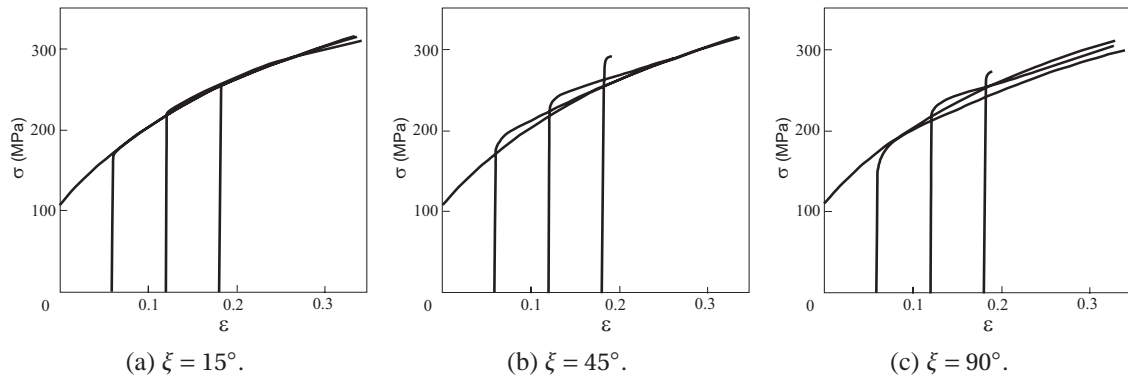


Figure 3.7 — Experimental stress-strain curves for tension tests of copper samples prestrained by tension in different directions ($\varepsilon_{pre}=0.06, 0.12, 0.18$) [Schmitt et al., 1991].

reached during the dissolution, however, decreases. The predicted rise of the strain path change effect with increasing prestrain is mainly provided by the decrease in the cell size and the increase in the internal stresses accumulated in both components at the moment of the strain change. The macroscopic effect of the prestrain is in good agreement with the experimental data presented in Fig. 3.7, which illustrates the path dependency of the deformation of prestrained copper. The mechanical responses for the tension-tension tests with different magnitudes of the strain path changes are shown. Fig. 3.8 displays the simulation results for the same tests. These results are obtained with accounting for the cell dissolution only, i.e. the cell disruption is left out of consideration, $A = 0$. The model predicts an increased reloading yield stress after a strain path change and the resulting effect increases with strain path change angles up to $\xi = 45^\circ$ and decreases for $\xi = 90^\circ$. This is in agreement with the experimental data.

The orientation-dependency of the strain path change enters the model via the parameter p in the evolution of the wall thickness. The amount of dissolution, expressed by an increase of the wall thickness, is thereby proportional to the magnitude of the strain path change ($1 - |\vartheta|$). In the test with a small strain path change, $\xi = 15^\circ$, the dissolution is very small as well as the macroscopic effect. The test with $\xi = 45^\circ$ ($\vartheta = 0.25$) is close to the cross test and therefore the dissolution is the highest here, i.e. w increases the most. Consequently, the highest rise of the reloading yield stress is obtained. The test with $\xi = 90^\circ$ has a lower absolute magnitude

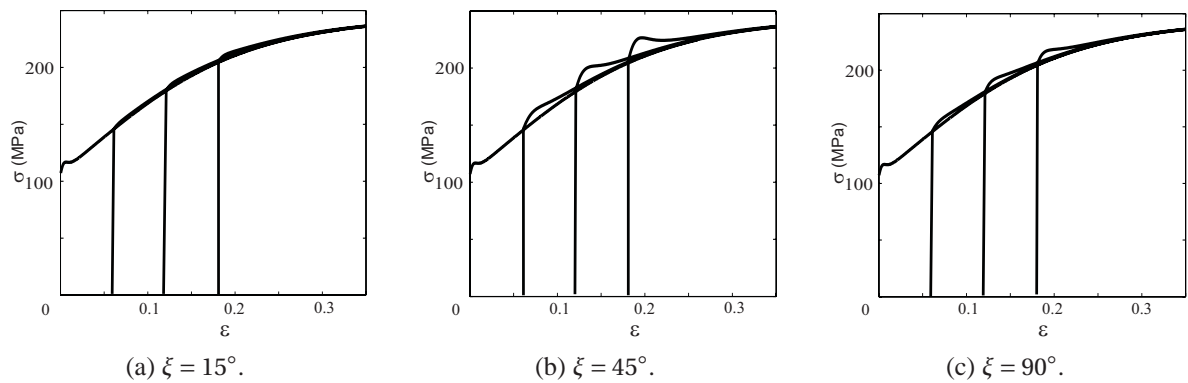
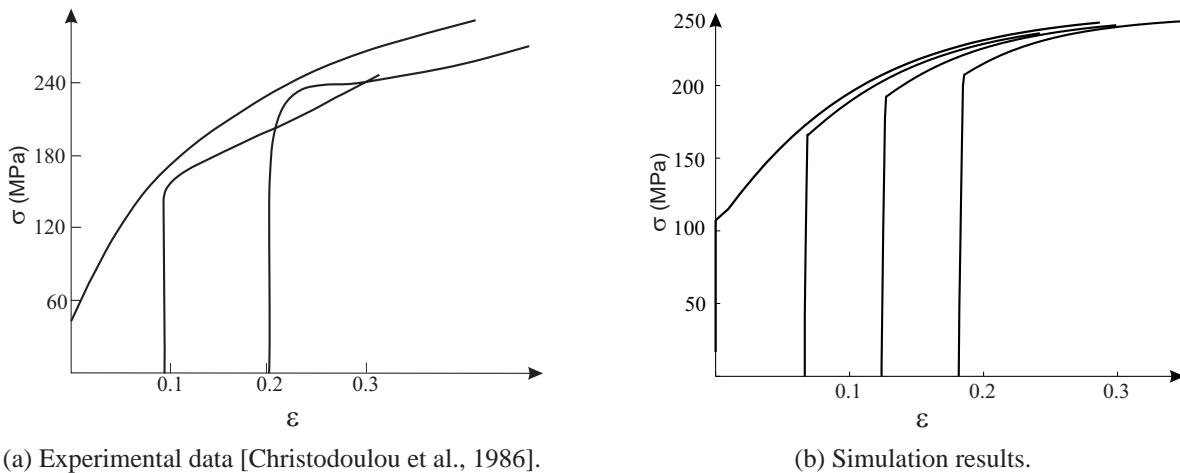


Figure 3.8 — Predicted stress-strain curves for tension of copper prestrained by tension in different directions ($\varepsilon_{pre}=0.06, 0.12, 0.18$).



(a) Experimental data [Christodoulou et al., 1986].

(b) Simulation results.

Figure 3.9 — Bauschinger effect for compression-tension tests of copper. Stress-strain diagrams for the tension steps, different offsets indicate different amounts of prestrain applied in compression.

of the path change ($\vartheta = -0.5$) compared to the test for $\xi = 45^\circ$. Hence, the dissolution is lower here and the effect is smaller. In conclusion, the strain path change effect as well as its orientation-dependency can be adequately explained by the dissolution of the dislocation cell structure.

Cell disruption

The cell disruption under stress reversal is taken into account through the evolution of the cell size r . To validate this part of the model the parameters a and k_c have been identified by fitting the model data to the experimental mechanical response upon stress reversal. So far, the experiments of Schmitt et al. [1991] were used here to identify the model parameters. Unfortunately, their description does not include data on stress reversal. Therefore, the experimental data on the compression-tension test of copper reported by Christodoulou et al. [1986] will be employed to incorporate the stress reversal effect. The parameters of the model, as presented in Tables 3.1 and 3.2, have been identified to fit the mechanical behaviour of the material used by Schmitt et al. [1991], which is regrettably not the same as the material used by Christodoulou et al. [1986]. Therefore, only a qualitative agreement between the experimental results and the model predictions can be expected. This is, however, sufficient to make a qualitative analysis on the main tendencies in the relation between the cell structure evolution and the strain path change effect.

Fig. 3.9 shows the experimental stress-strain diagram for the compression-tension test and the simulated results. After the stress reversal the cell size was fitted to decrease with 30% of the current value. The model predicts a decreased reloading yield stress followed by hardening recovery. Thus, the model captures the main features of the Bauschinger effect. The hardening evolution, however, still deviates from the experimental one – the hardening stagnation is not predicted by the model. To improve the model with respect to this item, further extensions are to account for other elements of cell disruption. This subject is discussed next in section 3.5.

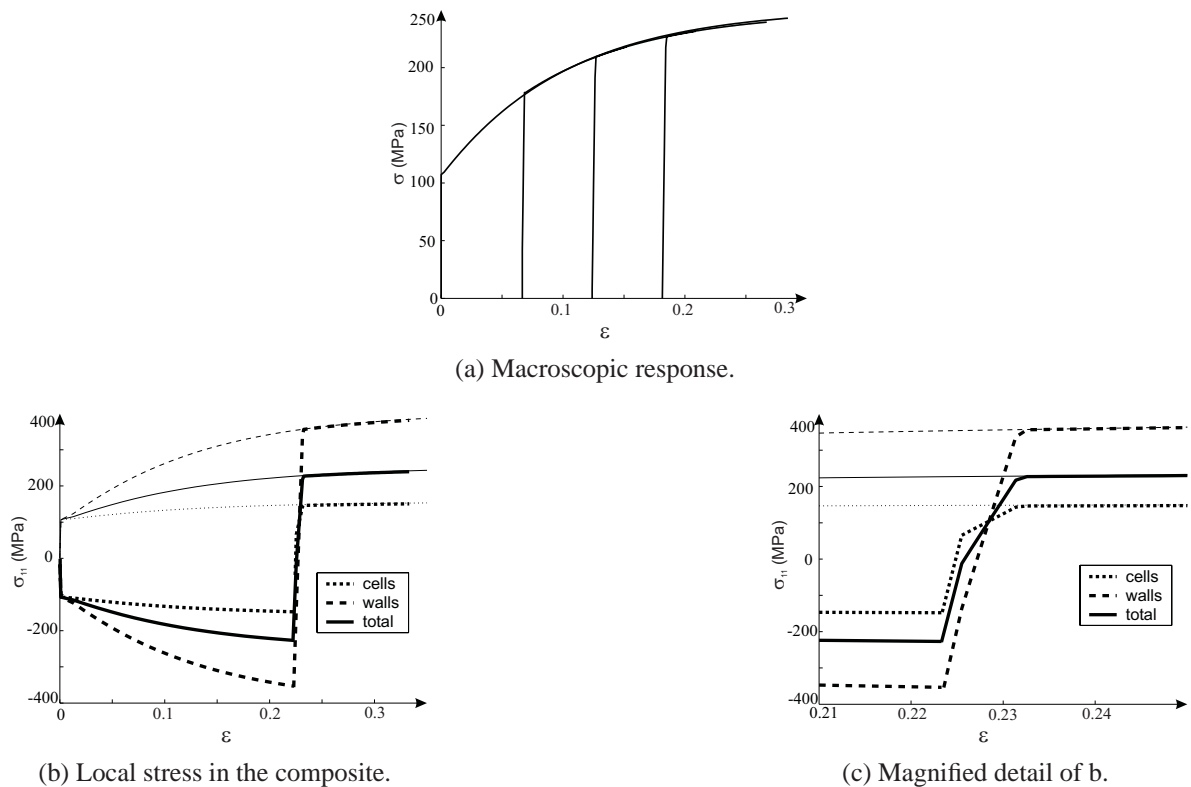


Figure 3.10 — Bauschinger effect predicted by the composite model. Compression-tension test (thick lines) and tension test (thin lines).

3.5 Discussion

The model proposed here includes two basic features of an FCC metal with a dislocation cell structure – material inhomogeneity and evolution of the cell morphology with increasing deformation. The effect of these features on the strain path changes is studied and discussed below.

The material inhomogeneity is taken into account by the composite model relying on the Taylor averaging of the response of the soft cell interior material and the hard walls. The composite model, i.e. the averaging scheme, does not have any capability to produce an increased reloading yield stress after a strain path change. However, the material inhomogeneity is often claimed to be responsible for the early plastic slip in the Bauschinger test. The simulations of a compression-tension test with the presented composite model are shown in Fig. 3.10. The cell structure model is used here without any cell dissolution or cell disruption ($A = 0$), i.e. reduced to a two-phase model with constant phase fractions. The magnification shown in Fig. 3.10c illustrates that due to the material inhomogeneity, residual stresses remain in the material after unloading. After compression, the residual stresses in the cell interior are positive and therefore assist the subsequent tension. This causes the cell material to yield at a lower applied stress compared to monotonic deformation. Thus, the material inhomogeneity clearly contributes to the early slip in the Bauschinger test. However, the elastic response of the walls increases the average response quickly to the level of the monotonic yield stress. Therefore, the effect of the early slip in the cell interior remains negligible in the macroscopic stress-strain diagram (Fig. 3.10a). Obviously, the simulations indicate that a composite model

with constant phase fractions is not sufficient to predict the strain path change effect nor the Bauschinger effect.

The most pronounced changes in the dislocation structure evolution after a strain path change were classified here as cell dissolution and cell disruption. The cell dissolution is modelled as an increase in the wall thickness and cell disruption as an increase in the cell size. The cell dissolution is a typical feature characterising the cross test, while the cell disruption is associated with stress reversals. These scenarios are, obviously, based on different physical mechanisms activated by the corresponding loadings. These mechanisms are not further studied, nor detailed in this work. The goal of this paper is to emphasise the mechanical contribution of the cell evolution to the macroscopic response in a quantitative sense.

The model states that after a small strain path change ($\vartheta > 0$) and up to a cross test ($\vartheta = 0$), the cell dissolution clearly promotes an increase of the reloading yield stress. Large strain path changes ($\vartheta < 0$) include a component of stress reversal that initiates the cell disruption. The cell disruption causes a decreased reloading yield stress. For these large changes in strain path, the effect of dissolution competes with disruption. Under complete load reversal ($\vartheta = -1$) only cell disruption takes place, reflecting a clearly decreased yield stress which is typical for the Bauschinger effect. As mentioned in the introduction, experimental data on microstructure evolution after strain path changes are difficult to obtain. The evolution assumed here does not conflict with the data collected so far. Yet, a quantitative comparison with the available data is not possible. In any case, the agreement between the predicted and experimentally obtained macroscopical responses indicates that the microstructural evolution is qualitatively correctly captured.

The contribution of the residual stress should be also mentioned here. In spite of the fact, that the macroscopic effect of the residual stress is negligible, it plays an important role in the Bauschinger effect. The early yield stress in the cell interior, promoted by the residual stress, activates the cell disruption responsible for the decrease in the macroscopic yield stress. Without the early slip in the cells, the effect of the cell disruption would be a macroscopic softening, after the reloading stress reaches the level of the stress in monotonic tension.

The results of this study permit to conclude that changes in the cell morphology have a marked contribution to the strain path change effect. The cell dissolution observed in cross tests promotes an increased reloading yield stress after a strain path change, while the disruption of cells observed under stress reversals causes a decreased reloading yield stress, known as the Bauschinger effect.

The evolution of the cell structure after a strain path change has been modelled here by the evolution of the cell size and wall thickness only. The complete evolution of the dislocation structure is evidently more complex. Experimental observations also report changes in the cell orientation and dislocation redistributions that are not taken into account in the present analysis. Besides, an increasing amount of indications in the literature [Straub et al., 1996; Borbely et al., 1997; Müller et al., 1996; Ungar et al., 1984] seem to confirm the presence of internal stresses in the structure and its significant contribution to the strain path change effects. The slip anisotropy is also believed to have an effect on the cell structure evolution and the macroscopic effects. The contribution of these features to the strain path change effect should be additionally studied and is the subject of future research.

3.6 Conclusions

With the aim of describing the mechanical response that results from a strain path change, a phenomenological model of the cell structure evolution has been developed. This model is based on a composite aggregate, considering a material with a cell structure with two components: a soft cell interior component and a hard cell wall component. The evolution of the dislocation cell structure is taken into account by the evolution equations for three internal variables: the cell size, the wall thickness and the dislocation density inside the walls. The cell dissolution is modelled by an increase of the wall thickness, which is typically associated with the cross test. The cell disruption is assumed to be associated with a stress reversal and is modelled by an increase of the cell size.

Experimental data on monotonic and complex deformation of copper was used to identify the parameters and to qualitatively assess the model. In spite of the simplifications made at the cell structure level, the model adequately reflects the behaviour for monotonic deformation and complex deformation, including the cross and the Bauschinger effect. The strain path change effect, its dependency on the amount of prestrain, and the magnitude of the strain change predicted by the model are in reasonable agreement with the available experimental data.

Chapter 4

Modelling of the internal stresses in dislocation cell structures

Reproduced from: Viatkina, E.M., Brekelmans, W.A.M., and Geers, M.G.D., (submitted). Modelling of the internal stresses in dislocation cell structures.

4.1 Introduction

It is common knowledge nowadays that the deformation of metals is accompanied by the development of dislocation structures. During ongoing deformation, dislocations in the material tend to pattern such that 3D structures with areas of high and low dislocation density are formed. This nonuniform distribution of dislocations provides an additional source of inhomogeneity and anisotropy in the material.

The anisotropy induced by dislocation structures becomes essential in deformations with complex loading paths. Macroscopically the effect of a strain path change manifests itself in an altered reloading yield stress, followed by transient hardening with a decreased hardening rate and, eventually, hardening recovery [Vieira et al., 1990, 2000; Zandrahimi et al., 1989; Bate and Wilson, 1986; Pedersen et al., 1981]. The effect depends on the amount of prestrain and the difference between successive deformation modes. Experimental investigations dealing with strain path changes revealed that the effect of the texture on the reloading behaviour is weak at moderate deformations [Schmitt et al., 1991; Jensen and Hansen, 1990] and that slip anisotropy alone does not provide a satisfactory explanation for the observed strain path change effect [Li and Bate, 1991; Bate, 1993; Jensen and Hansen, 1990]. Therefore, it was concluded that the effect of strain path changes originates from the anisotropy induced by the dislocation structure. This was also experimentally confirmed by correlating the presence or absence of dislocation structures with the macroscopic behaviour after a strain path change [Bate, 1993].

Experimental observations of dislocation structures suggest a strong correlation between the structure evolution and strain path change effects [Schmitt et al., 1991; Hasegawa et al., 1975; Christodoulou et al., 1986]. Indeed, the morphology of the dislocation structure developed after a particular loading path is clearly depending on the loading characteristics. A dislocation structure – a non-homogeneous, yet partly regular distribution of dislocations – is formed to accommodate the current deformation history at the microscopical level. After a strain path change the previously formed dislocation structure becomes unstable under a new loading since its morphology is not ‘favourable’ anymore and, moreover, it degenerates by newly activated plastic slip. The resistance and adaptation of the dislocation structure to the loading in a new direction is typically accompanied by an increased reloading yield stress and transient hardening.

It is commonly accepted that changes in morphology of the dislocation structure after a strain path change are related to macroscopic transient effects. Dissolution and disruption of the cell structure is observed to coincide with a reduction of the hardening rate, relative to the rate in monotonic deformation, while formation of a new structure occurs together with a recovery of the hardening rate towards the one found for monotonic deformation. Recent investigations [Wilson et al., 1990; Barlat et al., 2003], however, emphasise the importance of the internal stress developed in the cell structure and its resulting effects on the deformation behaviour of the material.

It has been confirmed by many experimental observations that deformation of a metal with a dislocation cell structure causes the development of long-range internal stresses [Straub et al., 1996; Borbely et al., 1997; Müller et al., 1996; Ungar et al., 1984]. In earlier experimental and theoretical works it was believed that the long-range internal stresses are caused by pile-ups of dislocations which were considered as a typical feature of a heterogeneous dislocation distribution [Seeger et al., 1957]. Later, however, the presence of internal stresses was also

discovered in ideal cell structures, where pile-ups are not expected. Since Mughrabi [1983], the evolution of long-range internal stresses is considered to be a natural consequence of the compatibility requirements during plastic deformation in the presence of a heterogeneous dislocation distribution.

Much of the present understanding of the influence of the long-range internal stresses on the material hardening has been acquired from observations made in fully reversed plastic deformation [Christodoulou et al., 1986; Hasegawa et al., 1975]. After prestraining, the long-range residual stresses within the softer cell interiors act in a direction opposite to that of the originally applied stress. When the direction of the applied stress is reversed, these internal stresses act in the same direction as the newly applied stress, causing reversed plastic deformation to be initiated at an applied stress level lower than that attained at the end of the prestrain. Thus, long-range internal stresses in the cell structure are intrinsically associated to the decreased reloading yield stress, commonly known as the Bauschinger effect.

After the reloading yield stress has been reached, the plastic deformation in the new direction triggers a gradual evolution of the deformation incompatibility, resulting in a reorientation of the internal stresses. Wilson et al. [1990] studied the effect of internal stresses on the hardening behaviour of aluminium after various strain path changes. It was concluded that the reorientation of the long-range internal stresses acting in the soft cell interiors constitutes a source of increasing hardening rates at the early stages of deformation following a strain path change.

Experimental observations suggest that an adequate model of the dislocation cell structure might enable a correct prediction of the macroscopic behaviour, especially under complex loading conditions. A recognised contribution in the modelling of the effects of dislocation structures was delivered by Mughrabi [1987], who suggested to consider the structure as a composite with a hard component representing the dislocation walls and a soft component representing areas of low dislocation densities. This approach has been further sophisticated in the literature to describe the actual evolution of the dislocation distribution [Estrin et al., 1998; Argon and Haasen, 1993; Goerdeler and Gottstein, 2001]. The latter models successfully predict the influence of the microstructure on the macroscopic behaviour. However, these models do not consider anisotropic effects associated with the cell structure and are therefore unable to describe strain path dependency.

In the previously published paper [Viatkina et al., 2003] (Chapter 3) the composite model was enhanced to predict the strain path change and Bauschinger effects. The model was developed in an isotropic continuum environment, anisotropy of the reloading yield stress was introduced via the strain path dependent evolution of the volume fraction of the cell walls. The dependency of the cell morphology evolution on the difference between successive deformation modes allowed a correct prediction of macroscopic tendencies. It was emphasised thereby, that the orientation of the cell structure as well as the presence of internal stresses should be taken into account to complete the model and to improve the quality of the predictions.

Recently, Peeters [2002] employed a composite model in a crystal plasticity framework, allowing an anisotropic three-dimensional approach accounting for the orientation of the structure. The model also includes an anisotropic evolution of the dislocation distribution depending on the deformation history. The approach was successfully applied to predict the macroscopic behaviour of steel after various strain path changes. This BCC model, however,

also bypasses the internal stress characterising a dislocation structure.

The approaches mentioned above concentrate on the morphological changes of the dislocation structure after a strain path change and their effect on the macroscopic behaviour. It is believed here that from a modelling perspective, the effect of the internal stresses developed in the cell structure is as important as the cell morphology. A classical way to account for an internal stress distribution in a continuum model is the incorporation of kinematic hardening. A number of models have been developed to introduce kinematic hardening in prestrained material [Mollica et al., 2001; Abdi and Samrout, 2000; Chun et al., 2002; Harder, 1999; Sedláček and Blum, 2002; Fernandes et al., 1998; Teodosiu and Hu, 1995; Besseling and Giessen, 1994]. The evolution of the internal stresses, also called back stresses, is usually modelled through the evolution of internal variables and phenomenological evolution equations, which are fitted to the macroscopic response. In these approaches, the physical interpretation of the internal variables and their evolution is a challenging problem [Teodosiu and Hu, 1995].

The objective of the present paper is to develop a continuum model of the cell structure that incorporates internal stresses in a physically-based manner. The internal stress is derived here as a natural result of deformation incompatibility. The approach incorporates the morphology and orientational anisotropy of the cell structure in an idealised manner. The model offers a tool to predict strain path change effects and enables a theoretical study of the internal stress and its influence on the macroscopic behaviour. Moreover, the implementation of the model is relatively straightforward, resulting in a computationally efficient method that lends itself for use in macroscopic engineering computations.

4.1.1 Experimental observations of the dislocation cell structure

Experimental investigations of dislocation structures developing in metals under deformation have been carried out for half a century. Extensive information on the morphology of this particular microstructure, its formation and evolution under various loading conditions can be found in the literature, e.g. Young et al. [1986]; Mughrabi et al. [1986]; Barker et al. [1989]; Bay et al. [1992]; Hansen et al. [2001]; Huang and Hansen [1997]; Hansen and Huang [1997]; Winther et al. [2000]; Liu et al. [1998]; Zimmer et al. [1983]; Ungar et al. [1984]; Park and Parker [1989]; Liu and Hansen [1995]; Hughes et al. [1997]. The experimentally identified features, which are essential for the elaboration of the present model, are shortly summarised below.

Dislocation cell structures are the first structures recognised as such in metals under deformation. In an undeformed metal, the dislocation distribution is close to statistically homogeneous (random). However, at the beginning of the deformation process, interacting dislocations tend to cluster and form tangles, thereby creating regions with relatively increased dislocation densities. As the strain increases, more dislocations participate in the evolution of the structure and the tangles link up to form 'dislocation boundaries', which envelop regions that are relatively free of dislocations. The structure created in this way can be observed as a network of volume elements within which the dislocation density is well below average, mutually connected through boundaries in which dislocations are concentrated. This structure is known as a cell structure (Fig. 4.1) and the dislocation boundaries forming this structure are the so-called cell walls.

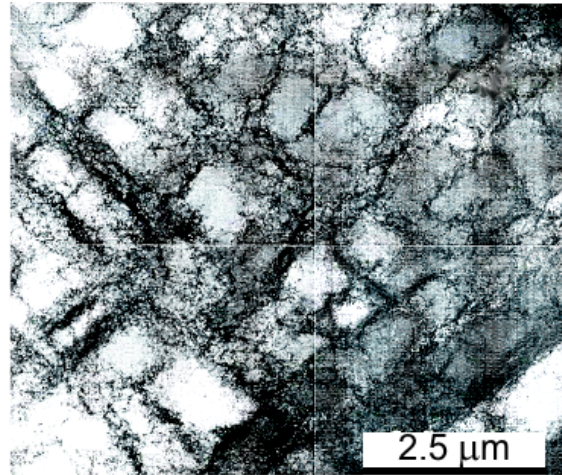


Figure 4.1 — Dislocation cell structure [McCabe et al., 2004].

Upon visualisation with transmission electron microscopy (TEM), the cells appear in equiaxed or elongated two-dimensional shapes with a typical size in the order of a few microns. The dislocation walls, or boundaries, are distinguishable as fractions with a high concentration of dislocations occupying about 10% – 20% of the total volume. The dislocations inside the walls are irregularly jogged and tangled and therefore do not produce high lattice curvatures. The cell structure differs from other dislocation structures, such as cell blocks and shear bands, through the low misorientation of the dislocation boundaries, i.e. there appears to be a negligible variation in slip activity across the cell walls.

The orientation of the dislocation structure has received a lot of attention in the past decade [McCabe et al., 2004; Huang and Hansen, 1997; Hansen and Huang, 1997; Winther et al., 2000; Liu et al., 1998; Wert et al., 1995]. In polycrystals, the structure develops quite uniformly inside grains, reflecting a regular array of aligned dislocation boundaries. The morphology and orientation of the dislocation structure in each grain are clearly influenced by the crystallographic orientation of the grain [Winther et al., 2000; Driver et al., 1994; Godfrey et al., 1998]. In grains exhibiting single slip the dislocation cell walls are often observed to align with the crystallographic system. In contrast, grains deforming through multislip, form cell structures along the macroscopic planes of maximum shear stress [Bay et al., 1992; Hansen and Huang, 1997], with negligible correlation with slip planes [Hurley et al., 2003]. The intrinsic relation between the dislocation cell orientation, grain crystallography and the macroscopic loading direction appears to be complex and still unclear in several aspects. In a recent review on the subject [Winther, 2003], the author concluded that in most deformations favouring multislip, the macroscopic orientation of the cell structure can be assumed uniform across the polycrystal and related to the macroscopic planes of maximum shear stress. This suggestion is followed in the present paper.

The deformation of a metal developing dislocation cell structures is accompanied by the presence of long-range internal stresses. The existence of these stresses in structures has been demonstrated on the basis of in-situ TEM observations. The internal stress field was evaluated by inspection of the curvature of bowed dislocation segments in and near substructural boundaries [Mughrabi, 2001, 1983]. The analysis of asymmetric X-ray line diffraction profiles [Straub et al., 1996; Borbely et al., 1997; Müller et al., 1996; Ungar et al., 1984] provided another experimental technique to highlight and quantify the internal stress distribution.

Experimental investigations indicate that the long-range stresses in the cell structure are of the same order as the applied stress. This high level is reached in the cell walls, while in the cell interior the internal stress is significantly lower. The internal stresses appear to amplify the externally applied stresses in the cell walls and to reduce the applied stress in the cell interiors [Straub et al., 1996; Mughrabi et al., 1986; Hecker et al., 2002]. The spatial distribution of the internal stresses is periodic and accommodates the periodicity of the cell structure. Experimental investigation of the internal stress anisotropy [Hecker et al., 2002] shows that the orientation of the principal stress axes is insensitive to the grain orientation but is rather defined by the macroscopic loading axes and the mesoscopic heterogeneity of the plastic strain. Accordingly, the level of the internal stress grows with deformation as heterogeneity increases. It should be mentioned here that the internal stress observed in deformed cell structures is a consequence of the deformation applied to an intrinsically heterogeneous material. In this respect, this long-range stress differs from the lower internal stress commonly associated with the low-energy dislocation arrangement cell structures, studied by Kuhlmann-Wilsdorf [1996].

4.2 Composite cell structure model

The objective of this paper is to predict the average macroscopic behaviour of metals on the basis of a developing dislocation structure under deformation. The attention is here concentrated on the contribution of the dislocation cell structure. The morphology and orientation of the cell structure might vary between grains. However, as discussed in the introduction, these variations are small if the structure has been developed under deformation favouring multislip. The considerations here will be restricted to such loadings, allowing the following simplification. The material behaviour of a polycrystal with a nonuniform cell structure is modelled by the behaviour of a material with uniformly distributed cells. The considered geometry and orientation of the cells represent the average morphology of the real cell structure in a polycrystal. Using a mean field approximation, the mechanical behaviour of the model material with uniform cells is identified with the mean response of the actual polycrystal material with a nonuniform dislocation structure.

The mean field approach, pursued here, is motivated by experimental observations reporting that the morphology of the cells is dominantly influenced by the macroscopic loading. Under multislip conditions, the cell structure is defined by the loading and hardly varies between the grains. In the general case, differences in the lattice orientation cause variations in the local deformation behaviour between grains and, consequently, in the cell structure formed. It is believed though, that, for an FCC material, due to the high symmetry of the lattice, enough slip systems are available to accommodate the applied macroscopic loading and therefore, the local fluctuations of the cell geometry over the grains is expected to remain small. Consequently, it is assumed that nonuniformity within each grain is the dominant factor, and not the variations from grain to grain.

Consistent with the mean field approach adopted, an FCC polycrystal is represented here by a material with corresponding averaged properties, in which the 'mean' dislocation cell structure is the prime source of nonuniformity. The mechanical problem, expressing the behaviour of the material under external loading, is formulated by the following system of equations to be

satisfied in every material point of the specimen:

$$\begin{cases} \vec{\nabla} \cdot \boldsymbol{\sigma}(\vec{x}) = \vec{0} \\ \mathbf{F}(\vec{x}) = [\vec{\nabla}_0 \vec{x}]^c \\ \boldsymbol{\sigma}(\vec{x}, t) = \boldsymbol{\sigma} \{ \mathbf{F}(\vec{x}, \tau) | \tau \leq t \} \end{cases} \quad (4.1)$$

where \vec{x} is the position vector of a material point in the current configuration, and $\vec{\nabla}_0$ and $\vec{\nabla}$ are the gradient operators in the initial and current configurations, respectively. The field quantities $\boldsymbol{\sigma}(\vec{x}, t)$ and $\mathbf{F}(\vec{x})$ are the Cauchy stress tensor and the deformation gradient tensor. The first equation in (4.1) represents the standard local equilibrium equation, the second one is the classical definition of \mathbf{F} , implying compatibility at the material point level. The last equation expresses the local history dependent constitutive relation for the material. Next, the averaging equations are applied with the assumption of a negligible volume change of the polycrystal specimen during the whole deformation process:

$$\tilde{\mathbf{F}} = \frac{1}{V} \int_V \mathbf{F}(\vec{x}) dV \quad \text{and} \quad \tilde{\boldsymbol{\sigma}} = \frac{1}{V} \int_V \boldsymbol{\sigma}(\vec{x}) dV \quad (4.2)$$

where V is the volume; the averages $\tilde{\boldsymbol{\sigma}}$ and $\tilde{\mathbf{F}}$ are taken identical to the macroscopic stress tensor and deformation gradient tensor applied externally to the specimen.

To solve the problem (4.1)–(4.2) for a material configuration with a cell structure, the morphology of it should be specified and the constitutive relations for the cell components should be specified. As it was proposed by Mughrabi et al. [1986], a material with a dislocation cell structure is idealised here as a two-phase periodic composite consisting of cell walls and cell interiors. The cell wall component represents the phase with a dislocation density ρ_w , which is significantly higher than the average dislocation density ρ_{total} of the composite. The cell interior component typically represents the volume enclosed by the dislocation walls, with a dislocation density ρ_c significantly lower than the average. The dislocation density is assumed to be the only independent variable distinguishing the two phases considered.

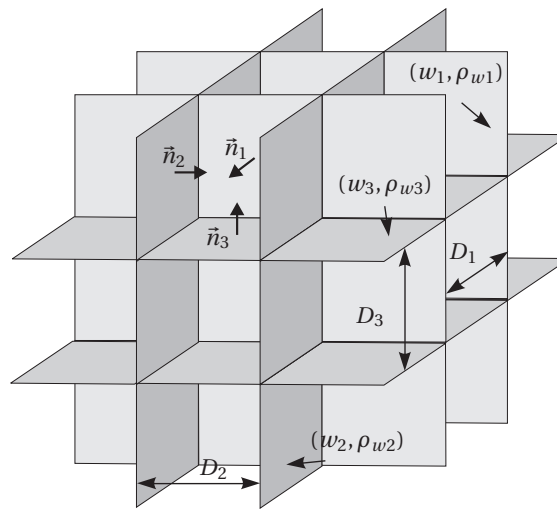


Figure 4.2 — Model geometry of the cell structure and its components.

The morphology of the composite, adopted in this paper, is shown in Fig. 4.2. Inspired by experimental observations (e.g. see Fig. 4.1), the cell structure is modelled as a 3D

periodic stacking of cubic cells with dimensions $D_1 \times D_2 \times D_3$, separated by three mutually perpendicular sets of cell walls with unit normals $\vec{n}_1, \vec{n}_2, \vec{n}_3$ and with different thicknesses w_1, w_2 and w_3 . The dislocation densities in the cell walls, $\rho_{w1}, \rho_{w2}, \rho_{w3}$, respectively, depend on the orientation, as a result of prior deformation. The spatial orientation of the cell structure is given by the normals $\{\vec{n}_1, \vec{n}_2, \vec{n}_3\}$.

The dislocations inside the cell and wall components are assumed to be distributed uniformly, along with the stress and deformation tensors inside each component:

$$\{\boldsymbol{\sigma}(\vec{x}), \mathbf{F}(\vec{x})\} = \begin{cases} \{\boldsymbol{\sigma}_c, \mathbf{F}_c\}, & \vec{x} \in \text{cell interior} \\ \{\boldsymbol{\sigma}_{wi}, \mathbf{F}_{wi}\}, & \vec{x} \in \text{wall } i, i = 1, 2, 3 \end{cases} \quad (4.3)$$

Consequently, four uniform material components have been distinguished: the cell walls with three mutually perpendicular orientations and the cell interior. A geometrical distinction between the differently oriented walls has been made, since a difference in the orientation will generally lead to a different mechanical response even in the case of initially equal dislocation densities. Here and further on, the variables referring to the cell interior are denoted by the subscript c and the variables belonging to the cell walls by w_1, w_2 or w_3 .

Since the stresses and strains are assumed to be uniform inside each phase, the equilibrium and compatibility equations (4.1) are here satisfied trivially. Thus, at the level of the individual phases, the system (4.1) is reduced to the constitutive relation of the corresponding phase only. However, at the interfaces between the components the traction continuity and the interface kinematic compatibility have to be taken into account. The cell composite includes three orientations of cell-wall interfaces. The wall-wall junctions are very small and will be left out of consideration. At the planar interface between the cell interior and wall i the traction continuity of the stresses is represented by:

$$(\boldsymbol{\sigma}_c - \boldsymbol{\sigma}_{wi}) \cdot \vec{n}_i^t = \vec{0}, \quad i = 1, 2, 3 \quad (4.4)$$

while the compatibility of deformation at the interface is provided by:

$$(\mathbf{F}_c - \mathbf{F}_{wi}) \cdot (\mathbf{I} - \vec{n}_i^0 \vec{n}_i^0) = \mathbf{0}, \quad i = 1, 2, 3 \quad (4.5)$$

where \vec{n}_i^0, \vec{n}_i^t are the normal vectors to the walls in the initial and the current configuration, respectively. They are related according to:

$$\vec{n}_i^t = \frac{\vec{n}_i^0 \cdot [\mathbf{F}_c]^{-1}}{\|\vec{n}_i^0 \cdot [\mathbf{F}_c]^{-1}\|} \quad (4.6)$$

In summary, the solution of the original problem (4.1) is approximated by piecewise uniform fields (4.3), which are satisfying the system:

$$\begin{cases} \boldsymbol{\sigma}_c = \boldsymbol{\sigma}(\mathbf{F}_c) \\ \boldsymbol{\sigma}_{wi} = \boldsymbol{\sigma}(\mathbf{F}_{wi}) \\ (\boldsymbol{\sigma}_c - \boldsymbol{\sigma}_{wi}) \cdot \vec{n}_i^t = \mathbf{0} \\ (\mathbf{F}_c - \mathbf{F}_{wi}) \cdot (\mathbf{I} - \vec{n}_i^0 \vec{n}_i^0) = \mathbf{0}, \quad i = 1, 2, 3 \end{cases} \quad (4.7)$$

Solution of this system instead of the original one (4.1) evidently offers a significant advantage with respect to the computational effort. Approximations of the above type are successfully used for materials with a lamellae structure [Van Dommelen et al., 2003].

To determine the average stress and deformation gradient of the cell composite, Eqs. (4.2) can be rewritten as:

$$\tilde{\boldsymbol{\sigma}} = f_{w1}\boldsymbol{\sigma}_{w1} + f_{w2}\boldsymbol{\sigma}_{w2} + f_{w3}\boldsymbol{\sigma}_{w3} + (1 - f_{w1} - f_{w2} - f_{w3})\boldsymbol{\sigma}_c \quad (4.8)$$

$$\tilde{\mathbf{F}} = f_{w1}\mathbf{F}_{w1} + f_{w2}\mathbf{F}_{w2} + f_{w3}\mathbf{F}_{w3} + (1 - f_{w1} - f_{w2} - f_{w3})\mathbf{F}_c \quad (4.9)$$

in which the volume change during deformation has been neglected. The volume fractions f_{wi} of the walls are given by:

$$f_{w1} = \frac{V_{w1}}{V} = \frac{w_1(D_2 + \frac{w_2}{2})(D_3 + \frac{w_3}{2})}{(D_1 + w_1)(D_2 + w_2)(D_3 + w_3)} \quad (4.10a)$$

$$f_{w2} = \frac{V_{w2}}{V} = \frac{w_2(D_1 + \frac{w_1}{2})(D_3 + \frac{w_3}{2})}{(D_1 + w_1)(D_2 + w_2)(D_3 + w_3)} \quad (4.10b)$$

$$f_{w3} = \frac{V_{w3}}{V} = \frac{w_3(D_1 + \frac{w_1}{2})(D_2 + \frac{w_2}{2})}{(D_1 + w_1)(D_2 + w_2)(D_3 + w_3)} \quad (4.10c)$$

The system of equations (4.7)–(4.10) determines the constitutive behaviour at the cell level and the resulting macroscopical response of a material with a dislocation cell structure. The next section completes the description by specifying the local relations between the stresses and the deformations inside each component.

4.3 Constitutive equations

In this section, attention is focused on the local material behaviour of the components of the cell structure material consisting of the cell walls and the cell interiors. As previously emphasised, the composite model aims to represent the average behaviour of a polycrystal using a mean field approach. Accordingly, the material behaviour attributed to the cell interior component reflects the average behaviour of all cell interiors in the polycrystal and the material behaviour in the cell walls is representative for the average of all walls. Microscopic details of the material behaviour as described by dislocation dynamics, slip anisotropy, etc. are assumed to contribute in a second-order manner only and are therefore not taken into account. Consequently, the material behaviour of the distinct phases will be described by continuum elastoplasticity in the context of finite deformations. The typical equations for elastoplastic material behaviour in the presence of isotropic and kinematic hardening are outlined below (here i refers to w_1, w_2, w_3 or c , denoting the different components).

In the classical theory of elastoplasticity for finite deformations the deformation gradient tensor \mathbf{F}_i of a phase i is multiplicatively decomposed into a plastic part \mathbf{F}_i^p and an elastic part \mathbf{F}_i^e according to:

$$\mathbf{F}_i = \mathbf{F}_i^e \cdot \mathbf{F}_i^p \quad (4.11)$$

The velocity gradient tensor \mathbf{L}_i in each phase is given by:

$$\mathbf{L}_i = \dot{\mathbf{F}}_i \cdot [\mathbf{F}_i]^{-1} \quad (4.12)$$

The symmetric and skew-symmetric parts of \mathbf{L}_i are the rate of deformation tensor \mathbf{D}_i and the spin tensor \mathbf{W}_i , respectively. By substitution of Eq. (4.11) into (4.12) these tensors can also be decomposed in an elastic and a plastic part:

$$\begin{aligned}\mathbf{L}_i &= \dot{\mathbf{F}}_i \cdot [\mathbf{F}_i]^{-1} = \dot{\mathbf{F}}_i^e \cdot [\mathbf{F}_i^e]^{-1} + \mathbf{F}_i^e \cdot \dot{\mathbf{F}}_i^p \cdot [\mathbf{F}_i^p]^{-1} \cdot [\mathbf{F}_i^e]^{-1} \\ &= \mathbf{L}_i^e + \mathbf{F}_i^e \cdot \mathbf{L}_i^p \cdot [\mathbf{F}_i^e]^{-1} = (\mathbf{D}_i^e + \mathbf{W}_i^e) + \mathbf{F}_i^e \cdot (\mathbf{D}_i^p + \mathbf{W}_i^p) \cdot [\mathbf{F}_i^e]^{-1}\end{aligned}\quad (4.13)$$

It is well-known that the decomposition in Eq. (4.11) is not unique because rotational effects can be assigned either to \mathbf{F}_i^p or to \mathbf{F}_i^e . Uniqueness is restored by an extra condition, e.g. that the plastic deformation occurs spin-free: $\mathbf{W}_i^p = \mathbf{0}$. As a consequence of this choice, additional rotations superimposed to the original deformation process are fully attributed to the elastic deformation gradient tensor \mathbf{F}_i^e , while the plastic deformation gradient tensor \mathbf{F}_i^p is not affected.

The intermediate stress-free configuration defined by the plastic deformation gradient tensor \mathbf{F}_i^p is considered as the reference state for the elastic behaviour, implicitly assuming that the elastic constitutive response is not affected by the plastic slip. The second Piola-Kirchhoff stress measure $\boldsymbol{\tau}_i$ is defined with respect to that configuration and is related to the Cauchy stress tensor $\boldsymbol{\sigma}_i$ by:

$$\boldsymbol{\tau}_i = \det(\mathbf{F}_i^e) [\mathbf{F}_i^e]^{-1} \cdot \boldsymbol{\sigma}_i \cdot [\mathbf{F}_i^e]^{-T} \quad (4.14)$$

The stress measure $\boldsymbol{\tau}_i$ is determined from its work-conjugated elastic Green-Lagrange strain measure \mathbf{E}_i^e through the Hookean isotropic linear elastic relation

$$\boldsymbol{\tau}_i = \mathbb{C} : \mathbf{E}_i^e \quad \text{with} \quad \mathbf{E}_i^e = \frac{1}{2}([\mathbf{F}_i^e]^T \cdot \mathbf{F}_i^e - \mathbf{I}) \quad (4.15)$$

where \mathbf{I} is the second-order unit tensor. Since the model material is actually a mean field approximation of a polycrystal, the anisotropy of the local elastic behaviour is assumed to be averaged out, justifying the use of isotropic elasticity. The fourth-order isotropic elasticity tensor \mathbb{C} is defined by the bulk modulus K and the shear modulus G :

$$\mathbb{C} = K\mathbb{I}\mathbb{I} + 2G(\mathbb{I} - \frac{1}{3}\mathbb{I}\mathbb{I}) \quad (4.16)$$

with \mathbb{I} the fourth-order unit tensor. The plastic yield criterion is determined by a yield function Ψ_i (defining the yield surface in stress space). The Von Mises yield function Ψ_i including isotropic and kinematic hardening is here adopted:

$$\Psi_i = \bar{s}_i - \sigma_i^y \quad \text{with} \quad \bar{s}_i = \sqrt{\frac{3}{2} \mathbf{s}_i^d : \mathbf{s}_i^d} \quad \text{and} \quad \mathbf{s}_i = \boldsymbol{\tau}_i - \hat{\boldsymbol{\beta}}_i \quad (4.17)$$

where the superscript d indicates the deviatoric part. This yield function is formulated with respect to the stress-free intermediate configuration and evaluates the difference between the equivalent stress measure \bar{s}_i (which depends on the second Piola-Kirchhoff stress tensor $\boldsymbol{\tau}_i$ and a back stress tensor $\hat{\boldsymbol{\beta}}_i$) and the yield stress σ_i^y . The back stress tensor is a symmetric tensor defined in the stress-free intermediate configuration and triggers a shift of the yield surface in stress space, inducing kinematic hardening. The dominating physical origin of the back stress is the long-range dislocation interaction. The dislocation network present in the material

induces an internal stress β_i which, together with the applied stress, is the driving force of the plastic slip. The back stress in Eq. (4.17) is related to the internal stress β_i by:

$$\hat{\beta}_i = -\beta_i \quad (4.18)$$

The calculation of the internal stresses is discussed in the next section.

The resistance of the material to plastic deformation enters the model through the yield stress. Here, the yield stress σ_i^y is considered as the stress value required to overcome the resistance resulting from e.g. a dislocation forest. This yield stress, resulting from short-range interactions of dislocations, is often postulated to be inversely proportional to the dislocation spacing d_i :

$$\sigma_i^y = \frac{\alpha_i M G b}{d_i} = \alpha_i M G b \sqrt{\rho_i} \quad (4.19)$$

where b is the length of the Burgers vector and M is a parameter. factor which relates the axial stress to the shear stress. The local density ρ_i of a network of dislocations is related to the spacing d_i by $\rho_i = d_i^{-2}$. The dimensionless coefficient α_i is in the range from 0.05 to 2.6 and can be physically interpreted as an interaction constant whose magnitude is proportional to the energy gain when pairwise dislocation interactions take place during deformation. Thus, α_i depends on the dislocation type and distribution prevailing in the material. Since the dislocation arrangements in cells and walls differ, the coefficient might be different for every phase α_i .

The yield function Ψ_i properly defines the occurrence of elastoplastic behaviour of the material if complemented by the Kuhn-Tucker conditions:

$$\Psi_i \leq 0, \quad \dot{\lambda}_i \geq 0, \quad \dot{\lambda}_i \Psi_i = 0 \quad (4.20)$$

where $\dot{\lambda}_i$ is the plastic multiplier, a scalar measure quantifying the magnitude of plastic flow rate. The plastic deformation rate is assumed to be governed by an associative flow rule:

$$\mathbf{D}_i^p = \dot{\lambda}_i \frac{\partial \Psi_i}{\partial \mathbf{s}_i} \quad (4.21)$$

The set (4.11)–(4.21) provides a system of equations to determine the stress response σ_i of each individual composite component, given deformation history $\mathbf{F}_i(t)$. To solve this system, \mathbf{F}_i^p should be calculated using (see Eq. (4.13)):

$$\dot{\mathbf{F}}_i^p = \mathbf{D}_i^p \cdot \mathbf{F}_i^p \quad (4.22)$$

whereby a time integration should be performed. The implicit integration of (4.22) yields [Bronkhorst et al., 1992; Kalidindi et al., 1992; Evers et al., 2002],

$$\mathbf{F}_i^p(t + \Delta t) = (\mathbf{I} + \mathbf{D}_i^p(t + \Delta t)) \cdot \mathbf{F}_i^p(t) \quad (4.23)$$

The cell structure model will be next completed by micromechanical relations for the calculation of the internal stresses β_i present in the material as a result of the dislocation network.

4.4 Statistically stored dislocations

The isotropic hardening in the material depends on the density of statistically stored dislocations $\rho_c, \rho_{w1}, \rho_{w2}, \rho_{w3}$, see Eq. (4.19). The evolution of the statistically stored dislocations in the cell structure is described by the following equations:

$$\dot{\rho}_c = \frac{M}{b} (I\sqrt{\rho_c} - R\rho_c)\dot{\epsilon}_c - \dot{\rho}^{c-w} \quad (4.24a)$$

$$\dot{\rho}_{wi} = \frac{M}{b} (I\sqrt{\rho_{wi}} - R\rho_{wi})\dot{\epsilon}_{wi} + \dot{\rho}^{c-w} \frac{1 - f_{w1} - f_{w2} - f_{w3}}{3f_{wi}}, \quad i = 1, 2, 3 \quad (4.24b)$$

$$t = 0 : \rho_{wi}^0 = \rho_c^0 = \rho^0 \quad (4.24c)$$

where ρ^0 defines the initial dislocation density in the undeformed material, which is assumed to be homogeneous. In Eq. (4.24b), $\dot{\rho}^{c-w}$ is scaled to preserve the total amount of dislocations. The quantities $\dot{\epsilon}_c$ and $\dot{\epsilon}_{wi}$ are the equivalent plastic strain rates in the cell and walls, respectively, and they are related to the corresponding plastic strain rate tensors as $\dot{\epsilon}_i = \sqrt{\mathbf{D}_i^p : \mathbf{D}_i^p}$. The first two contributions in (4.24a) and (4.24b) are the same for cells and walls and reflect the widely-used continuum evolution of the dislocation density: the first term accounts for dislocation creation and the second – for dislocation annihilation. The material parameters I and R associated with these processes are related to the effective slip length and to the critical annihilation distance, respectively. The last terms in both equations are introduced to describe the dislocation flux from the cell interior to the cell walls. This flux triggers the creation and development of the dislocation structure and manifests itself through an increasing difference between the dislocation densities in the cell and walls. For simplicity, it is assumed that the dislocations leaving the cell interior are equally distributed between all walls.

To quantify the cell-wall flux, it is assumed that a fraction of all mobile dislocations in the cell interior leave the interior to join the cell walls. The amount of mobile dislocations present in the cells is given by the first contribution in the evolution Eq. (4.24a). Thus, the assumption can be formalised by:

$$\dot{\rho}^{c-w} = C \frac{M}{b} I \sqrt{\rho_c} \dot{\epsilon}_c \quad (4.25)$$

with C a material dependent factor.

4.5 Internal stress

4.5.1 Geometrically necessary dislocations

This section addresses the calculation of the internal stress $\boldsymbol{\beta}$ introduced in the constitutive model to describe the kinematic hardening of the material. Since the back stress is the opposite of the internal stress created by the dislocation network, attention is next focused on the presence of geometrically necessary dislocations and their associated stress fields.

The dislocations introduced in the model so far are uniformly distributed in the walls and in the cell interiors of the cell structure. These are the so-called statistically stored dislocations (SSDs) because they are due to statistical mutual trapping of gliding dislocations. The statistically stored dislocations are randomly oriented and therefore the stress fields associated with individual dislocations will cancel each other out. As a result, these dislocations do not create long-range effects and they influence the deformation behaviour only by means of short-range interactions with gliding dislocations. Therefore these dislocations are taken into account in the yield stress parameter (4.19) only and they do not contribute to the back stress.

On the contrary, dislocations arranged in configurations with a nonzero net Burgers vector produce long-range stresses. These dislocation arrangements are required to accommodate the incompatibility of the plastic deformation field and therefore dislocations of this type are called geometrically necessary dislocations (GNDs).

Geometrically necessary dislocations are naturally present in a material with heterogeneous plastic deformation and hence also in a material with a cell structure. Under external loading, a nonuniform field of plastic strains will be present in the cell structure. In the cell interior phase, plastic slip is easier compared to the cell walls, where the deformation is impeded by a high density of tangled dislocations. To ensure compatibility of the plastic deformation across the interface between the hard and soft phases, polarised layers of geometrically necessary dislocations will develop at this interface. The long-range stresses created by the interface dislocations are considered to be the main source of the internal stresses in a material with a cell structure. These interface dislocations will, therefore, be included in the cell structure model.

The geometrically necessary dislocations are incorporated in the model by assuming that they are concentrated in (fictitious) thin layers at the interfaces between the cell interior component and the wall components (Fig. 4.3). In this way, these GND interface layers constitute an additional ingredient of the cell composite. Two approaches to deal with these interfaces are considered here.

In the first approach, the interfaces are treated as isolated areas with a negligible thickness. Following this assumption, the GNDs will influence the mechanical behaviour of the components only through long-range stresses. The contribution of the interface layers to the averaged response of the composite, in Eqs. (4.8)–(4.9), can be neglected due to the negligible volume fraction of these layers and since the stresses and strains inside the layers are expected to be of the same order of magnitude as the stresses and strains in the other components. Hence, in this approach, the short-range effect of the GNDs is excluded from the model and the interface dislocations enter the model only as a source of internal stress, i.e. in the calculation of the back stress only.

In the second approach, the interface layers are considered to be part of the corresponding cell walls. Then, the geometrically necessary dislocations also contribute to the yield stress in the walls in addition to the statistically stored dislocations and (4.19) is reformulated accordingly:

$$\sigma_i^y = \alpha_i M G b \sqrt{\rho_i + \rho_i^{GND}}, \quad i = w_1, w_2, w_3 \quad (4.26)$$

where ρ_i^{GND} is the density of the dislocations in the interface averaged over the area of the corresponding wall. In this way both the short-range and the long-range effects of the interface GNDs are taken into account. From a modelling perspective, the difference between the two

approaches results only in a somewhat different isotropic hardening: the first approach ignores the contribution of the GNDs, the second does not.

Both approaches handling the interface layers can be supported by a physical motivation. In the first approach, the isolated interface layers can be interpreted as pile-ups of dislocations arrested at the interfaces by non-penetrable walls. The second approach corresponds to the case that the plastic incompatibility is accumulated by a nonzero net geometrical effect of all dislocations in the wall. Since the actual dislocation arrangement in the dislocation walls is still an open question [Jackson, 1985; Jackson and Siedersleben, 1984; Prinz et al., 1982], there is no clear reason to give preference to one of the approaches and both will be used and compared in this paper.

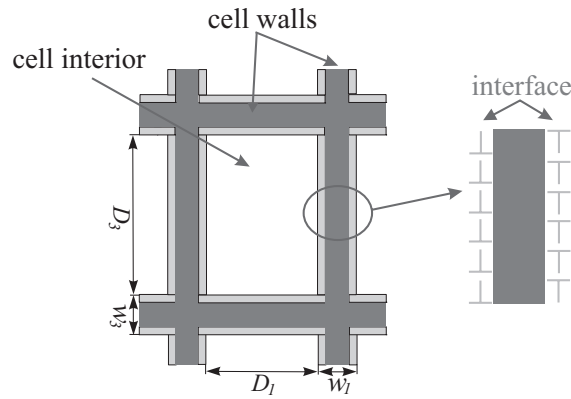


Figure 4.3 — Geometry of a cell structure cross-section with the interface layers. The edge dislocations represent an example of the dislocation configuration in the layers.

Finally, it is worth to mention that the introduction of the interfacial geometrically necessary dislocations does not cause a lattice misorientation between adjoining cells. Indeed, the interface dislocations induce a lattice misorientation in the adjoining volume elements, i.e. cell interiors and walls, however, they do not create a misorientation across the walls. In fact, the spatial variations of the plastic deformation over the interfaces at both sides of a wall counteract each other. Thus, the two interfaces edging a cell wall from opposite sides have equal dislocation densities, yet with an opposite sign. GNDs on opposite sides of a cell wall rotate the crystal lattice in opposite directions and compensate each other.

The density of the geometrically necessary dislocations can be quantified by the dislocation density tensor. This tensor $\mathbf{\Lambda}$ was introduced by Nye [1953] to relate the net Burgers vector of dislocations piercing a unit surface area, \vec{B} , to the unit normal \vec{n} on that surface:

$$\vec{B} = \mathbf{\Lambda} \cdot \vec{n} \quad (4.27)$$

Within the context of finite deformation kinematics the tensor $\mathbf{\Lambda}$ is determined as¹ [Steinmann, 1996]:

$$\mathbf{\Lambda} = \mathbf{F}_p \cdot [\vec{\nabla}_p \times [\mathbf{F}^p]^{-T}]^T \quad (4.28)$$

Here, the dislocation density tensor $\mathbf{\Lambda}$, as well as \vec{B} and \vec{n} , are defined in the intermediate configuration defined by \mathbf{F}^p , and $\vec{\nabla}_p$ is the gradient operator in that configuration.

¹Note that the dimension of $\mathbf{\Lambda}$ is $[\frac{1}{m}]$, since it is related to the Burgers vector [m] per unit surface area [m²]

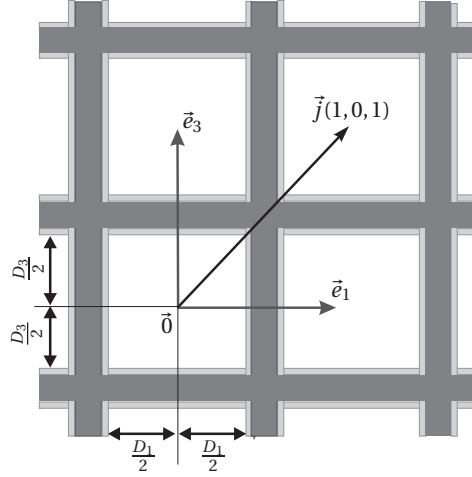


Figure 4.4 — Cartesian vector basis associated with the cell structure.

Different expressions can be found in the literature relating the dislocation density tensor to derivatives of the plastic deformation or inverse elastic deformation gradients [Acharya and Bassani, 2000; Evers et al., 2002; Arsenlis et al., 2004]. Steinmann [1996] has shown that all of these tensor measures of the dislocation density are related through appropriate configurational mappings. Expression (4.28) defined in the intermediate configuration is adopted here, since the geometry of the cell structure and further derivations of the internal stresses are related to that configuration. The components of the dislocation density tensor with respect to a given vector basis can be interpreted as the density of the dislocations with a Burgers vector in direction i and a line vector in direction j :

$$\Lambda_{ij} = \sum_{\zeta} \rho^{\zeta} b_i^{\zeta} t_j^{\zeta} \quad (4.29)$$

where \vec{t} is the unit vector in the direction of the dislocation line, \vec{b} is the Burgers vector ($\|\vec{b}\| = b$) and the summation is performed over all types ζ of dislocations present in a unit volume of the material. It should be noticed that only densities of the geometrically necessary dislocations are involved in the calculation of Λ , since the statistically stored dislocations have a zero net contribution. Thus, the density of the geometrically necessary dislocations is determined by the plastic deformation incompatibility through (4.28) and Λ will be used as the associated quantifying tensor.

In the following, the distribution of the geometrically necessary dislocations $\Lambda(\vec{x})$ is derived for the cell structure model. In the cell composite, the deformation is assumed to be uniform inside cells and walls (4.3) and to vary only across the interfaces. Since the width of the interfaces is assumed to be negligible, the plastic deformation distribution over the composite can be approximated by a step function with a jump at the interfaces:

$$\mathbf{F}^p(\vec{x}) = \begin{cases} \mathbf{F}_c^p, & \vec{x} \in \text{cell interior} \\ \mathbf{F}_{wi}^p, & \vec{x} \in \text{wall } i = 1, 2, 3 \end{cases} \quad (4.30)$$

Clearly, the gradient of the plastic deformation is only non-vanishing at the interfaces. In order to ease further derivations, the geometry of the cell structure is next defined in the intermediate configuration: the cells are assumed to be cuboid, i.e. the walls are mutually

perpendicular in the intermediate configuration. This assumption was motivated earlier by experimental observations (Fig. 4.1) of approximately perpendicular cell walls in metals after elastic unloading. A Cartesian coordinate system $\{\vec{e}_1, \vec{e}_2, \vec{e}_3\}$ in the intermediate configuration is introduced with the origin in the centre of a cell (Fig. 4.4). Then, in the cell containing the origin, two vertical interfaces with the normal in \vec{e}_1 -direction are given by the following functions:

$$\check{I}_1^-(\vec{x}) = \delta\left(x_1 + \frac{D_1}{2}\right) B\left(x_2 + \frac{D_2}{2}, x_2 - \frac{D_2}{2}\right) B\left(x_3 + \frac{D_3}{2}, x_3 - \frac{D_3}{2}\right) \quad (4.31a)$$

$$\check{I}_1^+(\vec{x}) = \delta\left(x_1 - \frac{D_1}{2}\right) B\left(x_2 + \frac{D_2}{2}, x_2 - \frac{D_2}{2}\right) B\left(x_3 + \frac{D_3}{2}, x_3 - \frac{D_3}{2}\right) \quad (4.31b)$$

where $\delta(a)$ denotes the Dirac function, with $\delta(a) = 0$, if $a \neq 0$, and $B(a, b)$ is the Boxcar function, defined through the Heaviside step function as $B(a, b) = H(a) - H(b)$. Similarly for the interfaces with the normal in the \vec{e}_2 -direction:

$$\check{I}_2^-(\vec{x}) = B\left(x_1 + \frac{D_1}{2}, x_1 - \frac{D_1}{2}\right) \delta\left(x_2 + \frac{D_2}{2}\right) B\left(x_3 + \frac{D_3}{2}, x_3 - \frac{D_3}{2}\right) \quad (4.32a)$$

$$\check{I}_2^+(\vec{x}) = B\left(x_1 + \frac{D_1}{2}, x_1 - \frac{D_1}{2}\right) \delta\left(x_2 - \frac{D_2}{2}\right) B\left(x_3 + \frac{D_3}{2}, x_3 - \frac{D_3}{2}\right) \quad (4.32b)$$

and with the normal in the \vec{e}_3 -direction:

$$\check{I}_3^-(\vec{x}) = B\left(x_1 + \frac{D_1}{2}, x_1 - \frac{D_1}{2}\right) B\left(x_2 + \frac{D_2}{2}, x_2 - \frac{D_2}{2}\right) \delta\left(x_3 + \frac{D_3}{2}\right) \quad (4.33a)$$

$$\check{I}_3^+(\vec{x}) = B\left(x_1 + \frac{D_1}{2}, x_1 - \frac{D_1}{2}\right) B\left(x_2 + \frac{D_2}{2}, x_2 - \frac{D_2}{2}\right) \delta\left(x_3 - \frac{D_3}{2}\right) \quad (4.33b)$$

Then, the interfaces in the periodic cell structure are defined by the following periodic functions:

$$I_i^\pm(\vec{x}) = \check{I}_i^\pm(\vec{x} + \vec{j}(r, s, t)), \quad i = 1, 2, 3 \quad (4.34)$$

Here the vector $\vec{j}(r, s, t)$ defines a shift for the interfaces of a cell to account for the spatial periodicity in the \vec{e}_1 , \vec{e}_2 and \vec{e}_3 directions:

$$\vec{j}(r, s, t) = \{(D_1 + w_1)r; (D_2 + w_2)s; (D_3 + w_3)t\} \quad (4.35)$$

with r , s and t integer numbers indexing cells in the composite under consideration, varying from $-N_1$ to N_1 , from $-N_2$ to N_2 and from $-N_3$ to N_3 , respectively, to define a composite domain covering $(2N_1 + 1) \times (2N_2 + 1) \times (2N_3 + 1)$ cells.

With the use of the notation introduced for the interfaces ², the derivatives of the inverse plastic deformation tensor (4.30) are given by their discrete approximations:

$$\frac{\partial[\mathbf{F}^p]^{-1}}{\partial \vec{x}_1} = \Delta[\mathbf{F}^p]_1^{-1} [I_1^-(\vec{x}) - I_1^+(\vec{x})] \quad (4.36a)$$

² Note that the dimension of $I_i^\pm(\vec{x})$ is $\frac{1}{m}$.

density tensor and the scalar densities ρ^ζ , where ζ refers to the dislocation type. Then, the total dislocation density ρ^{GND} can be determined by summing up over ζ . However, as pointed out by Arsenlis and Parks [1999], the decomposition of the tensor Λ into a set of scalars ρ^ζ is not unique for FCC crystals and has to be solved in the context of a minimisation problem. That problem requires information about the crystal lattice orientation which is not available in the present model. Therefore, in this paper the total density of GNDs is approximated by the minimum density of ‘continuum’ dislocations required to accommodate the plastic incompatibility Λ when there are no crystallographic restrictions on the formation of dislocations. In that case, the dislocation density can be related to a Burgers vector averaged over the surface of the corresponding interface, containing GNDs, with the use of the Eq. (4.27). For instance, the continuum dislocation density of geometrically necessary dislocations ρ_{w1}^{GND} in the wall 1 can be calculated as:

$$\rho_{w1}^{GND} = \frac{2 \int_S \|\vec{B}\| ds}{b S_w} = \frac{2}{b S_w} \int_S \|\Lambda \cdot \vec{N}(s)\| ds, \quad (4.41)$$

where \vec{B} is again the net Burgers vector per unit surface area, S the complete surface area of the interface 1 in the intermediate configuration and \vec{N} the normal to the surface ds . Here, the amount of dislocations contained in the interface 1 is firstly calculated, i.e. the net Burgers vector of all dislocations piercing the surface of the interface 1 is calculated by the integral over the complete surface of the interface, which is a 2D plane with dimensions $D_2 \times D_3$. Then, the result is scaled with the surface area of the corresponding wall S_w and the magnitude of the Burgers vector. The factor 2 accounts for the fact that two interfaces, on the opposite sides of the wall, supply GNDs to each wall 1. The kernel of the integral in (4.41) can be approximated from (4.40), resulting in:

$$\|\Lambda \cdot \vec{N}\|(\vec{x}) = \|\mathbf{F}_c^p \cdot \Delta[\mathbf{F}^p]_1^{-1} \cdot (\vec{n}_1 \times \vec{N})\| I_1^\pm(\vec{x}) \quad (4.42)$$

Obviously, along the interface surface the normal vector $\vec{N}(s)$ takes three perpendicular directions, coinciding with the wall normals: $\vec{N}_1 = \vec{n}_1$, $\vec{N}_2 = \vec{n}_2$, $\vec{N}_3 = \vec{n}_3$, see Fig. 4.5. Thus the integral in (4.41) can be further decomposed in the sum:

$$\int_S \|\Lambda \cdot \vec{N}(s)\| ds = 2(\|\mathbf{F}_c^p \cdot \Delta[\mathbf{F}^p]_1^{-1} \cdot \vec{n}_2\| D_2 + \|\mathbf{F}_c^p \cdot \Delta[\mathbf{F}^p]_1^{-1} \cdot \vec{n}_3\| D_3) \quad (4.43)$$

where $\vec{N}_1 \times \vec{n}_1 = \vec{0}$ has been used and the coefficient 2 accounts for equal contributions of the opposite sides of the interface. Finally, the GND density in the wall 1 is expressed as:

$$\rho_{w1}^{GND} = \frac{2(D_2 \|\mathbf{F}_c^p \cdot \Delta[\mathbf{F}^p]_1^{-1} \cdot \vec{n}_2\| + D_3 \|\mathbf{F}_c^p \cdot \Delta[\mathbf{F}^p]_1^{-1} \cdot \vec{n}_3\|)}{b(D_2 D_3 + w_1 D_2 + w_1 D_3)} \quad (4.44a)$$

In the same manner the continuum dislocation densities in walls 2 and 3 can be obtained:

$$\rho_{w2}^{GND} = \frac{2(D_1 \|\mathbf{F}_c^p \cdot \Delta[\mathbf{F}^p]_2^{-1} \cdot \vec{n}_1\| + D_3 \|\mathbf{F}_c^p \cdot \Delta[\mathbf{F}^p]_2^{-1} \cdot \vec{n}_3\|)}{b(D_1 D_3 + w_2 D_1 + w_2 D_3)} \quad (4.44b)$$

$$\rho_{w3}^{GND} = \frac{2(D_1 \|\mathbf{F}_c^p \cdot \Delta[\mathbf{F}^p]_3^{-1} \cdot \vec{n}_1\| + D_2 \|\mathbf{F}_c^p \cdot \Delta[\mathbf{F}^p]_3^{-1} \cdot \vec{n}_2\|)}{b(D_1 D_2 + w_3 D_1 + w_3 D_2)} \quad (4.44c)$$

Eqs. (4.44) will be used to calculate the yield stress in the walls with (4.26) while the back stress in (4.17) follows from the internal stress on the basis of the distribution (4.40) of Λ . An explicit equation for the internal stress is elaborated in the next section.

4.5.2 Approximation of the internal stress field

This section deals with the calculation of the internal stresses resulting from the geometrically necessary interface dislocations. The internal stress field will be determined for the dislocation distribution described by (4.40). The most straightforward approach to calculate stresses created by this dislocation distribution is the use of the well-known expressions for the stress field arising from a single straight dislocation in an infinite elastic medium [Hull and Bacon, 2001]. To obtain stresses caused by finite dislocation walls the contributions of the single dislocations should be integrated over the wall volume. The result for a finite wall of straight edge dislocations is e.g. given by Lubarda and Kouris [1996]. Summing up the individual contributions of all walls results in the total internal stress. Sedláček [1996] applied this method to straight edge dislocations arranged in an infinite series of parallel finite walls. This arrangement corresponds to the configuration with the GNDs located in one row of parallel cell walls. Hecker and Burmeister [1996] analysed the same arrangement of dislocations by introducing wedge disclination dipoles as an equivalence to the polarised interface layers.

The approaches mentioned above provide proper analytical expressions for the internal stress state. However, these expressions only hold for a specific type of dislocation arrangement, i.e. edge dislocations forming tilt boundaries. Obviously, this analysis can be repeated for any type of dislocations but the type should be known a priori. In the present cell structure model the interface dislocations can be of a mixed type determined by the load imposed. Therefore, a more general approach for the internal stress calculation is desirable allowing for any dislocation type. Furthermore, considering straight dislocations only, would imply that the dislocation walls are infinite in the direction of the dislocation lines, whereas, the geometry assumed for the cell structure restricts the interface layers of GNDs to be finite. Therefore, the formulae for straight dislocations are not applied here.

Relations between an arbitrary plastic incompatibility and the associated internal stresses have been established in the continuum theory of defects [Kröner, 1981; Mura, 1987]. This theory deals with the calculation of self-equilibrated stress distributions created in an elastic material due to the presence of internal kinematical incompatibilities, or defects. The approach was recently used by Sedláček and Hecker [1998] to determine the stress fields due to tilted dislocation walls under 2D shear. The cell walls were modelled by a row of plastically sheared inclusions and the equilibrium problem for the material was solved by combining the stress function approach with a discrete Fourier transform. The same approach was used in Sedláček [1995], Sedláček and Blum [1998] and Sedláček and Forest [2000] to calculate the internal stress related to plastic incompatibilities caused by dislocations bowing out between the cell walls.

The theory of defects applied to an inhomogeneous material allows for the calculation of the internal stress created by any plastic incompatibility, i.e. by any distribution of geometrically necessary dislocations. Moreover, the analytical expressions used by Lubarda and Kouris [1996] and Sedláček [1996] are included as particular cases. In the present contribution, the theory of defects is used to relate the internal stress to the plastic incompatibility associated with the interface dislocations in the cell structure.

To make use of the theory of defects, it is assumed here that the internal stress created by the geometrically necessary dislocations in the cell material under deformation can be approximated by the stress induced by the same distribution of dislocations in an elastic medium that is free from external stresses.

The density measure for the geometrically necessary dislocations was introduced before in relation to the plastic deformation by (4.28) or (4.40). However, the plastic incompatibility associated with the GNDs is actually defined by the incompatible part of the plastic deformation. Roughly formulated, the compatible plastic deformation is provided by the slip of the dislocations that glide through the lattice. The incompatible plastic deformation is due to the slip of the dislocations that are arrested inside the material and give rise to lattice distortions. Therefore the dislocation tensor $\mathbf{\Lambda}$ is rather related to the incompatible plastic deformation:

$$\mathbf{\Lambda} = \mathbf{F}_{inc}^p \cdot [\vec{\nabla}_p \times [\mathbf{F}_{inc}^p]^{-T}]^T \quad (4.45)$$

This expression is in conformity with Eq. (4.28); the plastic deformation is multiplicatively decomposed into a compatible part \mathbf{F}_{com}^p and an incompatible part \mathbf{F}_{inc}^p according to $\mathbf{F}^p = \mathbf{F}_{inc}^p \cdot \mathbf{F}_{com}^p$. Then expression (4.45) can be derived from definition (4.28), see Steinmann [1996].

Since the incompatible deformations are small compared to the total deformation, Eq. (4.45) can be approximated by:

$$\mathbf{\Lambda} \simeq - [\vec{\nabla}_p \times [\mathbf{d}^p]^T]^T \quad (4.46)$$

and the related problem of calculating the internal stress can be approximated in the context of small deformations. Above, the symbol \mathbf{d}^p stands for the distortion tensor corresponding to \mathbf{F}_{inc}^p , $\mathbf{d}^p = \mathbf{F}_{inc}^p - \mathbf{I}$. Following the theory of defects, the self-equilibrated stress $\boldsymbol{\beta}$ created by the presence of the dislocations $\mathbf{\Lambda}$ in the elastic material can be found as the solution of the following problem:

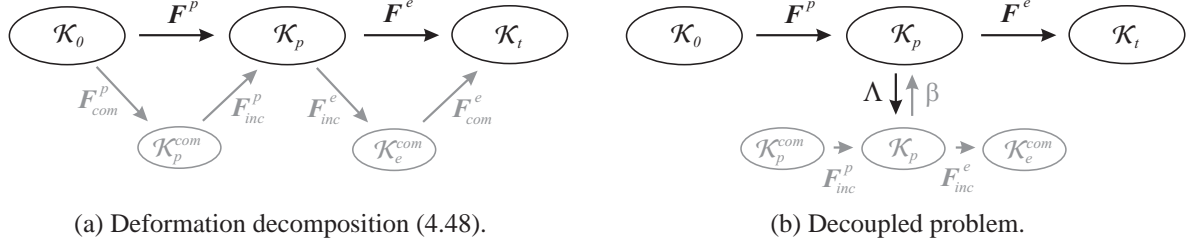
$$\begin{cases} \vec{\nabla}_p \cdot \boldsymbol{\beta} = \vec{0} \\ (\vec{\nabla}_p \mathbf{u})^T = \mathbf{d}^p + \mathbf{d}^e \\ \boldsymbol{\beta} = \mathbb{C} : \frac{1}{2} (\mathbf{d}^e + (\mathbf{d}^e)^T) \\ \mathbf{\Lambda} = - [\vec{\nabla}_p \times [\mathbf{d}^p]^T]^T \end{cases} \quad (4.47)$$

The first equation here is the local equilibrium equation for the internal stress $\boldsymbol{\beta}$. The second equation restores the compatibility condition for the total distortion based on an additive strain decomposition. The incompatible elastic distortion \mathbf{d}^e is related to the stress $\boldsymbol{\beta}$ by the Hookean elasticity law, and as previously elaborated the plastic distortion \mathbf{d}^p is connected to the given plastic incompatibility $\mathbf{\Lambda}$. Note that all equations are formulated in the intermediate configuration defined by \mathbf{F}^p since $\boldsymbol{\beta}$ is defined in this configuration as needed for the evaluation of the yield condition (4.17)–(4.18). It also seems more physical to relate the incompatible deformations \mathbf{d}^p and \mathbf{d}^e to the intermediate configuration. Actually, these considerations imply the following decomposition of the total deformation (see Fig. 4.6a):

$$\mathbf{F} = \mathbf{F}^e \cdot \mathbf{F}^p = (\mathbf{F}_{com}^e \cdot \mathbf{F}_{inc}^e) \cdot (\mathbf{F}_{inc}^p \cdot \mathbf{F}_{com}^p) \quad (4.48)$$

The introduced approach can be considered as a decoupling of the original problem with unknown $\boldsymbol{\sigma}$ and $\boldsymbol{\beta}$ into two sub-problems (black and grey states represented in Fig. 4.5.2b). The first problem deals with the calculation of the applied stress $\boldsymbol{\sigma}$, in which the internal stress $\boldsymbol{\beta}$ is included by (4.17)–(4.18) for a fixed dislocation configuration. The second problem deals with the calculation of the internal stress $\boldsymbol{\beta}$ for a given $\mathbf{\Lambda}$. This problem is formulated for

the incompatible parts of the deformation only and decoupled from the applied stress σ (i.e. dependent on the current microstructural configuration only). These two separate problems are connected in the intermediate configuration by Λ and β : the plastic incompatibility, calculated from the σ -problem, is the input for the β -problem while the internal stress, calculated in the β -problem, governs plastic deformation in the σ -problem. Note also that for both problems the intermediate configuration \mathcal{K}_p is identical and defined by F^p .



The solution of the problem defined by (4.47) has been studied by Mura [1987] for the case of an infinite medium, i.e with the following boundary conditions:

$$\|\beta(\vec{x})\| \rightarrow 0 \text{ for } \|\vec{x}\| \rightarrow \infty \quad (4.49)$$

The method of Green's functions [Myint-U and Debnath, 1987] has been applied to the equilibrium problem (4.47) along with the boundary condition (4.49). The internal stresses were obtained as a function of the dislocation density tensor [Mura, 1987]:

$$\beta_{ij}(\vec{x}) = \int C_{ijkl} \epsilon_{lnh} C_{pqmn} G_{kp,q}(\vec{x} - \vec{x}') \Lambda_{mh}(\vec{x}') d\vec{x}' \quad (4.50)$$

where C_{ijkl} are the components of the fourth-order elastic Hookean material tensor \mathbb{C} , see (4.16), and ϵ_{lnh} are the components of the third-order permutation tensor ${}^3\epsilon$. All indices here and in the following are supposed to vary from 1 to 3 and the Einstein summation convention applies. The Green's function $\mathbf{G}(\vec{x} - \vec{x}')$ is defined as the displacement solution of the associated elastic equilibrium problem with the source term replaced by the Dirac delta function $\delta(\vec{x} - \vec{x}')$, satisfying the applied boundary conditions. More specifically, in components, Green's function $G_{kp}(\vec{x} - \vec{x}')$ can be interpreted as the p -component of the displacement in a point \vec{x} when a unit concentrated force is applied at a point \vec{x}' in the k -direction. The plastic incompatibilities given by Λ are the source of the stresses in this problem. Thus, the kernel of the integral (4.50) determines the stress created at the point \vec{x} by the geometrically necessary dislocations located in the point \vec{x}' , and the integration over the material in \mathcal{K}_p is performed to determine the total internal stress state. For isotropic materials the Green's function can be determined explicitly. After lengthy elaborations, it can be derived that [Mura, 1987]:

$$C_{pqmn} G_{kp,q}(\vec{x}) = \frac{-1}{8\pi(1-\nu)} \left\{ (1-2\nu) \frac{\delta_{mk}\bar{x}_n + \delta_{nk}\bar{x}_m - \delta_{mn}\bar{x}_k}{\|\vec{x}\|^3} + 3 \frac{\bar{x}_m\bar{x}_n\bar{x}_k}{\|\vec{x}\|^5} \right\} \quad (4.51)$$

with $\vec{x} = \vec{x} - \vec{x}'$, with ν Poisson's ratio and with δ_{ij} the Kronecker symbol.

The stress tensor field β is a self-equilibrated stress distribution created by the geometrically necessary dislocations Λ in an infinite elastic medium. In a finite volume, with the dislocation cell structure, the internal stress induced by GNDs is close to the stress β calculated with

(4.50) in areas far enough away from the external boundary. In the vicinity of the external boundary the internal stress should be zero to satisfy the traction boundary conditions. Thus, to apply the expression (4.50) to finite geometries, the stress $\boldsymbol{\beta}$ should be corrected to be zero at the boundary [Mura, 1987; Nabarro, 1967]. In this work, stresses will be evaluated in material points that are always at a sufficiently large distance from the external boundary. Therefore, it will be assumed that the internal stress $\boldsymbol{\beta}$ can be approximated by (4.50) and that the deviations at the boundary can be ignored. Note also that the back stress introduced in the continuum material model acts as an internal variable only, and is not further entering the balance equations. The system (4.47) can be considered as a micro-scale model used to calculate the internal variable $\hat{\boldsymbol{\beta}}$ of the mesoscale cell model description (4.7)–(4.10), (4.11)–(4.21).

To calculate the internal stress associated with the cell structure, the distribution of the plastic incompatibility (4.40) should be inserted into (4.50) and then the integration over the geometry of the cell structure in the configuration \mathcal{K}_p can be performed, resulting in:

$$\begin{aligned} \boldsymbol{\beta}(\bar{\mathbf{x}}) = \mathbb{C} : & \left(\bar{\mathbf{n}}_1 [\mathbf{F}_c^p \cdot \Delta[\mathbf{F}^p]_1^{-1}]^T : {}^3\Pi^1(\bar{\mathbf{x}}) - [\mathbf{F}_c^p \cdot \Delta[\mathbf{F}^p]_1^{-1}]^T \cdot [{}^3\Pi^1(\bar{\mathbf{x}})]^T \cdot \bar{\mathbf{n}}_1 \right. \\ & + \bar{\mathbf{n}}_2 [\mathbf{F}_c^p \cdot \Delta[\mathbf{F}^p]_2^{-1}]^T : {}^3\Pi^2(\bar{\mathbf{x}}) - [\mathbf{F}_c^p \cdot \Delta[\mathbf{F}^p]_2^{-1}]^T \cdot [{}^3\Pi^2(\bar{\mathbf{x}})]^T \cdot \bar{\mathbf{n}}_2 \\ & \left. + \bar{\mathbf{n}}_3 [\mathbf{F}_c^p \cdot \Delta[\mathbf{F}^p]_3^{-1}]^T : {}^3\Pi^3(\bar{\mathbf{x}}) - [\mathbf{F}_c^p \cdot \Delta[\mathbf{F}^p]_3^{-1}]^T \cdot [{}^3\Pi^3(\bar{\mathbf{x}})]^T \cdot \bar{\mathbf{n}}_3 \right) \end{aligned} \quad (4.52)$$

with

$$\Pi_{mnk}^1(\bar{\mathbf{x}}) = \int C_{pqmn} G_{kp,q}(\bar{\mathbf{x}} - \bar{\mathbf{x}}') [I_1^-(\bar{\mathbf{x}}') - I_1^+(\bar{\mathbf{x}}')] d\bar{\mathbf{x}}' \quad (4.53a)$$

$$\Pi_{mnk}^2(\bar{\mathbf{x}}) = \int C_{pqmn} G_{kp,q}(\bar{\mathbf{x}} - \bar{\mathbf{x}}') [I_2^-(\bar{\mathbf{x}}') - I_2^+(\bar{\mathbf{x}}')] d\bar{\mathbf{x}}' \quad (4.53b)$$

$$\Pi_{mnk}^3(\bar{\mathbf{x}}) = \int C_{pqmn} G_{kp,q}(\bar{\mathbf{x}} - \bar{\mathbf{x}}') [I_3^-(\bar{\mathbf{x}}') - I_3^+(\bar{\mathbf{x}}')] d\bar{\mathbf{x}}' \quad (4.53c)$$

where the components $C_{pqmn} G_{kp,q}(\bar{\mathbf{x}} - \bar{\mathbf{x}}')$ are given by (4.51). The formulae (4.53) reveal that the integration should be performed over the areas containing the geometrically necessary dislocations, consequently over the interface layers (4.31)–(4.34). The interface layers in the cell structure are rectangles periodically distributed in space. Therefore the integration over each interface can be performed fully analytically and the contributions of individual interfaces are summed up giving

$${}^3\Pi^i(\bar{\mathbf{x}}) = \sum_{r=-N_1}^{N_1} \sum_{s=-N_2}^{N_2} \sum_{t=-N_3}^{N_3} {}^3\tilde{\Pi}^i(\bar{\mathbf{x}}, \vec{\mathbf{j}}(r, s, t)), \quad i = 1, 2, 3 \quad (4.54)$$

where ${}^3\tilde{\Pi}^i(\bar{\mathbf{x}}, \vec{\mathbf{j}}(r, s, t))$ are analytical expressions found for the integrals (4.53) over a single cell wall, determined by the shift vector $\vec{\mathbf{j}}(r, s, t)$.

Eqs. (4.53) specify ${}^3\Pi^1(\bar{\mathbf{x}})$, ${}^3\Pi^2(\bar{\mathbf{x}})$ and ${}^3\Pi^3(\bar{\mathbf{x}})$ as spatially continuous functions, and consequently the internal stresses found by evaluating (4.52) will also vary continuously through the cell structure. However, for the constitutive model used, uniformity of all variables inside each composite component has been assumed previously. Therefore, the distribution $\boldsymbol{\beta}(\bar{\mathbf{x}})$ should be approximated by a piecewise uniform function with values $\boldsymbol{\beta}_c$ inside the cell interiors, and $\boldsymbol{\beta}_{w1}$, $\boldsymbol{\beta}_{w2}$ and $\boldsymbol{\beta}_{w3}$ inside the corresponding cell walls.

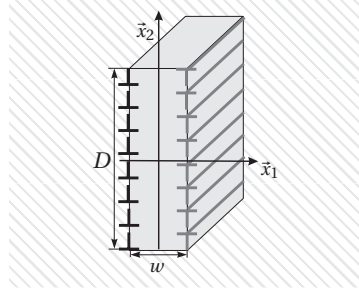


Figure 4.6 — Configuration with a single cell wall.

The next section deals with some details on the calculation of the internal stresses. Firstly, the stresses created by dislocations in simple configurations are calculated with (4.52)–(4.53) to examine the features of the method suggested here. Then the stepwise approximation $\{\boldsymbol{\beta}_c, \boldsymbol{\beta}_{w1}, \boldsymbol{\beta}_{w2}, \boldsymbol{\beta}_{w3}\}$ is considered for $\boldsymbol{\beta}(\vec{x})$. For the desired accuracy, the minimum amount of walls N_1, N_2, N_3 contributing to (4.54) is determined such that the computational costs can be minimised.

4.6 Computation of the internal stress

In the previous section, the internal stress tensor has been derived by solving the equilibrium problem for an inhomogeneous material with plastic incompatibilities, resulting in the formulation given by (4.51)–(4.53). These equations are rather complex and difficult to analyse in their general form. Therefore, in this section, the elaboration is firstly demonstrated for a number of relatively simple configurations. These examples will help to understand the main features of the internal stress distribution in the cell structure. In the second part of this section, some simplifications of Eqs. (4.52)–(4.53) are introduced, to enable further numerical computations with the cell structure model.

4.6.1 Continuum case

All computations below are based on Eqs. (4.51)–(4.53) using the material parameters of copper at room temperature [Mughrabi et al., 1986]. The elastic behaviour is determined by the shear modulus $G = 41$ GPa and Poisson's ratio $\nu = 0.35$. The length of the Burgers vector is taken as $b = 0.25$ nm.

First, a single wall in an infinite isotropic matrix is considered, see Fig. 4.6. The size of the wall is given by the wall height $D = 1.4$ μm and the wall width $w = 0.14$ μm , typical values for a dislocation structure in copper [Mughrabi et al., 1986]. Moreover, the wall is assumed to be infinite in the third direction. Pure shear, with deformation gradient components $F_{12} = F_{21}$ applied to that composite will result in a nonuniform deformation with jumps of the plastic deformation $\Delta F_{12}^p = \Delta F_{21}^p = -\delta\gamma$ across the matrix-wall interface and $\Delta F_{12}^p = \Delta F_{21}^p = \delta\gamma$ across the wall-matrix interface, where $\delta\gamma$ is the magnitude of the jumps. This plastic incompatibility corresponds to a nonzero Λ_{13} component and can be associated with two interface layers of straight edge dislocations, see (4.29). The layers can actually be considered as tilt dislocation boundaries with equal dislocation densities but opposite signs (Fig. 4.6).

To compute the stresses created by the interface dislocations in this single wall example (Fig. 4.6), the following geometrical configuration has been applied, consistent with (4.31):

$$I_1^-(\vec{x}) = \delta \left(x_1 + \frac{w}{2} \right) B \left(x_2 + \frac{D}{2}, x_2 - \frac{D}{2} \right) \quad (4.55a)$$

$$I_1^+(\vec{x}) = \delta \left(x_1 - \frac{w}{2} \right) B \left(x_2 + \frac{D}{2}, x_2 - \frac{D}{2} \right) \quad (4.55b)$$

and according to (4.39):

$$\Delta F_1^p = \delta \gamma (\vec{x}_1 \vec{x}_2 + \vec{x}_2 \vec{x}_1); \quad \Delta F_2^p = \mathbf{0}; \quad \Delta F_3^p = \mathbf{0} \quad (4.56)$$

the coordinate system with the basis vectors \vec{x}_1 and \vec{x}_2 and the coordinates x_1 and x_2 is defined in Fig. 4.6. The internal stress can then be calculated.

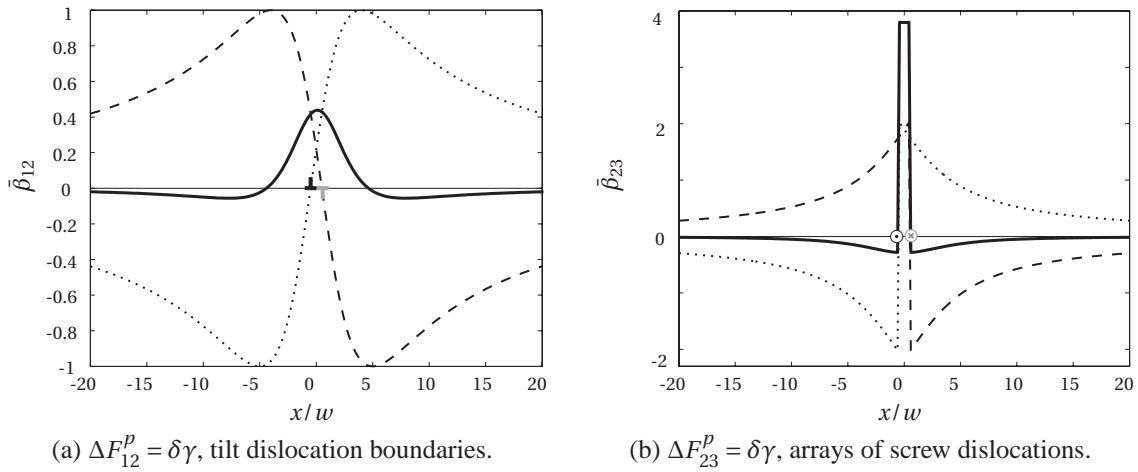


Figure 4.7 — The distribution of the internal stresses in the single wall example along \vec{x}_1 ($x_2 = 0$). Dashed lines: Stress due to the right interface; dotted lines: Stress due to the left interface; solid lines: their superposition. Dimensionless stress $\bar{\beta}$ defined as $\bar{\beta}_{ij} = \frac{2\pi(1-\nu)}{G\delta\gamma} \beta_{ij}$.

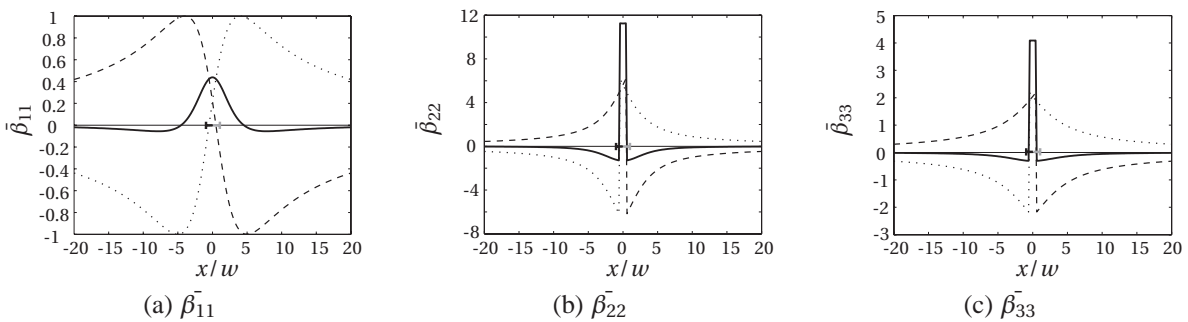


Figure 4.8 — The distribution of the internal stresses in the single wall example along \vec{x}_1 ($x_2 = 0$). Configuration with a single cell wall, $\Delta F_{22}^p = \delta \gamma$, edge-dislocation arrays with the Burgers vector parallel to the \vec{x}_2 -axis. Dashed lines: stress due to the right interface; dotted lines: Stress due to the left interface; solid lines: their superposition. Dimensionless stress $\bar{\beta}$ defined as $\bar{\beta}_{ij} = \frac{2\pi(1-\nu)}{G\delta\gamma} \beta_{ij}$

Fig. 4.7a shows the distribution of the nonzero internal stress component β_{12} . It can be observed that the individual finite dislocation boundaries, representing the interface layers, do

produce long range stresses (dashed and dotted curves in the figure). This is due to their finite size D , contrary to infinite dislocation boundaries which are low-energy configurations that do not lead to long-range stresses. Note that the superposition of two neighbouring boundaries with opposite signs of dislocations still provides a significant stress close to the cell wall with a maximum in the middle of the wall, the total stress decays at larger distances. This is essentially due to the finite width of the wall, i.e. the spacing between both boundaries.

Figs. 4.7b and 4.8a–4.8c show the nonzero stress components developed in the same single wall configuration, however with a plastic incompatibility ΔF_{23}^p (Fig. 4.7b) and ΔF_{22}^p (Figs. 4.8a–4.8c). These plastic incompatibilities can be obtained by applying an external shear F_{23} or a stretching F_{22} , respectively, to the composite. The interface layers can be recognised here as arrays of screw dislocations in the case of Fig. 4.7b and arrays of edge dislocations with a Burgers vector parallel to the \vec{x}_2 -axis in the case of Figs. 4.8a–4.8c. Similar conclusions can be drawn here as in the case of the tilt dislocation boundaries before.

Note, that since the wall considered above is infinite in the third direction, the interface layers can be associated with arrangements of straight dislocations for this particular case. Accordingly, Eqs. (4.51)–(4.53) can then be reduced to the well-known expressions for stress fields for straight dislocations in an elastic medium [Hull and Bacon, 2001]. Thus, the results shown in Figs. 4.7 and 4.8 can also be reconstructed by integrating the stress fields due to single dislocations [Hull and Bacon, 2001] over the area of the interface layers. In the more general case of interest here, interface layers of a wall are finite in the third direction and cannot be assembled from straight dislocations and, therefore, their stresses can only be calculated from the general expressions (4.51)–(4.53). The stress distribution calculated for a wall finite in the third direction is nonuniform in the \vec{x}_3 -direction as well. The stress distribution in \vec{x}_1 -direction for such a wall has the same profile as depicted in Figs. 4.7 and 4.8.

Fig. 4.9 shows the results of the internal stress calculations through (4.51)–(4.53) for a more complex configuration. A 3D cell structure (as in Fig. 4.2), infinitely spread over the material, is considered here. The geometry of the cell structure is given by the cell size $D_1 = D_2 = D_3 = 1.4 \mu\text{m}$ and the wall thickness $w_1 = w_2 = w_3 = 0.14 \mu\text{m}$. The interface layers in this structure are finite and given by (4.31)–(4.35). To calculate the internal stresses with (4.52), the plastic incompatibilities developed at the cell-wall interfaces have to be known. In this example, plastic incompatibilities, typically developing under simple shear applied to the cell structure in the \vec{x}_1 direction are considered:

$$\Delta \mathbf{F}_1^p = \delta\gamma (\vec{x}_1 \vec{x}_2 + \vec{x}_2 \vec{x}_1), \quad \Delta \mathbf{F}_2^p = \delta\gamma (\vec{x}_1 \vec{x}_2 + \vec{x}_2 \vec{x}_1), \quad \Delta \mathbf{F}_3^p = \mathbf{0} \quad (4.57)$$

where the directions \vec{x}_1 and \vec{x}_2 coincide with the normal vectors \vec{n}_1 and \vec{n}_2 to the cell walls, respectively.

The internal stress developed in this example is shown in Fig. 4.9. It can be observed that the stress distribution is periodic and follows the periodicity of the cell structure. A remarkable feature of this distribution is the strong nonuniformity in the areas of the wall junctions. This is a consequence of the assumptions made in the underlying composite model. The piecewise uniform material behaviour assumed here provides a strong nonuniformity of the stress and strain in the areas around the corners. Consequently, the interface dislocations are distributed uniformly along the straight interfaces as well. Thus, the dislocation density is discontinuous in the corner areas where the walls cross. As a result, the internal stress is highly nonuniform in those areas. In the actual cell structure the stress and strain fields are not discontinuous and will have gradients smoothed over finite areas, especially in the corners. The interface

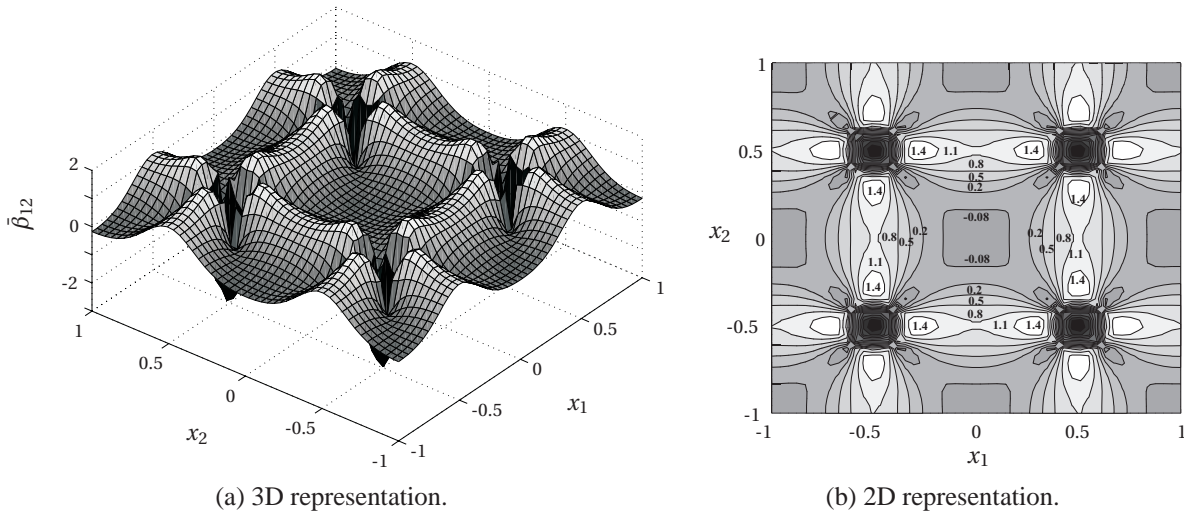


Figure 4.9 — The distribution of the internal stress in the 3D cell structure as visualised in Fig. 4.2. The cross-section $x_3 = 0$. Dimensionless stress $\bar{\beta}_{12} = \frac{2\pi(1-\nu)}{G\delta_Y} \beta_{12}$.

dislocations are also expected to be redistributed in the corner areas to reduce these artificial high internal stresses. Therefore the actual internal stresses are smoothed over a finite area at the corners and will not have the sharp peaks as calculated here. Considering the small volume fraction of the corner areas and the remark made above, it seems reasonable to assume that the internal stresses in the cell interiors and cell walls, away from the corners, do not depend on the computed peaks at the corners. More importantly, since the corner areas are indeed relatively small, the mean behaviour of the material is not affected by its local state neither. The corner areas will therefore be left out of consideration.

Away from the wall junctions, the distribution of β in Fig. 4.9 has maximum values locally in the wall components and minimum values in the cell interior components. The stress appears to be quite uniform inside each component. In this example, the stresses inside the vertical and horizontal walls have the same magnitude. This is due to symmetry of β : β_{12} is induced by ΔF_{12} in the vertical walls and by ΔF_{21} in the horizontal ones.

The examples above confirm that the geometrically necessary dislocations concentrated in the interface layers produce non-negligible internal stresses with a maximum value at the cell walls and a minimum value in the cell interior. The same tendency was observed in experimental observations dealing with dislocation cell structures [Mughrabi, 2001, 1983; Straub et al., 1996; Borbely et al., 1997; Müller et al., 1996; Ungar et al., 1984]. A qualitative verification of the predicted internal stress level will be done in Section 4.7.

4.6.2 Discrete approximation

As mentioned in the previous section, the internal stress distribution calculated with (4.51)–(4.53) is nonuniform over the cell structure and has to be approximated by a piecewise uniform distribution inside the cell interiors and the cell walls. In Fig. 4.9 it can be observed that the variation of the internal stresses inside each component is small compared to the differences between the components. This holds for all types of plastic deformation discontinuities experienced by the composite under deformation. Therefore, the approximation by means of a

uniform stress distribution inside the individual components appears to be appropriate and the stress distribution $\boldsymbol{\beta}(\vec{x})$ is then given by a stepwise function with values $\{\boldsymbol{\beta}_c, \boldsymbol{\beta}_{w1}, \boldsymbol{\beta}_{w2}, \boldsymbol{\beta}_{w3}\}$. In this paper, the values of the piecewise uniform internal stress are chosen to be equal to the internal stresses, calculated using (4.52) at the centre of the components:

$$\begin{aligned}
 \boldsymbol{\beta}_c &= \boldsymbol{\beta}(0,0,0) && \text{in the cell interiors} \\
 \boldsymbol{\beta}_{w1} &= \boldsymbol{\beta}\left(\frac{D_1 + w_1}{2}, 0, 0\right) && \text{in the cell walls 1} \\
 \boldsymbol{\beta}_{w2} &= \boldsymbol{\beta}\left(0, \frac{D_2 + w_2}{2}, 0\right) && \text{in the cell walls 2} \\
 \boldsymbol{\beta}_{w3} &= \boldsymbol{\beta}\left(0, 0, \frac{D_3 + w_3}{2}\right) && \text{in the cell walls 3}
 \end{aligned} \tag{4.58}$$

Another detail to be clarified for the proper quantification of the internal stresses is the number of cell walls N_1, N_2, N_3 involved in the computations. Eq. (4.54) deals with the summation of the contributions of all walls in a cell structure, which might be computationally expensive. However, the stress due to an individual wall decreases to zero with an increasing distance from that wall (see Fig. 4.7). Therefore it might be expected that the number of cell walls contributing to the internal stress in a given point will be limited. To examine this issue the internal stress has been calculated in the middle of an $N_1 \times N_2$ array of ‘‘vertical’’ cell walls (with normal vector \vec{n}_1) with $N_3 = 1$. The dependency of the stress $\boldsymbol{\beta}_w$, in the central wall, on the number of walls N_1 and N_2 in the calculation has been investigated. Fig. 4.10 shows the results for the case of a plastic shear incompatibility across the interfaces as given by (4.56).

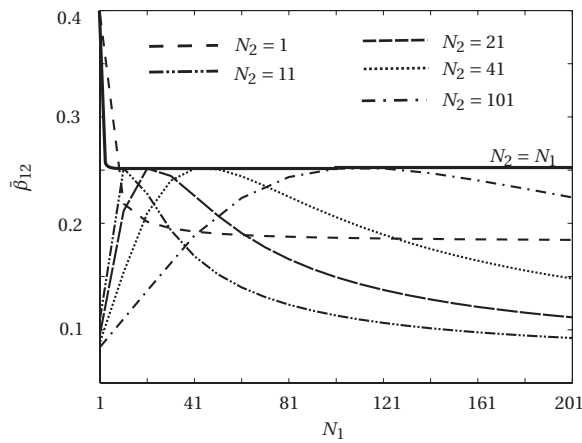


Figure 4.10 — The internal stress created by an array of $N_1 \times N_2 \times 1$ cell walls in the central wall as a function of N_1 and N_2 ; dimensionless stress defined as $\bar{\beta}_{ij} = \frac{2\pi(1-\nu)}{G\delta\gamma} \beta_{ij}$.

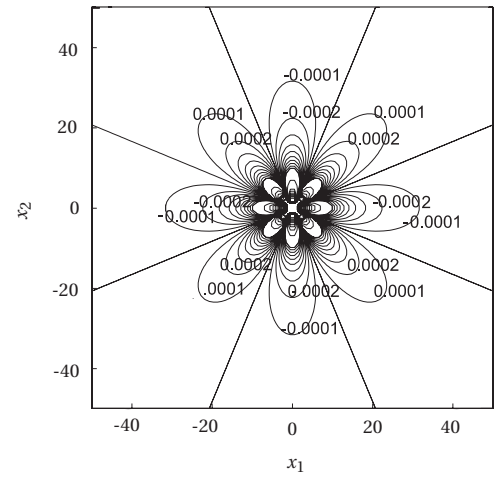


Figure 4.11 — Long-range stress field $\bar{\beta}_{12}$ due to a single cell wall.

It can be observed that for a fixed N_2 an increase of N_1 leads to an asymptotic behaviour. However, there is no unique asymptote for different values of N_2 . Nevertheless, in one particular yet relevant case, i.e. a symmetrical array ($N_1 = N_2$), an asymptote exists for values of the internal stresses (Fig. 4.10), which is rapidly reached for $N_1 = N_2 > 5$. This result is better understood by considering the long-range stress distribution (Fig. 4.11) of a single cell wall (Fig. 4.6). The stress level decays with the distance but still has a substantial value even

30 wall-heights away from the wall. Besides, at large distances, the stress distribution shows two 4-fold symmetries with opposite signs and a 45° rotation (Fig. 4.11). Therefore, in the non-symmetrical case $N_1 \neq N_2$ (Fig. 4.10), the total stress in the centre of the array will be influenced by the distant walls. In spite of the fact that the individual contributions of the distant walls are small, their superposition is not negligible. For an array of walls with equal numbers in both directions, the specific long-range symmetry of the stress distribution of walls avoids this problem. Roughly speaking, the stress induced by the walls added in the \bar{x}_1 and \bar{x}_2 directions will be compensated by the stress induced by the walls added in diagonal directions.

A comparable conclusion can be drawn for other plastic incompatibilities or other wall orientations. Therefore, for the stress created in a particular point by all dislocations in the cell structure, a reasonable estimate is obtained by taking into account only the contributions of walls in a patch of 5×5 surrounding cells. Eq. (4.54) is replaced by:

$${}^3\Pi^i(\bar{x}) = \sum_{r=-N}^N \sum_{s=-N}^N \sum_{t=-N}^N {}^3\tilde{\Pi}^i(\bar{x}, \vec{j}(r, s, t)), \quad i = 1, 2, 3 \quad (4.59)$$

where N is chosen equal to 2 ($N_1 = N_2 = N_3 = 5$). As illustrated, (4.59) is a reasonable approximation of (4.54) in the middle of the cell structure, away from the boundary. At the external boundaries of the specimen under consideration the amount of cells in outward direction is limited by the presence of the boundary and approximation (4.59) cannot be applied anymore. However, the stress will always be calculated in material points that are at non-negligible distance from the boundary and the effect of specimen boundaries will therefore be ignored.

4.7 Numerical analysis

4.7.1 Parameter identification

To perform numerical simulations the model parameters are here identified to describe the mechanical behaviour of copper. The values used for the elasticity parameters and the magnitude b of the Burgers vector are given in Table 4.1. Values for the parameter M and the coefficients $\alpha_i = \alpha$ are chosen following the recommendations of Mughrabi [1987] for a continuum cell structure model. The value $M = 2.5$ corresponds to lattice orientations providing symmetrical multiple slip and $\alpha = 0.4$ is obtained for multiple slip involving mutual intersection of dislocations of different slip systems [Mughrabi, 1987]. The mentioned values are adopted for symmetric deformation modes as analysed further in this paper.

Next, the geometry of the cell structure is specified. The cells are assumed to be cubic, $D \equiv D_1 = D_2 = D_3$, with equally thick cell walls, $w \equiv w_1 = w_2 = w_3$. Moreover, the geometry of the cells is assumed fixed under deformation (but not the dislocation densities). These simplifications may deviate from experimental observations at large deformations, however they are sufficiently accurate for the present analysis that concentrates on the internal stresses induced by the cell structure. The values chosen for the cell size D and the wall size, defined here by the fraction $f = w/D$, (see Table 4.1) are typical for a cell structure observed at small to moderate deformations (Mughrabi et al. [1986]).

The evolution of the statistically stored dislocations is defined by (4.24)–(4.25) and the material parameters I , R , C and ρ^0 . These parameters should be identified by fitting simulation

Table 4.1 — Parameters for copper.

Parameter	Symbol	Unit	Value
Shear modulus	G	[GPa]	41.7
Poisson's ratio	ν	[-]	0.34
Length of the Burgers vector	b	[nm]	0.257
Coefficient	α	[-]	0.4
Mean orientation factor	M	[-]	2.5
Cell size	D	[μm]	2.5
Wall volume fraction	f	[-]	0.18

Table 4.2 — Parameters for copper.

Parameter	Symbol	Unit	Value
Initial dislocation density	ρ^0	[m^{-2}]	$9 \cdot 10^{13}$
Creation rate parameter	I	[-]	0.1
Annihilation rate parameter	R	[nm]	2
Dislocation flux constant	C	[-]	0.6

results to experimental data. Unfortunately, quantitative experimental data on the dislocation evolution in cell structures is rare. However, the dislocation density evolution influences the hardening evolution of the material under deformation for which experimental data is available. The initial dislocation density ρ^0 defines the initial macroscopic flow stress and I , R , and C affect the further macroscopic behaviour via local isotropic hardening. Thus, the parameters ρ^0 , I , R , and C might be estimated by fitting simulation results to experimental data on the macroscopic behaviour under monotonic deformation, for example as given by a stress-strain diagram. The macroscopic stress evolution under monotonic deformation, however, does not identify C in a unique way. The parameter C is associated with the material inhomogeneity and should be identified by, for instance, the dislocation density difference between cell and walls or the stress inhomogeneity or the quantitative level of the internal stresses.

In the following, experimental data obtained by Schmitt et al. [1991] for polycrystalline copper under complex deformations are used to extract the parameters and to evaluate the model's performance. Therefore, the material parameters I , R , C , and ρ^0 are identified here to fit the experimental data for monotonic tension given in Schmitt et al. [1991]. To simulate uniaxial tension the macroscopic deformation \tilde{F}_{11} is applied with a strain rate $\dot{\epsilon}_{11}$ equal to $5 \cdot 10^{-4}$ [1/s]. All other directions remain stress-free. I.e. the following components of the macroscopic stress and deformation gradient tensors are applied:

$$\tilde{F}_{11} = 1 + \dot{\epsilon}_{11} t; \quad \tilde{\sigma}_{ij} = 0, \quad \text{if } ij \neq 11 \quad (4.60)$$

During the simulations, the orientation of the cell structure remains fixed, so that the tensile axis coincides with the local cell direction [111], see Fig. 4.14. This choice for the structure orientation corresponds to the formation of a cell structure along the macroscopic planes with maximum shear as confirmed by experimental observations [Zhu and Sellars, 2001]. This assumption does not provide a unique choice of the cell orientation, since it does not define the rotation of the cells around the [111] direction. But, uniaxial tension along the [111] direction is invariant to this rotation due to symmetry of the deformation with respect to the tensile axis.

The parameters ρ^0 , I and R are found by fitting the stress-strain diagram for monotonic

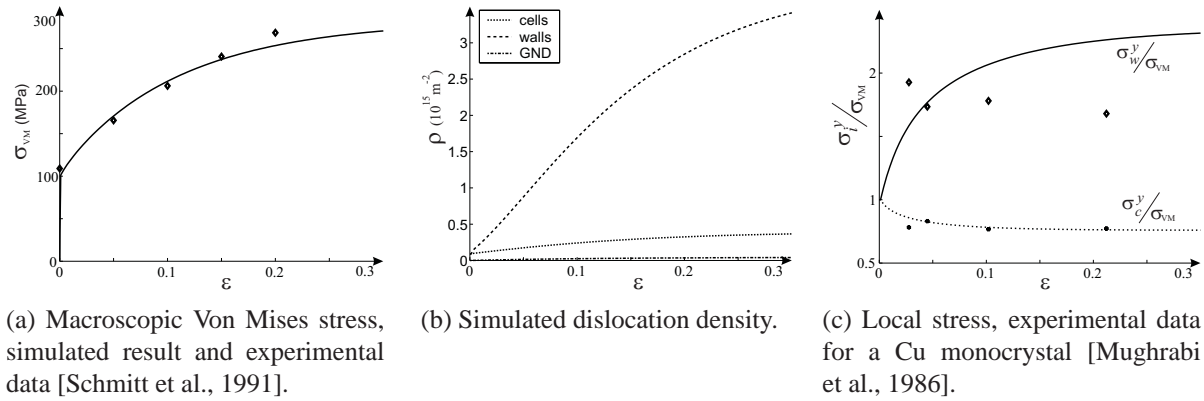


Figure 4.12 — Monotonic uniaxial tension, Cu.

uniaxial tension to the experimental data from Schmitt et al. [1991], Fig. 4.12a), and are given in Table 4.2. The macroscopic behaviour in Fig. 4.12a can, however, be realised with different levels of material inhomogeneity, i.e. with different values of the parameter C . To determine the value for C additional information on the material inhomogeneity should be available. Unfortunately, the paper of Schmitt et al. [1991] does not supply quantitative data on the microstructure. Therefore, information on the mesoscopic inhomogeneity developing in copper under uniaxial tension was taken from another source. Mughrabi et al. [1986] provided a detailed description of the dislocation cell structure in copper and the mechanical response of the material under uniaxial tension. The experiments however, were performed on a [001]-orientated copper single crystal. This symmetric orientation of the single crystal allows for deformation by multislip and, therefore, it is expected that a cell structure is formed that is comparable to the structure developing in polycrystals. Evidently, the deformation behaviour of a single crystal still differs from the behaviour of polycrystal material. Therefore, the data on the material inhomogeneity from Mughrabi et al. [1986] is only used here as an indication for the expected level of inhomogeneity in copper polycrystals, as used by Schmitt et al. [1991]. Fig. 4.12c shows the evolution of the local yield stress in the cell and wall phases, simulated with $C = 0.6$. The local yield stress as measured by Mughrabi et al. [1986] in a copper single crystal is also shown. It can be seen that the stress in cell interiors fits the experimental data better than the stress in the walls. The level of the stress inhomogeneity is however captured adequately, particularly since only a single parameter has been introduced to this purpose. Fig. 4.12b shows the corresponding evolution of the dislocation density.

Effect of GNDs on isotropic hardening

The calculations above have been performed accounting for the geometrically necessary dislocations in the isotropic hardening term, i.e. with the use of (4.26). Simulations showed that the density of the geometrically necessary dislocations is small compared to the density of the statistically stored dislocations (Fig. 4.12b) and, therefore, their influence on the isotropic hardening effect is negligible. Consequently, two approaches expressed by Eq. (4.19) and Eq. (4.26) yield equivalent results. In the following the effect of GNDs on the isotropic hardening will be neglected, i.e. (4.19) will be used for the yield stress.

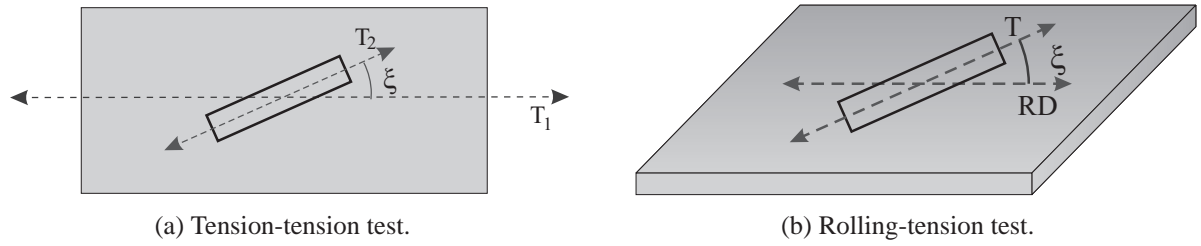


Figure 4.13 — Two step tests used for the simulations.

4.7.2 Model verification

Application to copper

To verify the model, tension-tension tests have been simulated and compared to the experimental data reported by Schmitt et al. [1991]. The initial tension load is modelled according to (4.60) until a certain amount of macroscopic strain defined as

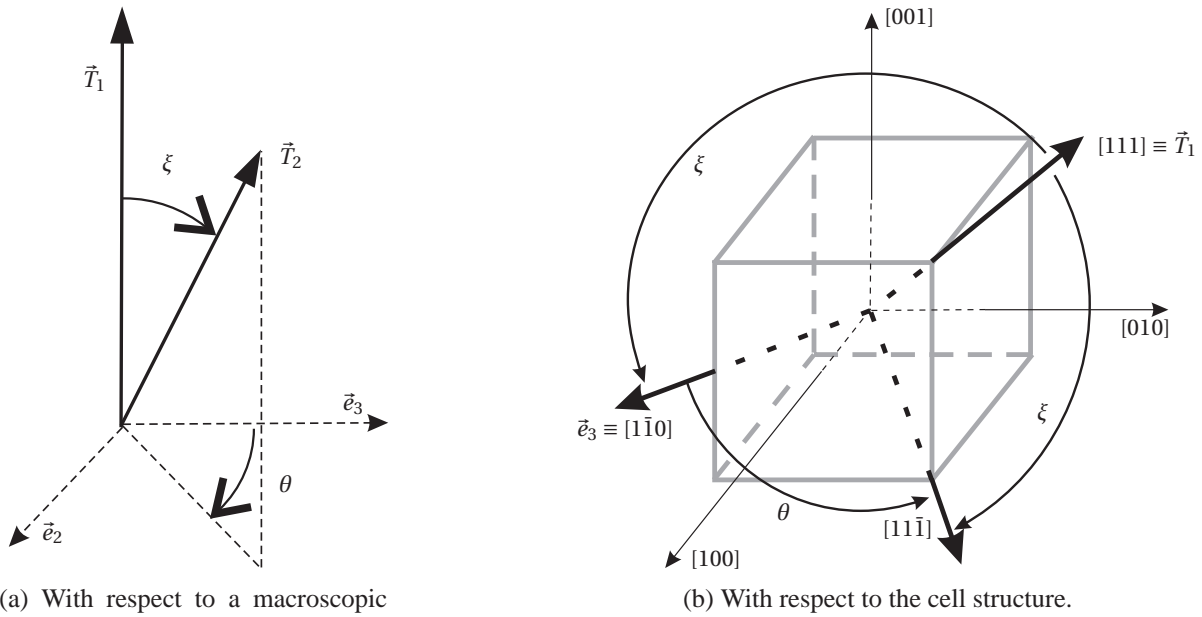
$$\varepsilon_{pre} = \int \sqrt{\tilde{\mathbf{D}} : \tilde{\mathbf{D}}} dt, \quad \tilde{\mathbf{D}} = \frac{1}{2}(\dot{\tilde{\mathbf{F}}} \cdot \tilde{\mathbf{F}}^{-1} + \tilde{\mathbf{F}}^{-T} \cdot \dot{\tilde{\mathbf{F}}}^T) \quad (4.61)$$

has been reached. Then the elastic unloading, defined as the state with a zero macroscopic stress, was simulated, followed by a second loading step in which the uniaxial tension was applied in another direction, see Fig. 4.13a. The material parameters used for the calculations are given in the Tables 4.1–4.2.

A tension-tension strain path change is given by two angles $\{\xi, \theta\}$ that define the orientation of the second tensile axes \vec{T}_2 with respect a macroscopic basis $\{\vec{T}_1, \vec{e}_2, \vec{e}_3\}$ associated with the first tension, see Fig. 4.14a. A dislocation cell structure develops during the first tensile step, which is assumed to orient with the $[111]$ cell direction³ along the tensile axis, Fig. 4.14b. Thus, with respect to the cell structure, the strain path change is defined by the rotation ξ of the tensile axis from the $[111]$ direction and by the rotation θ around the $[111]$ direction, see Fig. 4.14b. Since the first tension step is invariant to the cell rotation around $[111]$, the cell direction $[1\bar{1}0]$ was fixed in the simulations along the macroscopic direction \vec{e}_3 and the angle θ is measured from \vec{e}_3 (Fig. 4.14). Clearly, both strain path change angles influence the macroscopic reloading effects since they define different orientations of the cell structure with respect to the new loading axis. The effect of both angles on the strain path change effects will be discussed in the next section.

Experimental data, used here for verification, include information on the reloading yield stress as a function of the strain path change angle ξ , which is the angle between two succeeding tensile axes. The second angle θ was restricted by experimental settings. To determine the magnitude of θ , however, the 3D orientation of the cell structure with respect to the loading axis should be known. This information is rarely available and absent in Schmitt et al. [1991]. To resolve this, simulations with different values of θ were performed and $\theta = 0$ (i.e. with respect to the cells, the tensile axis has been rotated from the $[111]$ direction to the $[1\bar{1}0]$ direction) was found to provide the best correspondence to the experimental data. This angle $\theta = 0$ is further used for the tension-tension simulations, if not specified otherwise.

³Here and further on $[abc]$ denote directions with respect to the cell structure, in the coordinate system depicted in Fig. 4.14b.



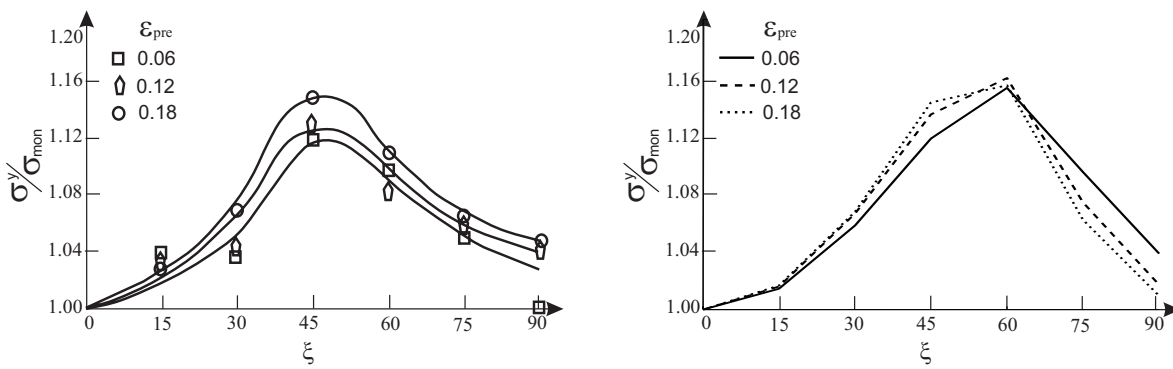
(a) With respect to a macroscopic basis.

(b) With respect to the cell structure.

Figure 4.14 — Definition of the strain path change angles ξ and θ for tension-tension tests.

The strain path change effect is often experimentally evaluated by comparing the macroscopic yield stress after reloading to the stress that is reached at the same total deformation in a monotonic test. Further on, these stresses are referred to as the reloading yield stress σ^y and the monotonic stress σ_{mon} respectively, e.g. see Fig. 4.16a. In all experimental studies used here for verification purposes, the reloading yield stress is determined by a back extrapolation of a macroscopic stress-strain diagram, e.g. see Schmitt et al. [1991]. To reproduce comparable data, the reloading yield stress is defined here as the macroscopic Von Mises stress at which the macroscopic hardening rate after reloading drops to the level of the macroscopic hardening rate in monotonic test, i.e. $d\sigma^y/d\varepsilon = d\sigma_{mon}/d\varepsilon$.

Fig. 4.15a shows the reloading yield stress experimentally determined from the tension-tension experiments [Schmitt et al., 1991]. The effect depends on the angle ξ between the tensile axes ($\theta = 0$) and the amount of prestrain. The simulation results are shown in



(a) Experimental results [Schmitt et al., 1991].

(b) Simulation results.

Figure 4.15 — Strain path change effect for Cu in a tension-tension test. Reloading yield stress as a function of the strain path change ξ ($\theta = 0^\circ$).

Table 4.3 — Parameters for aluminium.

Parameter	Symbol	Unit	Value
Shear modulus	G	[GPa]	26
Poisson's ratio	ν	[-]	0.35
Length of the Burgers vector	b	[nm]	0.286
Coefficient	α	[-]	0.4
Mean orientation factor	M	[-]	2.5
Cell size	D	[μm]	2.5
Wall volume fraction	f	[-]	0.15
Initial dislocation density	ρ^0	[m^{-2}]	$5.408 \cdot 10^{12}$
Creation rate parameter	I	[-]	0.0513
Annihilation rate parameter	R	[nm]	4.55
Dislocation flux constant	C	[-]	0.15

Fig. 4.15b. The predicted values of the reloading yield stress are well in the experimental range. The dependencies on the amount of prestrain and the angle between the successive tensile axes are also captured. The prediction however also demonstrates some deviations from the experiment. Considering the effect of the strain path change angle, the maximum reloading yield stress is found in a tension-tension test at $\xi \approx 55^\circ$, so-called cross test, while the experiment shows the maximum effect in the tests at $\xi = 45^\circ$. Further, the predicted effect of the amount of prestrain is qualitatively correct for small to medium strain changes only. For angles ξ larger than 75° the computed reloading yield stress decreases for larger prestrains, which is not consistent with the experimental data. It is believed that the main reason for these deviations is a more complex actual dislocation evolution than the one taken into account by the cell structure model. Nevertheless, the proposed simple 'continuum' cell structure model seems to capture the essential features of a strain path change effect on the reloading yield stress. This indicates that the internal stresses and the cell geometry, which are the main components of the model, indeed constitute the major elements triggering the strain path change effects.

Application to aluminium

To demonstrate the capability of the cell structure model to predict strain path change effects in other cases, two additional evaluations are performed next. Tension-tension and rolling-tension tests have been simulated for aluminium and the results are compared to experimental data, reported by Li and Bate [1991] and Jensen and Hansen [1990] respectively. The material parameters for commercially pure aluminium have been identified in the same manner as previously outlined for copper. Since experimental data on inhomogeneity evolution in aluminium was not directly available, the parameter C has been defined to fit the reloading yield stress in the tension-tension test with $\xi = 90^\circ$, $\varepsilon_{pre} = 0.1$. The same cell geometry was used. The parameters used for both simulations are given in Table 4.3.

The tension-tension tests were simulated in the same manner as for copper, with the same orientation of the cell structure. The strain path change angle θ , however, was fixed for this calculations to be equal to 30° . As before, the angle value $\theta = 30^\circ$ was chosen to provide the best fit to the experimental data. Fig. 4.16 shows the reloading yield stress, as defined before,

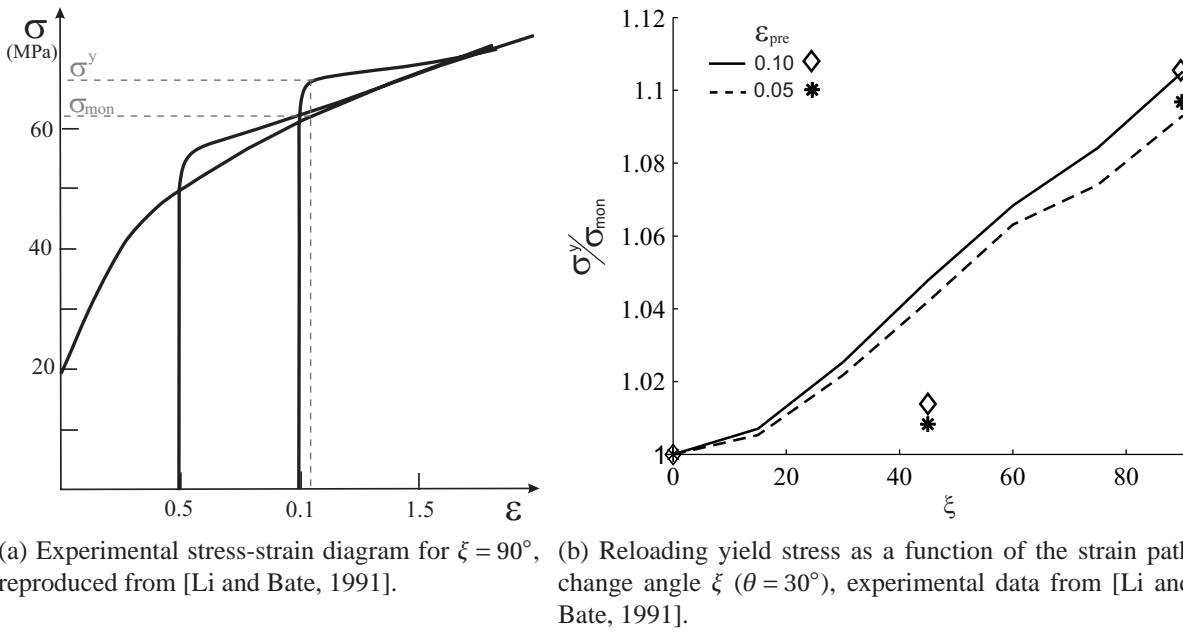


Figure 4.16 — Strain path change effect for aluminium in tension-tension tests.

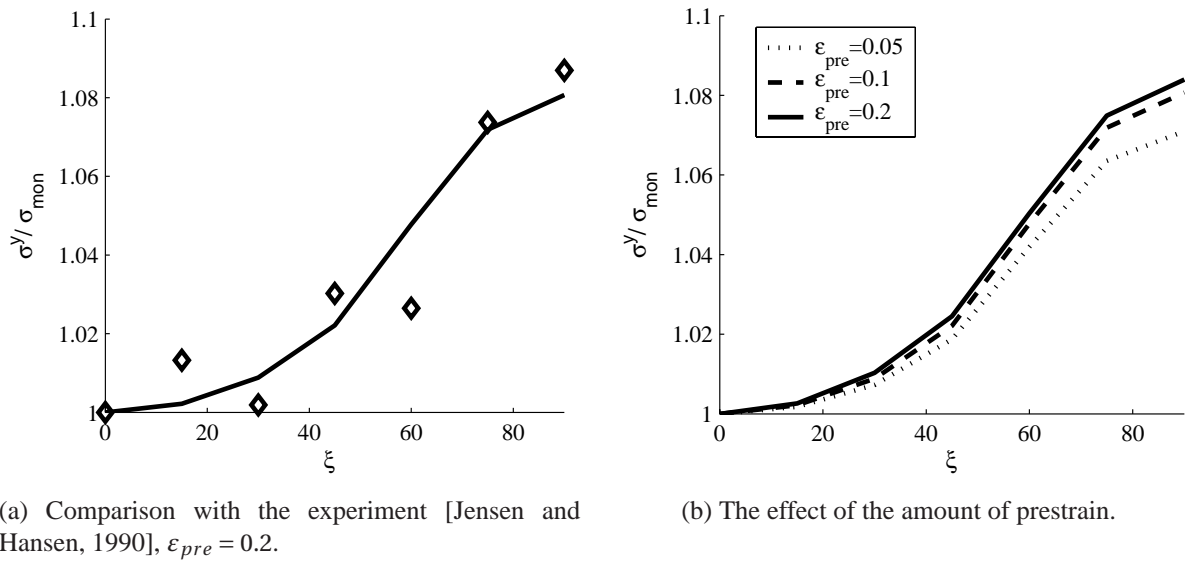
for a tension-tension deformation process for aluminium. The prediction is in qualitative agreement with the experimental data. Comparing the data in Fig. 4.15a and in Fig. 4.16b, the effects found in copper by Schmitt et al. [1991] and in aluminium by Li and Bate [1991] clearly differ. The difference in the macroscopic behaviour is likely due to the different values used for f and θ , implying a possible difference between the geometries and orientations of cells developed in the corresponding experiments of Li and Bate [1991] and Schmitt et al. [1991]. This issue is discussed in more detail in the next section.

In the experiment of Jensen and Hansen [1990], the specimens were initially cold-rolled to 20% of deformation. Then the specimens were unloaded and tensile test specimens were cut from the rolled sheet such that the angle ξ between the tensile axis and the rolling direction (RD) was 0° , 15° , 30° , 45° , 60° , 75° , and 90° , see Fig. 4.13b. The reloading yield stresses were measured in the tension experiments.

Monotonic rolling is here simulated by applying the following evolution of the deformation gradient:

$$\tilde{\mathbf{F}} = (1 + \hat{\epsilon}t)\vec{x}_1\vec{x}_1 + \vec{x}_2\vec{x}_2 + \frac{1}{1 + \hat{\epsilon}t}\vec{x}_3\vec{x}_3 \quad (4.62)$$

Here the basis vectors \vec{x}_1 , \vec{x}_2 and \vec{x}_3 define the rolling, transverse and longitudinal directions respectively. After $\epsilon_{pre} = 0.2\%$, elastic unloading was applied to obtain a macroscopically stress-free configuration. Next, the uniaxial tension (4.60) was simulated in the directions 0° , 15° , 30° , 45° , 60° , 75° and 90° with respect to the rolling direction (RD). The reloading yield stress was calculated in the same manner as before. In the simulations, the orientation of the cell structure was fixed again along the planes with maximum shear, inclined $\pm 45^\circ$ to the rolling direction in the longitudinal plane and perpendicular to the rolling direction in the rolling plane. This choice is also supported by experimental observations [Jensen and Hansen, 1990], where traces of the cell walls were found at 45° with respect to the RD in the longitudinal plane and perpendicular to RD in the rolling plane.



(a) Comparison with the experiment [Jensen and Hansen, 1990], $\epsilon_{\text{pre}} = 0.2$.

(b) The effect of the amount of prestrain.

Figure 4.17 — Strain path change effect for aluminium in rolling-tension tests. Reloading yield stress as a function of the strain path change angle.

Fig. 4.17 shows the calculated results and the experimental data for the rolling-tension experiments. The simulation results match the experimental data well. The model predicts the increased reloading yield stress and its dependency on the amplitude of the strain path change, i.e. on the orientation difference between the principal directions of the successive deformation steps. The increase of the reloading yield stress with the amount of prestrain is also predicted well for this case (Fig. 4.17) and agrees with the experimentally observed tendencies [Jensen and Hansen, 1990; Zandrahimi et al., 1989].

4.8 Discussion

4.8.1 Monotonic deformation

Under monotonic deformation the evolution of the statistically stored dislocations (Fig. 4.12b) tends to increase the material inhomogeneity. The local yield stress, related to the dislocation density by (4.19), develops in the cell phase slower than in the wall phase. Fig. 4.18a shows the evolution of the axial component of the local stress \mathbf{s} under uniaxial tension of copper. The calculations are performed with the material parameters identified for copper in the previous section. Here, the 11-component of the stress, which is along the tensile axis, is the same in all cell walls due to the symmetric orientation of the cell structure with respect to the loading axis. The inhomogeneity of the yield stress triggers the depicted evolution of the internal stresses, defined by plastic incompatibility. Fig. 4.18c demonstrates the evolution of the axial component of the internal stresses $\boldsymbol{\beta}$ in the cell structure. During monotonic tension this component of the internal stresses in the cell interior is negative while in the cell walls it is positive. As the strain increases, the internal stress gradient grows, as a consequence of the increasing inhomogeneity. The applied stress τ_{11} varies insignificantly between the cell components, see Fig. 4.18b, as a natural consequence of the stress continuity condition (4.4).

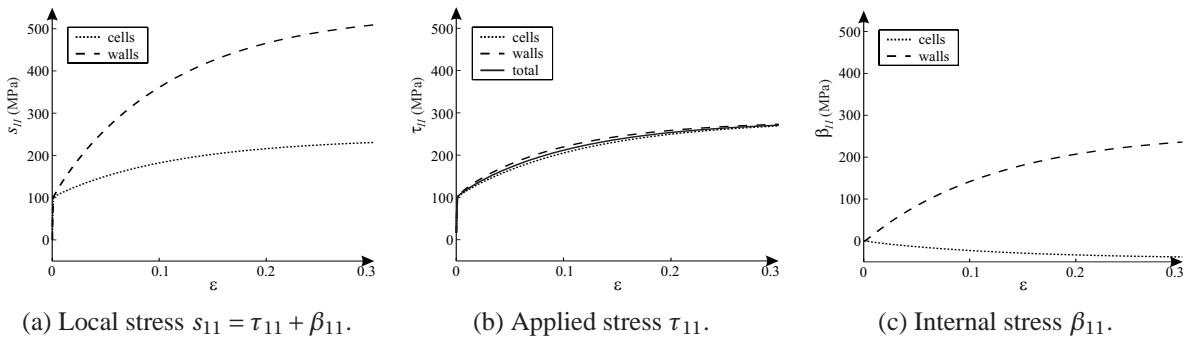


Figure 4.18 — Stress evolution in the monotonic uniaxial tension of copper.

The simulations for uniaxial tension demonstrate that a positive internal stress assists the applied stress inside the cell walls, while a negative internal stress counteracts the applied stress in the cell interior. Moreover, the internal stresses in the walls grow to a level approximately as high as the applied stress, accommodating half of the local yield stress. The value of the internal stress in the cell interior is significantly lower, less than 25% of the applied stress. Note that this distribution of the internal stress is confirmed by experimental estimations of internal stresses in materials with a cell structure [Straub et al., 1996; Borbely et al., 1993; Ungar et al., 1984].

Fig. 4.19 shows the internal stress developed after 10% of deformation. During monotonic tension the principal axis of the internal stress coincides with the principal direction of the applied macroscopic stress. In the directions perpendicular to the tensile axis, the internal stress and the applied stress are compressive in both phases, with values of ~ 1 MPa and ~ 60 MPa for the cell interior and walls, respectively. In the direction of the tensile axis, however, the internal stress is tensile in the cell walls, ~ 160 MPa, but compressive in the cell interior, ~ 25 MPa. This result qualitatively agrees with the experimental study of Hecker et al. [2002], who emphasised the tensor character of the internal stresses in nickel under tension.

It should be noted here that the mechanical response of material with a cell structure is anisotropic and depends on the orientation of the cells with respect to loading axis. In this paper uniaxial tension is always applied along the [111] cell direction. It is shown

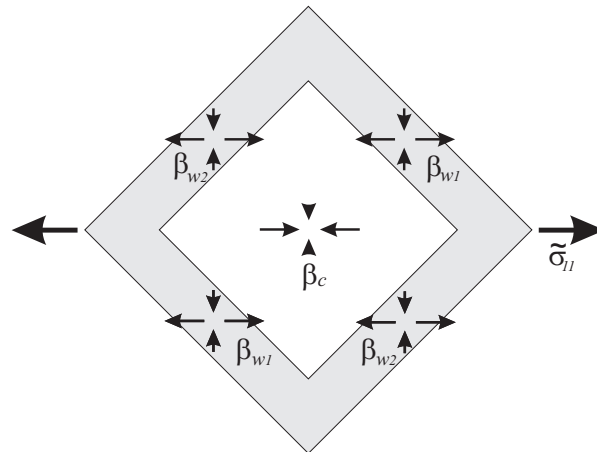


Figure 4.19 — The internal stresses in the cell structure after 10% of monotonic tension.

further that, in the context of the present model, this cell orientation is energetically the most favorable in tension and the cells are expected to preferably orient in this direction. In reality, the dislocation cells can be forced to deviate from this orientation by textural effects and anisotropy of the plastic slip. The present cell structure model does not account for these effects, but focuses on essential 'continuum' aspects of a cell structure only.

4.8.2 Strain path change: Reloading yield stress

This section discusses details of the mechanical behaviour of a cell material after a strain path change. Particularly, the study focuses on the previously introduced example of a complex deformation case for copper with two successive uniaxial tension modes. The tension-tension tests are simulated in the same manner as outlined in Section 4.7.1. The first tension is applied until the macroscopic strain (4.61) reaches 0.12. After elastic unloading, tension is applied again in a different direction, see Fig. 4.13a. The copper material parameters used for the calculations are given in Table 4.1 and 4.2. During prestraining, which is monotonic tension, the cell structure is assumed to develop with the [111] direction along the tensile axis, see Fig. 4.14. The strain path changes typically correspond to $\theta = 0$, as defined above, if not specified otherwise.

The reloading yield stress after a strain path change depends on the direction and magnitude of the change and, therefore, material anisotropy is dealt with. The effect increases with the amount of prestrain indicating that the associated anisotropy develops with deformation. This type of anisotropy is closely related to the development of a dislocation cell structure under deformation. The cell structure model, developed here, includes two major features associated with the presence of the cells, anisotropy related to the geometry of the cells and anisotropy due to the internal stresses. Their effects are considered in more detail below.

Geometrical anisotropy

Under monotonic deformation the dislocation structure constitutes a material heterogeneity with a geometry that is expected to be (at least partially) energetically favourable with respect to the current loading. A strain path change implies a change in the orientation of the cell geometry with respect to the loading axis, which triggers a change in the mechanical response of the material due to the anisotropy of the cells.

The composite model accounts for the anisotropy of the cells via Eqs. (4.3)–(4.5). The compatibility of the deformation, Eq. (4.4), and traction continuity, Eq. (4.5), on cell-wall interfaces, introduce a dependency of the stress and strain distributions on the orientation of the cubic cells. Besides, the internal stresses are intrinsically dependent on the cell geometry. As a result, the macroscopic response of the material is anisotropic and depends on the orientation of the cells with respect to the loading axis.

Fig. 4.20a shows the stress-strain diagrams for uniaxial tension applied to a material with a previously developed cell structure. The initial structure here corresponds to a cell structure developed after 12% of tensile strain. The loading is applied along different directions with respect to the cells, thereby reproducing a strain path change in tension-tension experiments. This procedure, however, neglects the effect of any deformation history before the reloading, except for the material heterogeneity. The analysed fictitious reloading thus starts from a

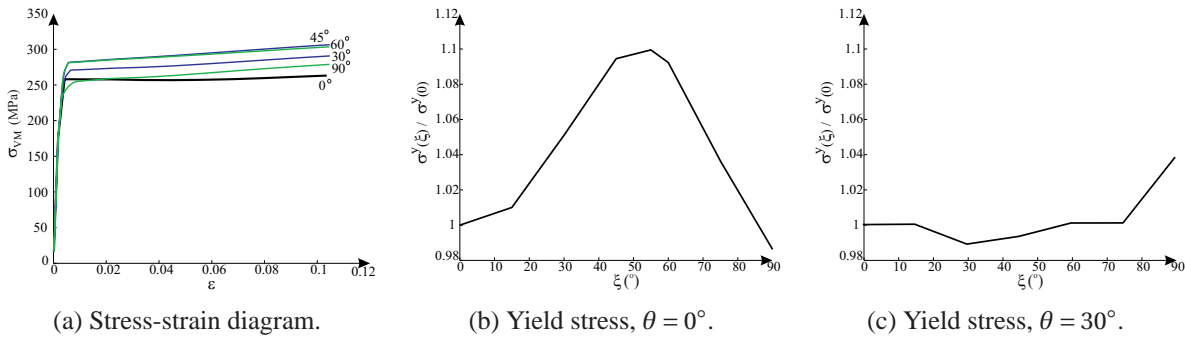


Figure 4.20 — Material anisotropy introduced by anisotropy of cells. Uniaxial tensions applied to a material with a developed cell structure (but without residual stresses).

completely unloaded state without residual stress or plastic inhomogeneity but with the cell structure.

Fig. 4.20 shows that accounting for the cell geometry only (i.e. without an *initial internal stress* contribution) introduces a significant anisotropy of the mechanical response. Fig. 4.20b shows the yield stress as a function of the cell orientation (which can be considered as the angle between the successive tensile axes). This result can be interpreted as the contribution of the cell structure anisotropy to the strain path change effect σ^y/σ_{mon} . It is clear that this contribution already provides a significant effect with qualitative tendencies as observed in the experiments, see Fig. 4.17a.

Figs. 4.20a and 4.20b show the anisotropy effect obtained in tension-tension tests with $\theta = 0^\circ$, i.e. with respect to cells, the orientation of the tensile axis changes with ξ from the [111] cell direction towards the $[1\bar{1}0]$ cell direction, see Fig. 4.14. variation of the strain path change angle θ defines different orientations of the cells with respect to new loadings and leads to different mechanical responses. Fig. 4.20c, for instance, shows the same effect but with $\theta = 30^\circ$, i.e with respect to the cells, the tensile axis orientation changes with ξ from the [111] cell direction towards the $[11\bar{1}]$ cell direction, see Fig. 4.14.

Residual stress

During monotonic deformation, an internal stress appears due to the plastic deformation of inhomogeneous material with a dislocation structure. Immediately after a strain path change the internal stresses remain in the material, unchanged by the elastic unloading, preserving significant residual stresses. Fig. 4.21 shows the components of the residual internal stresses with respect to the new loading axis. The tension-tension experiments are again used. In the figure, $\xi = 0^\circ$ corresponds to reloading in the same direction, during which the residual stress components are equal to the components of the internal stresses developed upon prestraining. If reloading is performed in a direction perpendicular ($\xi = 90^\circ$) to the prestrain direction, the 11 and the 22 components of the residual stress are interchanged compared to the $\xi = 0^\circ$ case.

In the general case of complex deformation, the nonuniform distribution of the applied stresses provides another source of residual stresses that retain in the material after elastic unloading. In tension-tension tests, however, the applied stresses develop almost uniformly during the first loading test, Fig. 4.18c, and create negligible residual stresses after unloading. The internal stresses, therefore, are the main source of the residual stresses in the tension-tension tests.

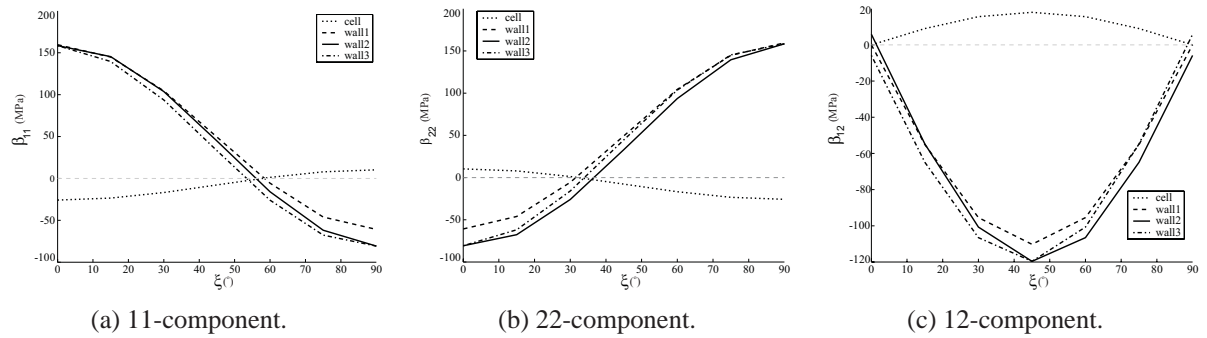


Figure 4.21 — Components of the residual internal stresses at the beginning of the second tensile step versus the strain path change angle ξ ($\theta = 0^\circ$).

To study the effect of the internal stress on the reloading behaviour, uniaxial tension is simulated first along the $[111]$ cell direction and then succeeded by tension in the $[1\bar{1}\bar{1}]$ cell direction, i.e. $\{\xi \sim 70^\circ, \theta = 30^\circ\}$. Tension along the $[111]$ cell direction and tension along the $[1\bar{1}\bar{1}]$ cell direction are equivalent with respect to the cell structure. Consequently, the geometrical anisotropy of the cell structure does not affect the reloading behaviour, and the strain path change corresponds to $\xi \sim 70^\circ$ in Fig. 4.20c. Thus, the effect of the strain path change observed in this test is caused by the residual stress only.

Fig. 4.22 shows the stress evolution during the tension-tension and monotonic tension tests. Only the components in the tensile direction are depicted here for clarity. During monotonic tension, a high tensile internal stress assists the applied stress in the walls, while the compressive internal stress resists the applied stress in the cells. After the strain path change, the prestrained material reflects the presence of the previously developed residual stress: in the direction of the new tensile axis it is compressive in the walls and tensile in the cell interiors, see Fig. 4.21a for $\xi \sim 70^\circ$. Consequently, the applied stress in the walls is resisted by the residual internal stress, Fig. 4.22d, and should grow much higher to create the same local yield stress, in comparison with monotonic deformation, Fig. 4.22c. Opposite in cells, the residual stress assists the applied stress, thus, a smaller applied stress is needed to start plastic deformation. Both, the increase of the applied stress in the walls and the decrease of the applied stress in the cells contribute to the macroscopic response. The effect in the cells is, however, smaller. As a result the macroscopic stress rises well above the stress corresponding to the same total deformation under monotonic loading (Fig. 4.22a). Thus an increased reloading yield stress is observed after the strain path change.

The analysis above shows that the presence of residual stresses in prestrained material changes the reloading yield stress compared to the stress reached in monotonic deformation at the same total strain. The effect depends on the difference between the residual stresses and the internal stresses corresponding to the current deformation⁴. In a tension-tension test the deviation of the residual stress from the monotonic internal stress increases with the angle between the successive tensile axes (see Fig. 4.21, at $\xi = 0$, where the residual stress is equal to the monotonic internal stress). Moreover, the residual stress in the walls has a major effect, since it provides the increased reloading yield stress. As the result of the residual internal stresses,

⁴In the general case of a strain path change, the residual stresses should be rather compared to the internal stresses corresponding to the new loading, i.e. to the current relation between the cell orientation and loading. Simulations showed that, for uniaxial tension, the dependency of the internal stresses on the cell orientation is not significant and can be omitted in this qualitative discussion.

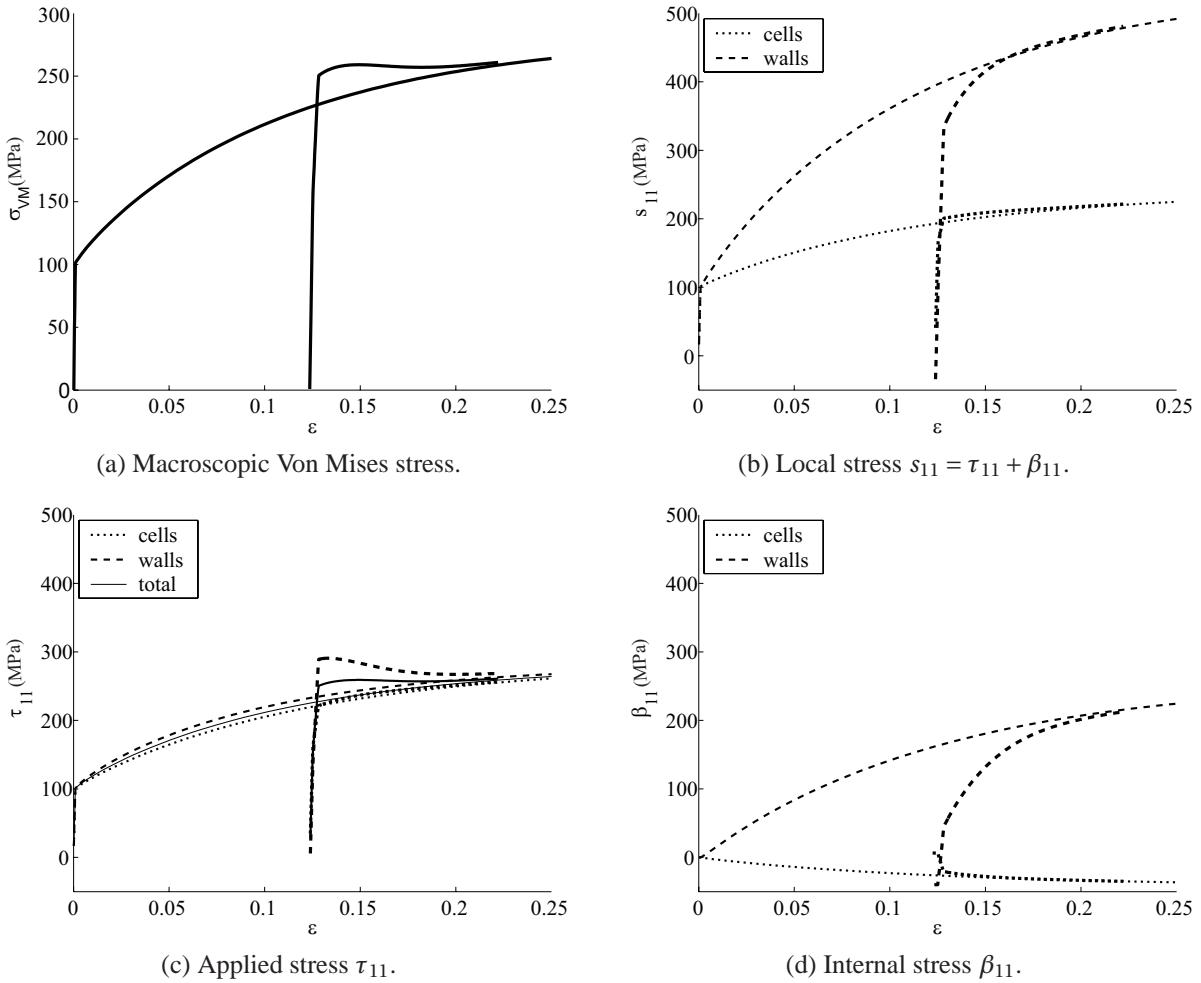


Figure 4.22 — Stress evolution after a strain path change with $\{\xi \sim 70^\circ, \theta = 30^\circ\}$, $\varepsilon_{pre} = 0.12$. With respect to the cell structure the tensile axis changes from the $[111]$ orientation to the $[1\bar{1}\bar{1}]$ orientation. Monotonic response for uniaxial tension (along the $[111]$ -cell direction) is also shown.

the macroscopic reloading yield stress is therefore expected to increase with the angle of the strain path change.

Fig. 4.23 shows the reloading yield stress in different tension-tension simulations. For tension-tension experiments in general, the effect of the residual stress is inevitably combined with the effect of geometrical anisotropy (Fig. 4.20). The result in Fig. 4.23 is therefore a collective effect of the anisotropy due to the cell geometry and due to the residual stresses. It seems that both effects are superimposed on each other. In Fig. 4.23a, $\theta = 0^\circ$, the effect of the cell geometry appears to define the tendency: an increase of the reloading yield stress until the angle ξ equals approximately 55° , representing a cross test effect, and a decrease of the effect for higher angles. The effect of the residual internal stresses provides an additional increase of the reloading yield stress, almost linearly growing as a function of the angle ξ (the cross test is not specially distinguished by this mechanism). Fig. 4.23b shows the reloading yield stress after a strain path change in another direction with $\theta = 30^\circ$. This result differs from the response in Fig. 4.23a due to a different effect of the geometrical anisotropy contribution, while the effect of the residual stress is almost the same. Remarkably, for the tension-tension tests considered here, the residual stresses are almost invariant with respect to θ .

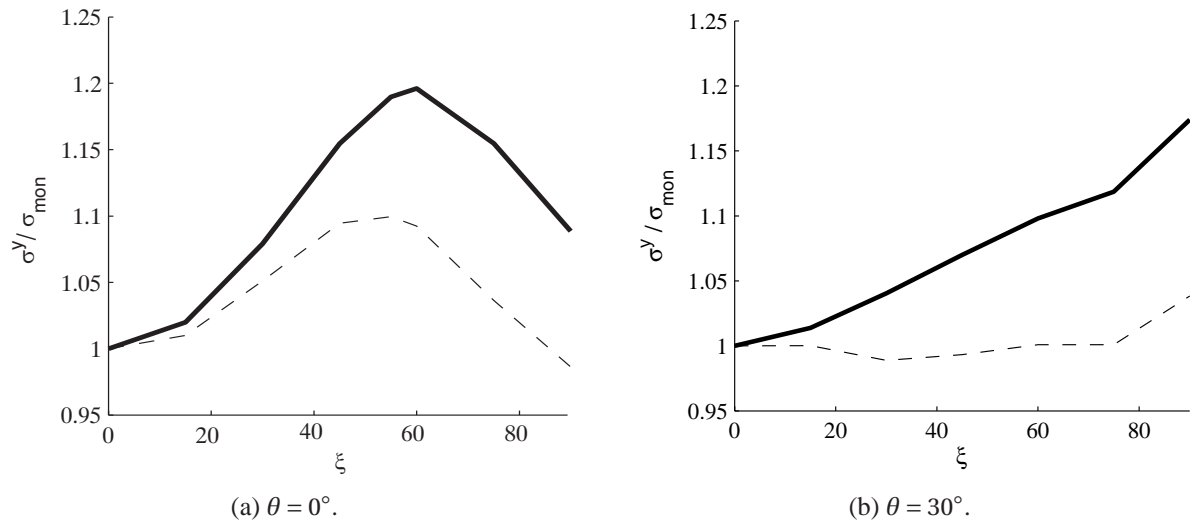


Figure 4.23 — Reloading yield stress as a function of the strain path change. Total effect of the residual stresses and the geometrical anisotropy (solid lines) and the contribution of the geometrical anisotropy (dashed lines).

Effect of the wall fraction f

As emphasized above, the reloading yield stress after a strain path change is defined by the contributions of the geometrical anisotropy and the residual stresses. As a result of the geometrical anisotropy, the reloading yield stress rises with the angle between the subsequent tensile axes up to the angle reflecting a cross test, after which it shows a decrease for higher angles (Fig. 4.23a). The effect of the residual stress was found to grow approximately linear with the angle. In the case shown in Fig. 4.23a the contributions of both effects are of comparable magnitude and the combined effect shows a complex dependency on the angle, with a maximum around the angle representing the cross test. For the strain path change shown in Fig. 4.23b the contribution of the geometric anisotropy is small and the total effect demonstrates the typical influence of the internal stress, i.e. a linear increase with the angle.

The same qualitative change of the effect occurs if the volume fraction of the walls is reduced. In a cell structure with a small wall volume fraction the effect of the geometrical anisotropy is small. On the other hand, deformation of cell structures with thin walls causes the appearance of internal stresses in walls β_{wi} that are much higher than in cell structures with thicker walls. Thus, considering the strain path change effect, in a cell structure with thin walls the contribution of the cell anisotropy is small and the overall response is dominated by the effect of residual stresses. The reloading yield stress in such materials grows linearly with the angle of the strain path change, independently of the orientation of the strain path change.

The influence of the cell geometry on the strain path change effect has already been observed in the previous section, where the same type of tension-tension tests were simulated for copper and for aluminium. Different values for the volume fraction of the walls f and for the cell orientation θ were, however, used. Simulations with copper are strongly affected by the geometrical anisotropy and therefore demonstrate a maximum reloading yield stress at an angle corresponding to the cross test. In the simulations with aluminium the effect of the residual stresses dominates and a linear growth of the reloading yield stress with the angle is observed.

Recapitulating, the analysis of the reloading yield stress based on the cell structure model suggests that the material anisotropy due to the cell geometry and the internal stresses both determine the reloading macroscopic yield stress. Their relative contributions, and therefore the resulting overall effects, depend on the cell geometry and the cell orientation. This theoretical result can be used to explain the different types of reloading behaviour found in the experimental literature. In the experiments of Schmitt et al. [1991], the reloading yield stress has a maximum in a test close to a cross test. Li and Bate [1991] performed two sequences of tension-tension experiments with two different initial textures. It was found that one sequence showed a maximum reloading yield stress close to a cross test, while in the other sequence the reloading yield stress increased with the angle, beyond 55° corresponding to a cross test. This result was explained in Li and Bate [1991] by the difference in the initial texture and it was concluded that the texture is responsible for the strain path change effect, rather than a dislocation structure. The analysis based on the present cell structure model shows that the difference in the experimental results might also be due to a difference in the cell geometry, enforced by the initial texture. It was shown that a difference in the wall thickness can also lead to a change in the macroscopic strain path change effect.

4.8.3 Strain path change: Transient hardening

Another phenomenon observed after strain path changes is transient hardening. Upon deformation beyond the reloading yield stress, the macroscopic response evolves towards the value of the monotonic loading case. After an increased reloading yield stress, the macroscopic hardening rate drops and the macroscopic stress slowly decreases to the level corresponding to the nominal response under the current deformation. This type of transient hardening is observed e.g. in Fig. 4.22. The increased reloading yield stress is caused here by negative residual stresses in the cell walls. As soon as plastic deformation begins after a strain path change, the plastic incompatibility is redistributed and the internal stress is adjusted to the new loading direction (Fig. 4.22c). The internal stress in the walls grows towards the value typical for the current deformation under monotonic loading. This evolution of the internal stress causes the decrease of the applied stress in the walls. As a result, the macroscopic stress approaches the monotonic stress. The predicted transient hardening lasts up to 10% of deformation. This scenario of hardening evolution is in agreement with experimental observations. Thus, the cell structure model predicts the transient hardening as a result of an adjustment of the internal stresses to the new deformation mode.

In the general case of a complex deformation, the geometrical anisotropy also influences the macroscopic hardening process. After a strain path change the internal stress recovers to the level corresponding to the current relation between the new loading and cell orientation. Thus, the macroscopic stress evolves towards the stress corresponding to monotonic deformation with the current orientation of the cell structure, i.e. not the stress corresponding to monotonic loading according to the prestrain. Fig. 4.24 shows the evolution of the macroscopic stress in a cross test ($\xi \approx 55^\circ$). The cross test involves loading along the $[111]$ cell direction followed by loading along the $[22\bar{1}]$ direction. Two stress-strain diagrams for monotonic tension along the $[111]$ and the $[22\bar{1}]$ cell directions are shown as well. Since in this paper the $[111]$ cell orientation is assumed to correspond to monotonic tension, the first curve represents monotonic tension, while the second curve is considered as fictitious. It can be seen that after the strain path change the stress approaches the stress corresponding to the $[22\bar{1}]$ cell

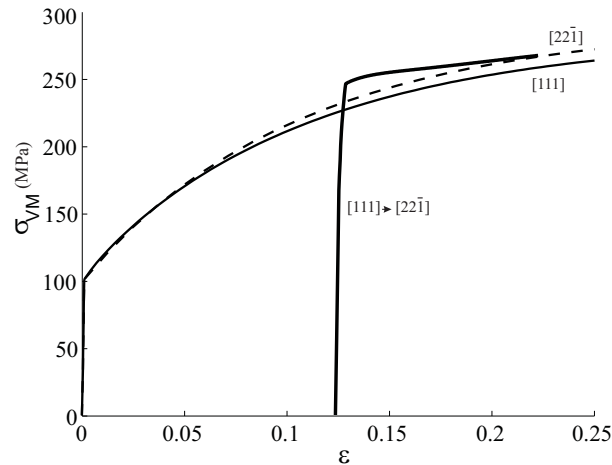


Figure 4.24 — Cross test $\{\xi \sim 55^\circ, \theta = 30^\circ\}$. Responses corresponding to monotonic deformations with the prestrain mode (along the $[111]$ -cell direction) and the reloading mode (along the $[22\bar{1}]$ -cell direction) are also given.

orientation, which is higher than the stress in the monotonic case. This result deviates from experimental observations reporting that the macroscopic stress recovers to the level of the monotonic test. The discrepancy is due to the fixed orientation of the cell structure assumed in the simplified model. It is also confirmed by experiments that after a strain path change the cell structure reorients itself accommodating the new loading. To predict the transient hardening correctly the extended model should account for the reorientation of the dislocation structure. This is a subject for future research.

4.8.4 Reversed loading

Reversed loading is a strain path change reflecting the well-known Bauschinger effect, i.e. a decreased reloading yield stress followed by a decreased hardening and hardening recovery [Christodoulou et al., 1986]. To reproduce the loading reversal, compression deformation was applied as a first loading step succeeded by tension step. Fig. 4.25 shows the macroscopic response predicted by the cell structure model for the compression-tension test. Fig. 4.26 gives details on the internal and applied stress evolutions.

During monotonic tension a cell structure develops and internal stresses are induced in the material. The 11 component is positive in the walls and negative in the cells, see Fig. 4.26b. After the loading reversal, the internal stresses remain in the material as residual stresses. Now, the tensile residual stresses in the walls counteract the compressive applied stress while the compressive residual stresses in the cell interiors assist the compressive applied stress. The latter contribution of the residual stress in the cell interiors is often held responsible for the Bauschinger effect's earlier yield. It can be seen in Fig. 4.26 that the plastic deformation in the cells indeed starts at an applied stress lower than the corresponding stress in forward tension. However, the residual stress in the walls resist the applied compression and cause an increase of the applied stress level in the walls. On average, the contribution of the increased applied stress in walls neutralises the contribution of the decreased applied stress in cells. Fig. 4.25b shows a resulting macroscopic stress that is initially decreased by the effect of the residual stress in the cells but grows quickly again thereafter due to the effect of the residual stress

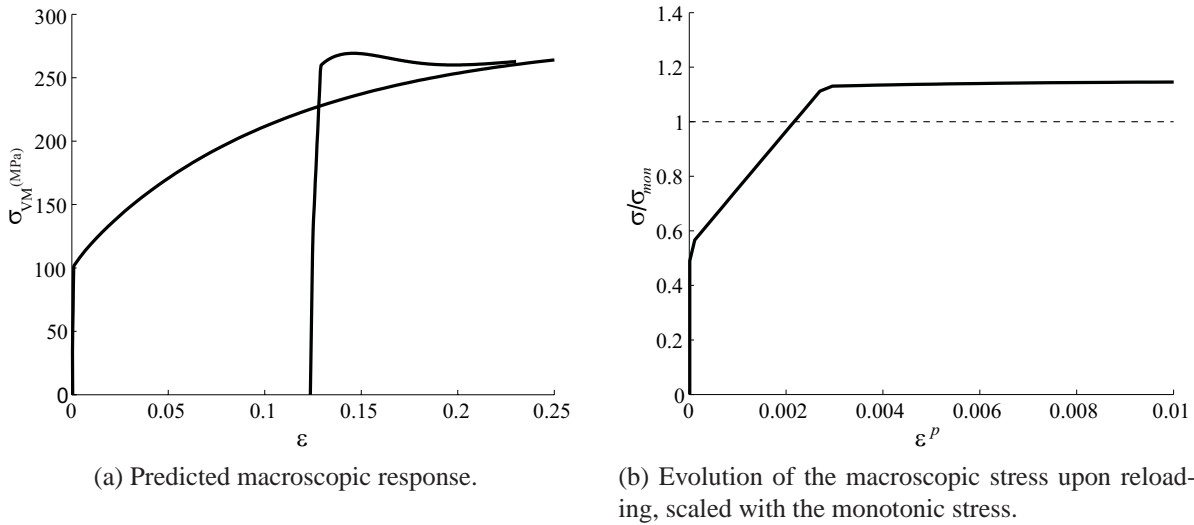


Figure 4.25 — Compression-tension test.

in the walls. As a result, the more prominent contribution of the tensile residual stress in the walls macroscopically causes an effect opposite to the Bauschinger effect. Summarising, internal stresses developed in the cell structure under forward deformation do not produce a macroscopic Bauschinger effect. However, they do cause earlier plastic deformation in the cell interiors which may trigger other mechanisms reducing the macroscopic stress. For example, it has been shown in Viatkina et al. [2003] (Chapter 3) that cell disruption reduces the macroscopic stress. The residual stresses after loading reversal provide an early start of plastic deformation in the cells, initiating cell disruption and leading to a macroscopic Bauschinger effect. Redistribution of dislocations in the structure initiated by cell slip has a similar effect. This mechanism is dealt with in Viatkina et al. [2005c] (Chapter 5).

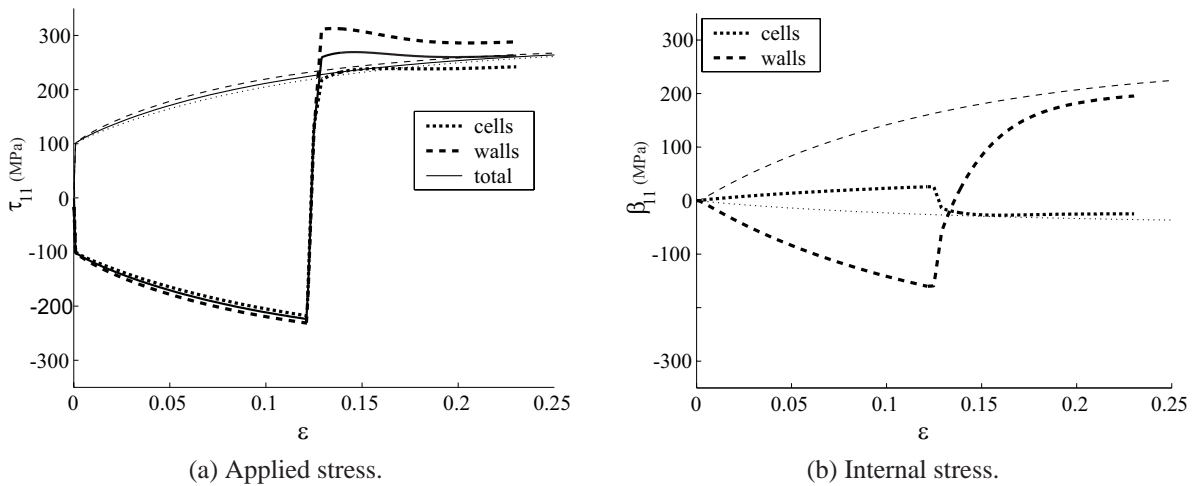


Figure 4.26 — Stress evolution during compression-tension test and monotonic tension test.

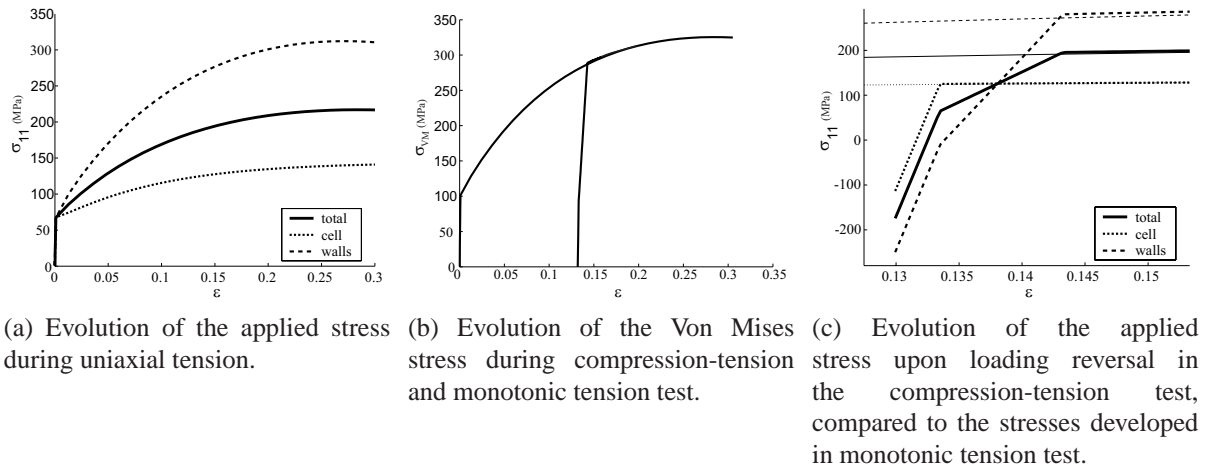


Figure 4.27 — Results of the simulations with the composite model, *omitting internal stresses*.

4.8.5 Composite model

This paragraph of the discussion deals with the performance of the composite model in which the heterogeneous nature is the only contribution, i.e. the cell structure model is considered *without* the internal stress field due to incompatibility. The implementation of the cell structure model is adapted here by removing kinematic hardening from the yield function evolution (4.17). In this version of the model the inhomogeneous yield stress is accommodated by the applied stress only ($\mathbf{s} = \boldsymbol{\tau}$). This leads to a higher inhomogeneity of the locally applied stress than in the model including the back stresses, viz. Figs. 4.18 and 4.27a, provided by high elastic rotations.

The model accounts for the geometrical anisotropy in the same manner as discussed above and also predicts residual stresses after elastic unloading. The residual stresses here are a consequence of the inhomogeneity of the applied stress in the material (there are no internal stresses in these calculations). These residual stresses are, however, small and do not have a significant influence on further reloading. Simulations proved that the strain path change effect on the reloading yield stress predicted by the composite model is reduced to the influence of geometrical anisotropy, see Fig. 4.20. Upon stress reversal, the composite model also predicts early plastic deformation in the cells due to the residual stresses, Fig. 4.27, but the effect is also small and the predicted backward stress quickly approaches the forward stress.

4.8.6 Internally stored energy as a function of cell geometry

In the literature, it is often stated that a microstructure in a material is essentially formed in order to relax the free energy, even though the kinetic path towards such a low energy microstructure may be more important than the minimum itself. It is often claimed that dislocation cell structures represent such a minimum in the free energy [Kuhlmann-Wilsdorf, 1996]. Although the kinetics of the underlying deformation processes may result in serious deviations from this assumption, it is accepted that the thermodynamics tries to push a microstructure towards *accessible* minima.

This tendency is evidently present in the composite model formulated for a heterogeneous material, even if the internal stresses are not taken into account. In this case, the solution

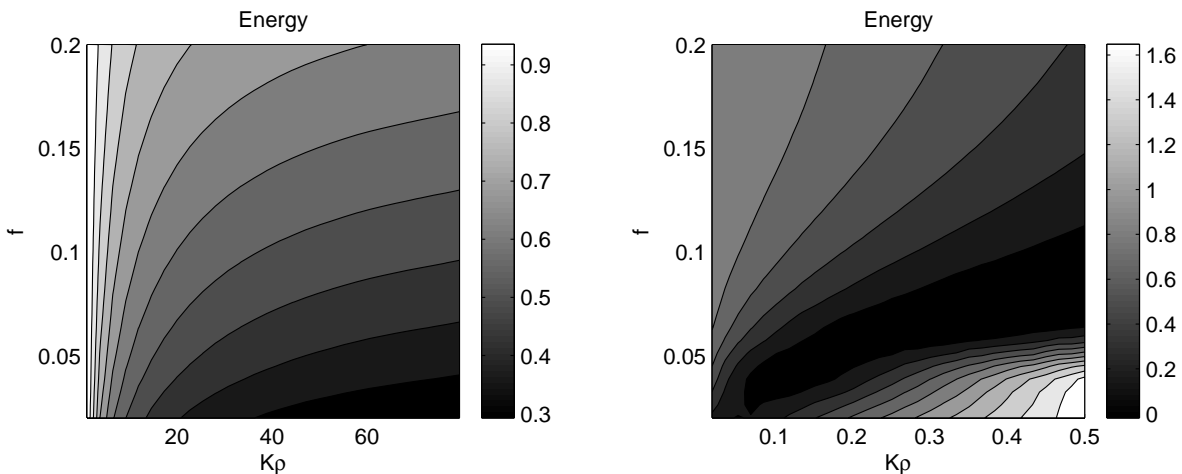
of the equilibrium problem for a uniform material demonstrates a higher stored energy than the solution for a heterogeneous material, consisting of soft and hard phases. Thus, the formation of the cell structure is energetically favourable and might be, indeed, pursued by the material under deformation. However, this consideration fails to predict the morphology of the energetically favourable microstructure, i.e. the finite morphology for which such a minimum of the stored energy exists, at a given level of applied strain and keeping other material parameters fixed.

Fig. 4.28 shows the elastic energy as a function of the volume fraction of the walls and the ratio of the dislocation densities in walls and cells after 10% tension. The elastic energy is defined as follows:

$$E = \frac{1}{2} \int_V (\mathbf{E}^e : \mathbf{C} : \mathbf{E}^e) dV, \quad \mathbf{E}^e = \frac{1}{2} ([\mathbf{F}^e]^T \cdot \mathbf{F}^e - \mathbf{I}) \quad (4.63)$$

The material parameters for copper were used here according to Table 4.1 and 4.2. Here, only two parameters of the cell morphology are investigated, the wall thickness ratio $f = \frac{w}{D}$ and the dislocation inhomogeneity $K_\rho = \frac{\rho_w}{\rho_c}$. The rest of the parameters, i.e. I , R , D and cell orientation, are fixed as in the previous sections. The use of the evolution equations (4.24) for the dislocation density guarantees the same evolution of the total density for any set of $\{f, K_\rho\}$ variables. The results in Fig. 4.28a show that minimum values of the true energy are provided by a microstructure with infinitely thin and infinitely dense walls. Experimental observations, however, report a finite sized microstructure, developed in materials under deformation.

Recent discussions [Geers et al., 2005] in the mechanics community on the prediction of the microstructure evolution in metals, emphasise the role of the energy associated with interfaces, which are expected to bring a length scale into the picture. In the cell structure model proposed here, interfaces are introduced to define the internal stresses. The internal stresses are determined as a function of the cell geometry and have a significant influence on the macroscopic behaviour of the material, as shown in the previous sections.



(a) Composite model *without* internal stresses.

(b) Cell structure model *with* internal stresses.

Figure 4.28 — Effect of the cell geometry on the stored elastic energy (E) after 10% of tension. The energy is scaled with the energy obtained for the uniform material.

Fig. 4.28b shows the elastic energy obtained with the cell structure model including the internal stresses. It can be seen that the lowest energy location is shifted towards finite values of the

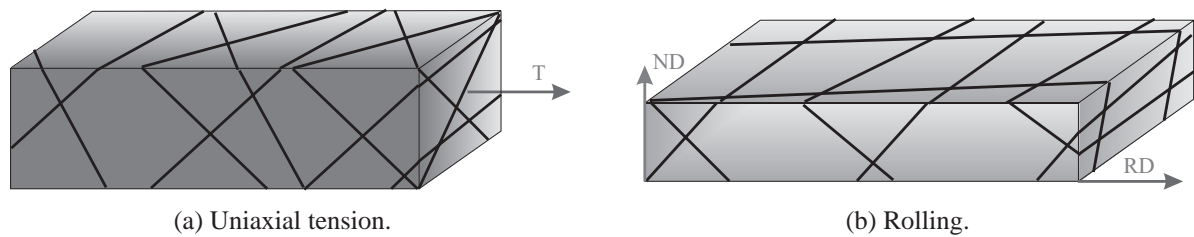


Figure 4.29 — Orientation of the cell structure minimising the elastic energy. The figure shows the traces of the cell walls on the prestrained specimens.

wall thickness ratio f and the dislocation density ratio K_ρ . Though a clear unique minimum of the energy does not exist, the results demonstrate the tendency of the material to develop a finite sized microstructure. The calculations illustrate that a finite sized microstructure is energetically favourable and that a proper incorporation of the internal stresses in the microstructure is a key factor in modelling the microstructural evolution.

Considerations based on the stored elastic energy might also help to reveal the role of thermodynamics indicating the orientation of the cell structure developing under deformation. To this purpose, the elastic energy has been calculated for uniaxial tension tests with different orientations of the cell structure with respect to the loading axis. The same geometry of cells and the material parameters were used as in the previous sections. The orientation of the cells was defined with respect to the loading axis by three Euler angles. The orientation $\{20; 50; 60\}$ was found to provide a minimum energy. The cells with this orientation with respect to the macroscopic axis are shown in Fig. 4.29a. The found orientation $\{20; 50; 60\}$ represents cells with the wall planes close to the macroscopic planes of maximum shear, that are planes with a normal inclined 45° to the tensile axis.

Similar calculations were performed for a rolling test and the orientation $\{70; 40; 70\}$ was found to provide deformation with a minimum elastic energy (Fig. 4.29b). In the case of rolling the planes of maximum shear are inclined $\pm 45^\circ$ to the rolling direction in the longitudinal plane and are perpendicular to the rolling direction in the rolling plane. The found cell orientation of minimum elastic energy aligns with these macroscopic planes. These results support the statement that the cell orientation develops in relation to the loading axis, along planes of maximum shear.

Considering the above, the assumption in this paper that the cell structure is oriented aligned with the planes of maximum shear is justified.

4.9 Conclusions

A continuum model of an FCC metal with a dislocation cell structure has been developed to deal with strain path dependency effects. The approach incorporates the morphology and orientational anisotropy of the cell structure, along with the internal stresses developed within the cell structure under deformation. Essential features of the cell structure model can be summarised as follows:

- Mean field approximation:
The mean response of a polycrystal material with a nonuniform dislocation structure

is described by means of the mechanical behaviour of a model material containing uniform dislocation cells. The geometry and orientation of the cells represent the average morphology of the real cell structure in a polycrystal.

- **Composite model:**
A material with a dislocation cell structure is idealised as a two-phase periodic composite consisting of cell walls and cell interiors, differing by their local dislocation densities. Traction continuity and deformation compatibility are enforced at the interfaces.
- **Continuum elastoplasticity:**
Consistent with the mean field approximation, the local material behaviour in the cell and wall components is assumed to be piecewise uniform and is modelled by J_2 elastoplasticity, including combined isotropic and kinematic hardening. The isotropic hardening is related to the local dislocation density of the statistically stored dislocations, evolving according to the adopted phenomenological equations. The kinematic hardening is associated with the development of internal stresses.
- **Internal stresses:**
The internal stresses are derived as a natural result from the plastic deformation incompatibility between the cell interiors and the cell walls. They represent the long-range effect emerging from the geometrically necessary dislocations that appear at the interfaces to accommodate the jumps in the plastic deformation. The internal stresses have been shown to be a function of the plastic deformation incompatibility and the cell geometry.

The model has been verified by comparing predicted and experimentally determined reloading yield stresses after various strain path changes. The model correctly captures the essential features of the strain path change effects for moderate strain path changes, i.e. the anisotropy of the effect and the dependency on the amount of prestrain. Since cell dissolution is not yet incorporated, the model is not able to predict a reduced reloading yield stress after a load reversal.

The deformation behaviour of copper with a developing dislocation cell structure has been analysed using the cell structure model. The following conclusions can be drawn:

- During monotonic loading the internal stresses are developing up to the level of the applied stresses.
- After a strain path change, the value of the reloading yield stress is determined by the geometrical anisotropy due to the cell structure morphology and by the internal stresses developed during prestraining.
- The transient hardening behaviour after a strain path change is related to the adaptation of the internal stresses to the new loading. Reorientation of the cells after a strain path change was found to have a substantial contribution and should be introduced in the model to improve the predictions.
- The exclusive contribution of the internal stresses, which develop in a metal with a cell structure, does not explain the experimentally found reduced reloading yield stress after load reversal associated with the Bauschinger effect.

The developed cell structure model has been proven to be a powerful tool for the theoretical study of the internal stresses and their influence on the macroscopic behaviour. The model predicts strain path change effects and offers a computationally efficient method which lends itself for use in macroscopic engineering computations.

Chapter 5

Modelling the dislocation structure evolution upon stress reversal

Reproduced from: Viatkina, E.M., Brekelmans, W.A.M., and Geers, M.G.D., (submitted). Modelling the dislocation structure evolution upon stress reversal.

5.1 Introduction

The effect of a strain path change during the loading of a material manifests itself through an altered reloading yield stress and transient hardening compared to the response during a monotonic deformation path of the same material [Vieira et al., 1990, 2000; Zandrahimi et al., 1989; Bate and Wilson, 1986; Pedersen et al., 1981]. In particular, moderate changes of the deformation mode give rise to an increased reloading yield stress followed by relatively low hardening. On the contrary, deformation histories that include a stress reversal demonstrate a pronounced so-called Bauschinger effect. In comparison with continuous forward loading, reversed reloading exhibits a decreased reloading yield stress followed by a short stage of increased hardening behaviour, after which the hardening rate drops, to finally show recovery to the same level as observed for the monotonic loading case.

The macroscopic effect of a strain path change is commonly associated with the occurrence of a dislocation structure in the material and its adaptation to the new loading. The morphology of the dislocation structure developed during a particular loading path is clearly depending on the loading characteristics. The dislocation structure is formed to accommodate the current deformation in a preferable way. After a strain path change, the previously formed dislocation structure becomes 'unstable' under the new loading since its morphology is not favourable anymore and, moreover, it degenerates by newly activated plastic slip. The resistance and adaptation of the dislocation structure to the loading in a new direction is typically accompanied by an increased reloading yield stress and a relatively low transient hardening. The Bauschinger effect is usually related to the degradation and reappearance of the dislocation structure under stress reversal.

In a previous paper [Viatkina et al., 2005b] a cell structure model was developed to predict the effect of a dislocation cell structure on the macroscopic response of a material under complex loading. The model takes into account the intrinsic material heterogeneity due to the dislocation structure, the effects of the cell geometry and the presence of internal stresses. The simulations based on the developed model demonstrated its capability to predict the experimentally observed material response after moderate strain path changes. The Bauschinger effect, however, was not predicted correctly. After load reversal, the stress applied to the material retained the same orientation with respect to the cell structure, although opposite in sign. Hence, the material anisotropy will not trigger a Bauschinger-like effect on the mechanical behaviour. The orientation of the internal stresses developed in the cell interiors, on the contrary, indicated an expected significant contribution to the Bauschinger effect. In spite of this expectation, it was shown that the internal stresses in the cell interior, which assist the applied reloading, do not decrease the macroscopical yield stress during reversed loading. Initially, these internal stresses cause some plastic deformation in the cell interior during the early reloading stage. However, this effect is rapidly compensated by the high internal stresses in the wall component, which resist the reloading, triggering an opposite influence. Based on this analysis, it was concluded that the internal stresses originating from the dislocation cell structure in a metal cannot provide the experimentally observed macroscopical Bauschinger effect. Yet, the occurrence of early plastic slip in the cell interior might trigger other mechanisms reducing the macroscopic stress, which are the subject of the present paper.

Experimental observations of the microstructure under reversed loading reveal a dissolution of the cells. The change of the cell morphology and the associated dislocation redistribution

towards a more homogeneous configuration, denoted as 'cell dissolution', are promoted by the plastic deformation and reduce the macroscopic stress. It has been shown in Viatkina et al. [2003] that under stress reversal the increase of the cell size, which is a characteristic feature of cell dissolution, in combination with the influence of the residual stresses, provides a decreased macroscopic reloading yield stress. In the present paper, attention is focused on another mechanism affecting cell dissolution; dislocation redistribution. Under continuous forward loading the dislocations tend to form a cell structure. After stress reversal, the driving force behind the cell formation is reversed and dislocations start to redistribute towards a more homogeneous structure. Redistribution of dislocations is accompanied by a redistribution of the local yield stresses and, consequently, the macroscopic response of the material is influenced accordingly.

The objective of this paper is to enhance the cell structure model, developed in Viatkina et al. [2005b], with an improved description of the dislocation density evolution. The main purpose of this enhancement is to enable a correct prediction of strain path change effects under complete or partial stress reversal. Therefore, the attention is particularly concentrated on the dislocation mechanisms accompanying a stress reversal.

A dislocation dynamics approach concentrates on the analysis of the dislocation movement and interactions in a deforming material. There have been several attempts in this area to describe the dislocation redistribution during deformation towards the formation of cells [Argaman et al., 2001; Neumann, 1985; Groma and Balogh, 1999]. The associated models, however, are still unsuccessful in describing the complex evolution of a cell structure. Furthermore, discrete dislocation dynamics is not applicable within a continuum model as the presently developed cell structure model. In the context of a continuum model, the dislocation redistribution is typically represented by the evolution of dislocation densities [Bergstrom, 1983]. The classical cell structure model [Mughrabi, 1987] has been enhanced by evolution equations for the dislocation density by a number of authors [Estrin et al., 1998; Argon and Haasen, 1993; Goerdeler and Gottstein, 2001]. Dislocation densities in the cell interiors and in the walls are introduced in these models and corresponding evolution equations are suggested to describe the development of the cell structure. However, these formulations do not account for a change in the dislocation evolution after a strain path change.

Recently, Peeters [2002] proposed a composite model with a dislocation density evolution that accounts for the deformation history. The model is developed to predict the mechanical response of BCC metals with a cell-block structure. Two mechanisms activated by a strain path change are introduced in the model: 1) reverse flux of interface dislocations causing additional annihilation and 2) activation of new slip systems causing destruction of a previously formed structure.

In this paper, the dislocation evolution under complex deformation is considered for FCC metals containing a cell structure. Dislocation mechanisms for cell formation and dissolution are introduced and the corresponding evolution equations are proposed.

5.1.1 Experimental observations of the dislocation structure

Extensive information on the morphology of cell structures, their formation and evolution under various loading conditions can be found in the literature, e.g. Young et al. [1986]; Mughrabi et al. [1986]; Barker et al. [1989]; Bay et al. [1992]; Hansen et al. [2001]; Huang and

Hansen [1997]; Hansen and Huang [1997]; Winther et al. [2000]; Liu et al. [1998]; Zimmer et al. [1983]; Ungar et al. [1984]; Park and Parker [1989]; Liu and Hansen [1995]; Hughes et al. [1997]. Much of the present understanding of dislocation processes resulting from a strain path change has been achieved from observations made in fully reversed plastic deformation [Christodoulou et al., 1986; Hasegawa et al., 1975; Rauch et al., 2002; Hasegawa et al., 1986; Marukawa and Sanpei, 1971; Pedersen et al., 1981]. The evolution of the cell structure after a stress reversal received most attention due to its direct relation to the Bauschinger effect. The essential features to be incorporated in the present model are shortly summarised below.

In an undeformed material, the dislocation distribution is close to statistically homogeneous. However, at the beginning of a deformation process, dislocations cluster together to form tangles, which constitute regions with relatively increased dislocation densities. As the strain increases, more dislocations participate in the evolution of the structure and the tangles link up to form dislocation boundaries, which envelop regions relatively free of dislocations. The structure created in this manner can be observed as a network of volume elements within which the dislocation density is well below average, mutually separated through boundaries in which dislocations are concentrated. This structure is known as a cell structure and the dislocation boundaries forming this structure are the so-called cell walls. As the deformation proceeds, the dislocation density inside the cell walls increases which can be observed as sharpening of the walls. The dislocation density in the walls can rise more than a factor 20 above the density found in the cell interiors. The dislocation density in cell interiors also increases but much slower.

The morphology of the dislocation structure developed during a particular loading path is clearly depending on the loading characteristics. The dislocation structure is formed to accommodate the current deformation in a preferable way. After a strain path change, the previously formed dislocation structure becomes 'unstable'. The applied stress, which forced the dislocations to form the present cell structure, changes. If the change has a reverse component, i.e. such that the stress is fully or partially reversed, a reverse dislocation glide initiates, accompanied by a remobilisation of dislocations that were previously immobilised in locks, dipoles, pile-ups and on cell-wall interfaces [Hasegawa et al., 1975; Rauch et al., 2002]. A strain change might also trigger dislocation glide in new crystallographic planes [Schmitt et al., 1991]. The interaction of newly activated dislocations with the already present dislocation structure (formed by prestrain) leads to the destruction of the last one. Some secondary dislocation mechanisms, like dislocations cutting through the cell structure will be not considered here.

After a load reversal, experimental observations reveal a dissolution of the cell structure, either partial or complete. The dissolution appears as a redistribution of dislocations towards a more homogeneous structure. The dislocation density drops in the walls and rises in the cells, resulting in smaller gradients. The total dislocation density is often observed to decrease as well. As the deformation in the new direction proceeds, the cell structure gradually reappears. The dislocation density evolves to accommodate the variations that are typical for the current plastic deformation. The degree of the dissolution is found to be related to the amount of prestrain applied before the change. A higher prestrain is associated with a higher degree of dissolution and consequently a postponed recovery. The dissolution and reappearance of a cell structure are typically related to a drop in the macroscopic hardening and a hardening recovery, respectively.

The morphology of the cell structure also changes after a load reversal. A smaller number

of walls are found, which can be considered as an increase of the mean cell size. The morphological evolution after a strain path change has been studied in Viatkina et al. [2003] and will be not investigated further. Here, the cell structure is assumed to have a constant geometry.

5.2 Cell structure model

The deformation behaviour of FCC metals with a dislocation cell structure is modelled here on the basis of the cell structure model introduced in Viatkina et al. [2005b]. The main features of the model are shortly summarised in this section.

The material with the cell structure is idealised by a composite consisting of four uniform components: the cell interiors and three mutually perpendicular cell walls. The cell wall components represent the phases with a high dislocation density and the cell interior component represents the areas enveloped by the dislocation walls with a low dislocation density. The cell structure is modelled as a 3D periodic configuration of cuboid cells formed by three mutually perpendicular sets of planar cell walls.

The local mechanical response of the composite is characterised by the Cauchy stress tensor $\boldsymbol{\sigma}$ and the deformation gradient tensor \mathbf{F} . The average mechanical response $\{\tilde{\mathbf{F}}, \tilde{\boldsymbol{\sigma}}\}$ of the composite is calculated from the relative contributions of these local responses of the walls, $\{\mathbf{F}_{wi}, \boldsymbol{\sigma}_{wi}\}$, $i = 1, 2, 3$, and the cell interiors, $\{\mathbf{F}_c, \boldsymbol{\sigma}_c\}$:

$$\tilde{\boldsymbol{\sigma}} = f_{w1}\boldsymbol{\sigma}_{w1} + f_{w2}\boldsymbol{\sigma}_{w2} + f_{w3}\boldsymbol{\sigma}_{w3} + (1 - f_{w1} - f_{w2} - f_{w3})\boldsymbol{\sigma}_c \quad (5.1)$$

$$\tilde{\mathbf{F}} = f_{w1}\mathbf{F}_{w1} + f_{w2}\mathbf{F}_{w2} + f_{w3}\mathbf{F}_{w3} + (1 - f_{w1} - f_{w2} - f_{w3})\mathbf{F}_c \quad (5.2)$$

where f_{w1} , f_{w2} and f_{w3} are the volume fractions of the corresponding wall components. Additionally, traction continuity and compatibility of deformations are enforced on the interfaces between the cell interiors and the walls:

$$(\boldsymbol{\sigma}_c - \boldsymbol{\sigma}_{wi}) \cdot \tilde{\mathbf{n}}_i^t = \mathbf{0} \quad (5.3)$$

$$(\mathbf{F}_c - \mathbf{F}_{wi}) \cdot (\mathbf{I} - \tilde{\mathbf{n}}_i^0 \tilde{\mathbf{n}}_i^0) = \mathbf{0} \quad \text{with } i = 1, 2, 3 \quad (5.4)$$

where $\tilde{\mathbf{n}}_1$, $\tilde{\mathbf{n}}_2$ and $\tilde{\mathbf{n}}_3$ are the normal vectors to the cell-wall interfaces, and the superscripts t and 0 indicate the vectors in their initial and current configuration, respectively.

The local material behaviour in the cell and wall components is assumed to be homogeneous and modelled by J_2 elastoplasticity with the following yield function:

$$\Psi_i = \bar{s}_i - \alpha M G b \sqrt{\rho_i} \quad \text{with } \bar{s}_i = \sqrt{\frac{3}{2} \mathbf{s}_i^d : \mathbf{s}_i^d} \quad \text{and } \mathbf{s}_i = \boldsymbol{\tau}_i + \boldsymbol{\beta}_i \quad (5.5)$$

where the subscript i stands for c , $w1$, $w2$ and $w3$. G is the shear modulus, b is the magnitude of the Burgers vector, α is a material parameter and M is the parameter related to mean orientation of crystal lattice in the polycrystal. The isotropic hardening is defined above by the local dislocation density ρ_i and the kinematic hardening is due to the internal stress $\boldsymbol{\beta}_i$. The yield function is formulated in the stress-free intermediate configuration, so that $\boldsymbol{\tau}_i$ is the

second Piola-Kirchhoff stress measure defined with respect to this configuration and related to the applied stress σ_i in the current configuration.

The heterogeneity of a material with a cell structure causes, during external loading, a nonuniform field of plastic deformation. To accommodate the plastic deformation jumps across the interface between the hard and soft phases, polarised layers of geometrically necessary dislocations (GND) will develop at the interface between cell walls and cell interiors. It is known that the resulting dislocation network may substantially affect the mechanical behaviour by inducing internal stresses. In the cell structure model, the statistically stored dislocations in the wall and cell interior phases are randomly distributed and therefore the resulting stress fields will compensate each other, excluding their contribution to long-range effects. On the contrary, the geometrically necessary dislocations are polarised in the interface layers and, therefore, constitute a source of non-vanishing internal stresses in the material. The internal stresses created by geometrically necessary dislocations on the interfaces were determined in Viatkina et al. [2005b] as a function of the plastic incompatibility and the composite geometry.

5.3 Dislocation density evolution

Local isotropic hardening was previously introduced in the cell structure model by the local dislocation density ρ . The relation (5.5) has been motivated through several experimental studies, e.g. Ungar et al. [1984]. It is widely used in continuum theories of plasticity and has been proven to yield a good agreement with experimental data. The main challenge in the present context is to derive a relationship between the evolution of ρ and the plastic strain. This is not a trivial task since upon deformation the dislocation density evolves rapidly and inhomogeneously. Furthermore, the constitutive laws of dislocation mechanics are complicated and defined on a scale that is far below the conventional continuum scale. To be used in continuum theories, the main features of dislocation evolution are commonly generalised in a density context [Bergstrom, 1983]. This implies that the equations are formulated to describe the average behaviour of a large number of dislocations in a 'continuum' material point.

In this section, evolution equations are proposed for the dislocation density in FCC metals with a cell structure. The equations are formulated to describe the formation of the cell structure under monotonic loading as well as dissolution of the structure after a strain path change. First, the general relations for the dislocation density evolution are summarised. Next, the evolution equations are adapted for the specific case of an inhomogeneous material with a cell structure.

5.3.1 Dislocation density fundamentals

This subsection summarises the general evolution equations for the dislocation density in metals under deformation. The relations below are widely used in mesoscopic continuum models for metals. Different kinds of adaptations can be found e.g. for continuum models [Bergstrom, 1983], cell structure models [Goerdeler and Gottstein, 2001], crystal plasticity models [Teodosiu et al., 1993].

The total dislocation density ρ is commonly assumed to consist of two parts: the density of

mobile dislocations ρ_m and the density of immobile dislocations ρ_{im} ,

$$\rho = \rho_m + \rho_{im} \quad (5.6)$$

Under plastic straining dislocation sources in the material produce mobile dislocations that accommodate the imposed plastic strain rate through their motion. The mobile dislocations interact with immobile dislocations or other obstacles during glide and will eventually be trapped as immobile dislocations or annihilated by reacting with dislocations of an opposite sign. Mobile dislocations are considered to carry the plastic strain evolution through their motion. In contrast, immobile dislocations are pinned in the material and obstruct plastic slip. Kinetic equations of the type $\dot{\rho} = \dot{\rho}^+ - \dot{\rho}^-$, with a dislocation source and dislocation drain contributions, will be set up for the net evolution of the mobile and the immobile dislocation densities, constituting a convenient representation of the underlying dislocation processes.

Mobile dislocations are created in the material by e.g. operating Frank-Read sources, with a rate $\dot{\rho}^{cr}$, and by remobilisation of immobile dislocations at a rate $\dot{\rho}^{im \rightarrow m}$. The decrease of the number of mobile dislocations is caused by dislocation interactions and takes place through immobilisation $\dot{\rho}^{m \rightarrow im}$ or annihilation $\dot{\rho}_m^{ann}$. Thus, the net evolution of mobile dislocations can be written as:

$$\dot{\rho}_m = \dot{\rho}^{cr} + \dot{\rho}^{im \rightarrow m} + \dot{\rho}^{flux+} - \dot{\rho}^{flux-} - \dot{\rho}^{m \rightarrow im} - \dot{\rho}_m^{ann} \quad (5.7)$$

where $\dot{\rho}^{flux+}$ and $\dot{\rho}^{flux-}$ are respectively the accumulation and loss associated with the dislocation flux that provides redistribution of dislocations in a nonuniform configuration. Obviously, mobile dislocations that become immobilised trigger an increase of the density of immobile dislocations. Vice versa, the remobilisation of immobile dislocations leads to a loss of immobile dislocations and an increase of mobile dislocations. Immobile dislocations can also annihilate by interaction with mobile dislocations. This leads to:

$$\dot{\rho}_{im} = \dot{\rho}^{m \rightarrow im} - \dot{\rho}^{im \rightarrow m} - \dot{\rho}_{im}^{ann} \quad (5.8)$$

where $\dot{\rho}_{im}^{ann}$ is the total rate of loss of immobile dislocations due to annihilation. The system of equations (5.6)–(5.8) represents the evolution of the local dislocation density. The relation between the dislocation density evolution and the deformation process is adopted from the Orowan equation. The total amount of mobile dislocations is related to the imposed effective plastic strain rate $\dot{\epsilon}$ by:

$$\dot{\gamma} = \dot{\epsilon} M = b v \rho_m \quad (5.9)$$

The effective plastic strain rate $\dot{\epsilon}$ above and further on is a scalar quantity related to the magnitude of the rate of deformation tensor \mathbf{D}^p by $\dot{\epsilon} = \sqrt{\mathbf{D}^p : \mathbf{D}^p}$. In Eq. (5.9) $\dot{\gamma}$ is the plastic shear rate, M is again a mean orientation factor which relates the axial stress to the shear stress and v is the mean dislocation glide velocity. Now, Eqs. (5.6)–(5.8) and (5.9) define the dislocation evolution under deformation. The separate contributions in the evolution equations will be specified in the following sections. First, some justifiable simplifications are introduced here. The Orowan equation (5.9) can be reformatted in a more convenient form by applying it to small time intervals. In Eq. (5.9) v is the average value of the expansion velocity of dislocation loops taken over the total length of mobile dislocations and over their whole average life time Δt before being immobilised or annihilated. When Δt is small with respect

to the characteristic time of variation of $\dot{\varepsilon}$, the dislocation motion is almost stationary and the density of mobile dislocations is practically constant [Teodosiu et al., 1993]:

$$\dot{\rho}_m = 0 \quad (5.10)$$

This assumption is confirmed by experimental observations [Michalak, 1965; Bergstrom, 1983] and commonly used in continuum descriptions. Taking assumption (5.10) into account, the Orowan equation can be approximated as follows [Teodosiu et al., 1993]. According to the evolution equation (5.7), in a time increment Δt a mobile dislocation density $(\dot{\rho}^{cr} + \dot{\rho}^{im \rightarrow m} + \dot{\rho}^{flux+})\Delta t$ is produced. All these dislocations travel a distance L_{eff} and either annihilate or immobilise, in agreement with (5.10). Thus, the amount of mobile dislocations in the material is $(\dot{\rho}^{cr} + \dot{\rho}^{im \rightarrow m} + \dot{\rho}^{flux+})\Delta t$ and the produced plastic strain rate is given [Goerdeler and Gottstein, 2001] by:

$$\dot{\varepsilon} \simeq \frac{\Delta \varepsilon}{\Delta t} = \left(\dot{\rho}^{cr} + \dot{\rho}^{im \rightarrow m} + \dot{\rho}^{flux+} \right) \frac{bL_{eff}}{M} \quad (5.11)$$

The effective slip length L_{eff} is related to the average spacing of obstacles that obstruct the dislocation glide [Goerdeler and Gottstein, 2001]. The dislocation slip is here considered to be obstructed by forest dislocations only and, therefore, L_{eff} is related to the average dislocation spacing [Teodosiu et al., 1993]:

$$L_{eff} = \frac{1}{I\sqrt{\rho}} \quad (5.12)$$

where I is a material parameter. Now, with the use of (5.11) and (5.12), Eqs. (5.6)–(5.8) can be simplified and the evolution of the total dislocation density is expressed by the following system of equations:

$$\begin{aligned} \dot{\rho} &= \dot{\rho}^{cr} + \dot{\rho}^{flux+} - \dot{\rho}^{flux-} - \dot{\rho}^{ann} \\ \dot{\varepsilon} &= (\dot{\rho}^{cr} + \dot{\rho}^{im \rightarrow m} + \dot{\rho}^{flux+}) \frac{b}{MI\sqrt{\rho}} \end{aligned} \quad (5.13)$$

where $\dot{\rho}^{ann} = \dot{\rho}_m^{ann} + \dot{\rho}_{im}^{ann}$ is the total loss of dislocations due to annihilation. In the next section these equations are elaborated for the case of a nonuniform dislocation distribution in the form of a cell structure.

5.3.2 Dislocation evolution in the cell structure

The dislocation cell structure is idealised here as a periodic composite of individually uniform components, i.e. cell walls and cell interiors. Since the mechanical behaviour inside each component is assumed to be uniform, the dislocation distributions inside cells and walls remain uniform. Though less obvious, this is consistent with the proposed evolution equations (5.13) as the fluctuations of the dislocation densities follow the strain gradient distribution, and the cell structure model only considers strain gradients at the wall-cell interfaces. Besides, the uniform distribution of dislocations in the cells and the walls has an obvious qualitative agreement with experimental observations. Thus, the dislocation distribution in the cell structure is represented by the dislocation densities in the cell interior ρ_c and the densities in the cell walls $\rho_{wi}, i = 1, 2, 3$. The equations (5.13) can be applied to each component yielding:

$$\dot{\rho}_c = \dot{\rho}_c^{cr} + \dot{\rho}_c^{flux+} - \dot{\rho}_c^{flux-} - \dot{\rho}_c^{ann} \quad (5.14a)$$

$$\dot{\epsilon}_c = (\dot{\rho}_c^{cr} + \dot{\rho}_c^{im \rightarrow m} + \dot{\rho}_c^{flux+}) \frac{b}{MI\sqrt{\rho_c}} \quad (5.14b)$$

$$\dot{\rho}_{wi} = \dot{\rho}_{wi}^{cr} + \dot{\rho}_{wi}^{flux+} - \dot{\rho}_{wi}^{flux-} - \dot{\rho}_{wi}^{ann} \quad (5.14c)$$

$$\dot{\epsilon}_{wi} = (\dot{\rho}_{wi}^{cr} + \dot{\rho}_{wi}^{im \rightarrow m} + \dot{\rho}_{wi}^{flux+}) \frac{b}{MI\sqrt{\rho_{wi}}} \quad (5.14d)$$

The dislocation fluxes here are the fluxes from cell to wall and from wall to cell: the cells are 'loosing' dislocations to the walls or vice versa. The interactions between the walls are neglected here as before. It seems consistent to assume that the dislocations travelling from cells to walls pile up or get immobilised immediately at the interface. Thus, these dislocations do not glide inside the walls and do not accommodate the plastic deformation of the walls. Consequently, in the last equation in (5.14) this flux contribution can be omitted. The evolution of the dislocation densities (5.14) is then given by:

$$\dot{\rho}_c = \dot{\rho}_c^{cr} + \dot{\rho}_c^{w \rightarrow c} - \dot{\rho}_c^{c \rightarrow w} - \dot{\rho}_c^{ann} \quad (5.15a)$$

$$\dot{\epsilon}_c = (\dot{\rho}_c^{cr} + \dot{\rho}_c^{im \rightarrow m} + \dot{\rho}_c^{w \rightarrow c}) \frac{b}{MI\sqrt{\rho_c}} \quad (5.15b)$$

$$\dot{\rho}_{wi} = \dot{\rho}_{wi}^{cr} + \dot{\rho}_{wi}^{c \rightarrow w} - \dot{\rho}_{wi}^{w \rightarrow c} - \dot{\rho}_{wi}^{ann} \quad (5.15c)$$

$$\dot{\epsilon}_{wi} = (\dot{\rho}_{wi}^{cr} + \dot{\rho}_{wi}^{im \rightarrow m}) \frac{b}{MI\sqrt{\rho_{wi}}} \quad (5.15d)$$

where $\dot{\rho}_{wi}^{c \rightarrow w}$ and $\dot{\rho}_c^{c \rightarrow w}$ are the contributions of the cell-to-wall fluxes to the walls and cell densities, respectively, while $\dot{\rho}_{wi}^{w \rightarrow c}$ and $\dot{\rho}_c^{w \rightarrow c}$ are the contributions of the wall-to-cell fluxes. The system (5.15) can be rearranged in the following more convenient format:

$$\dot{\rho}_c = \frac{MI}{b} \sqrt{\rho_c} \dot{\epsilon}_c - \dot{\rho}_c^{im \rightarrow m} - \dot{\rho}_c^{c \rightarrow w} - \dot{\rho}_c^{ann} \quad (5.16a)$$

$$\dot{\epsilon}_c = (\dot{\rho}_c^{cr} + \dot{\rho}_c^{im \rightarrow m} + \dot{\rho}_c^{w \rightarrow c}) \frac{b}{MI\sqrt{\rho_c}} \quad (5.16b)$$

$$\dot{\rho}_{wi} = \frac{MI}{b} \sqrt{\rho_{wi}} \dot{\epsilon}_{wi} - \dot{\rho}_{wi}^{im \rightarrow m} + \dot{\rho}_{wi}^{c \rightarrow w} - \dot{\rho}_{wi}^{w \rightarrow c} - \dot{\rho}_{wi}^{ann} \quad (5.16c)$$

$$\dot{\epsilon}_{wi} = (\dot{\rho}_{wi}^{cr} + \dot{\rho}_{wi}^{im \rightarrow m}) \frac{b}{MI\sqrt{\rho_{wi}}} \quad (5.16d)$$

The contributions $\dot{\rho}_c^{cr}$, $\dot{\rho}_{wi}^{cr}$ and $\dot{\rho}_c^{ann}$, $\dot{\rho}_{wi}^{ann}$ here are statistical and depend only on the local state of the material, i.e. the local dislocation density and the effective plastic strain rate. The dislocation processes associated with these rates are not influenced by strain gradients or the loading direction, and appear in the same way inside cells and inside walls.

The dislocation fluxes $\dot{\rho}_{wi}^{c \rightarrow w}$, $\dot{\rho}_c^{c \rightarrow w}$ and $\dot{\rho}_{wi}^{w \rightarrow c}$ are non-local contributions related to the inhomogeneity of the material and reflect the evolution of the cell structure. The cell-wall flux consists of dislocations driven towards cell walls by the applied stress. This flux is responsible for the creation and development of the cell structure. Here, it is assumed that this flux is independent from the strain path in the sense that it depends on the accommodated equivalent plastic strain $\int \dot{\epsilon} dt$ only.

On the contrary, the dislocation flux from the walls to the cell interiors comes into play only after a change in the loading direction. Under monotonic loading, the cell-wall flux is initially larger than the wall-cell flux since the dislocation density in the cell interiors is lower and, therefore, slip is promoted easier. During continuous deformation the cell-wall flux piles up dislocations at the cell-wall interfaces. The interface layers are impenetrable for the wall dislocations and therefore the wall-cell flux stagnates as soon as the layers are created. The dislocations in the layers are pushed towards the walls under the influence of the applied stress and do not leave the walls, unless the loading is changed. If the loading is reversed, however, the interface dislocations tend to leave the walls and are assisted in doing so by the new loading direction. This causes the wall-cell flux. Recapitulating, the wall-cell flux appears only after a strain path change, whereas there is no wall-cell flux under monotonic loading.

Finally, remobilisation represented by $\rho^{im \rightarrow m}$ is commonly considered to be a statistical process. However, a change in the loading direction initiates a substantial directional remobilisation. It is expected that this plays a significant role under reversed loading, when immobile dislocations, tangled during initial loading, untangle, get mobile, and contribute to the plastic deformation. In the following, the remobilisation is decomposed into a statistical and a directional component, which are considered separately.

The following subsections deal with each contribution to the dislocation density evolution in detail. First, the statistical processes of annihilation and immobilisation are specified. Then, the formation of the cell structure is described as a result of the dislocation flux from the cell interiors to the walls. Finally, the dislocation mechanisms activated by a stress reversal are formalised through the dislocation flux from the walls to the cell interiors and remobilisation.

5.3.3 Annihilation and statistical remobilisation

The dislocation annihilation and remobilisation considered in this section are statistical local processes. Therefore, they depend only on local material parameters and are the same in cells and walls. The expressions in this section are derived for local densities and are applicable to both phases of the material, thus the subscripts *c* and *wi* are skipped.

Only spontaneous annihilation is considered here. The annihilation by climb is assumed insignificant at moderate deformations and room temperature, as is the case for the present analysis. Spontaneous annihilation occurs when a mobile dislocation comes in the neighbourhood of another dislocation that has an opposite Burgers vector (Fig. 5.1). If the critical distance a^{ann} associated with this dislocation reaction is known, the probability for the event can be computed. During a time increment dt a mobile dislocation travels a distance $v dt$. Thus, annihilation will take place if there is a suitable dislocation within the area $2a^{ann} dt$. The number of mobile dislocations that serve as a possible annihilation partner within this area equals:

$$dp = P(2a^{ann}v dt)\rho \quad (5.17)$$

where P is the fraction of opposite dislocations in the area. If the number of active slip systems in the material is denoted as n , and if the dislocation densities on all slip systems are assumed to be equal, the fraction of dislocations on the same slip system is $\frac{1}{n}$. Assuming that on each slip system positive and negative dislocations are equally present, the fraction of dislocations opposite to a given one satisfies $P = \frac{1}{2n}$.

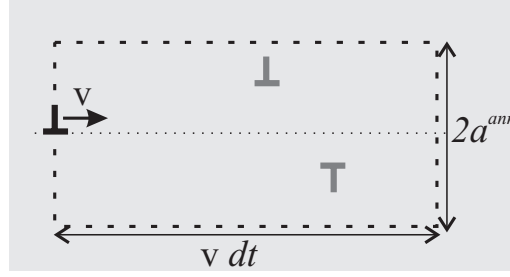


Figure 5.1 — Geometrical setup for calculating the annihilation probability (after Roters et al. [2000]).

Taking into account that, with each annihilation event, two dislocations are eliminated, the reduction of the total dislocation density due to spontaneous annihilation can be calculated as [Roters et al., 2000]:

$$\dot{\rho}^{ann} = 2\dot{\rho}\rho_m = 2P(2a^{ann}v)\rho\rho_m \quad (5.18)$$

Or, with the use of the Orowan equation (5.9) and $P = \frac{1}{2n}$, the well-known expression for the dislocation annihilation rate can be derived:

$$\dot{\rho}^{ann} = \frac{M}{b} \frac{2a^{ann}}{n} \rho \dot{\epsilon} \quad (5.19)$$

Next, the attention is focused on remobilisation, a mechanism by which the immobile dislocations become mobile again. Remobilisation is commonly considered to be a statistical process and it can be related to the density of immobile dislocations ρ_{im} and the strain rate, according to [Bergstrom, 1983]:

$$\dot{\rho}^{im \rightarrow m, s} = \theta \rho \dot{\epsilon} \quad (5.20)$$

where $\dot{\rho}^{im \rightarrow m, s}$ defines the statistical part of the remobilisation $\dot{\rho}^{im \rightarrow m}$ and θ is a material parameter. The contributions of the annihilation and statistical remobilisation can be combined, leading to:

$$\dot{\rho}^{ann} + \dot{\rho}^{im \rightarrow m, s} = \frac{M}{b} R \rho \dot{\epsilon} \quad \text{with} \quad R = \frac{2a^{ann}}{n} + \theta \frac{b}{M} \quad (5.21)$$

With the use of (5.21), the dislocation density evolution (5.16) can be reduced to the widely-used equation for homogeneous configurations under monotonic deformations ($\dot{\rho}_i^{flux} = 0$, $\dot{\rho}_i^{im \rightarrow m} = \dot{\rho}_i^{im \rightarrow m, s}$):

$$\dot{\rho} = \frac{M}{b} (I\sqrt{\rho} - R\rho) \dot{\epsilon} \quad (5.22)$$

5.3.4 Dislocation flux $\rho^{c \rightarrow w}$

The cell-wall flux is responsible for the creation and the development of the cell structure. In the present research, attention is restricted to cells with a fixed geometry during the entire deformation process. Thus, the contribution $\dot{\rho}^{c \rightarrow w}$ essentially describes the evolution of the difference between the dislocation density in cells and walls.

The cell-wall flux consists of dislocations that glide towards cell walls through the applied stress. The sign and crystallographic nature of these dislocations is defined by the relation between the loading and cell orientation. In the present approach the signs of the dislocations have been disregarded¹ and the cell-wall flux is assumed to be equally distributed between walls, i.e. $\dot{\rho}_{w1}^{c \rightarrow w} = \dot{\rho}_{w2}^{c \rightarrow w} = \dot{\rho}_{w3}^{c \rightarrow w}$. As a result, the amount of dislocations encountering a cell wall does not depend on the loading direction. The cell-wall flux can be related to the effective slip length and the dislocation density in the cell interior (see Goerdeler and Gottstein [2001]), independent of the current loading or deformation history.

To quantify the cell-wall flux, it is assumed that a fraction C of mobile dislocations in the cell interior leave the interior to join the cell walls. With the use of (5.11), this assumption can be formulated as follows:

$$\dot{\rho}_c^{c \rightarrow w} = C \frac{M}{b} I \sqrt{\rho_c} \dot{\epsilon}_c \quad (5.23)$$

Assuming that the dislocations leaving the cell interior are equally distributed between all walls, provides all walls with equal flux contributions:

$$\dot{\rho}_{wi}^{c \rightarrow w} = \frac{f_c}{f_{wi}} \dot{\rho}_c^{c \rightarrow w} \quad (5.24)$$

where f_c and f_{wi} are volume fractions of the cell interior and the walls respectively. This relation ensures that the total amount of dislocations remains preserved.

Under *monotonic* deformation, the directional remobilisation and the wall-cell flux are absent. Thus, the dislocation density evolution equations for the material with a cell structure (5.16) reduce to:

$$\begin{aligned} \dot{\rho}_c &= \frac{M}{b} (I \sqrt{\rho_c} - R \rho_c) \dot{\epsilon}_c - C \frac{M}{b} I \sqrt{\rho_c} \dot{\epsilon}_c \\ \dot{\rho}_{wi} &= \frac{M}{b} (I \sqrt{\rho_{wi}} - R \rho_{wi}) \dot{\epsilon}_{wi} + \frac{f_c}{f_w} C \frac{M}{b} I \sqrt{\rho_c} \dot{\epsilon}_c \end{aligned} \quad (5.25)$$

This evolution is defined by statistical dislocation processes and reflects the increase of the total dislocation density and the formation of the cell structure with increasing effective plastic strain. In the case of nonuniform loading, the dislocation evolution has a nonzero contribution of the remobilisation and the wall-cell dislocation flux. These processes are discussed next.

5.3.5 Dislocation structure evolution after a strain path change

The dislocation flux and the directional remobilisation in (5.16) are processes that are governed by the deformation history applied to the material. Under monotonic loading, dislocations gliding through the material are obstructed by the dense cell walls. The obstructed dislocations pile up at the interfaces, preventing any wall-cell flux. However, after a strain path change, the loading in a different direction may constitute a driving force on the dislocations towards the cell interiors and the interface dislocations may tend to move towards the sparse cells. It is assumed here that the motion of the interface dislocations from the walls to the cells is the main mechanism for the wall-cell flux.

¹Signs are disregarded for the statistical dislocations that are being considered here. The polarity of the dislocations enters the model on the larger scale level through the polarity of the GNDs.

Similarly, monotonic deformation stagnates the evolution of mobile dislocations, either by immobilising or annihilating them. As long as the loading direction remains unchanged, the directionally immobilised dislocations do not contribute to slip processes. After a strain path change, the new loading might alter the immobilising forces acting on these dislocations. The dislocation locks and dipoles, formed during the previous loading, may partially untangle through the subsequent loading and, eventually, those dislocations become mobile again. This mechanism is called directional remobilisation, in contrast to statistical remobilisation which is independent on deformation history.

The rates in both processes, the wall-cell flux and the directional remobilisation, depend on the directional changes in the strain path. A small variation does not sufficiently alter the local forces on the dislocations to initiate these processes. On the other hand, reversed loading is expected to activate a maximum of the wall-cell dislocation flux and remobilisation. The plastic deformation caused by reversed loading is mostly accommodated by the same dislocations as those acting during the previous loading, meaning that all dislocations created by the initial loading may contribute during the reversed loading as well. The interface dislocations can slip backwards from the walls with a maximum rate and pile-ups of immobile dislocations are subjected to a separation force. The resulting high values of $\dot{\rho}_i^{w \rightarrow c}$ and $\dot{\rho}^{im \rightarrow m}$ under reversed loading decrease the dislocation density in the material and, consequently, a reduction of the yield stress σ^y will result, see Eq. (5.5). Clearly, the wall-cell dislocation flux and the dislocation remobilisation typically lead to a Bauschinger effect.

The wall-cell flux and the dislocation remobilisation processes will be quantified here by considering the total dislocation balance within the cell structure, which is expressed by (5.16). Incorporating the results of the previous sections gives:

$$\begin{aligned}\dot{\rho}_c &= \frac{M}{b}(I\sqrt{\rho_c} - R\rho_c - CI\sqrt{\rho_c})\dot{\epsilon}_c - \dot{\rho}_c^{im \rightarrow m} \\ \dot{\epsilon}_c &= (\dot{\rho}_c^{cr} + \dot{\rho}_c^{im \rightarrow m} + \dot{\rho}_c^{w \rightarrow c}) \frac{b}{MI\sqrt{\rho_c}} \\ \dot{\rho}_{wi} &= \frac{M}{b}(I\sqrt{\rho_{wi}} - R\rho_{wi} + \frac{f_c}{f_{wi}}CI\sqrt{\rho_c})\dot{\epsilon}_{wi} - \dot{\rho}_{wi}^{w \rightarrow c} - \dot{\rho}_{wi}^{im \rightarrow m} \\ \dot{\epsilon}_{wi} &= (\dot{\rho}_{wi}^{cr} + \dot{\rho}_{wi}^{im \rightarrow m}) \frac{b}{MI\sqrt{\rho_{wi}}}\end{aligned}\tag{5.26}$$

System (5.26) consists of 8 ($2+2 \times 3$) equations and the unknowns are $\dot{\rho}_c$, $\dot{\rho}_{wi}$, $\dot{\rho}_c^{im \rightarrow m}$, $\dot{\rho}_{wi}^{im \rightarrow m}$, $\dot{\rho}_{wi}^{w \rightarrow c}$, $\dot{\rho}_c^{cr}$ and $\dot{\rho}_{wi}^{cr}$, where $i = 1, 2, 3$. The system is yet underdetermined and additional assumptions are required to complete the description of the dislocation density evolution. To this purpose, the plastic slip in the cell interior is first considered. The amount of plastic slip rate is given by $\dot{\epsilon}_c$, resulting from the solution of the cell structure model. The second equation in (5.26) implies that the plastic slip rate in the cell interiors is accommodated by the dislocations which are either created, remobilised or supplied from the walls:

$$\dot{\epsilon}_c = \dot{\epsilon}_c(\dot{\rho}_c^{cr}, \dot{\rho}_c^{im \rightarrow m}, \dot{\rho}_c^{w \rightarrow c})\tag{5.27}$$

Even though the plastic deformation is considered to be uniform inside the cell interiors, the sources of mobile dislocations can be different at different locations. This apparent inconsistency is only used to qualitatively assess the contribution of the terms present in (5.26). It seems reasonable to assume that in the vicinity of the walls a lot of wall dislocations enter the cell, as a part of the wall-cell flux. These dislocations are the first candidates to accommodate

the plastic slip and no additional contribution is needed by creation or remobilisation. On the other hand, at a distance from the cell-wall boundaries, the wall-cell flux will be less active and dislocations should be nucleated or remobilised to provide the slip. Therefore, equation (5.27) will be split into two parts: one representative for the areas close to the cell-wall boundaries and one representative for the core of the cells:

$$\dot{\epsilon}_c = \dot{\epsilon}_c(\dot{\rho}_c^{cr}, \dot{\rho}_{wi}^{w \rightarrow c}) \quad \text{in the vicinities of the walls } i \quad (5.28a)$$

$$\dot{\epsilon}_c = \dot{\epsilon}_c(\dot{\rho}_c^{cr}, \dot{\rho}_c^{im \rightarrow m}) \quad \text{in cell cores} \quad (5.28b)$$

Furthermore, when a wall-cell flux is present, many mobile dislocations enter the cell interiors and they are readily available to accommodate plastic deformation. Therefore, it is assumed that, if there are enough dislocations in the wall-cell flux to produce the slip associated with $\dot{\epsilon}_c$, no new dislocations will be created. If there is no wall-cell flux, new dislocations have to be created to carry the ongoing plastic deformation. This assumption allows a reduction of equation (5.28a) to the following form:

$$\dot{\epsilon}_c = \begin{cases} \dot{\epsilon}_c(\dot{\rho}_i^{w \rightarrow c}) = \frac{b}{MI\sqrt{\rho_c}} \dot{\rho}_{wi}^{w \rightarrow c} & \text{if } \dot{\rho}_{wi}^{w \rightarrow c} > 0 \\ \dot{\epsilon}_c(\dot{\rho}_c^{cr}) = \frac{b}{MI\sqrt{\rho_c}} \dot{\rho}_c^{cr} & \text{if } \dot{\rho}_i^{w \rightarrow c} = 0 \end{cases} \quad (5.29)$$

The same reasoning can be applied to the remobilisation of dislocations, affecting equation (5.28b). It is assumed that, if remobilisation is possible, this prevails over creation, leading to:

$$\dot{\epsilon}_c = \begin{cases} \dot{\epsilon}_c(\dot{\rho}_c^{im \rightarrow m}) = \frac{b}{MI\sqrt{\rho_c}} \dot{\rho}_c^{im \rightarrow m} & \text{if } \dot{\rho}_c^{im \rightarrow m} > 0 \\ \dot{\epsilon}_c(\dot{\rho}_c^{cr}) = \frac{b}{MI\sqrt{\rho_c}} \dot{\rho}_c^{cr} & \text{if } \dot{\rho}_c^{im \rightarrow m} = 0 \end{cases} \quad (5.30)$$

Repeating this for the walls, the last equation in (5.26) can be rewritten as:

$$\dot{\epsilon}_{wi} = \begin{cases} \dot{\epsilon}_{wi}(\dot{\rho}_{wi}^{im \rightarrow m}) = \frac{b}{MI\sqrt{\rho_{wi}}} \dot{\rho}_{wi}^{im \rightarrow m} & \text{if } \dot{\rho}_{wi}^{im \rightarrow m} > 0 \\ \dot{\epsilon}_{wi}(\dot{\rho}_{wi}^{cr}) = \frac{b}{MI\sqrt{\rho_{wi}}} \dot{\rho}_{wi}^{cr} & \text{if } \dot{\rho}_{wi}^{im \rightarrow m} = 0 \end{cases} \quad (5.31)$$

for $i = 1, 2, 3$. The assumptions resulting in the Eqs. (5.29)–(5.31) allow the calculation of $\dot{\rho}_{wi}^{w \rightarrow c}$, $\dot{\rho}_c^{im \rightarrow m}$, and $\dot{\rho}_{wi}^{im \rightarrow m}$ as functions of the corresponding local strain rates and dislocation densities. Now the dislocation evolution equations (5.26) and the local Orowan equations in the form of (5.29)–(5.31) constitute a complete system defining the evolution of the dislocation densities in the cell structure. To enable the calculations, the criteria used in (5.29)–(5.31) should be further specified to determine when the wall-cell flux and the remobilisation rates really contribute.

Wall-cell flux $\rho^{w \rightarrow c}$

The wall-cell flux was defined above as the flux created by the reverse motion of dislocations that were collected at the interfaces during the initial loading. After a strain path change, the interface dislocations will tend to move if their crystallographic configuration allows them to move under the current loading. Additionally, the dislocation motion should be in the direction of the cells. Thus, the wall-cell flux is governed by the type of dislocations collected at the interfaces by the deformation history and their ability to move to the cell interior under the current loading.

A straightforward way to reveal what type of dislocations have been stored at the cell-wall interfaces is to keep track of the dislocations appearing there during monotonic loading. That strategy would involve the introduction of additional history parameters and phenomenological evolution equations (e.g. see Peeters [2002]). In the present approach, the history information available in the cell structure model will be used instead. The dislocation density tensor has been introduced in the cell structure model by Viatkina et al. [2005b] and is related to the amount of dislocations in the cell-wall interfaces. This tensor also provides information on the type of dislocations that might help to extract information on the mobility of the dislocations under the current loading. However, it should be noted that the dislocation density tensor indicates an average quantity of GNDs only since it reflects the surplus of one type of dislocations over another, not the absolute densities of the dislocations. Thus, the dislocation density tensor can be used only as an indicator of the dislocations present in the interface. It is assumed here that dislocations of a specific type are present in the cell-wall interface if the associated GND density is non-vanishing. The dislocation density tensor is used to retrieve the information on the interface GNDs.

The wall-cell flux is next quantified by considering the local dislocation density tensor and its relation to the corresponding cell wall. This approach is applied to all cell walls and therefore the subscript *wi* is skipped for the clarity of the formulas. The dislocation density tensor can be determined by summation of the contributions of all dislocations present in a unit volume of the material:

$$\mathbf{\Lambda} = \sum_{\zeta} \rho^{\zeta} \vec{b}^{\zeta} \vec{t}^{\zeta} \quad (5.32)$$

with \vec{b} the Burgers vectors and \vec{t} the dislocation tangent vectors. The summation is performed over all types ζ of dislocations. The crystallographic decomposition (5.32) of Nye's tensor in contributions of physically possible dislocations is not unique, calling for additional crystallographic information that is not available in the cell structure continuum model. To solve this problem, a continuum crystallographic approach is adopted, in which dislocations can form on any geometrical plane (as a fictitious slip plane). For the purpose of establishing the wall-cell flux, this assumption appears to be reasonable for materials with a high crystallographic symmetry, such as FCC metals. Exploiting this assumption, the decomposition is rewritten as:

$$\mathbf{\Lambda} = \rho_1 \vec{b}_1 \vec{T} + \rho_2 \vec{b}_2 \vec{Q} + \rho_3 \vec{b}_3 \vec{N} \quad (5.33)$$

where \vec{N} is the unit normal to the dislocation wall of interest, while the unit vectors \vec{T} and \vec{Q} form an orthogonal basis in combination with \vec{N} . In the average continuum sense, all interface GNDs incorporated in $\mathbf{\Lambda}$ can be represented by 'continuum' dislocations with densities ρ_1 , ρ_2 and ρ_3 , Burgers vectors \vec{b}_1 , \vec{b}_2 and \vec{b}_3 and the corresponding dislocations tangents along \vec{T} , \vec{Q} and \vec{N} . Since dislocations always glide perpendicular to their tangents, the dislocations with tangents along the normal \vec{N} glide in the plane of the wall. Therefore, these dislocations do not contribute to the wall-cell flux, which represents dislocation slip away from the wall. Only dislocations with a dislocation tangent $\vec{t}_1 = \vec{T}$ and a Burgers vector \vec{b}_1 in the direction of $\mathbf{\Lambda} \cdot \vec{T}$, and dislocations with a tangent $\vec{t}_2 = \vec{Q}$ and a Burgers vector \vec{b}_2 in the direction of $\mathbf{\Lambda} \cdot \vec{Q}$ can glide away from the wall and contribute to the wall-cell flux.

If a dislocation is defined by a dislocation tangent \vec{t} and a Burgers vector \vec{b} , it can glide only in a plane containing \vec{t} and \vec{b} , i.e. in a plane with normal $\vec{n} = \vec{b} \times \vec{t}$. Furthermore, the dislocation

glide is always perpendicular to the dislocation tangent \vec{t} , i.e. the slip direction is given by $\vec{m} = \vec{t} \times \vec{n}$. According to (5.33), the wall-cell flux is created by two types of dislocations defined by $\{\vec{T}, \vec{b}_1\}$ and $\{\vec{Q}, \vec{b}_2\}$. Consequently, the 'continuum' flux stems from the dislocation slip on two fictitious slip systems $\{\vec{n}_1, \vec{m}_1\}$ and $\{\vec{n}_2, \vec{m}_2\}$. It is emphasized that this approximation assumes that plastic slip can be realised on any geometrical plane and in any direction. The resulting directional characteristics of the wall-cell flux are determined through the dislocation tensor Λ as:

$$\left\{ \begin{aligned} \vec{b}_1 &= \frac{\Lambda \cdot \vec{T}}{\|\Lambda \cdot \vec{T}\|} b, & \vec{n}_1 &= \vec{b}_1 \times \vec{T}, & \vec{m}_1 &= \vec{T} \times \vec{n}_1 \end{aligned} \right\} \quad (5.34)$$

$$\left\{ \begin{aligned} \vec{b}_2 &= \frac{\Lambda \cdot \vec{Q}}{\|\Lambda \cdot \vec{Q}\|} b, & \vec{n}_2 &= \vec{b}_2 \times \vec{Q}, & \vec{m}_2 &= \vec{Q} \times \vec{n}_2 \end{aligned} \right\}$$

Summarising, if the density of the interface dislocations is given by Λ and the orientation of the interface is known through the normal \vec{N} , then the interface dislocations are capable of creating a wall-cell flux by glide on the fictitious slip systems $\{\vec{n}_1, \vec{m}_1\}$ and $\{\vec{n}_2, \vec{m}_2\}$, defined above. Now the amount of dislocations that would actually glide on these slip systems has to be determined. Not all dislocations collected at the interface tend to slip from the wall to the cell interior under reversed loading. If all of these dislocations would move to the cell interior an excessively high plastic slip would occur. This is impossible since the plastic deformation rate is limited and given by the solution of the cell structure model. As already emphasized, a non-vanishing wall-cell flux is associated with a plastic strain rate given by the first equation in (5.29). Since the 'continuum' flux consist of slip contributions from the slip systems $\{\vec{n}_1, \vec{m}_1\}$ and $\{\vec{n}_2, \vec{m}_2\}$, the first equation in (5.29) can be specified as:

$$|\dot{\gamma}_1| = |\mathbf{D}_c^p : \vec{n}_1 \vec{m}_1| = \frac{b}{I\sqrt{\rho_c}} \dot{\rho}_1^{w \rightarrow c} \quad (5.35)$$

$$|\dot{\gamma}_2| = |\mathbf{D}_c^p : \vec{n}_2 \vec{m}_2| = \frac{b}{I\sqrt{\rho_c}} \dot{\rho}_2^{w \rightarrow c}$$

where \mathbf{D}_c^p is the plastic deformation rate tensor in the cell interior. The rates $\dot{\rho}_1^{w \rightarrow c}$ and $\dot{\rho}_2^{w \rightarrow c}$ are the contributions to the wall-cell flux by the corresponding fictitious slip systems and the total wall-cell flux is the sum of them:

$$\dot{\rho}^{w \rightarrow c} = \dot{\rho}_1^{w \rightarrow c} + \dot{\rho}_2^{w \rightarrow c} \quad (5.36)$$

Equation (5.35) indicates that the wall-cell flux takes place only if the corresponding slip systems are active, i.e. if $\dot{\gamma}_1 \neq 0$ and/or if $\dot{\gamma}_2 \neq 0$. However, the glide on these slip systems may occur in two opposite directions: from cell to wall and from wall to cell. Obviously, only the second case contributes to the wall-cell flux. The direction of the dislocation glide is defined by the Orowan relation $\dot{\gamma} \propto \vec{v} \cdot \vec{b}$, dependent on the orientations of the Burgers vector \vec{b} and the dislocation velocity \vec{v} . The dislocation velocity is defined here through the slip direction $\dot{\gamma} \vec{m}$. If the orientation of \vec{m} is fixed with respect to the cell wall, as shown in Fig. 5.2, then the direction of the dislocation glide is defined by the Burgers vector and the sign of $\dot{\gamma}$. Fig. 5.2 indicates the directional character of the flux for the example with edge dislocations. Here, for $\dot{\gamma} > 0$, the wall-cell flux is realised by negative dislocations, $\vec{m} \cdot \vec{b} < 0$, gliding in the $-\vec{m}$ direction. Thus, the dislocation flux from the wall to the cell interior is activated if the following relation between the current deformation and the interface dislocations is satisfied:

$$\dot{\gamma} \vec{m} \cdot \vec{b} < 0 \quad (5.37)$$

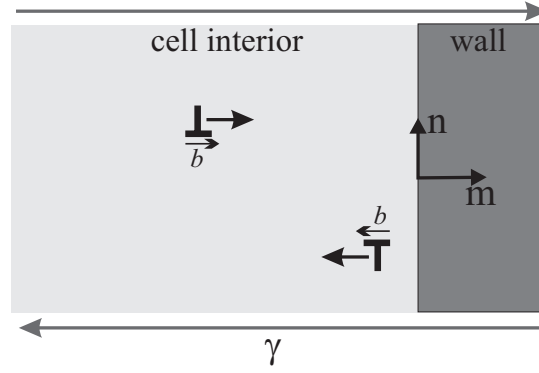


Figure 5.2 — Direction of the wall-to-cell flux of dislocations: Dislocations with $\vec{b} \cdot \vec{m} < 0$ move from the wall to the cell interior, while dislocations with $\vec{b} \cdot \vec{m} > 0$ move towards the wall.

Combining (5.35) and (5.37), the rate of the wall-cell flux is defined by the current loading, via \mathbf{D}_c^p . Repeating this reasoning for each of the cell walls results in the following expressions for $\dot{\rho}_{wi}^{w \rightarrow c}$:

$$\begin{aligned} \dot{\rho}_{wi,1}^{w \rightarrow c} &= |\mathbf{D}_c^p : \vec{n}_1^i \vec{m}_1^i| \frac{I\sqrt{\rho_c}}{b} \quad \text{if } \mathbf{D}_c^p : \vec{n}_1^i \vec{b}_1^i < 0 \\ \dot{\rho}_{wi,2}^{w \rightarrow c} &= |\mathbf{D}_c^p : \vec{n}_2^i \vec{m}_2^i| \frac{I\sqrt{\rho_c}}{b} \quad \text{if } \mathbf{D}_c^p : \vec{n}_2^i \vec{b}_2^i < 0 \\ \dot{\rho}_{wi}^{w \rightarrow c} &= \dot{\rho}_{wi,1}^{w \rightarrow c} + \dot{\rho}_{wi,2}^{w \rightarrow c} \end{aligned} \quad (5.38)$$

The direction properties of each wall-cell flux are defined through (5.34) by the local dislocation tensor Λ_{wi} determined on the corresponding interface. The equations (5.38) relate the dislocation rates $\dot{\rho}_{wi}^{w \rightarrow c}$ to the deformation rate in the cell interior, in conformity with the first equation in (5.29).

Remobilisation

Under monotonic loading, dislocations may get trapped creating an immobile dislocation structures, such as dipoles and locks. Since the immobile dislocations cannot participate in the plastic slip process, new dislocations have to be nucleated. In this way, the total dislocation density keeps increasing under deformation. However, if the loading is reversed, a decrease of the dislocation density is observed in experiments (Pedersen et al. [1981]) during initial reversed plastic deformation. It is believed that remobilisation of immobile dislocations contributes to this phenomenon. The immobile dislocation structures tend to become 'unstable' under reversed loading and the contributing dislocations become mobile again. The remobilised dislocations promote plastic slip and will annihilate or immobilise again. Thus, the initial plastic slip under reversed loading can be realised by remobilised dislocations and no substantial supplementary dislocation creation is needed. Consequently, the creation of new dislocations will be ignored, whereas the loss due to annihilation leads to a drop in the total dislocation density.

Since the dislocation remobilisation is associated with reversed loading, the rate of the remobilisation will be related to the amount of deformation that is reversed after a strain path

change:

$$\dot{\epsilon}_i^{im \rightarrow m} = \mathbf{D}_i^p : \frac{\mathbf{D}_{i,old}^p}{\|\mathbf{D}_{i,old}^p\|} \quad (5.39)$$

where $\mathbf{D}_{i,old}^p$ and \mathbf{D}_i^p are the plastic deformation rate tensors before and after the strain path change, respectively. Here the subscript i stands for c or wi . Remobilisation is assumed to take place if the deformation is reversed, i.e. if $\dot{\epsilon}_i^{im \rightarrow m} < 0$ and, following (5.30) and (5.31), all reversed plastic deformation is carried by the remobilised dislocations:

$$\dot{\rho}_i^{im \rightarrow m} = \begin{cases} \frac{MI\sqrt{\rho_i}}{b} f(\epsilon) |\dot{\epsilon}_i^{im \rightarrow m}| & \text{if } \dot{\epsilon}_i^{im \rightarrow m} < 0 \\ 0 & \text{if } \dot{\epsilon}_i^{im \rightarrow m} \geq 0 \end{cases} \quad (5.40)$$

The function $f(\epsilon)$ is added here to restrict the duration of the remobilisation process. Experimental observations, e.g. by Pedersen et al. [1981], reveal that the total dislocation density starts growing again shortly after the loading change. Apparently, remobilisation, that decreases the total density, does not last long after a strain path change. To incorporate this, the function $f(\epsilon)$ should be equal to 1 at the strain change instant and decrease to zero as the deformation proceeds in the new direction. The exhaustion of the remobilisation process evidently requires more research in order to define an adequate form of $f(\epsilon)$. For now, the following function is proposed based on phenomenological considerations:

$$f(\epsilon) = \left(\frac{\rho_i^{old}}{\rho_i} \right)^{K\epsilon'} \quad (5.41)$$

$$\dot{\rho}_i^{old} = -\dot{\rho}_i^{im \rightarrow m} \quad \rho_i^{old}|_{\epsilon'=0} = \rho_i$$

where ϵ' is the plastic strain accommodated *after* a strain path change, K is a fitting parameter and ρ_i^{old} is the density of the dislocations collected in the material during prestrain. The function, thus the remobilisation rate, decreases as the deformation progresses in the new direction due to an increase of ϵ' and a decrease of ρ_i^{old} . The dislocations corresponding to ρ_i^{old} were immobilised during prestraining and are remobilised after the strain path change. It is assumed here that ρ_i^{old} is the source of the remobilisation and, thus, remobilisation rate decreases if the fraction of these dislocations decreases.

Recapitulating the model description, the total dislocation density evolution in the material with a cell structure under complex deformation is described by:

$$\dot{\rho}_c = \frac{M}{b} (I\sqrt{\rho_c} - R\rho_c - CI\sqrt{\rho_c}) \dot{\epsilon}_c - \dot{\rho}_c^{im \rightarrow m} \quad (5.42a)$$

$$\dot{\rho}_{wi} = \frac{M}{b} \left(I\sqrt{\rho_{wi}} - R\rho_{wi} + \frac{f_c}{f_{wi}} CI\sqrt{\rho_c} \right) \dot{\epsilon}_{wi} - \dot{\rho}_{wi}^{w \rightarrow c} - \dot{\rho}_{wi}^{im \rightarrow m}$$

$$\dot{\rho}_c^{im \rightarrow m} = \begin{cases} \frac{MI\sqrt{\rho_c}}{b} f_c(\epsilon_c) \left| \mathbf{D}_c^p : \frac{\mathbf{D}_{c,old}^p}{\|\mathbf{D}_{c,old}^p\|} \right| & \text{if } \mathbf{D}_c^p : \frac{\mathbf{D}_{c,old}^p}{\|\mathbf{D}_{c,old}^p\|} < 0 \\ 0 & \text{otherwise} \end{cases} \quad (5.42b)$$

$$\dot{\rho}_{wi}^{im \rightarrow m} = \begin{cases} \frac{MI\sqrt{\rho_{wi}}}{b} f_{wi}(\epsilon_{wi}) \left| \mathbf{D}_{wi}^p : \frac{\mathbf{D}_{wi,old}^p}{\|\mathbf{D}_{wi,old}^p\|} \right| & \text{if } \mathbf{D}_{wi}^p : \frac{\mathbf{D}_{wi,old}^p}{\|\mathbf{D}_{wi,old}^p\|} < 0 \\ 0 & \text{otherwise} \end{cases}$$

$$\begin{aligned}
\dot{\rho}_{wi}^{w \rightarrow c} &= \dot{\rho}_{wi,1}^{w \rightarrow c} + \dot{\rho}_{wi,2}^{w \rightarrow c} \\
\dot{\rho}_{wi,1}^{w \rightarrow c} &= \begin{cases} |\mathbf{D}_c^p : \vec{n}_1^i \vec{m}_1^i| \frac{I\sqrt{\rho_c}}{b} & \text{if } \mathbf{D}_c^p : \vec{n}_1^i \vec{b}_1^i < 0 \\ 0 & \text{otherwise} \end{cases} \\
\dot{\rho}_{wi,2}^{w \rightarrow c} &= \begin{cases} |\mathbf{D}_c^p : \vec{n}_2^i \vec{m}_2^i| \frac{I\sqrt{\rho_c}}{b} & \text{if } \mathbf{D}_c^p : \vec{n}_2^i \vec{b}_2^i < 0 \\ 0 & \text{otherwise} \end{cases}
\end{aligned} \tag{5.42c}$$

where I , R and C are the relevant material parameters; \mathbf{D}_i^p and $\mathbf{D}_{i,old}^p$ are the local plastic deformation rate tensors – current and before a strain path change respectively; \vec{n}^i , \vec{b}^i and \vec{m}^i are defined by the current dislocation density tensor Λ . Besides, since undeformed material typically has a homogeneous distribution of dislocations, the dislocation densities are initially the same (in the average sense) throughout the material: $\rho_c|_{\varepsilon=0} = \rho_{wi}|_{\varepsilon=0} = \rho^0$.

5.4 Numerical analysis

5.4.1 Parameter identification

In order to perform numerical simulations describing the deformation behaviour of polycrystal copper, the model parameters have been identified. The values used for the elasticity parameters, the shear modulus G and Poisson's ratio ν , and the magnitude of the Burgers vector b , all known for copper, are listed in Table 5.1. The values for the mean orientation factor M and the coefficient α are chosen following the recommendations of Mughrabi [1987] for a continuum cell structure model. A value $M = 2.5$ corresponds to orientations providing symmetrical multiple slip, whereas a value of 0.4 for α typically reflects multiple slip, involving the mutual intersection of dislocations of different slip systems [Mughrabi, 1987]. The mentioned values are adopted for symmetric deformation modes as analysed in this paper.

Next, the geometry of the cell structure is further specified. The cells are assumed to be cubic, $D \equiv D_1 = D_2 = D_3$, with equally thick cell walls, i.e. $w \equiv w_1 = w_2 = w_3$. Furthermore the geometry of the cells is fixed during deformation, whereas the dislocation densities will evolve of course. The values adopted for the cell size D and the wall volume fraction $f = \frac{w}{D}$ (see Table 5.1) are typical for cell structures observed at small to moderate deformations ([Christodoulou et al., 1986]).

Next, the evolution of the statistically stored dislocations under *monotonic* deformation is defined by (5.25), which is a reduced version of (5.42). Thus, the material parameters necessary to describe the evolution of the dislocation densities are I , R , C and ρ^0 . Since only very few quantitative experimental data on the dislocation evolution in cell structures is available, these parameters are identified by fitting the macroscopic behaviour under monotonic deformation. This is justified, since the parameters ρ^0 , I and R define the evolution of the average dislocation density, and can therefore be derived from the average macroscopic behaviour. The initial macroscopic yield stress is related to ρ^0 , the hardening at small deformations is predominately influenced by I , and the hardening at large deformations by R . The parameter C is associated with the material inhomogeneity and should be identified

Table 5.1 — Parameters for copper.

Parameter	Symbol	Unit	Value
Shear modulus	G	[GPa]	41.7
Poisson's ratio	ν	[-]	0.34
Length of the Burgers vector	b	[nm]	0.257
Coefficient	α	[-]	0.4
Mean orientation factor	M	[-]	2.5
Cell size	D	[μm]	2.5
Wall volume fraction	f	[-]	0.2

Table 5.2 — Dislocation evolution parameters identified for copper.

Parameter	Symbol	Unit	Value
Initial dislocation density	ρ^0	[m^{-2}]	$15 \cdot 10^{13}$
Creation rate parameter	I	[-]	0.105
Annihilation rate parameter	R	[nm]	1.6
Dislocation flux constant	C	[-]	0.8
Coefficient	K	[-]	200

using data on, for instance, the dislocation density difference between cell and walls, the stress inhomogeneity, or the level of the internal stress. The inhomogeneity parameter C also affects the macroscopic hardening behaviour, i.e. the stress will be lower in material with a higher inhomogeneity.

The dislocation density evolution after a stress reversal, partial or complete, is defined by the wall-cell flux and remobilisation in cells and walls. The wall-cell flux is completely defined by the current state of the material (Λ , ρ_c , I), see Eq. (5.38), and it is therefore not necessary to introduce additional parameters. The remobilisation rate is controlled by the function $f(\varepsilon_p)$, which determines its duration after it has been activated. The adopted functions $f_c(\varepsilon_p)$ and $f_w(\varepsilon_p)$ provide the best fit to results on the experimentally observed Bauschinger effect after a complete stress reversal.

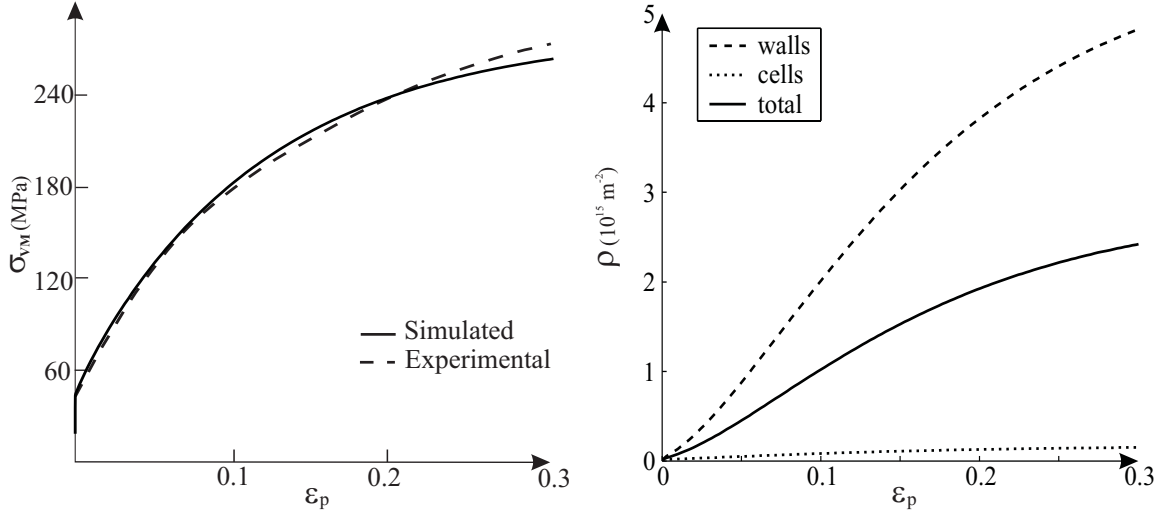
The experimental results reported by Christodoulou et al. [1986] for tension-compression tests on polycrystalline copper have been used here for parameter identification and model verification. To do so, the uniaxial tension test was simulated with a strain rate $\dot{\varepsilon}_{11} = 5 \cdot 10^{-4} \text{ s}^{-1}$. Similarly, compression is simulated by applying a negative strain rate. No stresses are assumed to occur in other directions:

$$\tilde{F}_{11} = 1 + \dot{\varepsilon}_{11} t; \quad \tilde{\sigma}_{ij} = 0, \quad \text{if } ij \neq 11 \quad (5.43)$$

The orientation of the cell structure was fixed, with the [111] direction of cells coinciding with the initial tensile axis. This orientation corresponds to the formation of a cell structure with the walls directed along the macroscopic planes of maximum shear. This tendency has been confirmed by experimental observations (Zhu and Sellars [2001]).

Fig. 5.3 shows the fit obtained for the monotonic tension experiment, with the parameter values given in Tables 5.1 and 5.2. The parameter C is chosen such that at large deformations the internal stress in the walls reaches the same level as the applied stress. This is in correspondence with measurements of the internal stresses in cell structures [Straub et al.,

1996; Borbely et al., 1993; Ungar et al., 1984]. Fig. 5.3 also shows the calculated evolution of the inhomogeneity in the dislocation density. The dislocation density in the walls reaches values that are 20 times higher than the dislocation density in the cells. This obtained inhomogeneity is of the same order of magnitude as observed experimentally, e.g. by Ungar et al. [1984]. The total dislocation density shown in Fig. 5.3 is obtained by the averaging: $\rho_{tot} = f_{w1}\rho_{w1} + f_{w2}\rho_{w2} + f_{w3}\rho_{w3} + (1 - f_{w1} - f_{w2} - f_{w3})\rho_c$.



(a) Von Mises stress against accumulated plastic deformation; experimental data [Christodoulou et al., 1986]

(b) Dislocation density evolution

Figure 5.3 — Monotonic uniaxial tension for copper.

Fig. 5.4 shows the curves for tension-compression experiments. Function (5.41), describing the remobilisation of dislocations, controls this mechanism in the walls and coefficient K is identified as to provide the best fit with the macroscopic behaviour (see Table 5.2). For remobilisation in cells a different function $f(\epsilon)$, than proposed in (5.41), was fitted. The most straightforward and best fit was found with the cell remobilisation controlled by the plastic flow in the walls according to:

$$f_c(\epsilon) = \begin{cases} 1 & \text{if } |\dot{\epsilon}_{wi}^p| = 0 \\ 0 & \text{if } |\dot{\epsilon}_{wi}^p| \neq 0 \end{cases} \quad (5.44)$$

If the remobilisation of dislocations in the cell interiors would continue longer than described by Eq. (5.44), this would lead to macroscopic softening which is not observed in the experiments.

5.4.2 Model verification

The performance of the cell structure model has been discussed in Viatkina et al. [2005b], including monotonic deformations and deformations containing strain path changes. The ability to predict strain path change effects was the principal objective. The model, however, failed to predict material behaviour under complex deformations that include reversed loading. In the present paper the model has been enhanced with evolution equations for the dislocation

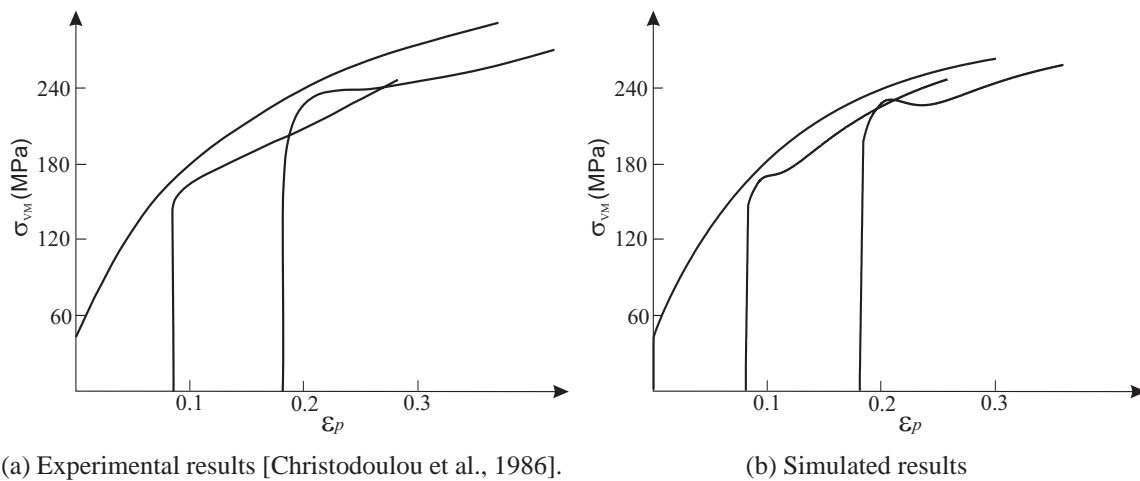


Figure 5.4 — The Bauschinger effect in tension-compression tests for copper. Von Mises stress against accumulated plastic deformation (the horizontal shift indicates the amount of prestrain undergone by material before load reversal).

densities with the purpose of adequately describing load reversals. The dislocation dissolution after a strain path change is assumed to be triggered by a load reversal. Consequently, the effect of the dislocation density evolution on the deformation behaviour is expected only after large strain path changes, that involve partial or complete reversal of the loading. The deformation behaviour after moderate strain path changes is unaffected by the modifications introduced here and consistent with the results discussed in Viatkina et al. [2005b]. The performance of the enhanced cell structure model is verified here for a load reversal where the dislocation dissolution is most substantial.

Fig. 5.4 shows the simulation results for a tension-compression test obtained with the parameters specified in the Tables 5.1 and 5.2. It can be seen that the model captures all the essential features associated with the Bauschinger effect. The simulation results demonstrate an early reloading yield followed by transient hardening. After the deformation is reversed, initially, the hardening rate is high, after which it drops rapidly below the rate of hardening exhibited during monotonic loading, see Fig. 5.5. The deformation continues with a slow hardening recovery to the same level as for monotonic loading. The duration of the hardening recovery increases with the amount of prestrain applied before the stress reversal. In the stress-strain diagram, Fig. 5.4a, the corresponding hardening features are observed as early yield followed by a quick increase of stress which almost reaches the monotonic loading curve, followed by a “plateau” of low hardening. The macroscopic stress under reversed loading is always lower than the monotonic stress obtained at the same total strain. All these features are confirmed by many experimental data on the Bauschinger effect [Christodoulou et al., 1986; Hasegawa et al., 1975; Rauch et al., 2002; Hasegawa et al., 1986; Marukawa and Sanpei, 1971; Pedersen et al., 1981].

A discrepancy between the experiments and the predictions may be observed in the duration of the transient hardening. This indicates that the description of the dislocation mechanisms proposed here can be improved. A better agreement may be expected through the use of more sophisticated (yet, also complex) dislocation evolution equations. The present model appears to be a reasonable compromise between complexity and accuracy. The strength of the current approach lies in its simplicity as only four parameters, I , R , C and K , are required to fit both

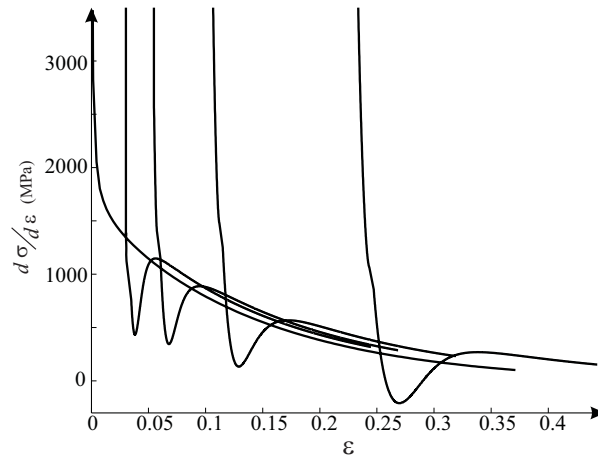


Figure 5.5 — Bauschinger effect in tension-compression tests for copper. Simulated macroscopic hardening rate against total deformation (the horizontal shift indicates the amount of prestrain undergone by material before load reversal).

the monotonic response and the behaviour after a strain path change. The combination of the simplicity of the model and its adequate prediction of the macroscopic material response makes the model attractive for theoretical research and practical applications.

5.5 Discussion

The ability of the model to capture macroscopic effects associated with stress reversal suggests that the microscopic mechanisms incorporated in the model induce the macroscopic Bauschinger effect. The material inhomogeneity, the internal stresses, and the evolution of dislocation densities are the main microscopic features of the model that define its macroscopic behaviour. The contributions of each of these features with respect to the resulting Bauschinger effect will be highlighted in this section.

5.5.1 Stress reversal: effect of the internal stress

The internal stress developed during prestraining of a material with a cell structure is often associated with a decreased reloading yield stress after a load reversal. For instance, monotonic tension applied to a material with a dislocation cell structure causes the development of positive internal stresses in the cell walls and negative internal stresses in the cell interiors. Thus, the internal stress in the cell interiors is opposite to the applied stress during monotonic deformation and will assist reversed deformation after a load reversal is applied. This is often suggested to be the origin of the decreased reloading yield stress [Christodoulou et al., 1986], i.e. the beginning of plastic yield at a lower macroscopic stress than the yield stress for monotonic loading at the same total strain.

Fig. 5.6 shows the evolution of the stress obtained from simulations for copper under monotonic tension and tension-compression tests. To investigate the contribution of the internal stress to the Bauschinger effect the dislocation dissolution was suppressed for this calculations, i.e. the dislocation densities evolve according to Eqs. (5.25). During monotonic

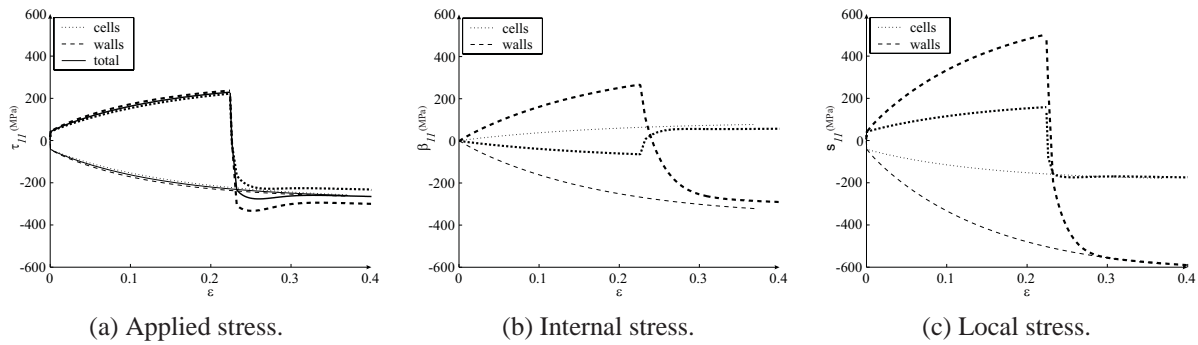


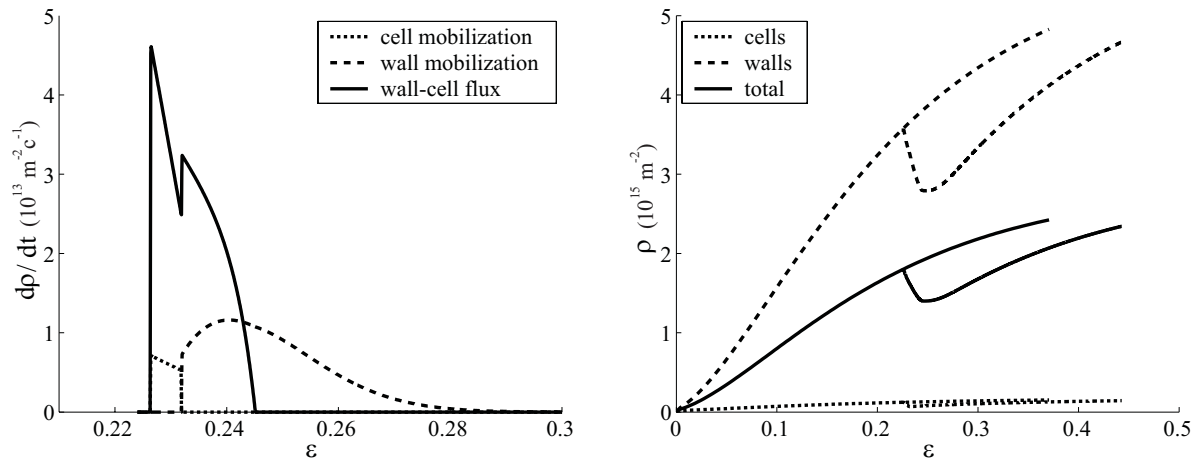
Figure 5.6 — Evolution of stresses under stress reversal, *no cell dissolution*. Thick lines correspond to the tension-compression test, thin lines to the compression test, for reference purposes.

deformation, either tension or compression, the internal stress in the walls reaches a level of the same order as the applied stress, while the internal stress in the cell interiors develops in a direction opposite to the applied stress. According to the cell structure model, the local plastic deformation is governed by the superposition of the applied and the internal stress. Consequently, in the walls, the internal stress assists the applied stress providing nearly half of the stress needed for plastic deformation. In the cells, the applied stress has to be higher than the local yield stress to compensate for the opposite internal stress.

When the loading direction is reversed, the applied stress is also reversed but the internal stress, as well as the yield stress, are unaffected by the elastic unloading. Immediately after the strain path change, the residual internal stress in the cell interior acts in the same direction as the new loading. Thus, the applied stress in the cells is assisted by the internal stress and the initiation of plastic deformation needs less external effort, i.e. the plastic deformation starts at a lower applied stress (Fig. 5.6a) compared to monotonic tension where the internal stress resists the deformation.

However, Fig. 5.6a also shows that the early yield in the cell interior does not lead to a noticeable early macroscopic yield (solid line in the figure). After the stress reversal, the high residual internal stress in the walls resists the applied stress, postponing the local yield. To initiate plastic slip in the walls after the strain path change, the applied stress has to compensate for the opposite internal stress, i.e. it has to be three times higher than in the forward loading where the same internal stress assisted the deformation. The value of the applied stress, however, is limited through the traction equilibrium at the interfaces. Nevertheless, it becomes significantly higher than the stress in monotonic tension. As a result of the decrease of the required applied stress in the cells and the increase of the required stress in the walls, the net macroscopic reloading yield stress is higher than the corresponding stress in monotonic loading. Clearly, without dislocation redistribution, the effect of the internal stress in the cell interior is neutralised by the much larger opposite effect of the internal stress in the walls.

The calculations show that the internal stress cannot be responsible for the reduced reloading yield stress associated with the Bauschinger effect. Yet, the internal stress substantially contributes to the effect by providing early yield in the cell interior. As soon as the plastic deformation starts, dislocation slip is activated in the new direction and cell dissolution starts, lowering the macroscopic hardening rate. If the dislocation dissolution is initiated at a low applied stress, due to the presence of the internal stress, the resulting low macroscopic hardening rate would lead to a reduced macroscopic yield stress, according to in the



(a) Density rates of microscopic mechanisms upon load reversal.

(b) Evolution of the dislocation densities. Density evolutions during monotonic tension are also given for reference purposes.

Figure 5.7 — Dislocation density evolution in the tension-compression test.

Bauschinger effect. Without the presence of the residual internal stress, the dissolution would start at an applied stress equal to the forward yield stress and would cause macroscopic softening, which is not observed experimentally. Thus, the effect of the internal stress does not directly cause early macroscopic yield but activates other mechanisms to do so.

5.5.2 Stress reversal: Effect of the dislocation evolution

The dissolution and reappearance of dislocation cells are the essential mechanisms contributing to the Bauschinger effect. Dissolution triggers by a decrease of the total dislocation density, a decrease of the dislocation density in the walls, and an increase of the dislocation density in the cells. Correspondingly, the reappearance of the cell structure after a load reversal is associated with the recovery of these parameters to values representative for monotonic deformation at the same total strain.

The model proposed here includes the evolution of the local dislocation densities as a function of the deformation history. A stress reversal activates a wall-cell dislocation flux, remobilisation in cells, and remobilisation in walls. All three dislocations mechanisms tend to reduce the local dislocation density and can be considered as mechanisms promoting cell dissolution. They have a finite duration and the local dislocation density recovers thereafter. The latter can be interpreted as the reappearance of the earlier dissolved cells.

The wall-cell flux is a flux of dislocations that were piled up against walls during the previous loading step and driven towards the cell interior by the applied reversal of the stress. The flux is activated by the plastic slip in the cell interior and continues until the source of interface dislocations is exhausted. This dislocation mechanism decreases the dislocation density in the walls and increases the dislocation density in the cells. It is assumed in the model, that this flux provides the dislocations necessary to accommodate further plastic slip in the cells, rendering the need for nucleation of dislocations superfluous. Compared to monotonic deformation, the dislocation density in the walls is decreased by this flux, whereas the dislocation density in the cell interiors follows the same evolution.

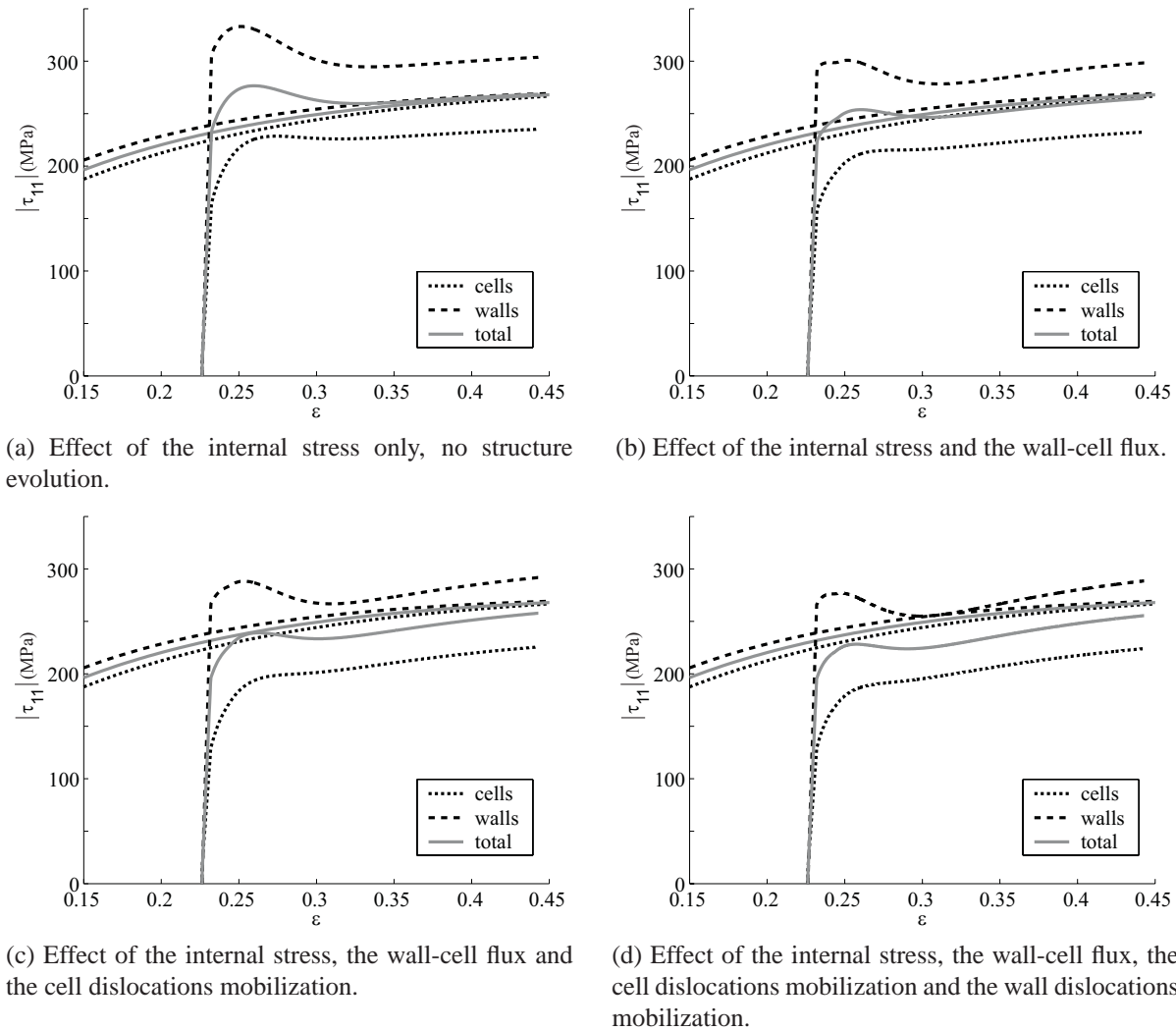


Figure 5.8 — Evolution of the applied stresses after a stress reversal ($\varepsilon_p = 0.18$). The stresses in monotonic tension are also given for reference.

To emphasize the effect of the wall-cell dislocation flux, a tension-compression test was simulated including the wall-cell dislocation flux –but excluding dislocation remobilisation– and compared to the case without this flux. The rate of the dislocation flux is shown in Fig. 5.7a. The flux is activated as soon as plastic slip in the cell interior occurs and lasts for about 2% of deformation. While active, the flux reduces the dislocation density in the walls for 24%.

Fig. 5.8b shows the results of the simulation with the wall-cell dislocation flux activated. Compared to the results obtained without this flux (Fig. 5.8a) a change in the hardening behaviour of the wall-phase can be observed. Reduction of the wall dislocation density causes a reduction in the local applied stress. As a result, the macroscopic stress lowers. The main effect of the flux is the reduction of the macroscopic hardening rate during the initial stage of reloading (the maximum of the macroscopic stress is significantly decreased in Fig. 5.8b). Yet, the exclusive effect of the wall-cell dislocation flux on the macroscopic reloading yield stress is not sufficient to correctly achieve the Bauschinger effect. The effect of the internal stress, discussed above, increases the reloading yield stress in the walls and consequently the macroscopic reloading yield stress. To neutralise this effect, the dislocation density in the

walls should drop severely, but such a rapid decrease of the density has never been observed in experiments. A realistic reduction of the local density only produces a small macroscopic effect, which is additionally reduced through the low volume fraction of the walls.

The remobilisation of immobile dislocations is another mechanism activated upon stress reversal. Immobile dislocations, such as those trapped in locks and dipoles, are partially released by reversed loading. The plastic slip is accommodated by the dislocations that are already present in the material and no additional dislocations are created, contrary to the monotonic loading case. The dislocation density thus only changes due to annihilation, lowering the total dislocation density.

The remobilisation in the cell interior is activated at the start of plastic slip in the cells and causes a reduction of the dislocation density in the cells, resulting in a decrease of the local yield stress and the average macroscopic stress. The remobilisation in the cell interior has a significant effect on the macroscopic behaviour due to the dominating volume fraction of the cells. The contribution of the cell remobilisation is shown in Fig. 5.8c. In this simulation, remobilisation is taken into account together with the internal stress and the cell-wall dislocation flux, whereas the remobilisation in the cell walls is excluded. Remobilisation in the cell interior decreases the dislocation density in the cells. Obviously, the reduction of the cell dislocation density prior to macroscopic yield, lowers the macroscopic yield stress, whereas a reduction after macroscopic yield would trigger softening. The macroscopic yield stress also corresponds to the beginning of plastic yield in walls. Since softening is not observed in the experiments, the remobilisation in cells in the simulation stagnates as soon as the walls yield, see Eq. (5.44). Fig. 5.7a shows that the remobilisation lasts for approximately 0.5% of deformation.

Clearly, by reducing the macroscopic yield stress, the reduction of the cell dislocation density due to remobilisation appears to play an important role in the Bauschinger effect.

The remobilisation in walls is activated at the start of plastic slip in the walls, i.e. after macroscopic yield. Therefore, this dislocation mechanism only influences the hardening behaviour. Fig. 5.8c shows the collective effect of the internal stress, the wall-cell flux, and the cell dislocations remobilisation, providing a macroscopic behaviour that is representative for the Bauschinger effect. The remobilisation of the dislocations in the walls causes a reduction of the dislocation density in the wall phase since no new dislocations are created and dislocation annihilation prevails. The applied stress in the walls is reduced further lowering the macroscopic stress more. Fig. 5.8d shows the results of a simulation with the dislocation remobilisation in the walls activated. The remobilisation lowers the macroscopic stress and the macroscopic hardening, although the effect is not that pronounced due to the low volume fraction of the walls.

5.5.3 Stress reversal: transient hardening

Fig. 5.9 shows the results of the simulation with the complete model, including the internal stress, the wall-cell flux, and the dislocation remobilisation in the cells and the walls. The graph of the average macroscopic stress demonstrates the Bauschinger effect with a low reloading yield stress and a transient hardening. Fig. 5.9b depicts the evolution of the internal stress and Fig. 5.7b shows the dislocation density evolution that accompanies the Bauschinger effect.

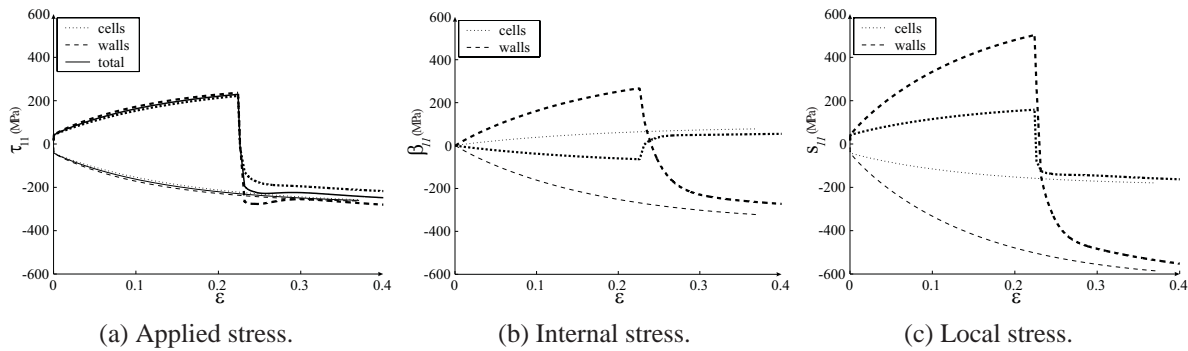


Figure 5.9 — Evolution of stresses simulated for tension-compression test using the complete cell structure model. Monotonic compression is given in thin lines for reference.

When the plastic deformation starts in the reversed direction, the internal stress adjusts to the new loading, Fig. 5.9b, i.e. evolves towards the distribution corresponding to the monotonic loading in the new direction. It is a gradual process continuing during 10% of the deformation. The evolution of the internal stress was found to correspond to the macroscopic hardening. Comparing the macroscopic stress evolution and the evolution of the internal stress, Figs. 5.9a and 5.9b, the high initial macroscopic hardening rate is related to the fast adjustment of the internal stress in the cell interior, while the subsequent “plateau” of low macroscopic hardening corresponds to the slow adjustment of the internal stress in the walls. Note that the dislocation mechanisms of cell dissolution do not alter the internal stress evolution significantly, see Fig. 5.6b.

The dislocation evolution in Fig. 5.7b, that accompanies the Bauschinger effect, includes a small drop in the dislocation density of the cells and a significant reduction in the dislocation density of the walls upon the load reversal. On the average, after stress reversal, the total dislocation density dropped with about 25% and the dislocation distribution becomes more uniform. The decrease of the dislocation density in the material lowers the macroscopic hardening. After stagnation of the cell dissolution mechanisms, the dislocation density regains a positive rate.

The results suggest that both the internal stress as well as the dislocation structure evolution play an important role in the Bauschinger effect. The internal stress, previously developed in the material during prestraining, triggers a plastic yield in the cell interior at a lowered applied stress. The early slip in the cells activates dissolution in the form of a wall-cell flux and dislocation remobilisation within the cells. The dislocation remobilisation in the cells provides a low macroscopic reloading yield stress. The simulation suggests that both, the internal stress and the dislocation remobilisation, are needed to explain the lowered macroscopic yield stress, consistent with the Bauschinger effect.

The transient hardening in the early stage after the stress reversal, i.e. before the hardening drop, is a collective effect of the internal stress adjustment in the cell interior and the decrease of the dislocation density in the walls. Further hardening evolution, associated with the “plateau”, is mainly governed by the adjustment of the internal stress in the walls.

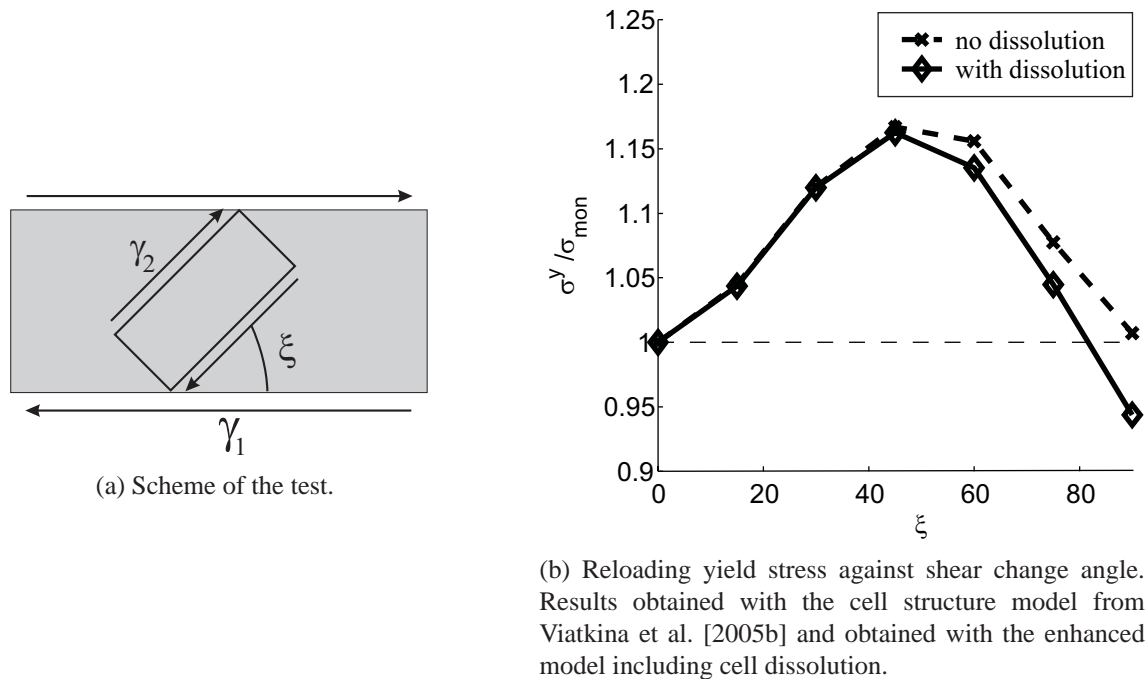


Figure 5.10 — Strain path change effect in shear-shear tests.

5.5.4 Strain path change effect

A simulation of a sequence of two successive shear deformations has been used as an example to study the effect of other strain path changes. The applied loading is depicted schematically in Fig. 5.10a. A shear-shear test is chosen, since it allows a wide range of strain path changes to be realised, including a cross test for $\xi = 45^\circ$ and a complete load reversal for $\xi = 90^\circ$.

The cell structure model introduced in Viatkina et al. [2005b] has been shown to predict the reloading yield stress correctly for moderate strain path changes. The effect results mainly from the geometrical anisotropy and the developing internal stress. The geometrical anisotropy is a consequence of the cubic cell structure in the material. The internal stress effect is induced by the cell geometry and plastic incompatibility. Fig. 5.10b shows the reloading yield stress as a function of the shear change angle ξ . The dotted line represents the result obtained with the cell structure model without cell dissolution, in which the dislocation evolution equation (5.25) has been used. The result shows an increase of the effect with the shear angle up to $\xi = 45^\circ$, i.e. the cross test. This tendency is in agreement with experimental observations, however, deviations are found for shear changes larger than $\xi = 45^\circ$. The simulations overpredict the reloading yield stress after large strain path changes, and a decreased reloading yield stress was never obtained for a load reversal with $\xi = 90^\circ$. This discrepancy was one of the motivations to include the dislocation evolution resulting from a strain path change in the cell structure model.

Fig. 5.10b also shows the result obtained with the cell structure model enhanced with the history dependent dislocation evolution. This enhanced model accounts for dislocation mechanisms activated by stress reversals, the wall-cell flux and the directional remobilisation. This allows an additional reduction of the reloading yield stress after strain path changes dealing with a reversal of the applied stress. Changes in the shear direction less than $\xi = 45^\circ$ do not have a reversed component, thus the reloading yield stress is hardly affected by the model

modification. Shear changes larger than $\xi = 45^\circ$ introduce a stress reversal component, with a complete reversal at $\xi = 90^\circ$. The dislocation dissolution, therefore, lowers the reloading yield stress at large strain path changes.

Quantitative verification of this result was not possible due to absence of experimental data on shear-shear tests for the material used. However, the results obtained with the enhanced model have a qualitative trend observed in the experiments for aluminium [Barlat et al., 2003] and steel [Peeters, 2002; Raphanel et al., 1987].

The discussion in the previous section highlighted that the transient hardening after a strain path change is mostly determined by the evolution of the internal stress, see Viatkina et al. [2005b]. The effect of the dislocation dissolution on the hardening behaviour in the simulations is only significant for high strain path change angles.

5.6 Conclusions

The cell structure model developed in Viatkina et al. [2005b] has been enhanced by the inclusion of a physically-based description of the evolution of the statistically stored dislocation distribution. The evolution equations for the local dislocation densities have been formulated to describe the evolution of a dislocation structure under deformation and its dissolution upon load reversal. The following dislocation processes are incorporated in the model:

- Local statistical dislocation mechanisms as creation, annihilation, mobilisation and remobilisation.
- Cell formation dislocation mechanism as dislocation flux from the cell interiors to the cell walls.
- Cell dissolution dislocation mechanisms as dislocation flux from the cell walls to the cell interiors and directional remobilisation, initiated by a load reversal.

To verify the model, a tension-compression and various shear-shear tests on copper have been simulated. The predicted strain path change effects and Bauschinger effect are in agreement with experimental data. The following conclusions were drawn from the analysis of the simulations:

- The increased reloading yield stress after a moderate strain path change results from the geometrical anisotropy due to the cell structure morphology and the internal stresses developed during prestraining.
- The decreased reloading yield stress after a large strain path change, which includes partial load reversal, is due to the internal stresses and the cell structure dissolution. The internal stresses, previously developed in the material during prestraining, trigger plastic yield in the cell interiors at a decreased value of the applied stress. The early slip in the cells activates structure dissolution mechanisms. The dislocation remobilisation in the cells and the wall-cell flux of dislocations decreases the macroscopic reloading yield stress.

- The transient hardening after a strain path change is mainly caused by the adaptation of the internal stresses to the new loading. The evolution of the internal stresses in the cell interiors affects the mechanical response in the early stages after reloading, whereas the adjustment of the internal stresses in the walls governs the further hardening behaviour. After a load reversal, the hardening rate is, moreover, lowered by a decrease of the dislocation density in the walls, caused by dissolution.

The enhancement of the cell structure model, introduced here, improved the prediction of the strain path change effects after large strain path changes, including the Bauschinger effect.

The role of plastic slip anisotropy in the modelling of strain path change effects

6.1 Introduction

In the engineering practice, most deformation processes are characterised by a non-monotonic strain history, in which different processing steps rapidly succeed each other. The effect of a strain path change manifests itself through an altered reloading yield stress and altered transient hardening compared to the response during the corresponding monotonic deformation of the same material [Vieira et al., 1990, 2000; Zandrahimi et al., 1989; Bate and Wilson, 1986; Pedersen et al., 1981]. The macroscopic effect of a strain path change is commonly associated with the presence and evolution of a dislocation structure in the material. The morphology of the dislocation structure developed during a particular loading path depends on the loading characteristics. A dislocation structure is formed to accommodate the current deformation in a more efficient way (in the sense of the underlying thermodynamics and kinetics). After a strain path change, the previously formed dislocation structure might have an 'unfavourable' morphology with respect to the new loading. The resistance and adaptation of the dislocation structure to the loading in the new direction is typically associated with an altered reloading yield stress and altered transient hardening.

The effect of the dislocation structure on the macroscopic material response has been actively investigated over the last half century, both experimentally [Barlat et al., 2003; Young et al., 1986; Mughrabi et al., 1986; Barker et al., 1989; Bay et al., 1992; Hansen et al., 2001; Huang and Hansen, 1997; Hansen and Huang, 1997; Winther et al., 2000; Liu et al., 1998; Zimmer et al., 1983; Ungar et al., 1984; Park and Parker, 1989; Liu and Hansen, 1995; Hughes et al., 1997] and theoretically [Mughrabi, 1987; Estrin et al., 1998; Argon and Haasen, 1993; Goerdeler and Gottstein, 2001; Peeters, 2002; Teodosiu and Hu, 1995]. The analysis of the microscopic deformation mechanisms is essential in order to develop an adequate model for describing the resulting deformation behaviour.

The material inhomogeneity caused by the formation of the dislocation cell structure has an obvious influence on the macroscopic deformation behaviour and has been described by means of a composite model [Mughrabi, 1987]. On this basis, the evolution of the cell morphology after a strain path change has been studied in Viatkina et al. [2003] (Chapter 3). This evolution was found to alter the reloading yield stress as well as the hardening rate during the initial stage following the onset of plastic deformation. The geometry of the cubic cell structure is one of the sources for the anisotropic behaviour of the material after a strain path change, which gives rise to a directional dependency of the reloading yield stress [Viatkina et al., 2005b]. Furthermore, internal stresses appear during the deformation of inhomogeneous materials. They develop during prestraining and are retained in the material as residual stresses, thereby affecting the reloading yield stress [Viatkina et al., 2005b]. The adjustment of the internal stresses to the new loading governs the transient hardening behaviour. Besides, a change in the applied loading causes a redistribution of the dislocations in the material. Dislocation redistribution in the cell structure triggered by a loading reversal has been analysed in Viatkina et al. [2005c] (Chapter 5) and was found to reduce the macroscopic reloading yield stress and the hardening rate.

Plastic slip anisotropy is another micromechanical aspect of the mechanical behaviour which is often related to the strain path change effect [Schmitt et al., 1991; Raphanel et al., 1987; Bate, 1993]. Plastic deformation in metals is promoted by crystallographic slip, which is restricted to closely-packed crystallographic planes. Even in the highly symmetric FCC-lattice, the 12 available slip systems do not trigger an isotropic plastic deformation. A change in the deformation mode causes a change of the active slip system set. For example, suppose a certain prestrain is realised by a multislip deformation process, subsequently followed by a new loading that promotes a condition favouring a single slip system; since multislip and single slip manifest themselves by different stress responses, the change of the deformation mode will lead to a change in the macroscopic response, even if other strain path change mechanisms are not considered.

Another source of material anisotropy, related to the crystallographic slip, is latent hardening. Latent hardening introduces a deformation history dependency into the plastic behaviour of metals. Plastic deformation promoted by a certain slip system increases the resistance to plastic slip on other slip systems, i.e. non-active slip systems may harden. Consequently, after a strain path change, the activation of previously non-active systems may require a different effort in comparison to the 'virgin' slip resistance upon activation of the previously active slip systems. Experimental studies often correlate the activation of new slip systems after a strain path change to an increased reloading yield stress [Schmitt et al., 1991]. Theoretical simulations including latent hardening, on the contrary, have proven the insignificance of this effect [Jensen and Hansen, 1990; Peeters, 2002] in materials with homogeneous grains, i.e. without dislocation structures.

This chapter concentrates on the role of the plastic slip anisotropy in the strain path dependency of materials containing a dislocation cell structure. The cell structure model, developed in Viatkina et al. [2005b], is extended here by employing a crystal plasticity model for describing the local material behaviour. This, more physically based description of the plastic behaviour allows plastic anisotropy resulting from the crystal lattice of a metal to be accounted for. Simulation results of the original and the extended model are compared to reveal the effect of slip anisotropy on the strain path change effect.

6.2 Cell structure model

The deformation behaviour of FCC metals with a dislocation cell structure is modelled here on the basis of the cell structure model introduced in Viatkina et al. [2005b] (Chapter 4). The main features of the model are shortly summarised in this section.

Material with a cell structure is idealised by a composite consisting of four uniform components: the cell interiors and three sets of cell walls. The cell wall component represents the phase with a high dislocation density and the cell interior component represents the low dislocation density areas enveloped by the dislocation walls. The cell structure is modelled as a 3D periodic configuration of cuboid cells formed by three sets of mutually perpendicular planar cell walls. The morphology of the composite, adopted in this chapter, is shown in Fig. 6.1. Inspired by experimental observations, the cell structure is modelled as a 3D periodic stacking of cubic cells with dimensions $D_1 \times D_2 \times D_3$, separated by three mutually perpendicular sets of cell walls with unit normals $\vec{n}_1, \vec{n}_2, \vec{n}_3$ and with different thicknesses w_1, w_2 and w_3 . The dislocation densities in the cell walls, $\rho_{w1}, \rho_{w2}, \rho_{w3}$, respectively, depend on the orientation, as a result of prior deformation. The spatial orientation of the cell structure is given by the normals $\{\vec{n}_1, \vec{n}_2, \vec{n}_3\}$.

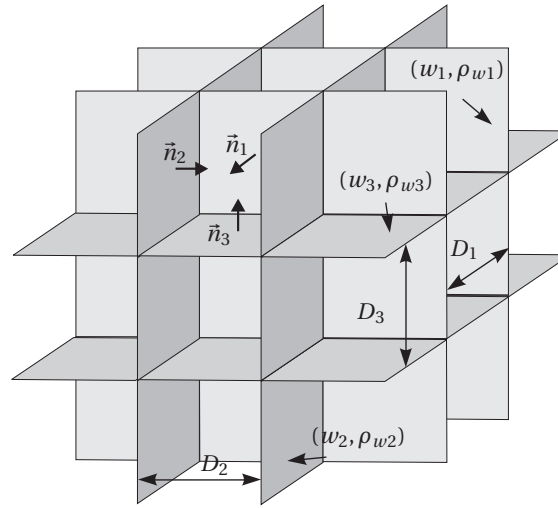


Figure 6.1 — Model geometry of the cell structure and its components.

The average mechanical response of the composite is calculated from the individual contributions of the local responses of the walls and the cell interiors:

$$\vec{\sigma} = f_{w1}\sigma_{w1} + f_{w2}\sigma_{w2} + f_{w3}\sigma_{w3} + (1 - f_{w1} - f_{w2} - f_{w3})\sigma_c \quad (6.1)$$

$$\vec{F} = f_{w1}F_{w1} + f_{w2}F_{w2} + f_{w3}F_{w3} + (1 - f_{w1} - f_{w2} - f_{w3})F_c \quad (6.2)$$

where σ is the Cauchy stress tensor, $F = (\vec{\nabla}_0 \vec{x})^T$ the deformation gradient tensor, and f the volume fractions of the components. The tilde symbol denotes an averaged quantity, while the subscripts indicate whether the quantity is associated with the cell interior c or one of the walls $w1, w2$, and $w3$. Additionally, traction continuity and compatibility of deformations are enforced on the interfaces between the cell interiors and the walls:

$$(\sigma_c - \sigma_{wi}) \cdot \vec{n}_i^t = \vec{0} \quad \text{for } i = 1, 2, 3 \quad (6.3)$$

$$(F_c - F_{wi}) \cdot (\mathbf{I} - \vec{n}_i^0 \vec{n}_i^0) = \mathbf{0} \quad \text{for } i = 1, 2, 3 \quad (6.4)$$

where \vec{n}_1 , \vec{n}_2 and \vec{n}_3 are the normal vectors to the cell-wall interfaces, and the superscripts 0 and t indicate if these vectors are defined in their initial or current configuration, respectively.

6.2.1 Crystal plasticity

According to the cell structure model, the local material behaviour in the cell and wall phases is assumed to be uniform. A conventional crystal plasticity theory is employed in this chapter to describe the local material response. The equations listed in this section are equally applied to the cell and wall components, each with their own deformation history; the subscripts $w1$, $w2$, $w3$ and c are omitted in the following.

Crystal plasticity theories originate from the early work of Taylor and Elam [1923] who presented a quantitative description of the plastic deformation in single crystals based on crystallographic slip. Plastic deformation is assumed to be the collective result of distinct shear contributions on well-defined slip systems given by the crystallographic planes and the directions of the highest atomic density. The theory was further developed in the works of Lee [1969]; Rice [1971]; Hill and Rice [1972]; Asaro and Rice [1977].

The kinematics commonly used in crystal plasticity depart from the multiplicative decomposition of the deformation gradient tensor \mathbf{F} into an elastic and a plastic part,

$$\mathbf{F} = \mathbf{F}_e \cdot \mathbf{F}_p \quad (6.5)$$

where the elastic deformation is represented by \mathbf{F}_e , which also accounts for superimposed rigid body rotations, and where \mathbf{F}_p is the plastic contribution arising solely from crystallographic slip in the undeformed configuration. The plastic slip rate $\dot{\gamma}^q$ on a slip system q , defined by the normal to the slip plane \vec{n}^q and the slip direction \vec{m}^q in the initial configuration, contributes to the plastic velocity gradient tensor \mathbf{L}_p through the following crystallographic split:

$$\mathbf{L}_p = \sum_q \dot{\gamma}^q \vec{m}^q \vec{n}^q \quad (6.6)$$

where \mathbf{L}_p determines the evolution of the plastic deformation gradient tensor \mathbf{F}_p according to:

$$\dot{\mathbf{F}}_p = \mathbf{L}_p \cdot \mathbf{F}_p \quad (6.7)$$

For the elastic part of the deformation, the fictitious stress-free intermediate configuration defined by the plastic deformation gradient tensor \mathbf{F}_p is considered as the reference state, implicitly assuming that the elastic behaviour is not affected by the plastic slip. In this contribution the isotropic elasticity tensor \mathbb{C} (expressed in the shear modulus G and Poisson's ratio ν) relates the stress tensor $\boldsymbol{\tau}$ to the elastic Green-Lagrange strain tensor \mathbf{E}_e in a classical manner

$$\boldsymbol{\tau} = \mathbb{C} : \mathbf{E}_e, \quad \mathbf{E}_e \equiv \frac{1}{2}(\mathbf{F}_e^T \cdot \mathbf{F}_e - \mathbf{I}) \quad (6.8)$$

The stress measure $\boldsymbol{\tau}$ used here is the second Piola-Kirchhoff stress related to the stress-free intermediate configuration and coupled to the Cauchy stress tensor $\boldsymbol{\sigma}$ by:

$$\boldsymbol{\tau} \equiv \mathbf{F}_e^{-1} \cdot [\det(\mathbf{F}_e)\boldsymbol{\sigma}] \cdot \mathbf{F}_e^{-T} \quad (6.9)$$

Further, in the present rate-dependent formulation each slip rate $\dot{\gamma}^q$ depends on the actual resolved shear stress s^q and the slip resistance σ_y^q on that slip system according to the slip law:

$$\dot{\gamma}^q = \dot{\gamma}_0 \left\{ \frac{|s^q|}{\sigma_y^q} \right\}^{1/m} \text{sign}(s^q), \quad s^q \equiv \mathbf{s} : \vec{m}^q \vec{n}^q, \quad \mathbf{s} = \boldsymbol{\tau} + \boldsymbol{\beta}, \quad (6.10)$$

where $\dot{\gamma}_0$ denotes a reference value of the slip rate, σ_y^q is the evolving slip resistance, m is the strain rate sensitivity parameter and $\boldsymbol{\beta}$ is the internal stress (opposite of the back stress). This slip law incorporates isotropic hardening through σ_y^q and kinematic hardening through $\boldsymbol{\beta}$.

The internal stresses developed under deformation in a material with a cell structure were determined in Viatkina et al. [2005b], accounting for a continuous approximation of the crystallographic cell-wall incompatibility. The heterogeneity of the material, introduced by the cell structure causes a nonuniform field of plastic deformation during external loading. As a result, the plastic deformation presents jumps across the interfaces between the hard (cell walls) and soft phases (cell interiors), which have to be accommodated by polarised layers of geometrically necessary dislocations (GNDs) at these interfaces. It is known that the resulting dislocation network may substantially affect the mechanical behaviour by inducing internal stresses. On the contrary, in the cell structure model, the statistically stored dislocations (SSDs) in the wall and cell interior phases are randomly distributed and therefore the resulting stress fields will compensate each other, cancelling out their contribution to long-range effects. The internal stresses created by the GNDs at the interfaces were determined in Viatkina et al. [2005b] (Chapter 4) as a function of the plastic incompatibility and the cell geometry within a continuum framework, i.e. without accounting for the crystallographical character of slip. These internal stresses will be used here as well, constituting an adequate approximation for the real stresses induced by the crystallographic plastic incompatibilities.

The slip resistance σ_y^q on a slip system q is related to the dislocation densities by the hardening relation [Evers et al., 2002]

$$\sigma_y^q = Gb \sqrt{\sum_u A^{qu} |\rho^u|}, \quad (6.11)$$

where G is the shear modulus, b the magnitude of the Burgers vector, A^{qu} are interaction coefficients between slip systems q and u , and ρ^u the local densities of the SSDs on the slip system u . The dislocation interaction coefficients of the matrix A^{qu} depend on the interaction types between dislocations on different slip systems, as documented by Franciosi and Zaoui [1982]. In this chapter, the interactions between the dislocations belonging to the same slip system, i.e. $u = q$, and different slip systems, i.e. $u \neq q$, are distinguished.

6.2.2 Statistically stored dislocations

The slip resistance σ_y^q is related to the local density of statistically stored dislocations (SSDs) ρ^u by Eq. (6.11). This relation is applied to the cell interiors as well as to the cell walls, each with their own SSD density. The dislocation densities in the corresponding phases are defined next. To describe the evolution of the SSDs in the cell structure under deformation the following equations are adopted:

$$\dot{\rho}_c^q = \frac{1}{b} \left(\frac{1}{L_c^q} - R\rho_c^q \right) |\dot{\gamma}_c^q| - Q_c^q \quad \text{with } \rho_c^q|_{t=0} = \rho^0 \quad (6.12a)$$

$$\dot{\rho}_{wi}^q = \frac{1}{b} \left(\frac{1}{L_c^q} - R\rho_{wi}^q \right) |\dot{\gamma}_{wi}^q| + Q_{wi}^q \quad \text{with } \rho_{wi}^q|_{t=0} = \rho^0 \quad \text{for } i = 1, 2, 3 \quad (6.12b)$$

The two first terms on the right-hand sides of the evolution equations account for dislocation creation ($|\dot{\gamma}^q|/[bL_c^q]$) and dislocation annihilation ($R\rho^q|\dot{\gamma}^q|/b$), respectively. The last terms on the right-hand sides of both equations are introduced to describe the dislocation flux from the cell interiors to the cell walls, analogous to the 'continuum' flux introduced in Viatkina et al. [2005b] (Chapter 4). The initial dislocation density in the undeformed material is defined by ρ^0 , which is assumed to be homogeneous. The material parameter R associated with annihilation is related to the critical annihilation distance, which is here taken constant. The parameters L_c^q and L_{wi}^q represent the mean free paths of the mobile dislocations in system q of cells and walls respectively. The following relations, adopted from Teodosiu et al. [1993], are used to quantify them:

$$L_c^q = \frac{1}{I} \left(\sum_{u \neq q} \rho_c^u \right)^{-1/2} \quad (6.13)$$

$$L_{wi}^q = \frac{1}{I} \left(\sum_{u \neq q} \rho_{wi}^u \right)^{-1/2} \quad i = 1, 2, 3 \quad (6.14)$$

where I is a material parameter.

The dislocation fluxes Q_c^q and Q_{wi}^q govern the redistribution of dislocations. These fluxes trigger the creation and evolution of the dislocation structure and manifest themselves through an increasing difference between the dislocation densities in the cell and walls. To quantify the flux Q_c^q from the cell interiors to the cell walls, it is assumed that, on each slip system, a fixed fraction of all created mobile dislocations in the cell interior leave the cell interior to join the cell walls. The amount of created mobile dislocations present in the cells is given by the first contribution in the evolution equation (6.12a). Thus, this assumption can be formalised by:

$$Q_c^q = C \frac{1}{bL_c^q} |\dot{\gamma}_c^q| \quad (6.15)$$

where the fixed fraction C represents a material dependent constant. Thus, the total density flux from cells to walls can be found by summation over all the slip systems:

$$Q = \sum_q Q_c^q \quad (6.16)$$

The dislocation flux Q_{wi}^q that arrives in the walls can be written as,

$$Q_{wi}^q = \frac{|\dot{\gamma}_{wi}^q|}{\sum_u |\dot{\gamma}_{wi}^u|} Q_{wi} \quad \text{with } Q_{wi} = \frac{1 - f_{w1} - f_{w2} - f_{w3}}{f_{w1} + f_{w2} + f_{w3}} Q \quad (6.17)$$

Here, it is assumed that the dislocations leaving the cell interior are equally distributed between all walls. First Q_{wi} is calculated such that the total amount of dislocations in the material is preserved, after which the dislocation flux on each system Q_{wi}^q is obtained by redistributing Q_{wi} over all walls proportionally to the slip activity in each wall.

Table 6.1 — Parameters for copper.

Parameter	Symbol	Unit	Value
Shear modulus	G	[GPa]	41.7
Poisson's ratio	ν	[-]	0.34
Length of the Burgers vector	b	[nm]	0.257
Cell size	$D_1 = D_2 = D_3$	[μm]	2.5
Wall volume fractions	$f_1 = f_2 = f_3$	[-]	0.18
Strain rate sensitivity	m	[-]	0.012
Reference slip rate value	$\dot{\gamma}_0$	[1/s]	0.001

Table 6.2 — Dislocation density parameters for copper.

Parameter	Symbol	Unit	Value
Initial dislocation density	ρ^0	[m^{-2}]	$9.0 \cdot 10^{13}$
Creation rate parameter	I	[-]	0.1
Annihilation rate parameter	R	[nm]	2.0
Dislocation flux constant	C	[-]	0.6
Interaction coefficient	A^{qq}	[-]	0.06
Interaction coefficient	$A^{uq}, q \neq u$	[-]	0.6

6.2.3 Polycrystal model

Together, the Eqs. (6.1)–(6.17) describe the deformation behaviour of a single crystal with a cell structure. The response of a polycrystal consisting of a number of single crystal contributions is obtained here by invoking the Taylor assumption. Hence the deformation in each separate grain of the polycrystal is taken equal to the macroscopic deformation of the polycrystal. The macroscopic value of the stress tensor is then obtained by averaging the stress tensors over the total number of grains.

6.3 Results

The material parameters used for the simulations in this section were identified in Viatkina et al. [2005b] for the deformation behaviour of copper. The additional parameters needed for describing the crystallographic slip, m , $\dot{\gamma}_0$ and A^{qu} , were chosen according to typical values for copper [Evers et al., 2002]. The parameters are summarised in Tables 6.1 and 6.2.

To verify the model performance, two-step sequential shear tests were simulated for polycrystalline copper with a cell structure. The scheme of the test is depicted in Fig. 6.2. To simulate the response of a material with a cell structure and crystal lattice anisotropy, the orientation of the structure as well as the orientation of the lattice should be defined with respect to a macroscopic basis. First, a polycrystal was assembled from 500 grains with lattice orientations defined with respect to a macroscopic basis $\{\vec{\mathcal{R}}_1, \vec{\mathcal{R}}_2, \vec{\mathcal{R}}_3\}$, introduced in Fig. 6.2. Next, a number of simple shear tests were calculated employing different shearing directions, defined in Fig. 6.2 with angle ξ between the shearing direction \vec{x}_1 and the basis vector $\vec{\mathcal{R}}_1$. Then, elastic unloading, defined as the state with zero macroscopic stress, was simulated and simple shear in the direction $\vec{\mathcal{R}}_1$ was applied. This procedure corresponds to a typical

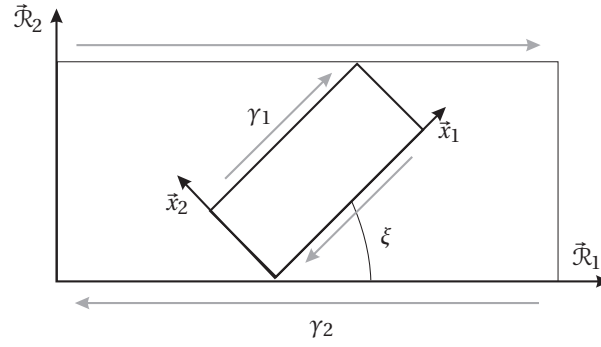


Figure 6.2 — Scheme for two-step sequential shear tests.

experimental setting to study strain path change effects, e.g. Schmitt et al. [1991]. In the experiments, the specimens for the first loading step are cut from the original metal in different directions with respect to a reference direction. I.e., the initial texture is inherited from the original material and defined with respect to the original metal sheet. Then the second loading steps are applied in the reference direction.

It is further assumed that during the first loading step, a cell structure develops along the macroscopic shear plane, i.e. one cell wall is parallel to the shear plane and one cell wall is perpendicular to the shear direction. This choice for the structure orientation corresponds to the formation of a cell structure along the macroscopic plane with maximum shear as confirmed by experimental observations [Zhu and Sellars, 2001]. Thus, with respect to the cell structure, the loading during the first step is equivalent for all test cases, while the loading in the second step, with respect to the cell structure, depends on the strain path change defined by ξ .

Simple shear is a deformation driven process, therefore the macroscopic deformation was applied to each grain of the polycrystal. In the shear-shear tests, the first shear step was simulated by applying the following deformation gradient tensor:

$$\tilde{\mathbf{F}} = \mathbf{I} + \dot{\epsilon} t \vec{x}_1 \vec{x}_2 \quad (6.18)$$

where \vec{x}_1 and \vec{x}_2 are local unit base vectors defined for each test case as shown in Fig. 6.2. The applied strain rate $\dot{\epsilon}$ is set equal to $5 \cdot 10^{-4} \text{ [s}^{-1}\text{]}$. The orientation of the shearing direction \vec{x}_1 with respect to the reference direction \vec{R}_1 is defined by the angle ξ . The calculations were performed for $\xi = 0^\circ, 15^\circ, 30^\circ, 45^\circ, 60^\circ, 75^\circ, 90^\circ$, until a macroscopic strain of 10% was reached.

For the second step of the shear-shear tests, the loading was always applied in the reference direction:

$$\tilde{\mathbf{F}} = \mathbf{I} + \dot{\epsilon} t \vec{R}_1 \vec{R}_2 \quad (6.19)$$

To evaluate the strain path change effect in the shear-shear tests, the reloading yield stress σ^y is found further as a function of the strain path change angle ξ . The reloading yield stress was defined as the macroscopic shear stress σ at which the macroscopic hardening rate after reloading drops to the level of the macroscopic hardening rate in the monotonic test at the prestrain value ϵ_{pre} , i.e.

$$\frac{d\sigma}{d\epsilon} = \left. \frac{d\sigma_{mon}}{d\epsilon} \right|_{\epsilon=\epsilon_{pre}} \quad (6.20)$$

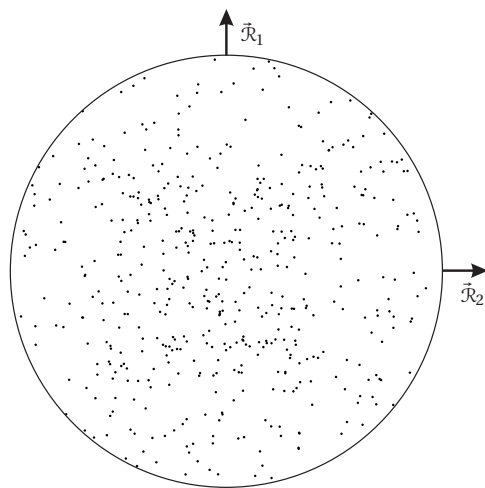


Figure 6.3 — Random distribution of initial grain orientation represented by a {111} stereographic pole figure.

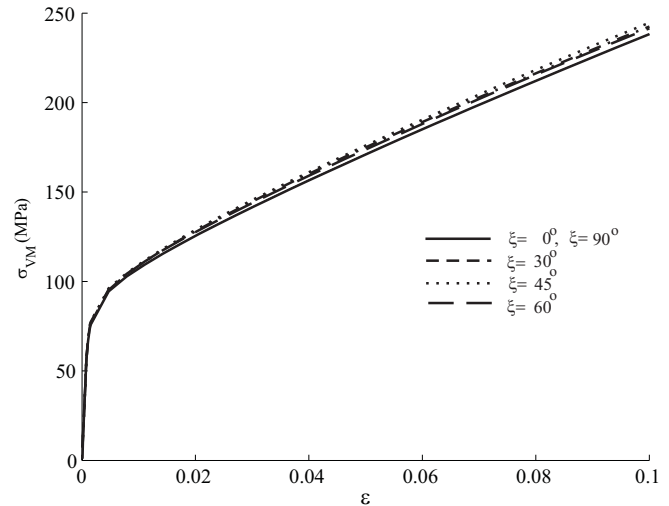


Figure 6.4 — Stress-strain diagrams for monotonic shear tests, to be considered as prestrain loadings, in different orientations with respect to the reference basis.

6.3.1 Polycrystal with random grain orientation

The cell structure model extended with a crystal plasticity framework, introduced in this chapter, accounts for four sources of anisotropy: 1) geometrical anisotropy due to the configuration of the cell structure; 2) anisotropy due to the internal stresses associated with the cell structure 3) slip anisotropy and 4) textural anisotropy. The qualitative and quantitative effects of the first two sources of strain path dependency were discussed in Viatkina et al. [2005b] (Chapter 4). In the following simulation results, textural anisotropy is inhibited by considering a random distribution of grain orientations in the polycrystal, as shown in Fig. 6.3. Fig. 6.4 shows the stress-strain diagrams simulated for the initial shear steps, i.e. for monotonic shearing in various directions defined by ξ . It can be seen that the random orientation of the grains in the polycrystal provides an almost isotropic macroscopical response. However, the reloading yield stresses, depicted in Fig. 6.5a, calculated for the shear-shear tests for the polycrystal depend on the prestrain direction, manifesting material anisotropy provided by the first three sources.

Alternatively, the mechanical response of the polycrystal with a random distribution of grain orientations can be predicted by applying the mean field approach adopted for the cell structure model in Viatkina et al. [2005b] (Chapter 4). The original cell structure model [Viatkina et al., 2005b] employs continuum Von Mises elastoplasticity for the local material behaviour. Besides the adopted Taylor assumption, the main difference between the present model and the model of Viatkina et al. [2005b] is the local material behaviour – the first accounts for slip anisotropy, while the latter assumes isotropic plastic deformation. Therefore, to estimate the contribution of the slip anisotropy to the strain path change effect, the present calculation results for the reloading yield stress will be compared with the results obtained employing the cell structure model of Viatkina et al. [2005b] (Chapter 4).

For the calculations with the cell structure model [Viatkina et al., 2005b] the same set of material parameters and the same cell geometry (Tables. 6.1 and 6.2) were used, leading to a comparable macroscopic response under monotonic shear as shown in Fig. 6.4. The reloading yield stresses were calculated with the use of this model for the shear-shear experiments and

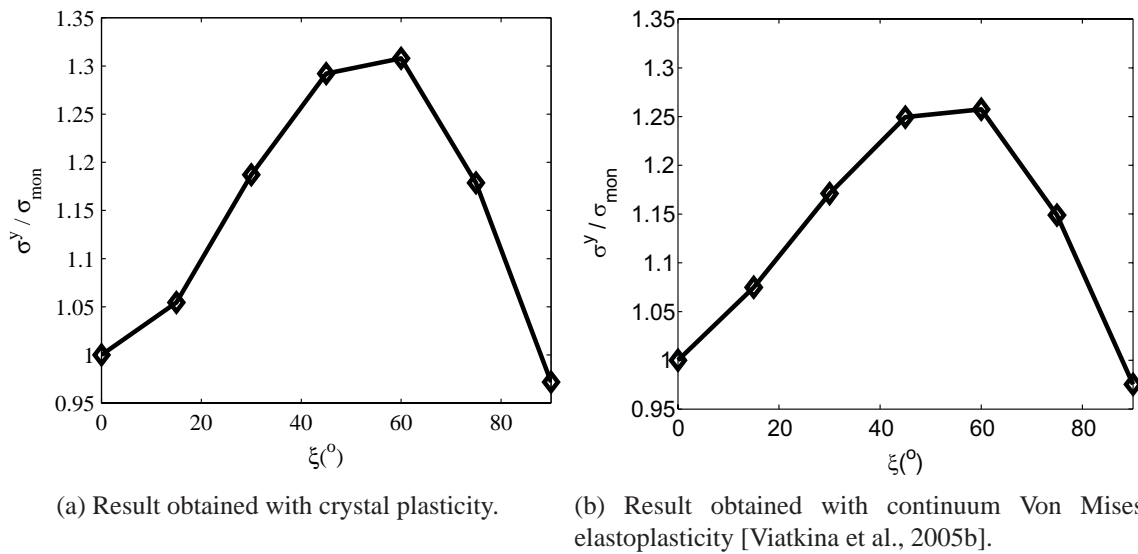


Figure 6.5 — Reloading yield stresses in shear-shear tests as a function of the strain path change angle ξ , $\varepsilon_{pre} = 0.1$.

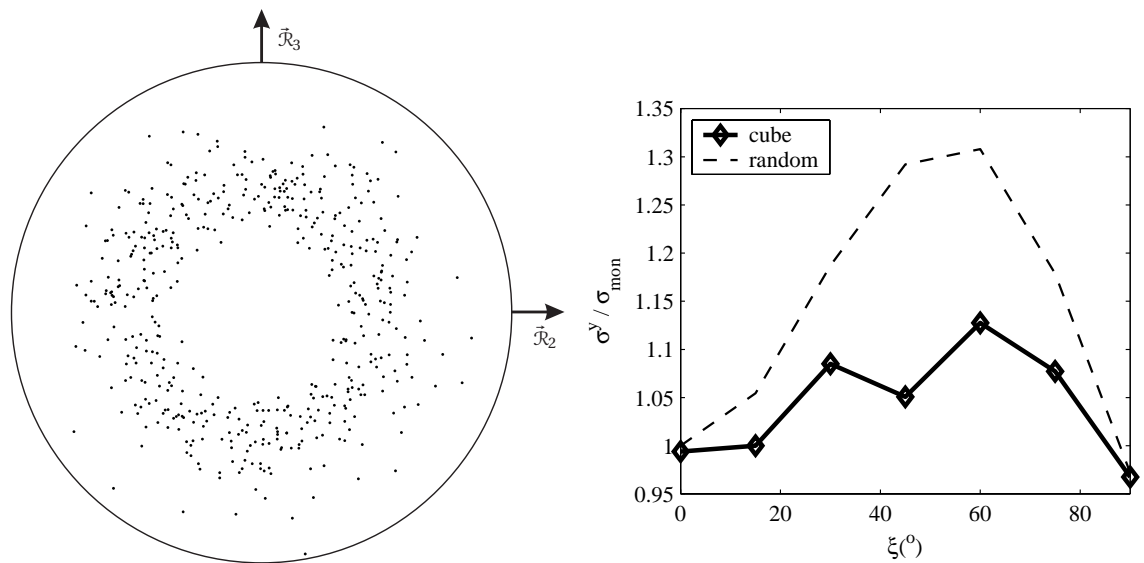
the results are shown in Fig. 6.5b.

The results of the two cell structure models can be compared by examining Figs. 6.5a and 6.5b. Note that only a qualitative comparison is possible, since the actual model accounts for the polycrystalline nature of the material, although with randomly distributed grains, while the original model [Viatkina et al., 2005b] operates under the mean field assumption. Besides, the models employ different evolution laws for the dislocation densities, which results in different evolutions of the material inhomogeneity. In spite of the differences, it can be seen that for small to moderate strain path changes the results of the two models are in qualitative agreement, which indicates that the effect of the cell structure is dominant and the slip anisotropy effect is less significant. The similarity between the results predicted with the two models also indicates that a “continuum” approach as presented in Viatkina et al. [2005b] is adequate for the modelling of the strain path dependency of polycrystals with random initial grain orientation.

6.3.2 Polycrystal with cube texture

To demonstrate the contribution of the textural anisotropy to the strain path dependency, a polycrystal with a cube texture is considered in subsequent simulations. The shear-shear simulations are performed in the same way as described above, using the parameters for copper, see Tables 6.1 and 6.2. The initial orientation of the grains in the simulated polycrystal is shown in Fig. 6.6a.

Fig. 6.6b shows the reloading yield stresses in shear-shear tests as a function of the strain path change angle ξ , after 10% of prestrain in shear. The simulation is performed using the cell structure model proposed in this chapter, i.e. the local material behaviour is described with crystal plasticity. The figure shows two results, one for a polycrystal with random grain orientation and another for a polycrystal with a cube texture. It can be seen that the textural anisotropy, present in the second case, has a significant effect on the reloading yield stress.



(a) Distribution of the initial grain orientation (b) Reloading yield stresses in shear-shear tests as a function of the strain path change angle ξ , $\varepsilon_{pre} = 0.1$.

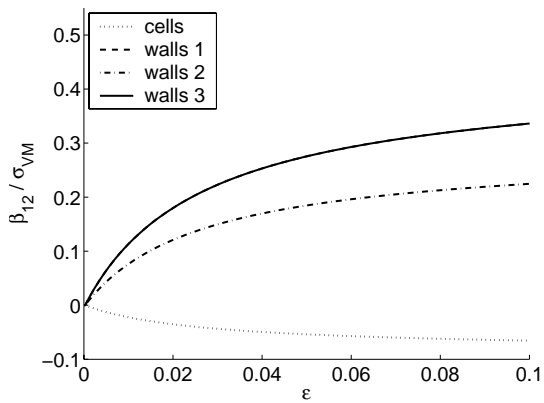
Figure 6.6 — Simulation for a copper polycrystal with cube texture.

It was shown in many theoretical investigations [Jensen and Hansen, 1990; Peeters, 2002] that in polycrystals with homogeneous grains, i.e. without a dislocation cell structure, slip and textural anisotropy alone produce a negligible strain path change effect. The effect found here is mainly due to the effect of the slip anisotropy on the distribution of the internal stresses in each grain. Fig. 6.7 shows the evolution of the internal stresses in the cell structure during monotonic shear simulated for grains with different lattice orientations, defined by the Euler angles. Due to the slip anisotropy, the internal stresses exhibit a strong dependency on the lattice orientation. Via the internal stresses, the grain orientation influences the reloading deformation behaviour of grains after strain path changes. In the case of a polycrystal with randomly oriented grains, the effects of the slip anisotropy on the deformation behaviour of individual grains cancel out each other and do not provide a contribution to the macroscopic behaviour. In the case of a textured polycrystal, due to textural anisotropy, the effects of the slip anisotropy on the internal stresses contribute to the macroscopic response. Thus, the slip anisotropy may have an essential quantitative influence on the strain path dependency in textured polycrystals.

6.4 Conclusions

The cell structure model proposed by Viatkina et al. [2005b], has been extended with a crystal plasticity framework for the description of the local deformation behaviour in the structure. The modification allows accounting for crystallographic slip anisotropy.

Two-step sequential shear tests were simulated for a random polycrystal with a cell structure. The influence of slip anisotropy on the strain path change effects has been investigated by comparing reloading stresses predicted with the use of crystal plasticity and when applying isotropic elastoplasticity [Viatkina et al., 2005b] to model the local material behaviour. The



(a) Predicted with the model in Viatkina et al. [2005b].

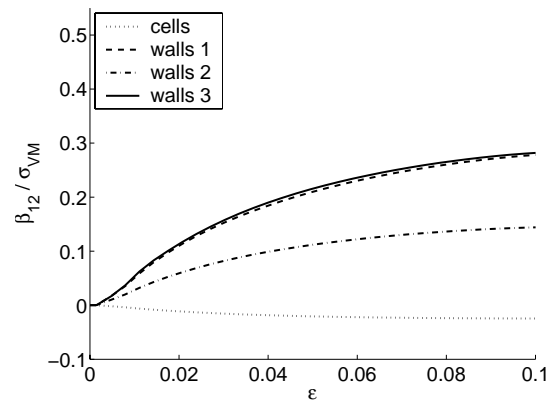
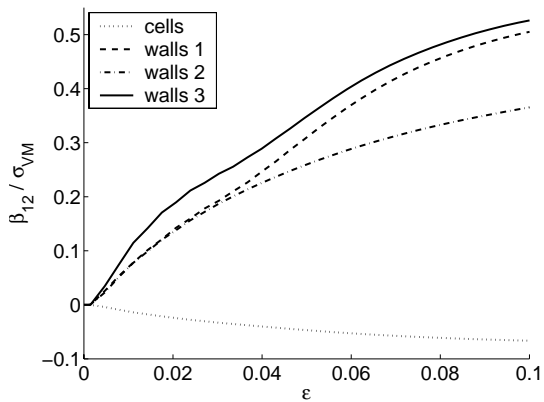
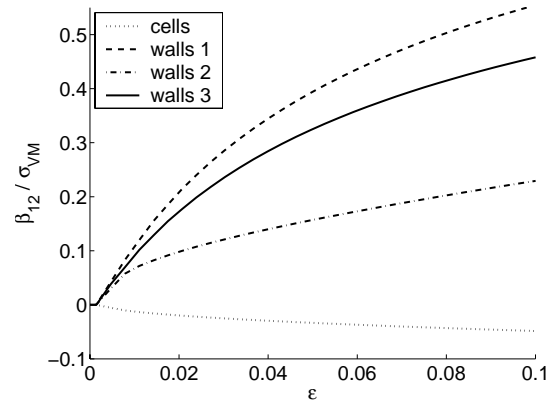
(b) Grain orientation $\{44^\circ, 113^\circ, 156^\circ\}$.(c) Grain orientation $\{67^\circ, 93^\circ, 95^\circ\}$.(d) Grain orientation $\{0^\circ, -135^\circ, -98^\circ\}$.

Figure 6.7 — Effect of the slip anisotropy on the distribution of the internal stresses. Evolution of the internal stresses β_{12} during monotonic shearing in the reference direction ($\xi = 0^\circ$). b)-d) Predicted with the present model for different grains, the grain orientations are given by the Euler angles.

prediction of the reloading yield stress employing the enhanced model demonstrates the same trend as predicted by the former model, without slip anisotropy. It was concluded that the continuum micromechanical version of the model, developed in Viatkina et al. [2005b], provides an adequate estimate of the average polycrystal behaviour in case of a random texture.

The slip anisotropy effect on the strain path dependency has been demonstrated with simulation results for a polycrystal with a cube texture. The effect of the slip anisotropy was explained by the sensitivity of the internal stress distribution to the plastic slip details. Thus, for an accurate prediction of strain path change effects in textured polycrystals plastic anisotropy should be taken into account.

Chapter 7

Conclusions

The research presented in this thesis has been dedicated to the investigation of the microstructural mechanisms responsible for the strain path dependent response observed in FCC metals. The approach introduced is based on the assumption that strain path change effects originate from the inhomogeneity introduced in the material by an evolving dislocation cell structure. Different aspects of the deformation behaviour of metals with a cell structure have been considered. In Chapter 3 the morphology evolution of a cell structure under complex deformation and its effect on the macroscopic behaviour was studied. Next, in Chapter 4, attention was focused on the influence of the geometrical anisotropy of the cell structure and the effect of the internal stresses developing in the material under deformation. In Chapter 5 the dislocation redistribution in a cell structure upon load reversal and the corresponding macroscopic effects were considered. This was followed by an analysis of the contribution of plastic slip anisotropy to the strain path change effects in Chapter 6. Moreover, in Chapter 2 the formability effects have been discussed.

A continuum model of a metal with a dislocation cell structure has been proposed in order to describe strain path dependency effects. The model was developed throughout the chapters to incorporate the corresponding deformation mechanisms. The main components introduced in the cell structure model can be summarised as follows:

- Mean field approximation:
The mean response of a polycrystal material with a nonuniform dislocation structure is described by means of the mechanical behaviour of a model material containing uniform dislocation cells. The geometry and the orientation of the modelled cells represent the average morphology of a real cell structure in a polycrystal.
- Composite model:
A material with a dislocation cell structure is idealised as a two-phase periodic composite, consisting of cell walls and cell interiors, differing through their local dislocation densities. Traction continuity and compatibility of the deformation are enforced at the interfaces.
- Local material behaviour:
Consistent with the mean field approximation, the local material behaviour of the cell

and wall components is assumed to be uniform and is modelled by elastoplasticity, including isotropic and kinematic hardening. Two different approaches have been pursued: J_2 elastoplasticity and crystal plasticity. In both cases, the isotropic hardening is related to the local densities of the statistically stored dislocations, while the kinematic hardening is associated with the development of internal stresses.

- **Internal stresses:**
The internal stresses are derived as a natural result of the plastic deformation incompatibility between the cell interiors and the cell walls. These stresses are interpreted as the long-range effect of the geometrically necessary dislocations that appear at the interfaces to accommodate the discontinuities in the plastic deformation. The internal stresses are shown to be a function of the plastic deformation incompatibility and the cell geometry.
- **Dislocation density evolution:**
Physically-based evolution equations for the local density of the statistically stored dislocations are formulated to describe the formation of a dislocation structure under deformation and its dissolution upon load reversal.
- **Morphology evolution:**
Phenomenological evolution equations are proposed for the cell size and the wall thickness. The equations describe dislocation cell development under deformation and cell dissolution and disruption after a strain path change.

The model has been verified by simulating two-step tests with various strain path changes and comparing the results with experimental data for FCC metals. The model captures the essential features of the strain path change effects:

- An increased reloading yield stress after small to moderate strain path changes.
- A decreased reloading yield stress after large strain path changes, including load reversal.
- An increase of the effects with the amount of prestrain.
- A dependency of the effect on the amplitude of the strain path change.
- Transient hardening and hardening recovery after a strain path change.

The deformation behaviour of metals with a developing dislocation cell structure has been analysed using the cell structure model, leading to the following conclusions:

- The increased reloading yield stress after a moderate strain path change results from (1) the geometrical anisotropy due to the cell structure geometry, (2) the internal stresses developed during prestraining, (3) the transient structural dissolution expressed as an increase of the thicknesses of the cell walls.
- The decreased reloading yield stress after a large strain path change, which includes (partial) load reversal, is due to the internal stresses and the dissolution of the cell structure. The internal stresses, previously developed in the material during prestraining,

trigger local plastic yield in the cell interior at lowered applied stress values. The early slip in the cells then activates the dissolution of the structure, which includes dislocation remobilisation in the cells, a dislocation flux from the walls to the cells, and cell disruption expressed as an increase of the cell size. These mechanisms lower the macroscopic reloading yield stress.

- The transient hardening after a strain path change is mainly influenced by the adjustment of the internal stresses to the new loading. The evolution of the internal stresses in the cell interiors affects the deformation behaviour in the early stages after reloading, whereas the adjustment of the internal stresses in the walls governs the subsequent hardening behaviour. After a load reversal, the hardening rate is also lowered by a decrease of the dislocation density in the walls, caused by dissolution.
- The increase of the strain path change effect along with the amount of prestrain is related to an increase of the inhomogeneity caused by the development of a cell structure.
- Slip anisotropy influences the reloading deformation behaviour mostly due to its effect on the internal stress distribution.

The developed cell structure model has been shown to be a powerful tool for the theoretical study of the deformation behaviour of metals with a dislocation cell structure. The model predicts strain path change effects and offers a computationally efficient method which lends itself for application in macroscopic engineering computations.

This research dealt with a detailed study of the micromechanical mechanisms causing the strain path change dependency in metals with a dislocation cell structure. Each of the studied mechanisms has been incorporated in the proposed cell structure model and their contributions to the strain path change effects have been investigated. Obviously, the unique identification of all material parameters remains a challenge. To this purpose, the relative contributions of the deformation mechanisms to the macroscopic effects should be investigated further. The experimental data available in the literature was, unfortunately, rather incomplete to resolve this problem in this thesis. Further theoretical research, therefore, should be inevitably combined with a thorough experimental study.

Based on the analyses performed and the results obtained, the following issues are recommended for further investigation:

- The cell structure geometry evolution has been proven to have a significant contribution to the deformation behaviour after a strain path change. A phenomenological model for the development of the structure has been proposed in Chapter 3, describing both the dissolution and the disruption. The model can be improved by a more physically-based approach. Additionally, as was emphasized in Chapter 4, the prediction of the transient hardening behaviour should be improved by taking into account the cell structure reorientation after a strain path change.
- The development of the cell structure under deformation causes an increase of the strain path change effect with an increase of the amount of prestrain. The development of the cell structure has been modelled with a phenomenological evolution equation for the dislocation flux from the cell interior to the walls. An improvement of this equation is required if a better prediction of the related macroscopic effect is desired.

-
- The cell structure model can be used for further research of strain path change effects. For instance, this thesis includes results obtained using cubic cells with equally thick cell walls. The model, however, is not restricted to this simplification and less regular geometries can be considered as well.
 - The cell structure model can be used to investigate the thermodynamical concept of the cell structure evolution. The approach used in the subsection “Internally stored energy as a function of the cell geometry” in Chapter 4 can be further developed to investigate the evolution of the structure, if this evolution driven by an energy minimisation during each deformation increment (power minimisation).
 - To investigate formability properties on the basis of a cell structure model and the crystallographic texture, this model can be incorporated in a predictive tool for the assessment of forming limits as developed in Chapter 2.

Bibliography

- Abdi, R.E. and Samrout, H., (2000). *A non-linear kinematic hardening model for a steel under complex loading*. Computers and Structures, 76: pp. 675–681.
- Acharya, A. and Bassani, A.J., (2000). *Lattice incompatibility and a gradient theory of crystal plasticity*. Journal of the Mechanics and Physics of Solids, 48: pp. 2213–2230.
- Argaman, N., Levy, O., and Makov, G., (2001). *When do 2D dislocations form cellular structures?* Materials Science and Engineering, A309-310: pp. 386–392.
- Argon, A.S. and Haasen, P., (1993). *A new mechanism of work hardening in the late stages of large strain plastic flow in (FCC) and diamond cubic crystals*. Acta Metallurgica et Materialia, 41(11): pp. 3289–3306.
- Arsenlis, A. and Parks, D. M., (1999). *Crystallographic aspects of geometrically-necessary and statistically-stored dislocation density*. Acta Materialia, 47(5): pp. 1597–1611.
- Arsenlis, A., Parks, D.M., Becker, R., and Bulatov, V.V., (2004). *On the evolution of crystallographic dislocation density in non-homogeneously deforming crystals*. Journal of the Mechanics and Physics of Solids, 52: pp. 1213–1246.
- Asaro, R. J. and Needleman, A., (1985). *Texture development and strain hardening in rate dependent polycrystals*. Acta Metallurgica, 33: pp. 923–953.
- Asaro, R. J. and Rice, J. R., (1977). *Strain localization in ductile single crystals*. International Journal of Solids and Structures, 25: pp. 309–338.
- Barker, I., Hansen, N., and Ralph, B., (1989). *The development of deformation substructures in face-centred cubic metals*. Materials Science and Engineering, A113: pp. 449–454.
- Barlat, F., Ferreira Duarte, J.M., Gracio, J.J., Lopes, A.B., and Rauch, E.F., (2003). *Plastic flow for non-monotonic loading conditions of an aluminium alloy sheet sample*. International Journal of Plasticity, 19: pp. 1215–1244.
- Barlat, F., (1987). *Crystallographic texture, anisotropic yield surfaces and forming limits of sheet metals*. Materials Science and Engineering, 91: pp. 55–72.
- Bassani, J.L., (2001). *Incompatibility and a simple gradient theory of plasticity*. Journal of the Mechanics and Physics of Solids, 49: pp. 1983–1996.
- Bate, P.S. and Wilson, D.V., (1986). *Analysis of the Bauschinger effect*. Acta Metallurgica, 34(6): pp. 1097–1105.
- Bate, P.S., (1993). *The effect of combined strain-path and strain-rate changes in Aluminium*. Metallurgical Transactions A, 24A: pp. 2679–2689.
- Bay, B., Hansen, N., and Kuhlmann-Wilsdorf, D., (1992). *Microstructural evolution in rolled aluminium*. Materials Science and Engineering, A158: pp. 139–146.
- Bergstrom, Y., (1983). *Reviews on powder metallurgy and physical ceramics: The plastic deformation of metals*, volume 2. Guildford, Surrey GU2 5XH, England.

- Besseling, J.F. and Giessen, E. van der, (1994). *Mathematical Modelling of Inelastic Deformation*. Applied Mathematics and Mathematical Computation. Chapman & Hall.
- Borbely, A., Hoffmann, G., Aernoudt, E., and Ungar, T., (1997). *Dislocation arrangement and residual long-range internal stresses in copper single crystals at large deformations*. *Acta Materialia*, 45(1): pp. 89–98.
- Borbely, A., Maier, H.J., Renner, H., Straub, S., Ungar, T., and Blum, W., (1993). *Long-range internal stresses in steady-state subgrain structure*. *Scripta Metallurgica et Materialia*, 29: pp. 7–12.
- Boudeau, N. and Gelin, J.C., (2000). *Necking in sheet metal forming. Influence of macroscopic and microscopic properties of materials*. *International Journal of Mechanical Science*, 42: pp. 2209–2232.
- Bronkhorst, C.A., Kalidindi, S.R., and Anand, L., (1992). *Polycrystalline plasticity and the evolution of crystallographic texture in FCC metals*. *Philosophical Transactions of the Royal Society of London A*, 341: pp. 443–477.
- Christodoulou, N., Woo, O.T., and MacEwen, S.R., (1986). *Effect of stress reversals on the work hardening behaviour of polycrystalline copper*. *Acta Metallurgica*, 34(8): pp. 1553–1562.
- Chun, B.K., Jinn, J.T., and Lee, J.K., (2002). *Modelling of the Bauschinger effect for sheet metals, part I: Theory*. *International Journal of Plasticity*, 18: pp. 571–595.
- Driver, J.H., Jensen, D.J., and Hansen, N., (1994). *Large strain deformation structures in aluminium crystals with rolling texture orientations*. *Acta Metallurgica et Materialia*, 42(9): pp. 3105–3114.
- Estrin, Y., Toth, L.S., Molinari, A., and Brechet, Y., (1998). *A dislocation-based model for all hardening stages in large strain deformation*. *Acta Materialia*, 46(15): pp. 5509–5522.
- Evers, L.P., Parks, D.M., Brekelmans, W.A.M., and Geers, M.G.D., (2002). *Crystal plasticity model with enhanced hardening by geometrically necessary dislocation accumulation*. *Journal of the Mechanics and Physics of Solids*, 50: pp. 2403–2424.
- Fernandes, J.V., Gracio, J.J., and Schmitt, J.H., (1993). *Development and persistence of microbands in copper deformed under complex strain paths*. *Scripta Metallurgica et Materialia*, 28: pp. 1335–1340.
- Fernandes, J.V., Rodrigues, D.M., Menezes, L.F., and Vieira, M.F., (1998). *A modified Swift law for prestrained materials*. *International Journal of Plasticity*, 14(6): pp. 537–550.
- Franciosi, P. and Zaoui, A., (1982). *Multislip in FCC crystals; a theoretical approach compared with experimental data*. *Acta Metallurgica*, 30: pp. 1627–1637.
- Fressengeas, C. and Molinari, A., (1987). *Instability and localisation of plastic flow in shear at high strain rates*. *Journal of the Mechanics and Physics of Solids*, 35: pp. 185–211.
- Friedman, P.A. and Pan, J., (2000). *Effect of plastic anisotropy and yield criteria on prediction of forming limit curves*. *International Journal of Mechanical Science*, 42: pp. 29–48.
- Gänsler, H.P., Werner, E.A., and Fecher, F.D., (2000). *Forming limit diagrams: A micromechanical approach*. *International Journal of Mechanical Sciences*, 42: pp. 2041–2054.
- Geers, M.G.D., Viatkina, E.M., and Brekelmans, W.A.M., (2005). *Microstructural instabilities: dislocation substructures with pronounced mechanical effects*. *Philosophical Magazine A*. (accepted).
- Godfrey, A., Jensen, D.J., and Hansen, N., (1998). *Slip pattern, microstructure and local crystallography in an aluminium single crystal of copper orientation $\{112\}\{111\}$* . *Acta Materialia*, 46(3): pp. 835–848.
- Goerdeler, M. and Gottstein, G., (2001). *A microstructural work hardening model based on three internal state variables*. *Materials Science and Engineering*, A309-310: pp. 377–381.
- Groma, I. and Balogh, P., (1999). *Investigation of dislocation pattern formation in a two-dimensional self-consistent field approximation*. *Acta Materialia*, 47(13): pp. 3647–3654.
- Hansen, N., Huang, X., and Hughes, D.A., (2001). *Microstructural evolution and hardening parameters*. *Materials Science and Engineering*, A317: pp. 3–11.

- Hansen, N. and Huang, X., (1997). *Dislocation structures and flow stress*. Materials Science and Engineering, A234-236: pp. 602–605.
- Harder, J., (1999). *A crystallographic model for the study of local deformation processes in polycrystals*. International Journal of Plasticity, 15: pp. 605–624.
- Hasegawa, T., Yakou, T., and Karashima, S., (1975). *Deformation behaviour and dislocation structures upon stress reversal in polycrystalline aluminium*. Materials Science and Engineering, 20: pp. 267–276.
- Hasegawa, T., Yakou, T., and Kocks, U.F., (1986). *Forward and reversal rearrangements of dislocations in tangled walls*. Materials Science and Engineering, 81: pp. 189–199.
- Hecker, M. and Burmeister, H.J., (1996). *Strain localization and internal stress fields in persistent slip bands*. Physica Status Solidi A, 158: pp. 87–100.
- Hecker, M., Thiele, E., and Hoste, C., (2002). *Investigating of the tensor character of mesoscopic internal stresses in tensile-deformed nickel single crystal by X-ray diffraction*. Acta Materialia, 50: pp. 2357–2365.
- Hill, R. and Rice, J. R., (1972). *Constitutive analysis of elastic-plastic crystals at arbitrary strain*. Journal of the Mechanics and Physics of Solids, 20: pp. 401–413.
- Hill, R., (1952). *On discontinuous plastic states with special reference to localised necking in thin sheets*. Journal of the Mechanics and Physics of Solids, 1: pp. 19–30.
- Hill, R., (1958). *A general theory of uniqueness and stability in elastic-plastic solids*. Journal of the Mechanics and Physics of Solids, 6: pp. 236–249.
- Huang, X. and Hansen, N., (1997). *Grain orientation dependence of microstructure in aluminium deformed in tension*. Scripta Materialia, 37(1): pp. 1–7.
- Hughes, D.A., Liu, Q., Chrzan, D.C., and Hansen, N., (1997). *Scaling of the microstructural parameters: Misorientations of deformation induced boundaries*. Acta Materialia, 45(1): pp. 105–112.
- Hull, D. and Bacon, D.J., (2001). *Introduction to dislocations*. Oxford: Butterworth Heinemann.
- Hurley, P.J., Bate, P.S., and Humphreys, F.J., (2003). *An objective study of substructural boundary alignment in aluminium*. Acta Materialia, 51: pp. 4737–4750.
- Hutchinson, J. and Neale, K. W., (1978). *Mechanics of sheet metal forming*. In *Sheet necking*, pp. 127–153. New York: Plenum Press.
- Inal, K., Wu, P.D., and Neale, K. W., (2002)a. *Instability and localized deformation in polycrystalline solids under plane-strain tension*. International Journal of Solids and Structures, 39: pp. 983–1002.
- Inal, K., Wu, P.D., and Neale, K. W., (2002)b. *Finite element analysis of localization in FCC polycrystalline sheet under plane stress tension*. International Journal of Solids and Structures, 39: pp. 3469–3486.
- Jackson, P.J. and Siedersleben, M., (1984). *The stability of dislocation cell boundaries in FCC crystals*. Scripta Metallurgica, 18: pp. 749–754.
- Jackson, P.J., (1985). *Dislocation modelling of shear in FCC crystals*. Progress in Materials Science, 29: pp. 139–175.
- Jensen, D.J. and Hansen, N., (1990). *Flow stress anisotropy in aluminium*. Acta metallurgica et Materialia, 38(8): pp. 1369–1380.
- Kalidindi, S.R., Bronkhorst, C.A., and Anand, L., (1992). *Crystallographic texture evolution in bulk deformation processing of FCC metals*. Journal of the Mechanics and Physics of Solids, 40: pp. 537–569.
- Kocks, U. F., (1970). *The relation between polycrystal deformation and single crystal deformation*. Metallurgical Transactions, 1: pp. 1121–1144.
- Kröner, E., (1981). *Continuum theory of defects*, pp. 217–315. North Holland Publishing Company.

- Kuhlmann-Wilsdorf, D., (1996). *Dislocation cells, redundant dislocations and the LEDS hypothesis*. Scripta Materialia, 34(4): pp. 641–650.
- Kuroda, M. and Tvergaard, V., (2000)a. *Effect of strain path change on limits to ductility of anisotropic metal sheets*. International Journal of Mechanical Science, 42: pp. 867–887.
- Kuroda, M. and Tvergaard, V., (2000)b. *Forming limit diagrams for anisotropic metal sheets with different yield criteria*. International Journal of Solid and Structures, 37: pp. 5037–5059.
- Laukonis, J.V. and Ghosh, A.K., (1978). *Effects of strain path changes on the formability of sheet metals*. Metallurgical Transactions A, 9A: pp. 1849–1856.
- Lee, E.H., (1969). *Elastic-plastic deformation at finite strains*. Journal of Applied Mechanics, 36: pp. 1–6.
- Lewandowska, M., (2003). *Dependence of the deformation microstructure of aluminium alloys on the strain path*. Materials Chemistry and Physics, 81(2-3): pp. 555–557.
- Li, F. and Bate, P.S., (1991). *Strain path change effect in cube textured aluminium sheet*. Acta Metallurgica et Materialia, 39(11): pp. 2639–262650.
- Liu, Q. and Hansen, N., (1995). *Geometrically necessary boundaries and incidental dislocation boundaries formed during cold deformation*. Scripta Metallurgica et Materialia, 32(8): pp. 1289–1295.
- Liu, Q., Jensen, D.J., and Hansen, N., (1998). *Effect of grain orientation on deformation structure in cold-rolled polycrystalline aluminium*. Acta Materialia, 46(16): pp. 5819–5838.
- Lubarda, V.A. and Kouris, D.A., (1996). *Stress fields due to dislocation walls in infinite and semi-infinite bodies*. Mechanics of Materials, 23: pp. 169–189.
- Marciniak, Z. and Kuczynski, K., (1967). *Limit strains in the process of stretch-forming sheet metal*. International Journal of Mechanical Sciences, 9: pp. 609–620.
- Marciniak, Z.A., Duncan, J.L., and Hu, S.J., (1992). *Mechanics of sheet metal forming*. Edward Arnold, London.
- Marukawa, K. and Sanpei, T., (1971). *Stability of the work hardened state against stress reversal in copper single crystals*. Acta Metallurgica, 19: pp. 1169–1174.
- McCabe, R.J., Misra, A., and Mitchell, T.E., (2004). *Experimentally determined content of a geometrically necessary dislocation boundary in copper*. Acta Materialia, 52: pp. 705–714.
- Mesrar, R., Fromentin, S., Makkouk, R., Martiny, M., and Ferron, G., (1998). *Limits to the ductility of metals sheets subjected to complex strain-paths*. International Journal of Plasticity, 14(4-5): pp. 391–411.
- Michalak, J.T., (1965). *The influence of temperature on the development of long-range internal stress during the plastic deformation of high-purity iron*. Acta Metallurgica, 13(3): pp. 213–222.
- Mollica, F., Rajagopal, K.R., and Srinivasa, A.R., (2001). *The inelastic behaviour of metals subject to loading reversal*. International Journal of Plasticity, 17: pp. 1119–1146.
- Mughrabi, H., Ungar, T., and Wilkens, W., (1986). *Long-range internal stresses and asymmetric X-ray line-broadening in tensile-deformed [001]-oriented copper single crystals*. Philosophical Magazine A, 53(6): pp. 793–813.
- Mughrabi, H., (2001). *Self-consistent experimental determination of the dislocation line tension and long-range internal stresses in deformed copper crystals by analysis of dislocation curvatures*. Material Science and Engineering, A 309-310: pp. 237–245.
- Mughrabi, H., (1983). *Dislocation wall and cell structure and long-range internal stresses in deformed metal crystals*. Acta Metallurgica, 31(9): pp. 1367–1379.
- Mughrabi, H., (1987). *A two-parameter description of heterogeneous dislocation distributions in deformed metal crystals*. Materials Science and Engineering, 85: pp. 15–31.
- Müller, M., Zehetbauer, M., Borbely, A., and Ungar, T., (1996). *Stage IV work hardening in cell forming*

- materials, Part I: features of the dislocation structure determined by X-Ray line broadening.* Scripta Materialia, 35(12): pp. 1461–1466.
- Mura, T., (1987). *Micromechanics of defects in solids.* Martinus Nijhoff Publishers.
- Myint-U, T. and Debnath, L., (1987). *Partial differential equations for scientists and engineers.* Amsterdam: North Holland.
- Nabarro, F.R.N., (1967). *Theory of crystal dislocations.* Oxford University Press, Oxford.
- Neumann, P., (1985). *Low energy dislocation configurations: a possible key to the understanding of fatigue.* Materials Science and Engineering, 81: pp. 465–475.
- Nye, J.F., (1953). *Some geometrical relations in dislocated crystals.* Acta Metallurgica, 1: pp. 153–162.
- Park, N.K. and Parker, B.A., (1989). *The development of the deformed microstructure in commercially pure nickel.* Materials Science and Engineering, A113: pp. 431–439.
- Pedersen, O.B., Brown, L.M., and Stobbs, W.M., (1981). *The Bauschinger effect in copper.* Acta Metallurgica, 29: pp. 1843–1850.
- Peeters, B., (2002). *Multiscale modelling of the induced plastic anisotropy in (IF) steel during sheet forming.* Ph.D. thesis, Katholieke Universiteit Leuven.
- Prinz, F., Argon, A.S., and Moffatt, W.C., (1982). *Recovery of dislocation structures in plastically deformed copper and nickel single crystals.* Acta Metallurgica, 30: pp. 821–830.
- Raphanel, J.L., Rauch, E., Shen, E.L., and Schmitt, J.-H., (1987). *Shear of prestrained steel specimens.* Scripta Metallurgica, 21: pp. 1087–1090.
- Rauch, E.F., Gracio, J.J., Barlat, F., Lopes, A.B., and Ferreira Duarte, J., (2002). *Hardening behaviour and structural evolution upon strain reversal of aluminum alloys.* Scripta Materialia, 46: pp. 881–886.
- Rice, J.R., (1971). *Inelastic constitutive relations for solids: an internal variable theory and its application to metal plasticity.* Journal of the Mechanics and Physics of Solids, 19: pp. 433–455.
- Roters, F., Raabe, D., and Gottstein, G., (2000). *Work hardening in heterogeneous alloys - a microstructural approach based on three internal state variables.* Acta Materialia, 48: pp. 4181–4189.
- Schmitt, J.H., Fernandes, J.V., Gracio, J.J., and Vieira, M.F., (1991). *Plastic behaviour of copper sheets during sequential tension tests.* Materials Science and Engineering, A147: pp. 143–154.
- Sedláček, R. and Blum, W., (2002). *Microstructure-based constitutive law of plastic deformation.* Computational Materials Science, 25: pp. 200–206.
- Sedláček, R. and Blum, W., (1998). *Internal stresses in dislocation subgrain structures.* Computational Material Science, 13: pp. 148–153.
- Sedláček, R. and Forest, S., (2000). *Non-local plasticity at microscale: A dislocation-based and a Cosserat model.* Physica Status Solidi B, 221: pp. 583–596.
- Sedláček, R. and Hecker, M., (1998). *Stress field of tilted dislocation walls.* Computational Materials Science, 11: pp. 270–276.
- Sedláček, R., (1995). *Internal stresses in dislocation wall structures.* Scripta Metallurgica et Materialia, 33(2): pp. 283–288.
- Sedláček, R., (1996). *Internal stresses in dislocation walls structure of persistent slip bands.* Computational Material Science, 7: pp. 21–26.
- Seeger, A., Diehl, J., Mader, S., and Rebstock, H., (1957). *Workhardening and worksoftening of face-centered cubic metal crystals.* Philosophical Magazine, 2: p. 323.
- Steinmann, P., (1996). *Views on multiplicative elastoplasticity and the continuum theory of dislocations.* International Journal of Engineering Science, 34(15): pp. 1717–1735.
- Stören, S., (1975). *Localized necking in the thin sheets.* Journal of the Mechanics and Physics of Solids, 23: pp. 421–441.

- Straub, S., Blum, W., Maier, H.J., Ungar, T., Borbely, A., and Renner, H., (1996). *Long-range internal stresses in cell and subgrain structures of copper during deformation at constant stress*. *Acta Materialia*, 44(11): pp. 4337–4350.
- Taylor, G.I. and Elam, C.F., (1923). *The distortion of an aluminium crystal during a tensile test*. *Proceedings of the Royal Society of London*, 102A: pp. 643–667.
- Teodosiu, C. and Hu, Z., (1995). Evolution of the intragranular microstructure at moderate and large strains: Modelling and computational significance. In Shen and Dawson, editors, *Simulation of Materials Processing: Theory, Methods and Applications*. Balkema, Rotterdam.
- Teodosiu, C., Raphanel, J.L., and Tabourot, L., (1993). *Finite element simulation of the large elastoplastic deformation of multicrystals*. Balkema.
- Ungar, T., Mughrabi, H., Ronnpagel, D., and Wilkens, M., (1984). *X-Ray line-broadening study of the dislocation cell structure in deformed [001]-oriented copper single crystals*. *Acta Metallurgica*, 32(3): pp. 333–342.
- Van Dommelen, J.A.W. van, Brekelmans, W.A.M., and Baajens, F.P.T., (2003). *Micromechanical modelling of the elasto-viscoplastic behavior of semi-crystalline polymers*. *Journal of Mechanics and Physics of Solids*, 51: pp. 519–541.
- Viatkina, E.M., Brekelmans, W.A.M., and Geers, M.G.D., (2005)a. *A crystal plasticity based estimate for forming limit diagrams from textural inhomogeneities*. *Journal of Materials Processing Technology*, 168: pp. 211–218.
- Viatkina, E.M., Brekelmans, W.A.M., and Geers, M.G.D., (2003). *Strain path dependency in metal plasticity*. *Journal de Physique IV*, 105: pp. 355–362.
- Viatkina, E.M., Brekelmans, W.A.M., and Geers, M.G.D., (2005)b. *Modelling of the internal stress in dislocation cell structures*. Submitted.
- Viatkina, E.M., Brekelmans, W.A.M., and Geers, M.G.D., (2005)c. *Modelling the dislocation structure evolution under stress reversal*. Submitted.
- Vieira, M.F., Fernandes, J.V., and Chaparro, B., (2000). *Yield stress after double strain-path change*. *Material Science and Engineering*, A284: pp. 64–69.
- Vieira, M.F., Schmitt, J.H., Gracio, J.J., and Fernandes, J.V., (1990). *The effect of strain path change on the mechanical behaviour of copper sheets*. *Journal of Materials Processing Technology*, 24: pp. 313–322.
- Wert, J.A., Liu, Q., and Hansen, N., (1995). *Dislocation boundaries and active slip systems*. *Acta Metallica et Materialia*, 43(11): pp. 4153–4163.
- Wilson, D.V., Zandrahimi, M., and Roberts, W.T., (1990). *Effect of changes in strain path on work-hardening in CP aluminium and an Al-Cu-Mg alloy*. *Acta Metallurgica et Materialia*, 38(2): pp. 215–226.
- Winther, G., Huang, X., and Hansen, N., (2000). *Crystallographic and macroscopic orientation of planar dislocation boundaries - correlation with grain orientation*. *Acta Materialia*, 48: pp. 2187–2198.
- Winther, G., (2003). *Slip patterns and preferred dislocation boundary planes*. *Acta Materialia*, 51: pp. 417–429.
- Wu, P.D., Naele, K.W., and Giessen, E. van der, (1997). *On crystal plasticity FLD analysis*. *Proceedings of the Royal Society of London A*, 453: pp. 1831–1848.
- Wu, P.D., Neale, K.W., and Giessen, E. van der, (1998). *Effects of strain paths on sheet metal limit strains*, chapter *Material Instabilities in Solids*, pp. 243–253. John Wiley & Sons Ltd.
- Xu, S. and Weinmann, K.J., (2000). *Effect of deformation-dependent material parameters on forming limits of thin sheets*. *International Journal of Mechanical Science*, 42: pp. 677–692.
- Young, C.T., Headley, T.J., and Lytton, J.L., (1986). *Dislocation substructures formed during the flow stress recovery of high purity aluminum*. *Materials Science and Engineering*, 81: pp. 391–407.

- Zandrahimi, M., Platias, S., Price, D., Barrett, D., Bate, P.S., Pobergs, W.T., and Wilson, D.V., (1989). *Effect of changes in strain path on work hardening in cubic metals*. Metallurgical Transactions A, 20A: pp. 2471–2482.
- Zhao, L., Sowerby, R., and Sklad, M.P., (1996). *A theoretical and experimental investigation of limit strains in sheet metal forming*. International Journal of Mechanical Science, 38(12): pp. 1307–1317.
- Zhou, Y. and Neale, K.W., (1995). *Predictions of forming limit diagrams using a rate-sensitive crystal plasticity model*. International Journal of Mechanical Sciences, 37(1): pp. 1–20.
- Zhu, Q. and Sellars, C.M., (2001). *Evolution of microbands in high purity aluminium-3magnesium during hot deformation testing in tension-compression*. Scripta Materialia, 45(1): pp. 41–48.
- Zimmer, W.H., Hecker, S.S., Rohr, D.L., and Murr, L.E., (1983). *Large strain plastic deformation of commercial pure nickel*. Metal Science, 17: pp. 198–206.

Acknowledgements

I would sincerely like to thank Marc Geers and Marcel Brekelmans for their guidance and many fruitful discussions that shaped this project and helped bring it to completion. I especially appreciate Marcel's kindness, his everyday support and the hard work he put into the proof reading of this thesis.

I would like to express my gratitude to all the other members of my PhD committee, Prof.Dr.Ir. E. van der Giessen, Prof.Dr.Ir. P. van Houtte, Dr.Ir. A. van de Ven, Prof.Dr.Ir. E. Busso, Prof.Ir. L. Katgerman, for their valuable comments and constructive criticism.

I would specially like to thank my boyfriend and most valuable colleague René Ubachs. I can not overestimate his contribution in this project. Many scientific discussions with him gave me inspiration for this work, while his love and patience helped me to get through hard times of doubts and frustration.

Many thanks go to my family. I am greatly indebted to my parents for allowing me to carry out this research far-far away from home without ever complaining. Their unconditional love, support and faith were my inspiration through all these years. I also want to thank Berthie and Chris for becoming my caring and warm family far away from home.

Last, but not least, I would like to thank all those people who stood by my side all these years. I thank all my friends for their patience and support, specially Larisa and Varya. I am grateful to my MaTe colleagues and friends who made the university a happier place for me, in particular Vinayak, Adnan, Ceren, Tibor, Sebastiaan, Edwin, Yuriy, Jesus, Müge, Roel and Ron. And, a big thanks goes to my current colleagues from Takumi Technology for their support and understanding.

Katja Viatkina

Eindhoven, December 2005.

Curriculum Vitae

- 13 June 1976 Born in Perm, Russia
- 1983 – 1991 Primary and secondary school
Perm, Russia
- 1991 – 1993 Lyceum
Perm State Technical University, Russia
- 1993 – 1999 Bachelor's and Engineering Degree in Applied Mathematics
Department of Mathematical Modelling of Systems and Processes
Perm State Technical University, Russia
- 1997 – 2000 Research assistant
Perm State Technical University, Russia
- 2000 – 2004 PhD, Mechanical Engineering
Eindhoven, University of Technology